université
PARIS-SACLAY

UNIVERSITÉ PARIS SUD
Comprendre le monde, construire l'avenir

NNT : 2018SACLS104

Le mouvement des parois des domaines magnétiques dans le fil de CoFeB induit par le courant polarisé

Spin-polarized current-induced domain wall motion in CoFeB nanowires

Thèse de doctorat de l'Université Paris-Saclay
préparée à Université Paris-Sud

École doctorale n°575 : electrical, optical, bio - physics and engineering (EOBE)
Spécialité de doctorat: Physique

Thèse présentée et soutenue à Orsay, le 15 Mai 2018, par

Xueying Zhang

Composition du Jury :

Vincent Jeudy Professeur, Université Paris-Saclay	Président
Catherine Gourdon Directeur de recherche, Université Pierre et Marie Curie-Paris 6	Rapporteur
Vincent Repain Professeur, Université Paris Diderot – Paris 7	Rapporteur
Stefania Pizzini Directeur de recherche, Institut Néel	Examinateur
Salim Mourad Chérif Professeur, Université Paris 13	Examinateur
Nicolas Vernier Maître de Conférence, HDR , Université Paris-Saclay	Directeur de thèse
Weisheng Zhao Professeur, Université de Beihang	Co-Directeur de thèse

Thèse de doctorat

Université Paris-Saclay
Espace Technologique / Immeuble Discovery
Route de l’Orme aux Merisiers RD 128 / 91190 Saint-Aubin, France

Remerciements

Je souhaite commencer ce manuscrit par adresser mes remerciements sincères aux personnes qui m’ont beaucoup aidé depuis quatre ans et qui ont contribué à l’achèvement de ce mémoire. Cette thèse a été menée dans le cadre de la coopération entre le centre de nanoscience et nanotechnologie (C2N) de l’Université Paris-Saclay et le Fert Beijing Institute de l’Université de Beihang.

Je voudrais tout d’abord adresser mes remerciements à mes directeurs de thèse Monsieur Nicolas Vernier, Professeur à l’Université Paris-Saclay et Monsieur Weisheng Zhao, Professeur à l’Universié de Beihang, qui m’ont accueilli dans leur équipe et qui m’ont soutenu tout au long des quatre ans de travail. J’ai commencé des recherche sur le magnétisme en 2014 sous la direction de M. Weisheng Zhao, qui m’a aidé à former des connaissance foundamentales sur le magnétisme, la spintronique et des méthode de recherche via simulations micromagnétique. En 2015, je commence des recherches expérimentales sur des parois du domaine magnétique sous la direction de M. Nicolas Vernier, qui a développé une microscope de Kerr très puissant et qui m’a appris des techniques de microscopie de Kerr, des technologies pour appliquer du champ magnétique et faire simultanément des tests électriques, des méthodes de recherche expérimentales sur la paroi du domaine. Tous les résultats dans cette thèse ont été obtenus sous la direction patiente de mes deux encadrants. Je tiens à les remercier également de m’avoir aidé à exploiter des démarches de recherche scientifique et à résoudre des problèmes scientifiques ou administratifs.

Je voudrais aussi adresser mes remerciements à Monsieur Dafiné Ravelosona, professeur à l’Université Paris-Saclay, qui m’a accueilli et qui m’a donné beaucoup de conseils précieux pendant la recherche de la thèse.

Je voudrais ensuite remercier les membres de mon jury de leur temps consacré à ma thèse. Je remercie particulièrement, mes rapporteurs professeurs Catherine Gourdon et professeur Vincent Repain pour le regard critique et leurs remarques constructives sur mon travail. Je remercie également Professeur Vincent Jeudy, professeur Stefania Pizzini, et professeur Mourad Cherif qui ont gentiment accepté d’examiner mes travaux de thèse.

J’aimerais aussi adresser mes remerciements à Monsieur Laurent Vila, qui a aidé à concevoir et fabriquer des nanostructures testées dans ce recherche, Monsieur Vincent Jeudy, qui m’a appris des connaissance sur le mouvement de paroi dans le régime transition de dépiégeage et qui m’a aidé à analyser des results expérimentals, Monsieur Bonan Yan, qui m’a appris à utiliser le logiciel Mumax3, Monsieur Yue Zhang, avec qui nous avons conçu la mémoire de racetrack de forme annulaire, Monsieur Qunwen

Leng, qui m’a donné des conseils sur le design de la capteur à base de l’élasticité de paroi du domaine, Monsieur Yu Zhang, pour les discussions sur des techniques de nano-fabrication et notre coopération sur la recherche du renversement magnétique des nanodots.

Un grand merci à l'atelier du C2N. Grâce à leur travail scrupuleux et efficace, la fabrication et la mis en place des appareil expérimentaux ont été possibles. Aussi, Je tiens à remercier tous mes collègues de C2N et de l’Université de Beihang, de leur gentillesse et de leur accompagnement. Leurs conseils voire les causeries menés pendant les déjeuners ou les pauses, qui ont beaucoup enrichi mes connaissances profesionnelles ainsi que ma vie quotidienne. Cela a été un grand plaisir de travailler avec eux.

Naturellement, je voudrais aussi remercier tous mes amis chinois et français: Ping Che, Sylvain Eimer, Gefei Wang, Qi An, Jiaqi Zhou, You Wang, Boyu Zhang, Chenghao Wang, Zhiqiang Cao... pour leur accompagnement durant les quatre ans.

Un grand merci à China Scholarship Council (CSC) pour son support de financement pendent ma recherche en France.

Enfin, je souhaite exprimer profonde gratitude à ma famille, dont notamment, mes parents, M. Cheng Zhang et Mme Shuchun Wang, qui m’ont accompagné et soutenu sans condition depuis toujours.

Symbols

α: Damping constant

γ: Gyromagnetic ratio

γ_{DW}: DW surface energy

θ_{SH}: Spin Hall angle

μ: Exponent constant of the creep law

μ_0: Permeability of vacuum

μ_B: Bohr magneton

$\vec{\boldsymbol{\mu}}_m$: Magnetic moment

ξ: Non adiabatic constant

ρ: Resistivity

σ: Conductivity

$\vec{\sigma}_{SH}$: Polarizing direction of the spin Hall current

τ: Spin torque

χ: DW tilting angle

φ: Azimuthal angle of magnetization

θ: Zenith angle of magnetization

ϕ': Kerr rotation

ϕ'': Kerr ellipticity

$\hbar$: Reduced Planck constant

A_{ex}: Exchange stiffness constant

B: Magnetic flux density

B_{ext}: Externally applied field

D: DMI constant

e: Electric charge

E_{ex}: Exchange energy

E_k: Anisotropy energy

E_d: Demagnetizing energy

E_{Zeem}: Zeeman energy

E_{DM}: DMI energy

F_{pin}: Pinning force

g: Landau factor

H: Magnetic field

H_{DM}: Effective DMI field

H_{demag}: Demagnetizing field

H_{ext}: Externally applied field

H_{p_intr}: Intrinsic pinning field

H_K: Anisotropy field

H_{dep}: Depinning field

I: Electric current

j: Current density

j_{HM}: Current density in heavy metal layer

j_{SH}: Spin Hall current density

j_{STT}: Current density for spin transfer torque

K_U: Uniaxial anisotropy

K_{eff}: Effective anisotropy field

k_B: Boltzmann constant

l: Length

$\vec{m}$: Reduced magnetization vector

$\vec{m}_{DW}$: Magnetic direction in the center of DW

$\vec{M}$: Magnetization

M_S: Saturation magnetization

P: Polarization ratio

P_γ: Laplace pressure associated to DW surface energy

R_{coil}: Resistance of coil

t: Time

t_M: Thickness of ferromagnetic layer

T: Temperature

T_C: Curie temperature

v: DW motion velocity

w: width

Acronyms

AD-STT: Adiabatic Spin Transfer Torque

BLS: Brillouin Light Scattering

BW: Block Wall

DMI: Dzyaloshinskii-Moriya Interaction

DW: Domain Wall

FM: FerroMagnetic

FMR: FerroMagnetic Resonance

GMR: Giant MagnetoResistance

HM: Heavy Metal

MTJ: Magnetic Tunnel Junction

NA-STT: Non-Adiabatic Spin Transfer Torque

NW: Néel Wall

PMA: Perpendicular Magnetic Anisotropy

RM: Racetrack Memory

SAF: Synthetic AntiFerromagnetic

SH: Spin Hall

SHE: Spin Hall Effect

SOC: Spin-Orbit Coupling

SOI: Spin-Orbit Interaction

SOT: Spin-Orbit Torque

SQUID: Superconducting Quantum Interference Device

STT: Spin Transfer Torque

TMR: Tunneling MagnetoResistance

VSM: Vibrating Sample Magnetometer

1D model: One Dimension model

Contents

Abstract

This thesis is dedicated to the research of the static and dynamic properties of magnetic Domain Walls (DWs) in CoFeB nanowires. A measurement system based on a high-resolution Kerr microscope was implemented and used for these research.

First, phenomena related to the DW surface tension was studied. A spontaneous collapse of domain bubbles was directly observed using the Kerr microscope. This phenomenon was explained using the concept of the Laplace pressure due to the DW surface energy. The surface energy of DW was quantified by measuring the external field required to stabilize these bubbles. The DW pinning and depinning mechanism in some artificial geometries, such as the Hall cross or the entrance connecting a nucleation pad and a wire, was explained using the concept of DW surface tension and was used to extract the DW surface energy. Benefited from these studies, a method to directly quantify the coefficient of Dzyaloshinskii- Moriya Interactions (DMI) using Kerr microscope has been proposed. In addition, a new type of magnetic sensor based on the revisable expansion of DW due to DW surface tension was proposed and verified using micromagnetic simulations.

Second, the dynamic properties of DWs in Ta/CoFeB/MgO film and wires were studied. The velocity of DW motion induced by magnetic fields or by the combined effect of synchronized magnetic field pulses and electrical current pulses was measured. In steady flow regime, the velocity of DW motion induced by the combined effect of the field and the current equals to the superposition of the velocities driven by field or current independently. This result allowed us to extract the spin-polarization of CoFeB in this structure. Pinning effects of DW motion in narrow wires was studied. Depinning fields of hard pinning sites for the field-driven DW motion in nanowires was measured. It was found that the pinning effects become severer as the width w of the wires scaled down. A linear relationship between the depinning field and w was found. The origin of these hard pinning sites, as well as their influences on the DW motion velocity, was discussed. Furthermore, it was found that the pinning effect was enhanced when a current was applied, no matter the relative direction between the DW motion and the current. We propose a possible explanation, which would be an effect of the spin Hall current from the sublayer (Ta). Although there was no DMI or in-plane field, the spin Hall current, which was polarized in the transverse direction, can still exert a torque on the Bloch DW, once the DW tilts away from the transverse direction.

At last, a ring-shaped racetrack memory based on the combined work of STT and has been proposed. Compared with the traditional line-shaped racetrack memory, this ring-shaped memory allows the DW moving in a ring-shaped nanowire and the data dropout problem can be avoided. The design and optimization work was performed with micromagnetic simulations.

Keywords: Domain Wall (DW), Kerr microscopy, CoFeB, Surface tension, Pinning effect, Spin transfer torque (STT), Spin-orbit torque (SOT), racetrack memory, magnetic sensor, Magnetism, Spintronics

Résumé

Cette thèse est consacrée aux recherches des propriétés statiques et dynamiques des parois de domaines magnétiques (DW pour Domain Wall) dans les nanofils CoFeB. Un système de mesure basé sur un microscope Kerr à haute résolution a été mis en place et utilisé pour ces recherches.

Tout d'abord, les phénomènes liés à la tension interfaciale des parois ont été étudiés. La contraction spontanée des bulles de domaine a été observée directement en utilisant le microscope Kerr. Ce phénomène a été expliqué en utilisant le concept de la pression de Laplace due à l'énergie interfaciale des parois. L'énergie interfaciale des parois a été quantifiée en mesurant le champ externe nécessaire pour stabiliser ces bulles. Le mécanisme de la piégeage et de la dépiégeage des parois dans certaines géométries artificielles, comme la croix de Hall ou l'entrée reliant un carré de nucléation et un fil, a été expliqué en utilisant le concept de tension interfaciale des parois et a été utilisé pour extraire l'énergie interfaciale des parois. Bénéficiant de ces études, une méthode permettant de quantifier directement le coefficient des Interactions de Dzyaloshinskii- Moriya (DMI pour Dzyaloshinskii- Moriya Interaction) à l'aide du microscope Kerr a été proposée. En outre, un nouveau type de capteur magnétique basé sur l'expansion réversible de paroi en raison de la tension interfaciale a été proposé et vérifié en utilisant des simulations micromagnétiques.

Deuxièmement, les propriétés dynamiques des parois dans le film et les fils Ta / CoFeB / MgO ont été étudiées. La vitesse du propagation des parois induite par le champ magnétique ou par l'effet combiné des impulsions de champ magnétique synchronisées et des impulsions de courant électrique a été mesurée. En régime précessionne, la vitesse du mouvement DW induite par l'effet combiné du champ et du courant est égale à la superposition des vitesses entraînées par le champ ou le courant indépendamment. Ce résultat nous a permis d'extraire la polarisation de spin de CoFeB dans cette structure. Les effets de piégeage du mouvement des parois dans les fils étroits ont été étudiés. Des champs de dépiégeage associés aux gros défauts pour le mouvement des parois induit par champ dans les nanofils a été mesurée. Il a été constaté que les effets de piégeage deviennent plus sévères lorsque la largeur w des fils diminue. Une relation linéaire entre le champ de piégeage et 1/w a été trouvée. L'origine de ces sites d'ancrage durs ainsi que leurs influences sur la vitesse de mouvement des parois ont été discutées. En outre, il a été constaté que l'effet d'épinglage était amélioré lorsque le courant était appliqué, quelle que soit la direction relative entre le mouvement des parois et le courant. Cet accroissement pourrait être expliqué par l'effet du courant de Hall de spin de la sous-couche (Ta). Bien qu'il n'y ait pas eu de DMI ou de champ planaire, le courant de

Hall de spin, polarisé dans la direction transversale, peut exercer un couple sur la parois de type de Bloch, une fois que la paroi s'éloigne de la direction transversale.

Enfin, un dispositif mémoire de circuit en forme d'anneau basée sur le travail combiné de STT et SOT a été proposée. Comparée à la mémoire de piste traditionnelle en forme de ligne, cette mémoire en forme d'anneau permet au paroi de demaine de se déplacer dans un nanofil en forme d'anneau sans être éjecté, évitant ainsi la perte des informations associées. Le travail de conception et d'optimisation a été réalisé avec des simulations micromagnétiques.

Mots clés: Paroi de domaine magnétique, Microscopie Kerr, CoFeB, Tension interfaciale, Effet de piégeage de paroi de domaine, Couple de transfert de spin, Couple d'orbite à spin, Mémoire de type Racetrack, Capteur magnétique, Magnétisme, Spintronique

Chapter 1 Introduction

1.1 Motivation

Magnetic domains and Domain Walls (DWs) are very common objects in the magnetic material. Static and dynamic properties of DWs have always been one of the central research topics of magnetism in the last hundred years. On the one hand, these researches provide varieties of ways to characterize the basic properties of the magnetic material or magnetic structures. For example, by analyzing the state or the behavior of DWs, some parameters such as the saturation magnetization M_S[1], the exchange stiffness A_{ex} [2–4], the strength of Dzyaloshinskii-Moriya Interactions (DMIs) [5] etc. can be quantified.

On the other hand, varieties of devices based on DWs have been proposed or developed for information processing, storage, and transport. For example, DWs based logic devices[6,7], DWs based Artificial Neural Networks (ANNs) computing[8–10], DW as the transmission channel of spin wave[11] etc. In particular, the prototype of Racetrack Memory (RM) proposed by S. Parkin[12,13], which stores the information using the flowing DWs in nanowires, triggered a sustained boom of the research on DWs motions in nanowires.

In the last two decades, varieties of emergent phenomena have been involved into the DW related phenomena. For example, different from the traditional field-induced DW motion, it was found that DWs could be moved in narrow wires by electrical current via spin transfer torque (STT). Owing to the DMI and Spin Hall effect (SHE), DWs can be moved by the spin-orbit torque (SOT) with an ultra-fast speed. In structures with perpendicular magnetic anisotropy (PMA), DWs with a smaller width were obtained. Some emergent materials have been widely explored to develop magnetic based devices, such as CoFeB[14–18], which has a low damping and a low depinning field, promising a better efficiency for DW based devices. All these developments provide chances for a better understanding of the underlying physical phenomena or for the development of novel DWs based devices.

The DW motion in nanowires with the heavy metal/CoFeB/MgO structure is very interesting in view of its potential applications for DW based device for information storage or processing. However, many underlying issues need to be better understand. The current-induced DW motion needs to be further studied because, in this system, many effects are potentially involved, such as the adiabatic STT (AD-STT), non-adiabatic STT (NA-STT), the Spin-Orbit Coupling (SOC), the SHE etc. The role of these various effects on the DW motion needs to be clarified.

Therefore, this thesis focus on the studies of static and dynamic properties of DWs in the CoFeB nanowires, including the basic parameters such as the DW surface energy, the current and field-induced DW motion velocities and the pinning effects.

1.2 Organization of the thesis

This thesis is organized into six chapters, including the introduction and the conclusion.

In chapter 2, the state of the art concerning to this thesis is introduced. We generally summarize the basic theory related to DWs, including the static properties such as DW surface energy, the dynamic properties such as the DW motion driven by field or current, the interest to study DWs and their applications.

In chapter 3, study methods of this thesis is introduced. This chapter includes the following contents: the configuration of a high resolution Kerr microscope; the design of magnetic coils, which are capable to nucleate a DW and to measure the DW velocity in a microstructure; the configuration of electric tests; the nature of the sample studied and the method to measure the DW velocity etc.

In chapter 4, we present the research on the DW surface tension. A series of experiments in which the DWs surface tension play the dominant role are introduced, including the stabilization of magnetic bubbles, the depinning of DW at artificial geometries. The Laplace pressure is used to explain these phenomena. The design and verification of sensors based on the DW surface energy are introduced.

In chapter 5, experiments about the field and current-driven DW motion in CoFeB nanowires are introduced. The velocity of the field-driven DW motion, as well as the velocity of the DW motion driven by the combined effects of magnetic field and electrical current are measured and analyzed. The DW pinning effect in the nanowire and its dependence on the width of wires and on the applied current are studied. At last, a ring-shape racetrack memory based on the complementary work of STT and SOT is proposed and verified using micromagnetic simulations.

Chapter 2 State of the art

2.1 Basics

In this thesis, we shall use exclusively the units and definitions of the Système International (S.I.).

The strength of the magnetization of a FerroMagnetic (FM) material is defined as the quantity of magnetic moments per unit volume[19],

$$\vec{M} = \frac{d\vec{\boldsymbol{\mu}}_m}{dV} \tag{2-1}$$

where $d\vec{\boldsymbol{\mu}}_m$ is the elementary magnetic moment, with a dimension of A $\cdot\, m^2$, and dV is the volume element. Magnetic moments may be contributed by the motion of the electrons in atoms, the spin of electrons and the spin of nuclei. However, the contribution from the spin of electrons are the major one[19].

The stable state of a magnetic system is determined by the equilibrium of different energy terms involved, including the exchange energy E_{ex}, the crystalline anisotropy energy E_K, the magnetostatic energy E_d (or demagnetizing energy) originated from the dipole-dipole interaction, and the Zeeman energy E_{Zeem} when an external field is applied etc.

Exchange interactions:

Benefited from the development of the quantum theory, W. Heisenberg constructed a model in 1926-1928, which explained the origin of the magnetism in the magnetic material, namely, the Heisenberg exchange interaction model[20]. A simple understanding of this model is: the unpaired spins in nearby atoms tend to align in parallel to reduce the electrostatic energy (i.e. energy associated with the Coulomb interaction). This interaction is very strong, orders of magnitude larger than any other interaction such as the dipole-dipole interaction. However, the exchange interaction diminishes rapidly as the distance of spins increases. The result is that the magnetization in a small range is aligned.

Microscopically, the energy aroused by this interaction can be written as[19],

$$E_{ex} = \int e_{ex} dV = A_{ex} \int (grad\, \vec{m})^2 dV \tag{2-2}$$

Where $\vec{m}$ is the magnetization vector, defined as $\vec{m} = \vec{M}/M_S$ with M_S the saturation magnetization, and A_{ex} is the exchange stiffness, with a dimension of J/m. A_{ex} is an intrinsic property of the material and it changes with the temperature [21].

Conventionally, the coordinate shown in Figure 2-1 is used to describe the magnetization direction,

$$\vec{m} = (\sin\theta \cos\varphi\, , \sin\theta \sin\varphi\, , \cos\theta) \tag{2-3}$$

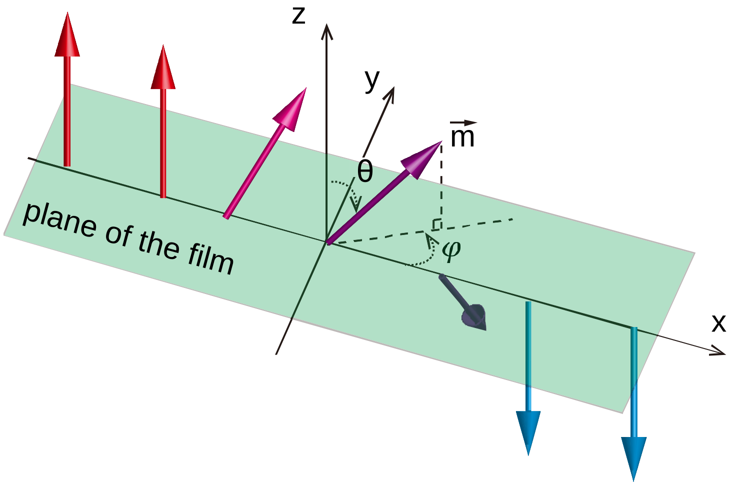

Figure 2-1 Sketch of the default coordinate and symbol of angle used in this thesis.

Then we have

$$e_x = A_{ex}[(grad\theta)^2 + \sin^2\theta\,(grad\varphi)^2] \tag{2-4}$$

Anisotropy energy

The magnetization direction in ferromagnetic material usually tends to align parallel to some specified axis, depending on the crystalline structure. The associated energy is called the anisotropy energy. The anisotropy energy (excluding the shape anisotropy) basically comes from the spin-orbit interaction (SOI)[21].

In the case of uniaxial anisotropy, the magneto-crystalline energy is described by a polynomial development in sinθ with only even terms for reasons of symmetry in the thin films studied,

$$e_{K_V} = K_{V1}sin^2\theta + K_{V2}sin^4\theta \tag{2-5}$$

K_{V1} and K_{V2} are the first and second order anisotropy constants. In general, K_{V1} is much larger than K_{V2}. A positive K_{V1} favors that the material has an easy axis while a negative K_{V1} favors an easy plane perpendicular to the anisotropy axis.

A perpendicular magnetic anisotropy (PMA) can be obtained in the ultra-thin multilayers structure due to the reduced symmetry of the atomic environment in the surface. The surface anisotropy was first introduced by Néel in 1953. Supposing that the surface is in the x-y plane, the surface anisotropy energy density is expressed as[21],

$$e_s = K_s[1 - (\vec{m} \cdot \vec{n})^2] = K_s \sin^2\theta \tag{2-6}$$

Where $\vec{n}$ is the surface normal. K_s has a dimension of J/m^2 and is in the order of 10^{-4} to $10^{-3} J/m^2$. This term becomes the predominant effect beyond the crystalline anisotropy only when the thickness of the ferromagnetic layer becomes very thin (~1 nm) and leads to the PMA in the ultra-thin multilayers structure. The material studied in this thesis has such an anisotropy.

Zeeman energy

For magnetic moment $\vec{\boldsymbol{\mu}}_m$ in a magnetic field $\vec{B}$, $\vec{\boldsymbol{\mu}}_m$ tends always to stay in parallel with $\vec{B}$. The associated potential energy is $E_M = -\vec{\boldsymbol{\mu}}_m \cdot \vec{B}$. The Zeeman energy indicates the magnetic energy introduced when an external field $\vec{B}_{ex}$ is applied to a magnetic material, expressed as,

$$E_Z = -\int \vec{B}_{ex} \cdot \vec{M}\, dV \tag{2-7}$$

Magneto-static energy

Inside a magnetic material, the magnetic flux density $\vec{B}$, the magnetic field intensity $\vec{H}$ and the magnetization $\vec{M}$ have the following relationship[21],

$$\vec{B} = \mu_0\left(\vec{H} + \vec{M}\right) \tag{2-8}$$

Where μ_0 is the permeability of vacuum. According to Maxwell's equation,

$$div\vec{B} = \mu_0 div\left(\vec{H} + \vec{M}\right) = 0 \tag{2-9}$$

So

$$div\vec{H} = -div\vec{M} \tag{2-10}$$

If there is no current nor alternating electric field,

$$rot\left(\vec{B}\right) = 0 \tag{2-11}$$

Combining these equations with the boundary condition, we can find that the magnetic field outside a magnet is not zero. This field is conventionally called the stray field. A magnetic field opposite to the magnetization inside the magnet exists. This field H is called the demagnetizing field.

In fact, the stray field and the demagnetizing field has the same origin. The different appellations depend on how to define the studied magnetic element. Here we use the symbol $\vec{H}_d$ as an indication. The associated energy, which is usually called the magneto-static energy, the stray field energy or the demagnetizing energy, is[21]

$$E_d = \frac{1}{2}\mu_0 \int_{all\ space} \vec{H}_d^2 dV = -\frac{1}{2}\mu_0 \int_{sample} \vec{H}_d \vec{M} dV \tag{2-12}$$

The calculation of this energy is very complex. References [21] gives several methods for the calculation of the demagnetizing energy. In particular, the density of demagnetizing energy in an infinite thin film with a uniform magnetization can be expressed as,

$$e_d = -\frac{1}{2}\mu_0 M_S^2 \sin^2\theta \tag{2-13}$$

This contribution favors an easy plane anisotropy, and a hard out-plane direction for the magnetization. The energy due to the demagnetization field is often called shape anisotropy.

Regarding the uniaxial anisotropy due to the crystalline as described in Eq. (2-5) and the surface anisotropy described in Eq. (2-6), neglecting the second order, one can describe the uniaxial anisotropy energy as [22],

$$e_K = K_U \sin^2\theta \tag{2-14}$$

with $K_U = K_{V1} + K_S$. If we further consider into the shape anisotropy described in Eq. (2-13), we can get an effective anisotropy energy density[22],

$$e_{K,eff} = K_{eff} \sin^2\theta \tag{2-15}$$

With,

$$K_{eff} = K_U - \frac{1}{2}\mu_0 M_S^2 \tag{2-16}$$

<u>Dzyaloshinskii-Moriya interactions</u>

Dzyaloshinskii-Moriya interactions (DMI) have been intensively studied in recent years. The DMI exists in the material in which the structure reversion symmetry is broken. The energy density associated with this interaction is[23],

$$e_{DM} = D\left[m_z \mathrm{div}\vec{m} - \left(\vec{m}\cdot\vec{\nabla}\right)m_z\right] \tag{2-17}$$

where *D* is DMI constant. Although DMI is negligible in the sample we have studied, the result presented in this work opens a new way to study DMI, as it will be seen at the end of this manuscript.

2.2 Magnetic domain walls

2.2.1 DW profile

Below a critical temperature (called Curie temperature), the magnetization in adjacent zone tends to spontaneously align in parallel due to the exchange integration in ferromagnetic material. The region in which the magnetization is in a uniform direction is called magnetic domain. Magnetic Domain Wall (DW) is the interface separating two domains in the magnetic material. In a static state, the configuration of a DW is determined by the equilibrium under the competition of different energy terms. Properties of DWs, including the arrangement of the magnetization, the DW width, and the surface energy, can be calculated by minimizing the free energy of the system. For example, the DW tends to stay in a Bloch Wall (BW) configuration in an infinite film or a wire (only when wire width is larger than DW width) with PMA and without DMI, because this configuration can minimize the demagnetizing energy. In a material with strong DMI, the DW is stabilized in a Néel Wall (NW) configuration because this type of DW can minimize the energy associated to the DMI[24].

Based on the 1D model (supposing that the magnetization is identical in the transverse direction, i.e. y-direction in Figure 2-1) and by minimizing the energy of the system, one can deduce a function to describe the rotation of the magnetization of a DW,

$$\theta(x) = \frac{\pi}{2} - 2\arctan\left(e^{\frac{x-x_0}{\Delta}}\right) \tag{2-18}$$

Where x_0 is the center position of the DW. The DW width is $\Delta = \sqrt{A_{ex}/K_{eff}}$ for BW in static state. Note that this width is defined by Thiele and is conventionally called the Thiele width. The geometrical width of the DW in this case is $\pi\Delta$[25]. For a NW, A. Thiaville et al. numerically calculated the DW width when DMI exists [23] and found that the width of NW is larger than the BW. The increase of DW width is caused by the magnetostatic field.

2.2.2 DW surface energy

After determining the DW profile by minimizing the total free energy, one can obtain the DW energy per unit surface (i.e. surface energy). For a BW [23],

$$\gamma_{BW} = 4\sqrt{A_{ex}K_{eff}} \tag{2-19}$$

If DMI or an in-plane field H_x exist, the expression of the DW surface energy becomes complex [5],

$$\gamma_{DW} = \begin{cases} \gamma_{\mathrm{BW}} - \frac{\pi^2 \Delta M_S^2}{8K_D}(H_x + H_{DM})^2 & for\ |H_x + H_{DM}| < \frac{4K_D}{\pi M_S} \\ \gamma_{\mathrm{BW}} + 2K_D - \pi\Delta M_S |H_x + H_{DM}| & otherwise \end{cases} \tag{2-20}$$

where K_D is the demagnetizing energy of DWs and H_{DM} is the effective field due to DMI.

In particular, for a pure NW fixed only by the DMI,

$$\gamma_{DW} = 4\sqrt{A_{ex}K_{eff}} - \pi \mathrm{D} \tag{2-21}$$

Note that this energy is defined with respect to the energy in the uniformly magnetized state.

A conventionally used method to experimentally quantify the DW surface energy is by observing the domain structure in the demagnetizing state[2,3]. As shown in Figure 2-2, in the demagnetizing state, the magnetic texture of thin film with PMA is of a labyrinthine like distributed stripes. This state is mainly the competition result of the demagnetizing energy and the DW surface energy. The characteristic period

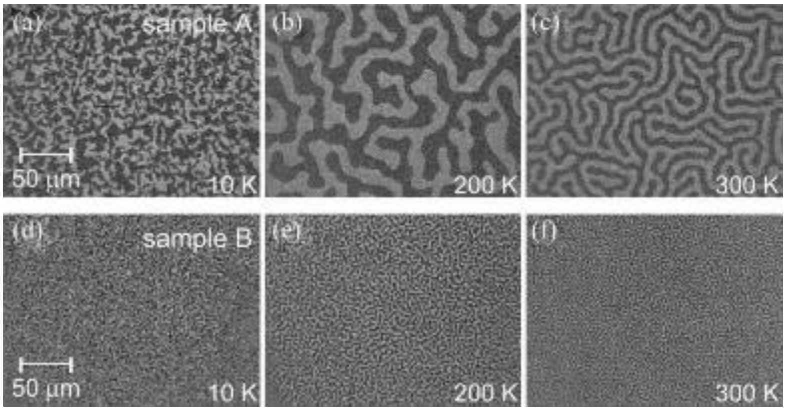

Figure 2-2 Fig. 2. MOKE microscope images of domain structures. Sample: Ta(5nm)/Co20Fe60B20(t)/MgO(1)/Ta(2). (a)–(c) sample A (as deposited, t=1.1), and (d)–(f) sample B (annealed, t=1.3) in demagnetized state at different temperatures (10, 200, and 300 K). Extracted from [IEEE MAGNETICS LETTERS, Volume 2 (2011)].

w_P of the domain can be obtained after analyzing the images. Then, the DW surface energy can be deduced using the following formula developed by Kaplan and Gehring[26],

$$w_p = 1.91 t_M exp(\pi w_0 / t_M) \tag{2-22}$$

where t_M is the thickness of the FM layer and,

$$w_0 = \gamma_{DW} / \mu_0 M_S^2 \tag{2-23}$$

However, the accuracy of the results obtained via this method depends on how the demagnetizing state is obtained. Usually, the as-prepared sample is in a naturally demagnetized state. However, once magnetized, it is difficult to return to the intrinsic demagnetized state, even after a demagnetizing process via an alternating and exponentially decaying magnetic field, as done in the above example (Figure 2-2). When the alternating field decays to a low value, the motion of the DW is usually trapped by the defects, one can never know how close the magnetization approaches the intrinsic demagnetizing state. Therefore, a more direct and accurate method to quantify the DW surface energy is desired.

The DW surface energy is a very important and fundamental parameter which affects the DW behaviors. A surface tension exists due to this energy. In some literature, this effect is also called as the DW elasticity[27,28]. For example, the DW depinning before pinning sites is determined by the competition between several energy terms such as the pinning barrier, the DW surface energy, and the Zeeman energy[29]. Another example, the stabilization of the domain bubble, the skyrmions are also affected by the DW surface energy.

2.3 DW dynamics

DW can be moved or manipulated through varieties of mechanism, for example, by an external magnetic field, by the STT, by the SHE current, by the an electric field[30–32], by the spin wave[33–37], by the polarized light[38] or by the thermal gradient[39]. Among them, the first three mechanisms were most studied.

2.3.1 Field-driven DW motions

2.3.1.1 Field-driven DW motions predicted by the 1D model

First, we consider the DW motion in a defect-free sample. In this case, as predicted by the one dimension model (1D model), the DW motion can be divided into three regimes: the steady regime for H between 0 and the Walker breakdown field H_W, the intermediate regime after Walker breakdown and the precessional regime[40], as shown in Figure 2-3(a).

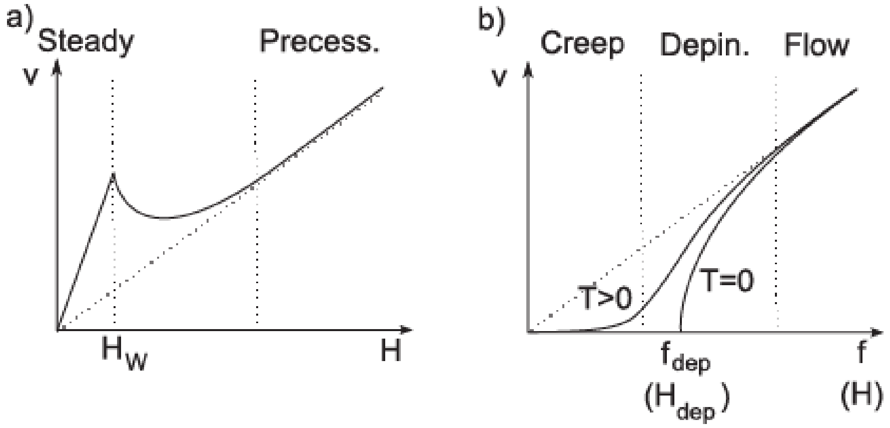

Figure 2-3 (a)) Regimes of domain-wall flow motion in an ideal ferromagnetic film without pinning. （b）Theoretical variation of the velocity, v, of a 1D interface (domain wall) in a 2D weakly disordered medium submitted to a driving force, f (magnetic field, H), at zero and finite temperature, T. The creep, depinning, and flow regimes are labeled. Extracted from [PRL 99, 217208 (2007)].

When the applied field is smaller than a critical value, the DW motion is in a steady regime, also called the viscous regime. The magnetization in the center of the DW $\vec{m}_{DW}$ rotates in the plane such that the azimuth angle $\varphi(H_{ext})$ (defined as the angle between and the longitudinal direction, as shown in Figure 2-1) is constant. The DW velocity is proportional to the magnitude of the applied field H_{ext}[41,42],

$$v = \frac{\gamma \Delta_{\varphi(H_{ext})}}{\alpha} \mu_0 H_{ext} \tag{2-24}$$

where γ is the gyromagnetic ratio, α is the damping parameter (note that the constant α can be obtained through different experiments. But, there is not yet agreement between them, values obtained through ferromagnetic resonance are quite different from the one obtained through DW propagation. It suggested that locally induced anisotropy due to structural relaxation and roughness increased the damping related to the DW motion [43,44]). $\Delta_{\varphi(H_{ext})}$ is the DW width parameter taking into consideration of the demagnetizing field, which changes with $\varphi(H_{ext})$,

$$\Delta_{\varphi(H)} = \sqrt{\frac{A}{K_{eff}+\frac{1}{2}\mu_0 M_S^2 cos^2\varphi}} \tag{2-25}$$

Here, K_{eff} is the effective anisotropy field including the magneto-static field, as defined by Eq. (2-16).

When the external field reaches a critical field, namely, the Walker breakdown field, the rotation of $\vec{m}_{DW}$ reaches π/2. After the Walker breakdown, the DW velocity drops rapidly because of the collective precession of the DW magnetization. The Walker breakdown field H_W is directly related to α[45],

$$H_W = \alpha M_S/2 \tag{2-26}$$

After the external field has exceeded the Walker breakdown field, the DW moves in a precessional mode. Figure 2-4 gives the numerically calculated dynamics of a DW as a function of time based on the 1 D model[46]. We can see that in the precessional flow mode, the azimuth angle of $\vec{m}_{DW}$ increases linearly and the position of the DW oscillates, leading to the low propagating velocity of DW.

In this case, the average DW velocity is,

$$\bar{v} = \gamma\Delta(H_{ext})\frac{\alpha}{1+\alpha^2}\mu_0 H_{ext} \tag{2-27}$$

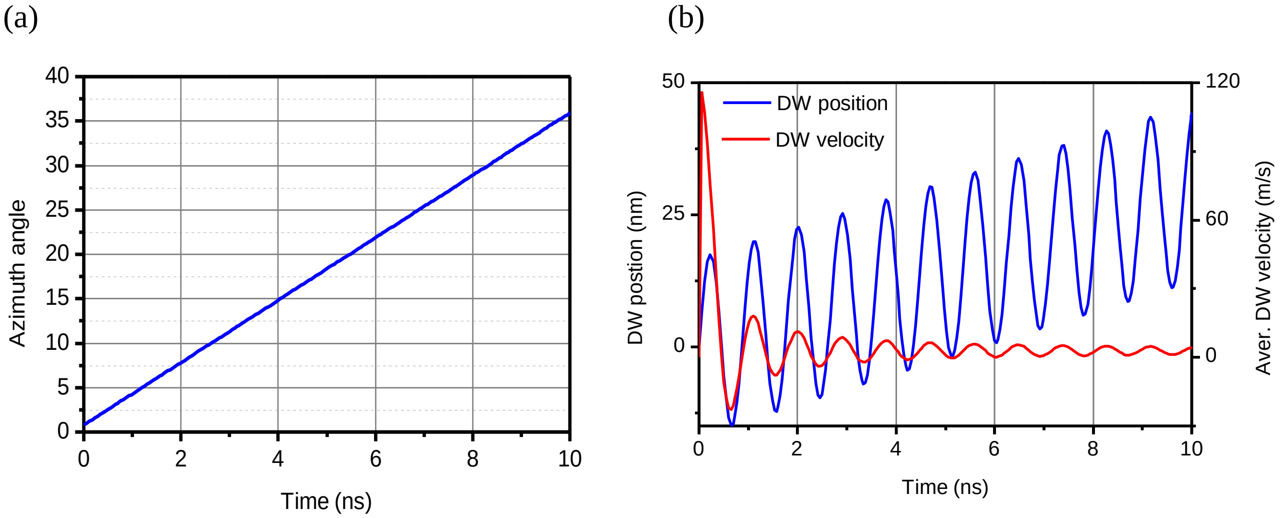

Figure 2-4 DWs motion predicted by the 1D model. (a) The azimuth angle of the center magnetization of DW and (b) the longitudinal coordinate and the average velocity of DW vs. time. The field applied is 20 mT. Parameters used are: damping α=0.013, DW width Δ=10.7 nm, and the demagnetizing anisotropy field is 10^5 A/m. The velocity is calculated via dividing the DW position by the time.

2.3.1.2 Field-driven DW velocity in 2D films with defects

- **DW pining in infinite film**

As a matter of fact, the magnetic film is not perfect. Some pinnings exist, which may arise from nanoscale defects such as atomic steps, grain boundaries[47], surface roughness, local variations of the thickness/composition[29,48], variation in stress, etc., leading to random fluctuations of the anisotropy or of the exchange interaction.

When the moving DW comes across a pinning site in the film, it may get over the pinning site through two regimes: (1) if the pinning site is strong enough so that the DW cannot get over the energy barrier directly, or if the distance between the two pinning sites is large enough, the DW may keep propagating on the left and the right of the site, until it has completely surrounded the sites, which disappear at last. (2) If the applied field is strong enough or if the pinning is not solid enough, the DW directly overcomes the energy barrier under the Zeeman force or assisted by the thermal activation. As shown in Figure 2-5, we

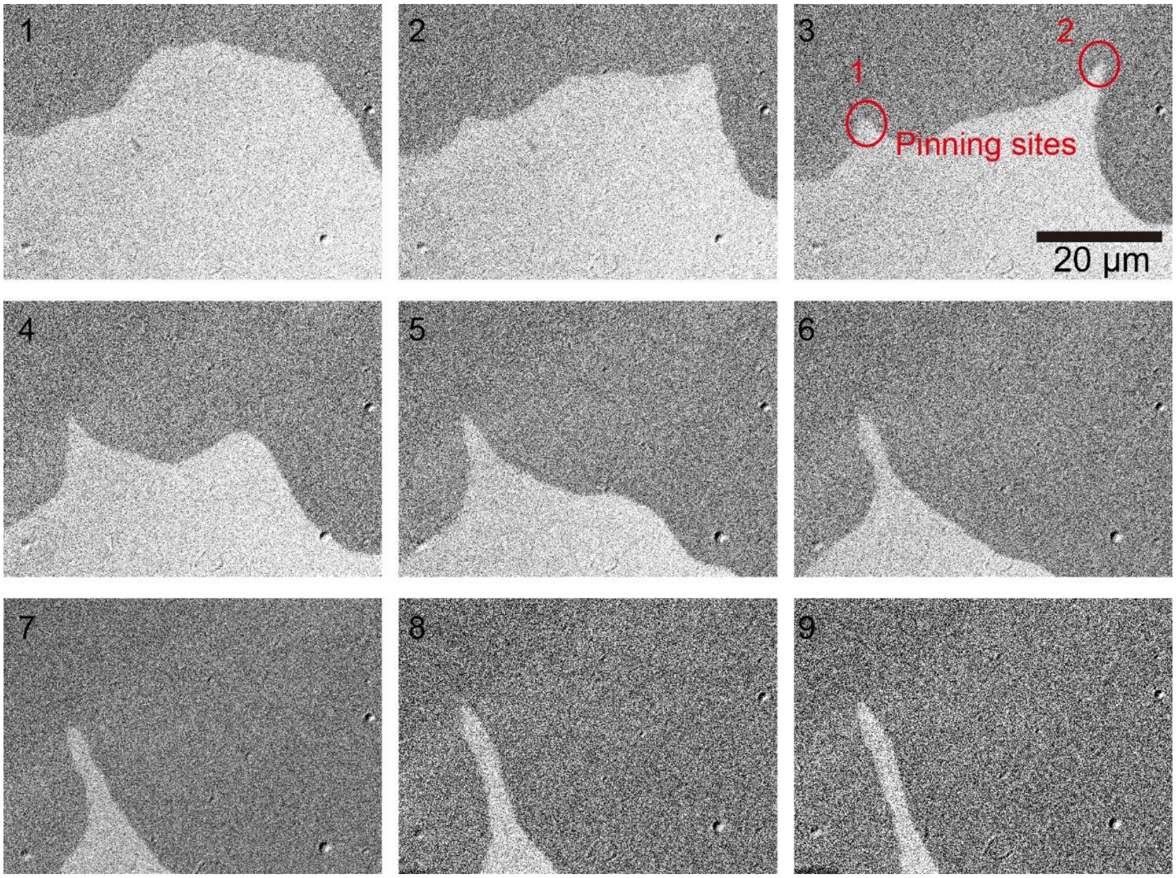

Figure 2-5 Interaction of the DW with pinning sites. Between every two figures, a field pulse of 0.35 mT and 0.5s was applied. Information of the sample: Ta(5nm)/CoFeB(1.0)/MgO(2.0nm)/Ta(5nm), annealed at 300℃ for 2 hours.

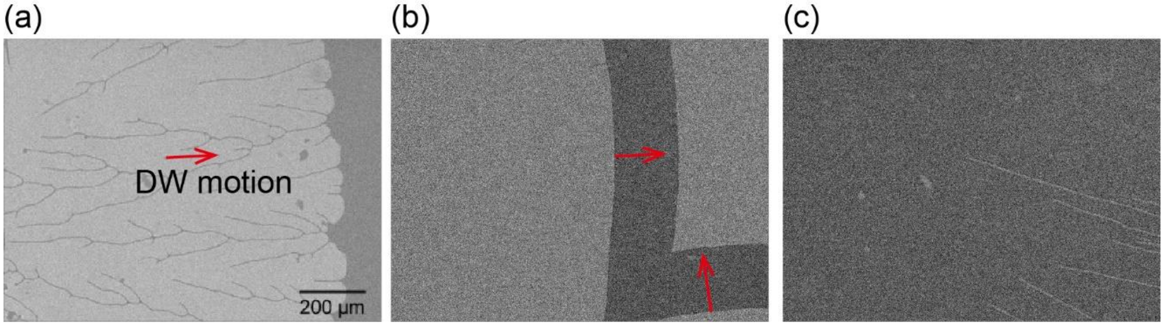

Figure 2-6 (a) DW propagation after a field pulse of 0.4mT and 30s. (b) DW propagation after a pulse of 3.1 mT and 0.2 ms. (c) the white lines denotes the disappeared domain stripes under the pressure of the field of 2.8 mT. Information of the sample: Ta(5nm)/CoFeB(1.0)/MgO(2.0nm)/Ta(5nm), annealed at 300℃ for 2 hours.

have directly observed these two processes using a Kerr microscope. In the field of vision, two hard pinning sites appeared and they induced the curvature of the propagating DW. The DW passed the pinning site 2 after reaching a short radius of curvature. However, the DW cannot go over the pinning site 1. At last, an unreversed domain stripe was formed. In fact, many strips of this kind can be found after the weak

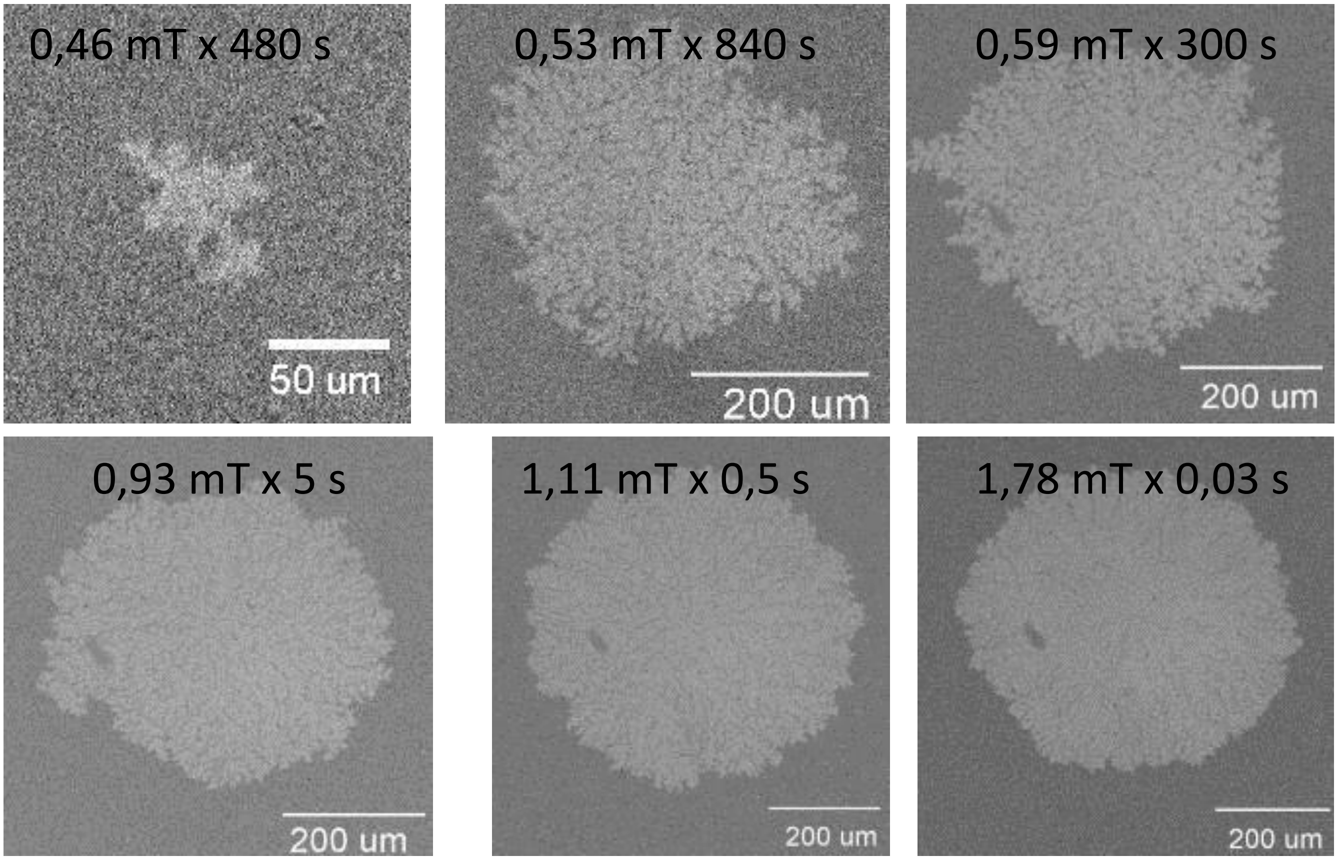

Figure 2-7Morphology of domains propagations under different fields, observed with a Kerr microscope. Information of the sample: Si/SiO_2/5Ta/40CuN/5Ta/1.1$Co_{40}Fe_{40}B_{20}$/1MgO/5Ta, annealed at 380°C during 20 minutes.

field-induced propagation of DWs, as shown in Figure 2-6 (a) and Figure 2-7. In Figure 2-6, we have done a comparison of the morphology of reversed domains after a weak field with that after a strong field. The unreversed domain stripes began to merge as the applied field increased to a critical value (about 2.8 mT in this sample). The distance of these strips can be used to estimate the magnetization of the material[1]. In the case when the defects in a sample are strong or when the driving field is relatively small, the trace of DWs propagation is dendritic, as shown in Figure 2-7. When the applied field increases, the edge of expanded domains becomes smoother.

- **DW motion in creep regime**

In ultra-thin magnetic films, the interaction of DWs with the random disorder at low magnetic fields leads to the well-known creep theory[29,49,50], which describes the motion of a 1D interface in a 2D random disorder. The DW velocity can be expressed as[29,50],

$$v = v_0 \exp\left[-\left(\frac{U_c}{k_B T}\right)\left(\frac{H_{p\_intr}}{H}\right)^{\mu}\right] \tag{2-28}$$

Where U_C is a parameter to characterize the strength the energy barriers due to defects in a material, k_B is the Boltzmann constant, T is the temperature, v_0 is constant related to the properties of material with a dimension of velocity, and μ is a constant. For the DW motion in a 2D system, $\mu = 1/4$. H_{p_intr} is called the intrinsic pinning field of a material. The theory of creep regime applies from zeros field until H_{p_intr}.

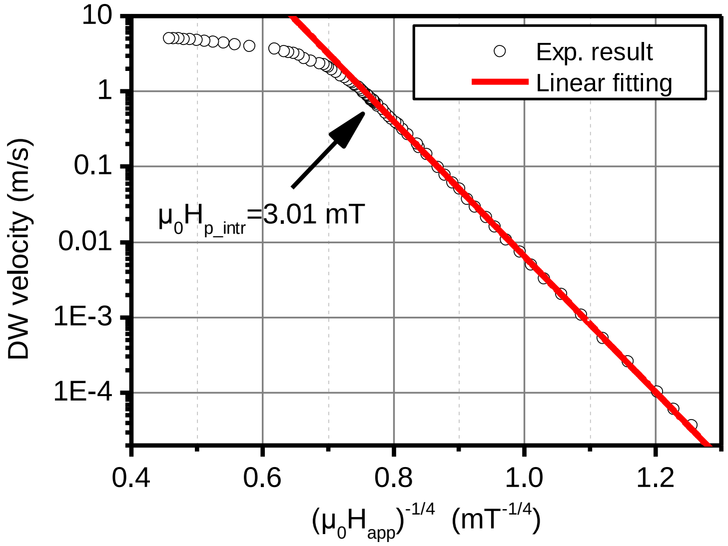

Figure 2-8 Field-induced DW motion velocity in creep regime, in this measurement, the temperature is 24°C. Information of the sample: Ta(5nm)/CoFeB(1.0)/MgO(2.0nm)/Ta(5nm), annealed at 300°C for 2 hours.

According to Eq. (2-28), a linear relationship can be found between ln(v) and $H^{-1/4}$. As an example, we show here the measured DW velocity on the sample we have studied in this thesis and the fitting result with the creep law, as shown in Figure 2-8. We can see that the measurement results get a good agreement with the prediction of Eq. (2-28). The intrinsic pinning field $\mu_0 H_{p\_intr}$ of the sample is extracted to be about 3 mT.

In addition, the dependence of the field-induced velocity on the temperature in creep mode has also been examined in this sample, as shown in Figure 2-9.The temperature effect was not the goal of the present work. So, to avoid artefact due to this dependency, we have been careful to work always at the temperature of about 25°C.

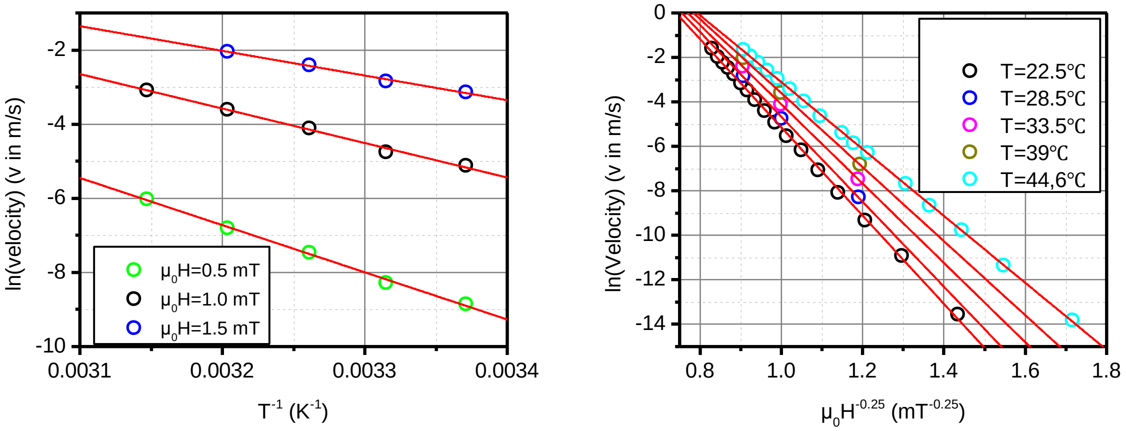

Figure 2-9 (a) Temperature dependence and (b) Field dependence of the DW motion velocity in creep regime. Information of the sample: Ta(5nm)/CoFeB(1.0)/MgO(2.0nm)/Ta(5nm), annealed at 300°C for 2 hours.

It can be noted that the dependency of v(H) is a very strong one, a small change of H can induce a big change in velocity. It can be used to calibrate the field created by a very small coil (see later, in chapter 3).

- **Depinning transition mode**

After the creep regime, the DW motion respect the so-called depinning transition mode as the applied field is a little higher than the intrinsic pinning field. After systematical studies of the DW behavior in this regime, R. Diaz Pardo, V. Jeudy et al. summarized the DW velocity law as following[51].

When the applied field is fixed to be H_{dep}, the variation of the DW velocity with the temperature is,

$$\mathrm{v}\left(H_{p\_intr}, T\right) = v_T \left(\frac{T}{T_d}\right)^{\psi} \tag{2-29}$$

and when the temperature is near zero ($T \ll T_d$), the variation of the DW velocity with the applied field can be written as,

$$v(H, T \ll T_d) = v_H \left(\frac{H - H_{p\_intr}}{H_{p\_intr}}\right)^{\beta} \tag{2-30}$$

where v_T and v_H are depinning velocities, T_d is a characteristic temperature related to the pinning strength of the material, ψ and β is constant.

At last, we verified this theory with the field-driven DW velocity we measured at room temperature. The sample used is still the Ta(5nm)/$Co_{40}Fe_{40}B_{20}$(1.0)/MgO(2.0nm)/Ta(5nm), annealed at 300℃ for 2 hours. The experiment results were fitted with the following formula,

$$v = v_d \left(\frac{H - H_{p\_intr}}{H_{p\_intr}}\right)^{\beta} \tag{2-31}$$

Here, v_d and H_{p_intr} is set as the variables and β is set as constant 0.25. As shown in Figure 2-10, a good agreement is obtained. We can find that the depinning transition law is effective from 3.4 mT until about 20 mT.

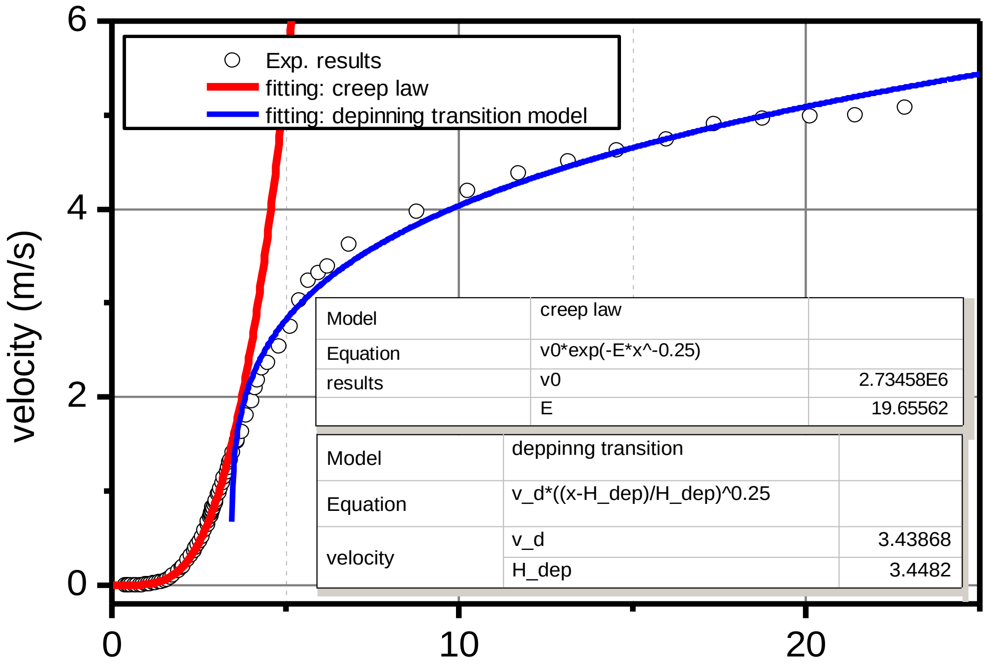

Model	creep law	
Equation	v0*exp(-E*x^-0.25)	
results	v0	2.73458E6
	E	19.65562

Model	deppinng transition	
Equation	v_d*((x-H_dep)/H_dep)^0.25	
velocity	v_d	3.43868
	H_dep	3.4482

Figure 2-10 The field induce DW motion velocity measured on Ta/CoFeB/MgO film and the fitting results with the creep law and the depinning transition model.

2.3.2 Spin transfer torque driven DW motion

The field-driven DW motion is the result of the expansion of the magnetic domains in the direction favored by the magnetic field. The adjacent DWs in wires move always in the opposite directions. This

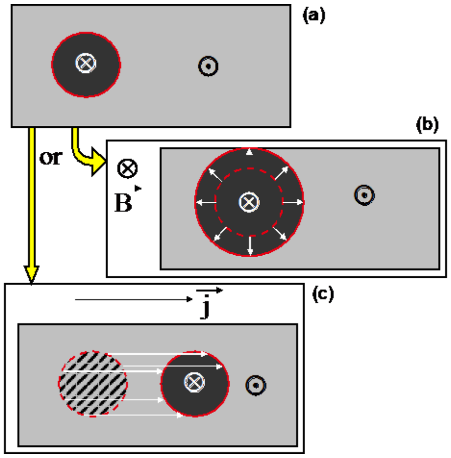

Figure 2-11 A sketch showing the difference between the field-induced DW motion and current-induced DW motion. (a) The initial position of a circular DW. (b) The expansion of a DW induced by a magnetic field. (c) The displacement of a DW induced by an electric current.

characteristic hinders its applications for information transmission and storage. On the contrary, the current-driven DW motion is different, as shown in Figure 2-11.

When electrons flow in the magnetic layer with DWs, the electrons will be locally spin-polarized due to the exchange interactions. Because of the conservation of angular momentum, the spin momentum is transferred by electrons, creating a torque to the local magnetization. This torque is called the spin transfer torque (STT)[52]. The STT can induce the magnetic switching[53,54] or induce the DW motions[55].

Berger had proposed the concept of the STT in as early as the 1970s and first predicted the STT-driven DW motion[56,57]. Thereafter, the STT driven domain wall motion was experimentally observed in a 30-40 nm thick permalloy films through Faraday effect[58,59]. In these experiments, DW displacement is observed when the applied current density is larger than 1.2 ×10^{11} A/m^2. However, because of the large dimension of the sample (3.5 mm wide), the critical current for DW motion had reached the huge value of 13A.

The STT driven DW motion became widely studied after the 2000s, when technology made it possible to create nano-sized devices, for which the critical current density could be easily reached.

Two terms of STT contribute to the DW motion: the adiabatic STT (AD-STT) and the non-adiabatic STT (NA-STT). The former one can be expressed as[60],

$$\vec{\tau}_{ad} = (\vec{u} \cdot \vec{\nabla})\vec{m} \tag{2-32}$$

Where $\vec{u}$ is called the spin-drift velocity and its value is $u = \frac{\mu_B g P j}{2eM_S}$. Here, μ_B is the Bohr magneton, g the Landau factor, P is the polarization, j is the current density, e is the elementary electrical[61].

Since the theoretically predicted DW motions considering only the AD-STT was not able to get an agreement with the experimentally observed ones, the non-adiabatic torque was introduced by S. Zhang et al[62] and A. Thiaville et al[63] the NA-STT, expressed as,

$$\vec{\tau}_{na} = \xi\left[\vec{m} \times \left(\vec{u} \cdot \vec{\nabla}\right)\vec{m}\right] \tag{2-33}$$

Here ξ is the non-adiabatic constant (different from that in Eq. (2-31)). The value of ξ is usually very small and the order of the NA-STT is much smaller than the AD-STT. However, the role of the NA-STT is very important for the DW dynamic. A. Thiaville et al.[63] has compared the DW dynamics with different weight of ξ, as shown in Figure 2-12. For zero ξ, the DW will not move until the spin drift velocity u reaches a threshold value u_c even in a perfect thin film. However, when NA-STT is introduced, the DW begins to move at low u. In fact, the value of u_c is expressed as[61],

$$u_c = \gamma\mu_0 H_K \Delta/2 \tag{2-34}$$

where H_K is the shape anisotropy field.

For STT-driven DW motion, there are also the flow regime, Walker breakdown, and the precessional regime. the Walker breakdown velocity is[61],

$$u_w = u_c \frac{\alpha}{|\xi-\alpha|} \tag{2-35}$$

In a defect-free film, the DW velocity before the Walker breakdown is[61],

$$v_{STT} = \frac{\xi\mu_B P}{\alpha e M_s} \mathrm{j} \tag{2-36}$$

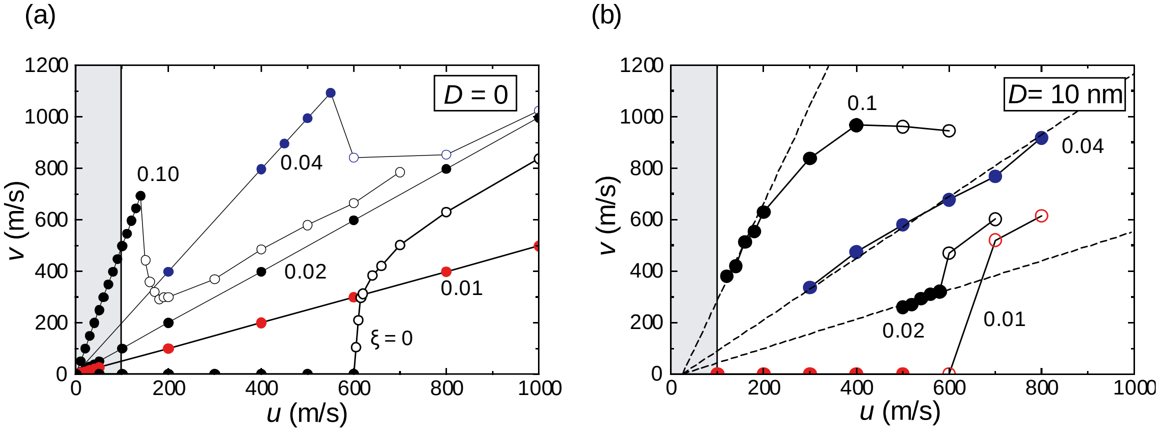

Figure 2-12 Steady velocity computed for a transverse domain wall by micromagnetics in a 120 × 5nm^2 wire as a function of the velocity u representing the spin-polarized current density , with the relative weight ξ. Open symbols denote vortices nucleation. The shaded area indicates the available experimental range for u. (a) Perfect wire and (b) wire with rough edges (mean grain size D = 10 nm). The dashed lines display a fitted linear relation with a 25 m/s offset. Extracted from [A. Thiaville et al. Europhys. Lett., 69 (6), pp. 990–996 (2005)]

After Walker breakdown, the DW move in a precessional mode, and the average velocity is[61],

$$\bar{v}_{STT} = \frac{1+\alpha\xi}{1+\alpha^2}u \tag{2-37}$$

The DW motion velocity as high as 110m/s when the driving current density is 1.5×10^{12} A/m^2 has been observed in Permalloy wires[64].

In samples with defects, the creep motion of STT-driven DW motion was observed and theoretically studied[65–67]. However, the exponent factor μ varied. In addition, the experimental results and the theoretical prediction cannot get a good agreement. More studies are required.

2.3.3 Spin orbit torque driven DW motion

The Spin-Orbit Coupling (SOC, sometimes also called SOI for Spin-Orbit Interaction) is the interaction between the spin of electrons and its own orbital angular momentum[68]. In a material with strong SOC (e.g. heavy metal such as Ta, the interface between heavy metal and FM layer), the SOC yields various interesting phenomena that affect the DW behavior[12]. First, the SOC at the interface between ferromagnetic (FM) layer and the nonmagnetic (e.g. heavy metal, HM) layer yields the PMA. This strong PMA promises a thinner DW, which is very helpful to improve the storage density for the DW based memory. Second, the strong interfacial SOC between the FM layer and the adjacent layers and the lack of structure reversion symmetry can induce DMIs. Third, the SOC in the HM layer yields a spin current, which can be injected into the adjacent FM layer[69].

The combination of the above effects can result in an efficient DW motion and the spin torque due to the SOC is called the spin-orbit torque (SOT). This phenomenon was first observed in the 500nm wide Pt/Co/AlO$_x$ nanowires by I. Miron et al. in 2011[70]. Subsequently, the SOT induced ultra-fast DW motion was found in other structures, such as the Pt/Co/Ni/Co multilayer[71], the Pt/CoFe/MgO and Ta/CoFe/MgO structures[72]. Some theoretical studies were conducted at the same time[23,73,74].

When a current j_{HM} flows in the HM layer, the density of the spin Hall (SH) current injected into the FM layer can be expressed as[69],

$$j_s = \theta_{SH} j_{HM}/e \tag{2-38}$$

and the polarization direction of the spin current is[69],

$$\vec{\sigma}_{SH} = sign\theta_{SH}(\vec{j}_{HM} \times \vec{z}) \tag{2-39}$$

Where $\vec{z}$ is the SH current injection direction. θ_{SH} is called the spin Hall angle. This parameter is related to the material and its phase. Table 2-1 gives some experimentally measured value of θ_{SH} of Ta, which should be considered in the following studies [69]. For example, in the β-Ta, θ_{SH} was found to be as large as 0.12, with a negative sign[75].

Table 2-1 Experimental spin Hall angles of Ta. SP = spin pumping, NL = nonlocal, STT+SHE = STT combined with SHE. Extracted from [*Jairo Sinova et al. RMP, Vol. 87, OCTOBER–DECEMBER 2015*]..

Temperature (K)	SH angle (%)	methode	reference
10	−0.37±0.11	NL	Morota et al. (2011)
295	-7.1±0.6	SP	Wang, Pauyac, and Manchon (2014)
295	$-2^{+0.8}_{-1.5}$	SP, spin Hall magnetoresistance (variable Ta thickness)	Hahn et al. (2013)
295	-(12±4)	STT +SHE (β-Ta)	Liu et al. (2012a)
295	-(3±1)	SP (β-Ta)	Gómez et al. (2014)

This SH current will produce two terms of Slonczewski torque, namely, the damping like SOT (DL-SOT) and the field like SOT (FL-SOT),

$$\vec{\tau}_{DL} = \tau_{DL}\big(\vec{m} \times (\vec{\sigma}_{SH} \times \vec{m})\big) \tag{2-40}$$

$$\vec{\tau}_{FL} = \tau_{FL}(\vec{\sigma}_{SH} \times \vec{m}) \tag{2-41}$$

where $\tau_{DL} = \frac{\gamma\hbar\theta_{SH}j_{HM}}{2eM_s t_M}$. It is generally admitted that the FL-SOT remains very weak in metallic systems[73].

For the SH current produced by an electric current flowing along a narrow wire, $\vec{\sigma}_{SH}$ is along the transverse direction (i.e. O-y on figure 2.13). In a wire with PMA, the DW is of Bloch type due to the demagnetizing field, providing that no DMI nor an external in-plane field H_X exists, and that the width of wire is larger than the DW width. Supposing also that the DW surface is along the transverse direction, without tilting or curvature, then the magnetization in the center of the DW $\vec{m}_{DW}$ is also in the transverse direction. According to Eq. (2-40), the SOT is zero in this case and the SH current cannot drive the DW motion. However, when DMIs or H_X exists, $\vec{m}_{DW}$ will tilt away from the transverse direction. If the direction of $\vec{m}_{DW}$ is fixed (no precession of $\vec{m}_{DW}$ occurs), as can be seen from Eq. (2-40), the DL-SOT act as an perpendicular (i.e. z-axis) field,

$$\vec{H}_{SH} = -\frac{\hbar\theta_{SH}j_{HM}}{2eM_s t_M}(\vec{\sigma}_{SH} \times \vec{m}_{DW}) \tag{2-42}$$

In addition, a strong DMI or H_X can prevent the precession of $\vec{m}_{DW}$. As a result, the SOT driven DW motion can achieve velocity as high as 350 m/s[70,71].

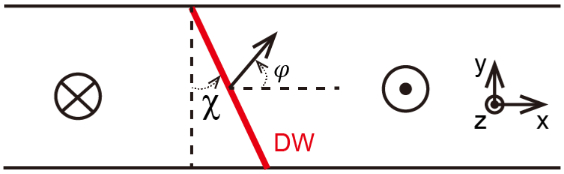

Figure 2-13 Tilting of a DW in the nanowire.

In addition to observing the DW motion velocity, some other effects of the SOT on the DW have been studied. For example, the DW depinning governed by the SOT[76,77], control of the magnetic chirality of DWs by changing the heavy-metal underlayers[78].

For the SOT-driven DW motion, as the current increases, the surface of DW as well as the magnetization of $\vec{m}_{DW}$ will tilt away from the longitudinal direction (i.e. x-axis, the direction along the wire), as shown in Figure 2-13. This tilting is the resultant effect of the DMI and the torque from the SH current[79]. According to Eq. (2-40), this tilting results in a decreases of the SOT driving efficiency and the DW motion velocity gets saturated[79–81]. S-H Yang et al. solved this problem by replacing the single FM layer with a synthetic antiferromagnetic (SAF) structure. A DW velocity as high as 750 m/s was observed[82].

At last, based on the calculation of [61,79,83–86], we summarize a group of equations developed from the 1D model, which can be used to describe the DW behavior in narrow wires with PMA under various effects. In these equations, magnetic fields in three directions, the effective field of DMI, the pinning potential, the DW tilting, the STT and the SOT are all included:

$$\dot{\varphi} + \frac{\alpha\cos\chi}{\varDelta}\dot{q} = \mathrm{Q}\gamma_0 H_Z + \frac{\xi u}{\Delta}\cos\chi + \mathrm{Q}\frac{\pi}{2}\gamma_0 H_{SH}\cos\varphi + \frac{\gamma}{2M_S}\frac{\partial \mathrm{V}_{pin}}{\partial \mathrm{q}} \tag{2-43}$$

$$-\alpha\dot{\varphi} + \frac{\cos\chi}{\varDelta}\dot{q} = \frac{\gamma_0 H_K}{2}\sin 2(\varphi-\chi) + \frac{u}{\varDelta}\cos\chi - Q\frac{\pi}{2}\gamma_0 H_{DM}\sin(\varphi-\chi) + \frac{\pi}{2}\gamma_0 H_x - \frac{\pi}{2}\gamma_0 H_y\cos\varphi \tag{2-44}$$

$$\dot{\chi}\frac{\alpha\mu_0 M_S\Delta\pi^2}{6\gamma_0}\left(\tan^2\chi + \left(\frac{w}{\pi\Delta}\right)^2\frac{1}{\cos^2\chi}\right) = \sigma\tan\chi - \pi D\sin(\varphi-\chi) - \mu_0 H_K M_S\Delta\sin 2(\varphi-\chi) \tag{2-45}$$

Where q is the position of the center of the DW, χ is the tilting angle of the DW surface from the transverse direction, Q is +1or −1 for up-down and down-up DW configurations, $\gamma_0 = \mu_0|\gamma|$, H_{SH} is the effective field of DL-SOT defined as Eq. (2-42), V_{pin} is the pinning poteitial, H_K is the shape anisotropy field, vector H includes the external applied field and the FL-SOT, H_x, H_y and H_z are its components along the 3 axis. Note that here the DW width Δ is considered as constant.

H_{DM} is the effective field of DMIs, written as,

$$H_{DM} = \frac{D}{\mu_0 M_S\Delta} \tag{2-46}$$

Although fruitful results have been obtained in the studies of current-driven DW motion, some open questions remain. For example, how to distinguish the contribution of AD-STT and NA-STT in STT driven-DW motion? What are the different contributions from STT and SOT in the HM/FM system?

Recently, research on the HM/CoFeB/MgO has attracted lots of interests because many distinct advantages have been found in these structures: both the SOI in the HM/FM interface and the FM/MgO interface contributes to a large PMA[22,87–89]; the CoFeB is very soft, with an intrinsic pinning field as low as 2 mT and a damping parameter in the order of 0.01[90]. A tunneling spin polarization rate as high as 0.53 has been measured in the CoFeB based MTJ structures[91–93]. A large SH current can be produced in the sub-HM layer[69] (a giant SH angle was found when the thickness of some HM is reduced to several nanometers and a phase change occurs, e.g. β-Ta, β-W[75,78]). The interfacial DMI can be tuned via the choice of the HM[78].

2.4 Micromagnetic simulations

Micromagnetic simulations is a very helpful means to study DWs in some cases, for example, to understand the DW behavior or state in very small size scale or in very short timescale that cannot be observed using experimental methods, to extract the energy fluctuation during a magnetic dynamic process, or to verify the performance of a device that are still under conception.

The micromagnetic simulation is based on a modified Landau-Lifshitz-Gilbert (LLG) equation that includes various effects. Here, we give an expression of this equation that includes various effects discussed in the above section[94],

$$\frac{\partial \vec{m}}{\partial t} = -\frac{\gamma}{M_S}\vec{m} \times \vec{B}_{eff} + \alpha \vec{m} \times \frac{\partial \vec{m}}{\partial t} + \vec{\tau}_{ad} + \vec{\tau}_{na} + \vec{\tau}_{DL} + \vec{\tau}_{FL} \tag{2-47}$$

Where $\vec{B}_{eff} = -\frac{1}{M_S}\frac{\delta E_{all}}{\delta \vec{m}}$ Effects such as exchange interactions, DMIs, dipolar interactions, perpendicular anisotropy can be introduced as an energy terms appearing in E_{all}.

In this thesis, simulations are performed using Mumax, a GPU-accelerated program developed by the DyNaMat group of Prof. Van Waeyenberge at Ghent University[94].

2.5 Applications of DW in storage, logic, communications and sensor

Magnetic materials are widely used for information detection, processing, transmission, and storage. Meanwhile, various DW based devices for different applications were proposed or developed. For example, the DW based logic device[95], the DW based spin wave transmission channel[11]. Here, we give two examples of the applications of DW for magnetic sensor and for information storage.

2.5.1 DW based sensors

Magnetic sensors are of great importance for the intelligent world, especially in the field of the positioning, the navigation and the automatic control etc. A variety of effects related to the magnetism were used to fabricate the magnetic sensors[96–98], such as Hall sensors, Anisotropic Magnetoresistance (AMR) sensors[99,100], fluxgate sensors[101], magnetic sensors based on the Giant Magnetoresistance (GMR) or Tunneling Magnetoresistance (TMR) effects [17,102–108].

Recently, a type of DW based multi-turn rotary sensor was sold in the market[109,110], the sketch of the geometry of which is shown in Figure 2-14. The purpose of this sensor is to count the number of rotations of a magnetic field. This type of sensor is made of magnetic wire with in-plane anisotropy. Under a rotating applied magnetic field, the structure nucleates one domain wall every 180° rotation. The nucleated DWs move with the rotation of the applied field. The absolute rotation is indicated by the combination of the DWs positions and their number within the device. The position of the DW is read out by GMR[111].

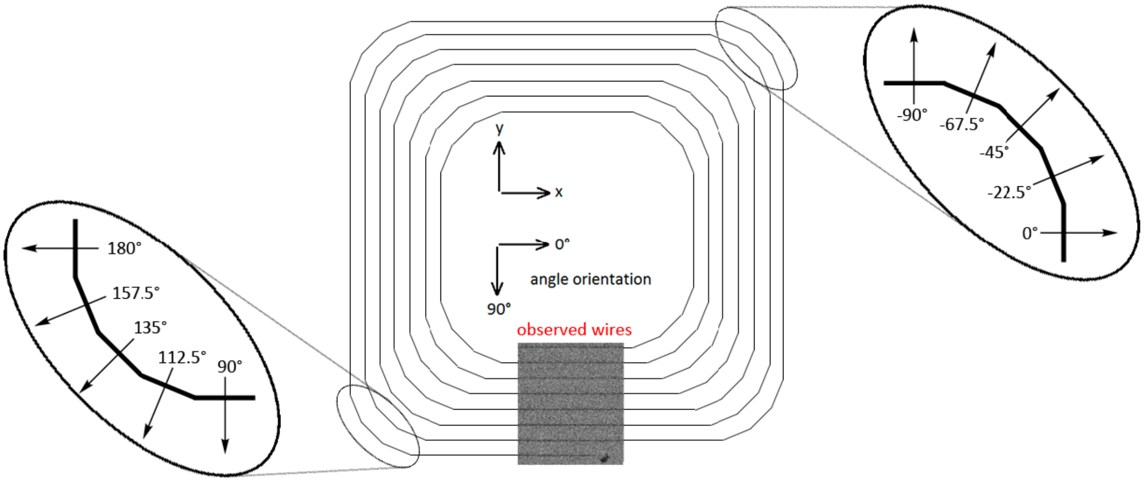

Figure 2-14 Sketch of a rotary DW based sensor with zoomed in bottom left and top right corners. A Kerr microscopy imaged shows the observed wires with the magnetic contrast visible. Extracted from [D. Heinze et al. OP Conf. Series: Journal of Physics: Conf. Series 903 (2017) 012053].

These DW based sensors exhibit two types of failure events, the pinning of domain walls if a particular propagation field threshold is not reached and the undesired nucleation of DWs at excessively high fields[111].

2.5.2 Racetrack Memory

Among all the DWs based devices, Racetrack Memory (RM) is the most eye-catching one, which was first proposed by S. Parkin in 2008[13]. As shown in Figure 2-15, in a nanowire with DWs, magnetic direction of each domain can be used to store one bit of logic information “1” or “0”[112].

The magnetization of domains can be sensed by measuring the magnetoresistance with MTJs arranged closed or in contact with the nanowire [12]. Information writing can be realized with a variety of schemes, e.g., the Oersted field of currents passed along neighboring metallic nanowires, or STT of current injected into the racetrack via an MTJ. Data can be shifted via the DWs motion along the nanowire. As discussed above, a uniform magnetic field cannot be used to shift data because neighboring DWs move in opposite directions and will annihilate each other. Spin current becomes a suitable method to realize an efficient, controllable and reliable DW motion.

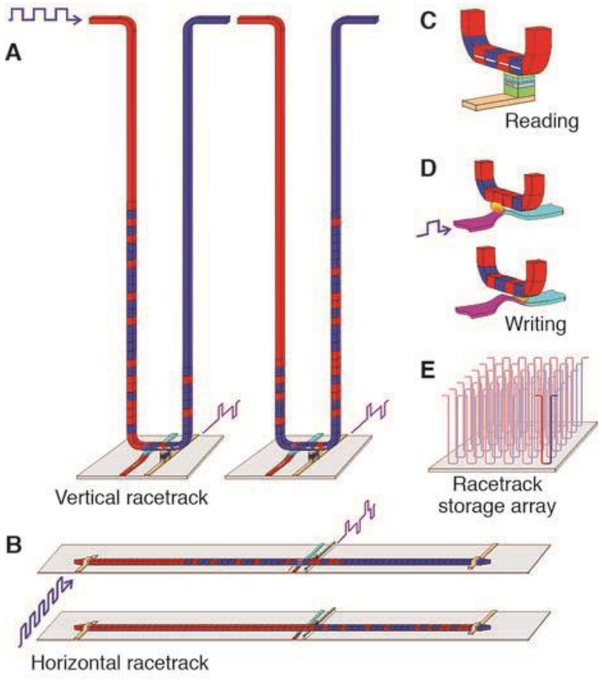

Figure 2-15 Full schematics of RM proposed by S. Parkin: data write in is through STT and read out is through TMR and data shift is through the current-driven DW motion. Extracted from [S. Parkin, Science 320, 190 (2008)].

Racetrack memory was first proposed based on the STT-driven DW motions in permalloy nanowires with in-plane anisotropy, see Figure 2-16 (a)[12]. Then, much narrower and more robust DWs are found in materials that exhibit strong PMA, such as Co/Ni superlattices[18,113,114], see Figure 2-16 (b). Since the discovery of the SOT-driven DW motion in 2011[70], a more power-efficient and faster RM is promised (Figure 2-16 (c)). Most recently, SAFs structure was adopted to reduce the demagnetizing field (See Figure 2-16 (d)), thus the DWs can be packed much closer together, which allows a larger storage density. Moreover, DW motion velocity increases as the net moment in the SAF structure is reduced, velocities of 750 m/s have been observed in this device[115].

Racetrack memory has many potential advantages than the other memories, for example, the high density, fast speed, low power data storage. One of the most interesting prospects of racetrack memory is that it can be implemented with 3D structure, as shown in Figure 2-15[13].

There are still many outstanding challenges, including the nanofabrication and integration technique and the precise manipulation of DWs. For example, the DW motion in nanowire is more complex than expected, pinning effects originated from the defects of film and roughness of edge of wire significantly influence the behavior of DW. Moreover, the position and displacement of DW must be precisely controlled to ensure the correctness of the transferred information. Therefore, further research on the mechanism of current-induced DW motion is very important for the application of DWs.

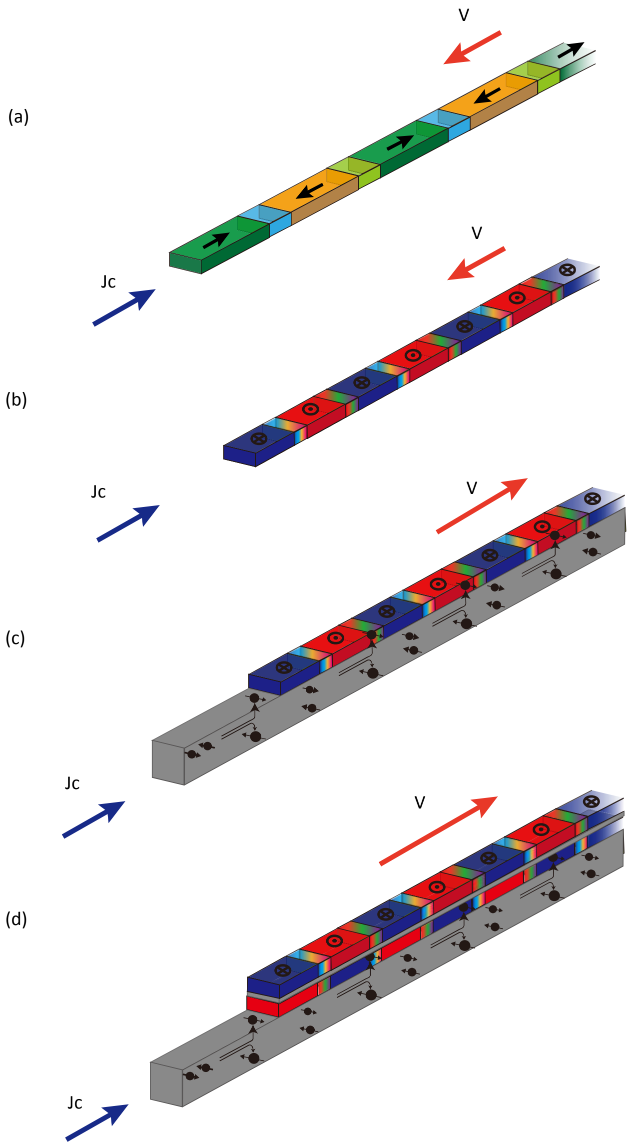

Figure 2-16 Evolution of racetrack memory. (a) Racetrack Memory 1.0, with in-plane magnetized racetracks; (b) Racetrack Memory 2.0, with perpendicularly magnetized racetracks. Conventional volume spin-transfer torque moves DWs in the direction of electron flow in (a) and (b); (c) Racetrack Memory 3.0: chiral spin torque drives DWs at high velocities along the current direction; (d) Racetrack Memory 4.0: a giant exchange coupling torque drives DWs in SAF racetracks at extremely high velocities. Jc, current through the device; v, DW velocity. Red and blue regions represent areas that are oppositely magnetized. Reproduced according to [S. Parkin, *Nat. Nanotechnol.* **2015**, *10*, 195–198].

Chapter 3 Experimental methods

In this thesis, the structure of magnetic domains and the behavior of DWs were mainly observed via a high-resolution Kerr microscope.

3.1 Magneto-Optical Kerr effect

When a beam of polarized light is reflected from a magnetic material, its polarization direction will rotate. This phenomenon is called the Magneto-Optic Kerr Effect (MOKE). It was first discovered by John Kerr in 1877[116–118]. In fact, before the discovery of the MOKE, another interaction between the polarized light and the magnetic material had already been found by Michael Faraday in 1845, named the Magneto-Optic Faraday effect. It refers to the effect that the polarization plane of the light can be rotated when it is transmitted through a material [118].

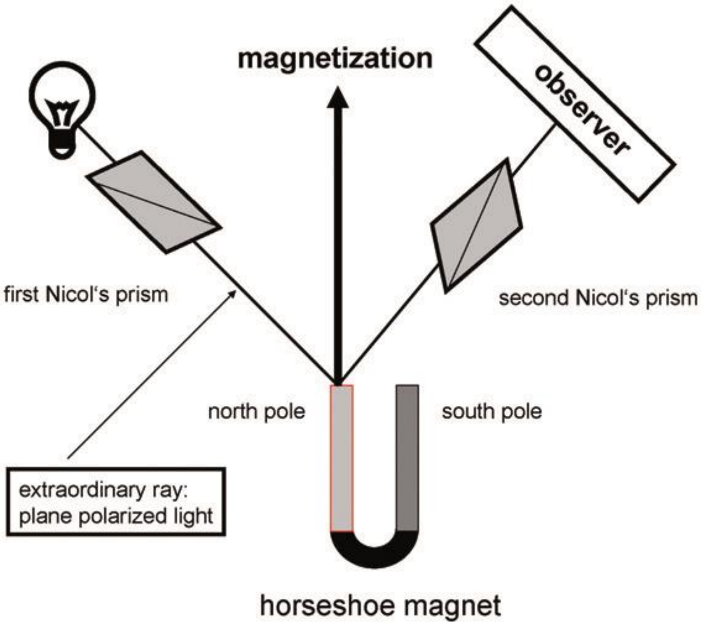

Figure 3-1 Experimental set-up used by John Kerr with which the Kerr effect was discovered. This sketch was reproduced by P. Weinberger according to the description of John Kerr in his publication [*Philos. Mag. Lett.* **2008**, *88*, 897–907].

MOKE can be divided into three types, depending on the magnetization direction of the reflecting sample with respect to the incident plane and the reflecting surface, as shown in Figure 3-2[119]. For the polar MOKE, the magnetization of the sample is perpendicular to the reflecting surface, thus parallel to the plane of incidence; For the longitudinal MOKE, the magnetization of the sample is parallel to the reflecting surface and parallel to the plane of incidence; For the transverse MOKE, the magnetization of

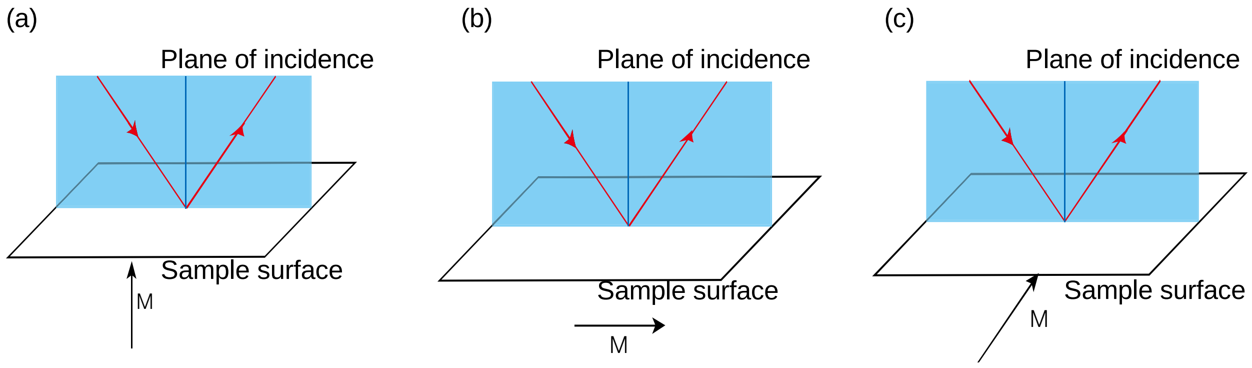

Figure 3-2 Geometry of three types of MOKE. (a) Polar MOKE; (b) Longitudinal MOKE; (c) Transverse MOKE. [Source: http://www.hindsinstruments.com/wp-content/uploads/Magneto-Optic-Kerr-Effect.pdf]

sample is parallel to the reflecting surface and perpendicular to the plane of incidence. It is to note that the above classification is just for the purpose of simplifying the understanding the MOKE. In fact, the above three MOKEs signal can exist simultaneously for an arbitrary direction of magnetization within a sample. It means that, depending on the wavevector of the light, the detected signal can be a sum of the three possible effects. So, one has to be very careful when analyzing the signal. However, if the optical wave arrives perpendicularly to the plane, then the signal is due only to the polar Kerr effect, the perpendicular component of the magnetization is the only one probed[120].

The magneto-optic effect can be understood with different models. First, from the view of quantum mechanics, Hulme pointed out in 1932 that the Faraday Effect is caused by the spin-orbit interaction (SOI) and he tried to calculate the different refraction indices of the right polarized and left polarized light using the Heisenberg model. Kittel further showed that it is the change of the wave function due to the SOI that gives the difference between these two refractions. Since a linearly polarized light can be seen as the composition of the R circularly polarized component and L circularly polarized component, the different reflection of the two components can cause a change of the polarization[118].

The MOKE signal can also be explained with the Lorentz force. The Kerr effect requires a linearly polarized light. The electric field of the incident light can excite the oscillation of the electrons along the polarization direction of the light. In magnetic material, a normal component of the motion will be generated on these oscillating electrons. Consequently, the polarization of the reflected light is changed. Using this model, the characteristics of the three different MOKEs can be understood[120]. First, the change of the polarization of reflected light occurs only on the longitudinal MOKE and the polar MOKE. Precisely speaking, the polarization of the light will change from the plane polarization (incident light) to elliptical polarization (reflected light). However, for the transverse MOKE, no change of polarization occurs. Instead, a change of the intensity of the light (Kerr reflectivity) occurs. Second, as the incident angle tends to zero, the longitudinal MOKE will diminish. However, the polar MOKE maintains. As a consequence, a microscope with perpendicular incident light is sensitive only to the polar Kerr effect. In other words, it probes only the perpendicular component of the magnetization. As it is the only component we are interested in the present work, it is perfectly suitable for our purpose. In addition, if the incident light is normal to the surface of the sample, the Kerr rotation is not affected by the polarization of the incident light. So, theoretically, the polarization direction of the incident light of a polar MOKE microscope does not matter.

The Kerr effect changes the linear polarized incident light into a slightly elliptical polarized light, with a main axis whose direction has rotated as compared to the incident polarization direction. Both the Kerr rotation and the ellipticity of the reflected light can be used to characterize the magnetic state of the sample. Analysis based on the dielectric properties of the medium and using the Maxwell boundary conditions at the interface can give an expression of the Kerr rotation $\phi'$and the ellipticity ϕ''. Both $\phi'$and ϕ'' are proportional to the magnetization of the material [118].

In general, a polarizer can be implemented before the photodetector to extract the Kerr rotation (this polarizer is conventionally called analyzer). Supposing that the intensity of the incident light is $\mathrm{I} = \left|E_p\right|^2$, with E_P the electric field vector of the incident light in the direction of the polarizer. After reflected by a magnetic material, an orthogonal component $\mathrm{E_S}$ appears. $\mathrm{E_P}$ can be filtered out by setting the analyzer in the crosswise direction with respect to the polarizer (i.e. extinction) before acquiring the signal. Usually, to get the rotation ϕ, the analyzer is a little deviate from the extinction with a small angle δ. Assuming $\delta >> \phi' >> \phi''$, the intensity of light passed the analyzer is[118],

$$\mathrm{I} \approx |E_P|^2 |\delta + \phi' + \phi''|^2 \approx I_0\left(1 + \frac{2\phi'}{\delta}\right) \qquad (3\text{-}1)$$

with $I_0 = |E_P|^2 \delta^2$, being the intensity of reflected light in the case without Kerr rotation.

The Kerr intensity is defined as the difference in the intensity for a sample magnetized in opposite directions and normalized by the total polarized light intensity[121],

$$\frac{\Delta I}{I} \approx \frac{4\phi'}{\delta - \phi'} \qquad (3\text{-}2)$$

The above formula is valid only for $\delta > \phi'$. One can find that δ should be set to an appropriate value according the Kerr rotation to maximize the Kerr intensity.

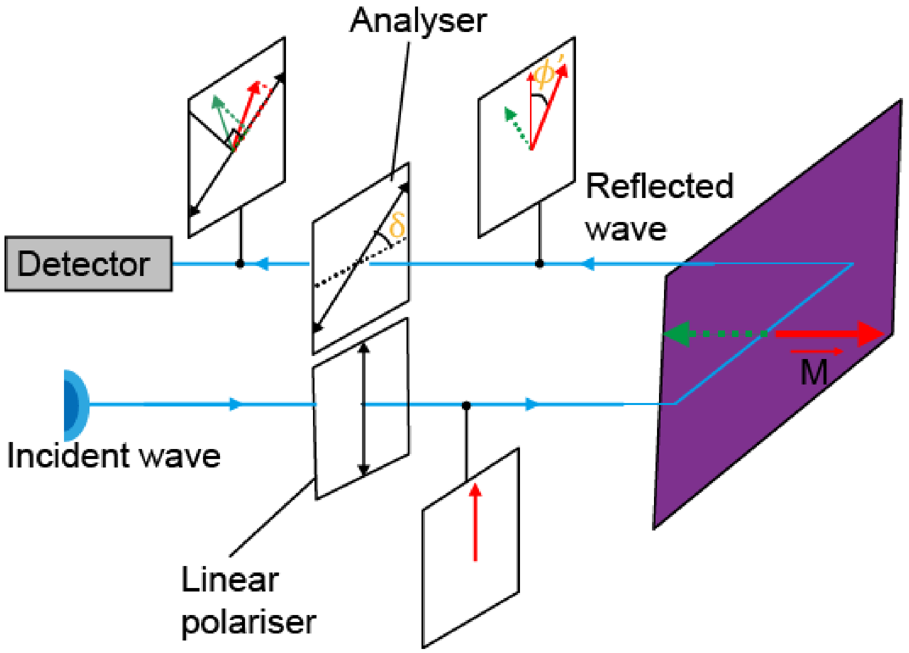

Figure 3-3 A sketch to describe the Kerr rotation of the reflected light and the polarization direction of the analyzer.

3.1.1 Typical optical circuits of Kerr microscopes

MOKE can be applied for two purposes. One is to measure the magnetization evolution of the sample when scanning the applied field, i.e., measuring the hysteresis loop. Another purpose is to image the magnetic state of the sample, i.e., the Kerr microscopy.

Figure 3-4 shows the layout of a polar Kerr microscope. For the Kerr microscopy, an objective is required before the sample. For a polar Kerr microscope, the light is usually incident from the normal direction of the surface of the sample. Both the incident light and the reflected light pass the objective and the two beams of light are separated by a splitter. First, the incident light is converged into a very narrow beam by a lens and becomes polarized after passing a polarizer. Then, the incident light beam is sent into the objective after the reflection by the light splitter. The incident light beam is transmitted through the objective and illuminates the field of vision on the sample. After reflected by the sample, part of the light returns to the objective and partially passed the splitter in the straight direction. This part of the light beam

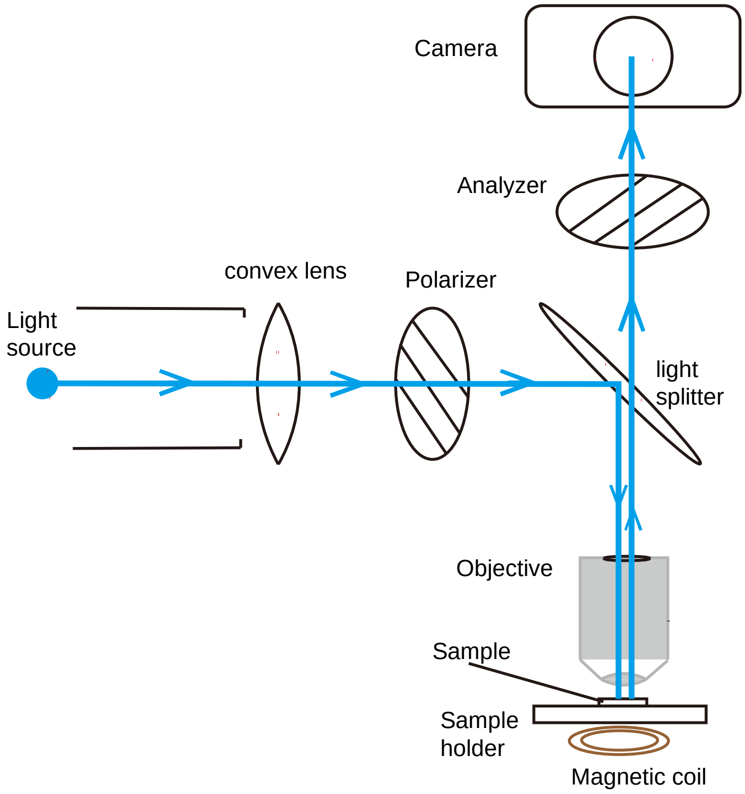

Figure 3-4 A typical configuration of the polar Kerr microscope designed by Mr. Nicolas VERNIER.

is captured by the camera after a filtering by the analyzer. In this way, the optical image of the tested structure is acquired and Kerr rotation caused by the ferromagnetic material presents in the form of a contrast of the intensity of the image.

Some key technique points:

The source of the light: a stable light source is strongly desired. After acquiring a series of Kerr images, a differential operation is required, i.e., subtracting the Kerr image by another one as a reference to maximize the signal to noise ratio, as shown in Figure 3-5. A stable light illumination can ensure a consistent intensity for all images. In addition, a light source with a large output power is preferred. Since the intensity of the light after the filtering by the polarizer and the analyzer has been significantly reduced, a powerful source ensures a meaningful signal much higher than the parasitic light coming from non controlled reflexions or light leak from the outside of the setup. In addition, a larger light intensity promises a shorter exposure time when acquiring a Kerr image, which is important to acquire some dynamics of the DW. It is very important that all the light arriving on the CCD is coming from the reflection on the sample, which is the interesting one. So, one must get rid of parasitic light such as leak

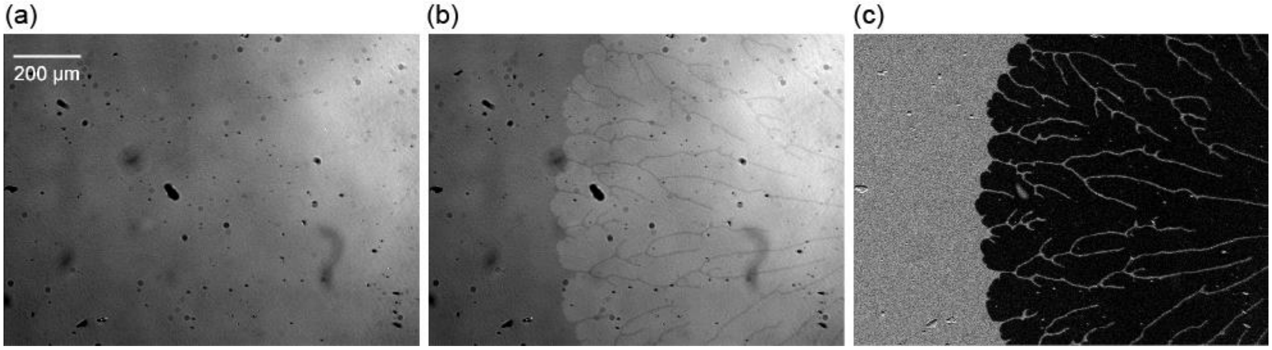

Figure 3-5 (a) Raw Kerr image of an infinite CoFeB magnetic film with saturated magnetization. (b) Kerr image of the film with a DW. The field of vision of (a) and (b) remains the same. (c) After subtracting (b) by (a), the background noise, such as the black spot caused by the dust in the sample or in the optical elements, was removed and a net image with a clear Kerr contrast was obtained.

from the lightning of the room or reflections of the beam on some of the setup elements. The Kerr microscope used in this thesis was completely covered by a double shade cloth to avoid the parasitical light from the outside. The light beam from the LED is confined in a tube.

The polarizer and analyzer: As the Kerr rotation is very small (at best a few tenths of degrees), very good polarizer and analyzer are required. An extinction ratio of at least 10^{-4} is needed, with a very well defined direction of polarization on the whole area of both polarizers.

The objective: the area of the field of vision and the resolution of the Kerr microscope is largely determined by the objective implemented. Generally, an objective with a smaller magnification gives a larger field of vision but a weaker resolution while an objective with a larger magnification gives a better resolution but the field of vision is reduced. Users can choose a suitable objective according to their application requirements. The objective should be polarization compatible. In addition, an objective with long working distance is required so that a large operation space for other configurations between the objective and the sample is possible. For example, if we want to insert a mini magnetic coil of 2 mm thick, a working distance of about 4 mm is required considering the space between the sample, the coil, and the objective.

Like the traditional optical microscopy, the resolution of Kerr microscopes is also constricted by the problem of the light diffraction. The resolution of a microscope can be described by the Rayleigh criterion [122–125]:

$$\delta_d \approx \frac{0.61\lambda}{n_a} \tag{3-3}$$

Where δ_d is the minimum distance between two points so that they can be distinguished, λ is the wave length of the light and n_a is the numerical aperture of the objective lens. From Rayleigh criterion, one can hope an ultimate resolution of around 400nm with an optical microscope. With the best lens we had (Olympus x100, n_a=0.80, which is not far from the maximum possible) and blue light of wavelength 480nm (fortunately for us, our samples had a good Kerr rotation in the blue), we had a resolution of 370nm. It was enough to view domains on nanowires as narrow as 200nm.

Camera: since the Kerr signal is finally presented in the form of the contrast of the intensity of light, a monochrome camera is sufficient for the image acquisition. Considering today's technology level, compared with the cameral with the CMOS photosensor, a CCD camera is better in terms of the signal to noise ratio for the acquisition of Kerr image. In addition, a camera with a cooling plant is preferred to reduce the noise caused by the heating of the camera.

3.1.2 Configurations of the Kerr microscope for these studies

In this thesis, the sample studied are all with PMA. Correspondingly, a polar Kerr microscope is used. The layout of the Kerr image is shown in Figure 3-4. This microscope is designed and implemented by Mr. Nicolas VERNIER. A blue-LED is used as the light source. With an objective of magnification of 100× and the numerical aperture of 0.8, produced by Olympus, the microscopy is able to detect the magnetic reversal of the 400-nm-large square (see Figure 3-6 (a)) and the DW motion in the 200nm wide

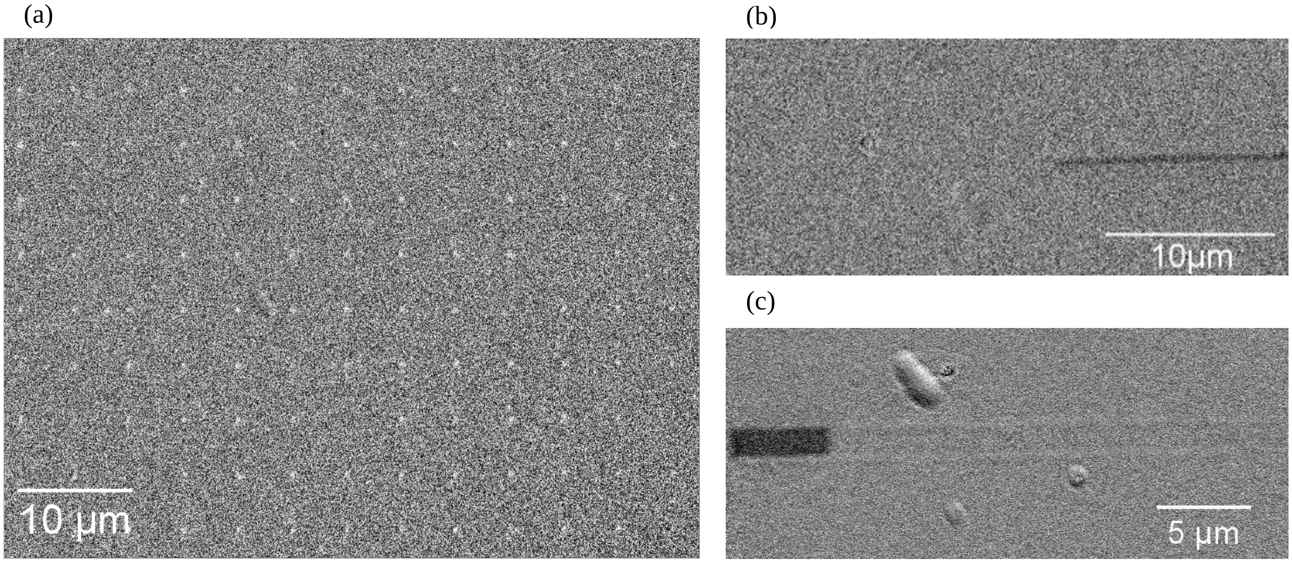

Figure 3-6 Examples of Kerr images (after subtracting the background, as explained in Figure 3-5) obtained with our Kerr microscope. (a) The magnetic reversal of a 400-nm-large square array. (b) The DW motion in a 200-nm-wide wire; (c) the DW motion in a 1.5-µm-wide wire.

nanowires (see Figure 3-6(b)). On the other hand, with an objective of magnification of 4×, the field of vision can be as large as 1 mm.

3.2 Configurations of magnetic coils

To study the field-induced DW motion in nanostructures, three problems have to be solved. First, the DW nucleation: although the DW nucleation in the magnetic nanowire can be achieved with the Oersted field produced by a large current pulse through a transverse metal wire, as shown in Figure 3-7 (a), but, the nanostructure is very easy to be destroyed by the Joule heating in this operation, as shown in Figure 3-7 (b), and this method should be avoided.

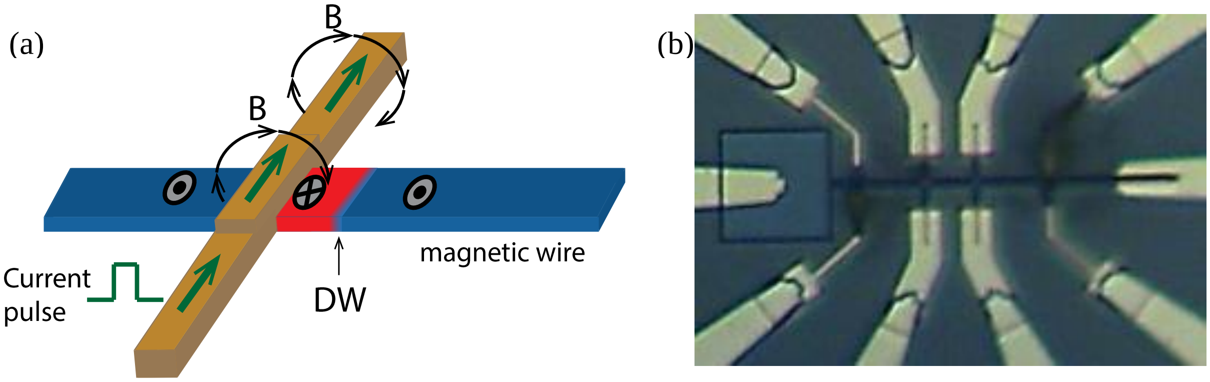

Figure 3-7 (a) Schematic diagram of the DW nucleation with Oersted field. A strong current pulse is applied on the transverse nonmagnetic metal wire and an Oersted field can be produced, resulting the DW nucleation. (b) A structure destroyed by the Joule heating of the current pulse.

Therefore, our strategy is to nucleate a DW by a large and short field pulse. It requires a very large field magnitude due to the lack of the nucleation point in the nanostructure, e.g., larger than 100 mT for our sample. Moreover, the field pulse width should be short enough, with a small rising edge and falling edge, so that the structure cannot be reversed completely because of the propagation occuring during the pulse. Second, to measure the DW motion velocity in the nanowire, the field pulse should be short enough so that the propagation distance of the DW is smaller than the length of the wire. For example, the velocity of the field-induced DW motion in the precessional flow regime is about 5 m/s in the CoFeB nanowire studied here. With an objective of 100×, the field of vision is about 50 μm. Accordingly, the length of the magnetic nanowire is usually designed to be less than 50 μm. If we want to observe this motion, the width of the field pulse applied should be less than 10 μs in order that the DW has not reached the end of the wire and the propagation length can be measured. Third, the rise time should be much shorter than the width of the pulse so that the magnetic field can be considered as constant in this duration. All these requirements demand an intentional design of the magnetic coils.

As known to all, to reduce the rise time, the number of turns of the coil should be reduced since the inductance of the coil increases as the turns of the coil increase. However, to obtain a larger field magnitude, more turns are required. We have to make a tradeoff. Other factors must also be considered, for example, the Joule heating due to the current passing the coil, which is related to the diameter of the varnished wire used; the small inductance required and the space of operation, which both limit the size of the coil; the homogeneity of the field produced in the field of vision observed. To obtain a fast response and to avoid the remanent field, a magnetic core cannot be used. Parameters which we can play include the structure, the diameter, the length of the coil, the varnished wire used to fabricate the coil and the electric configuration for the power supply. In the following, we discuss the design of the coil in a quantitative manner.

3.2.1 Design of magnetic coils

3.2.1.1 **Design**

Supposing a single turn closed coil with a radius R and that the principal axis is in the z-direction, as shown in Figure 3-8. When a current I flows in the circuit, the magnetic field produced in any point P(x,y,z) can be calculated with the Biot-Savart law. For simplification, we suppose that the projection of P in the x-y plane is in the x-axis. In this case, the in-plane component of the field produced at the position P is parallel to the x-axis, i.e., By=0. According to the calculation of [126], the perpendicular component and the in-plane component of the field produced in a point P(x,0,z) can be expressed as,

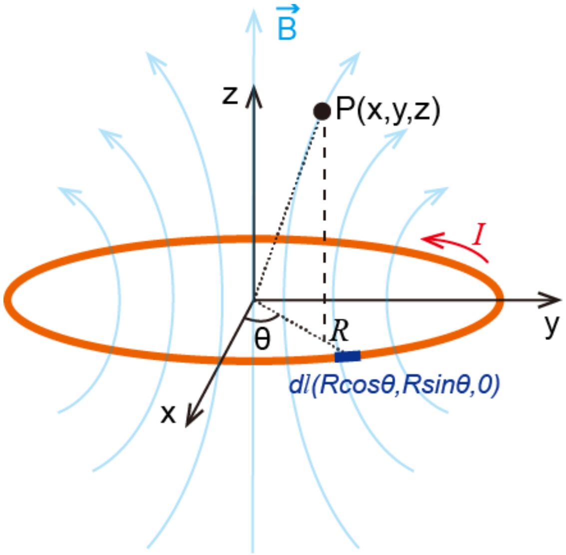

Figure 3-8 Sketch of a coil with single turn closed circuit.

$$B_Z = \frac{\mu_0 IR}{4\pi}\int_0^{2\pi} \frac{(R - x\cos\theta)d\theta}{[x^2+z^2+R^2-2Rx\cos\theta]^{3/2}} \tag{3-4}$$

$$B_x = \frac{\mu_0 IR}{4\pi}\int_0^{2\pi} \frac{z\cos\theta d\theta}{[x^2+z^2+R^2-2Rx\cos\theta]^{3/2}} \tag{3-5}$$

The out-of-plane magnetic field created in the center of the loop (x=y=0) is,

$$B_0 = \frac{\mu_0 I}{2R} \tag{3-6}$$

If z≠0 (which is the case for the sample), this value can be corrected by:

$$B_Z(z) = \frac{B_0}{\left(1+\frac{z^2}{R^2}\right)^{3/2}} \tag{3-7}$$

For x≠0, the integral Eq. (3-5) does not lead to a simple expression, it has to be calculated numerically.

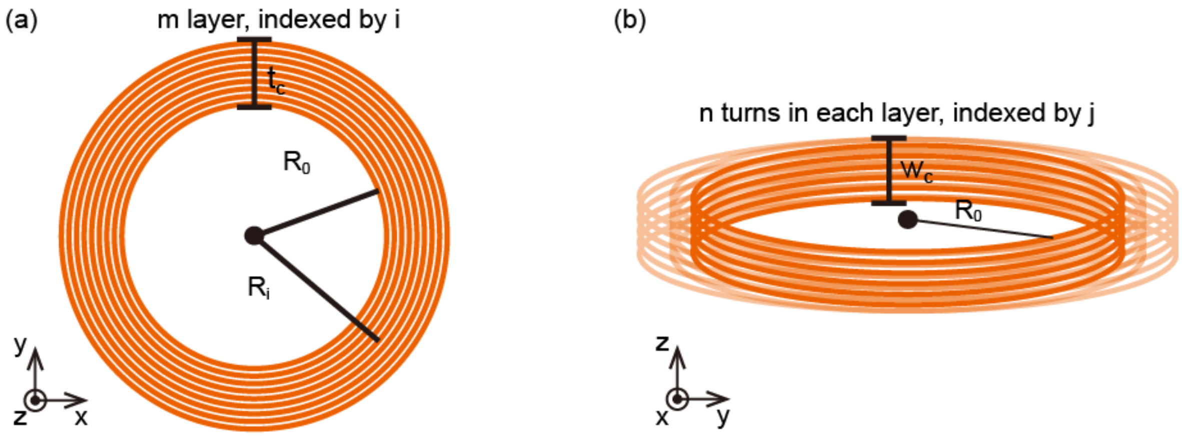

Figure 3-9 Sketch of a magnetic coil with m layer and n turns in each layer. (a) View from the principal axis; (b) View from the side.

For a coil with multi-turns, we suppose it to be an assembly of coils of single turn for simplification. As shown in Figure 3-9, a coil of multi-turns with m layer and n turns in each layer. The diameter of the varnished wire is d. Then, the total field produced can be calculated by a linear summation of the field produced by each turn,

$$\vec{B}_{total} = \sum_{j=0}^{n-1} \sum_{i=0}^{m-1} \vec{B}_{i,j} \tag{3-8}$$

Here, we take the center of the first coil closed to the point P as the original point. Supposing that every two turns are closely adjacent (i.e., there is no space between two turns of the coil). Then $\vec{B}_{i,j}$ can be calculated using the Eq. (3-4)(3-5), by substituting R by $R_0 + id$ and z by z $+ jd$ for the coil in the i-th layer an j-th turn.

The length of varnished wire to make the coil is:

$$l \approx 2n\pi \sum_{i=0}^{m-1} (R_0 + id) = n\pi(m2R_0 + m(m-1)d) \tag{3-9}$$

The resistance of the coil is predicted to be:

$$R_{coil} = \frac{l}{\sigma\pi(d/2)^2} \tag{3-10}$$

where σ is the conductivity of the wire.

By supposing the field produced by the coil is $\mu_0 NI/2R$ as an approximation, with N the number of turns, we can estimate the inductance of the coil, with the following formula,

$$L = \mu_0 \pi N^2 R/2 \tag{3-11}$$

where N is the total number of turns, N=m×n here. S is the cross-section area of the coil, we can take $S = \pi R^2$, where R is the radius of the coil. Here, we may take the average radius $\bar{R}$ as an approximation. w_c is the length of the solenoid, here, we take the width of the coil as an approximation, as indicated in Figure 3-9.

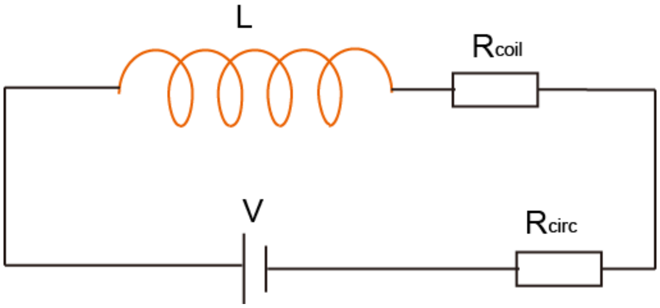

Figure 3-10 A simple sketch describing the circuit with a coil.

If the overall resistance of the power supply circuit (including the inner resistance of the power supply) is R_{circ}, the rise time can be deduced from the properties of an LR circuit. When applying a heavy side voltage, the current passing the coil is:

$$I(t) = I_0\left(1 - e^{-\frac{t}{\tau}}\right) \tag{3-12}$$

where I_0 is the saturation current, and τ the characteristic rise time,

$$\tau = \frac{L}{R_{coil}+R_{circ}} \tag{3-13}$$

The power transferred to the Joule heating in the coil can be calculated as,

$$P = I^2 R_{coil} \tag{3-14}$$

This equation can be used to evaluate the required output power of the adapted current supply system. Moreover, the temperature rise of the coil due to Joule heating can be roughly estimated with this equation. Supposing a coil without effective cooling configuration (e.g. cooling fin or water cooling system) and all the Joule heating is contributed to the temperature rise of the coil,

$$P\Delta t = C_{coil} m_{coil} \Delta T \tag{3-15}$$

Where Δt is the width of a pulse, C_{coil} is the specific heat capacity of the coil (0.39×10^3J/(kg·℃) for Cu), ΔT is the temperature rise after the pulse, and m_{coil} is the mass of the coil, which can be approximately evaluated with the expression $m_{coil} = \frac{1}{2}\pi^2 R d^2 N \rho_V$, with ρ_V the volume density of the coil (8.9×10^3kg/m^3 for Cu).

Considering Eq. (3-4), (3-5) & (3-8), three ways can help to obtain a high magnetic field: increasing the current flowing in the coil, reducing the size of the coil and increasing the number of turns of wires. The increase of the current is limited by the ability of the power supply and the heat dissipation efficiency

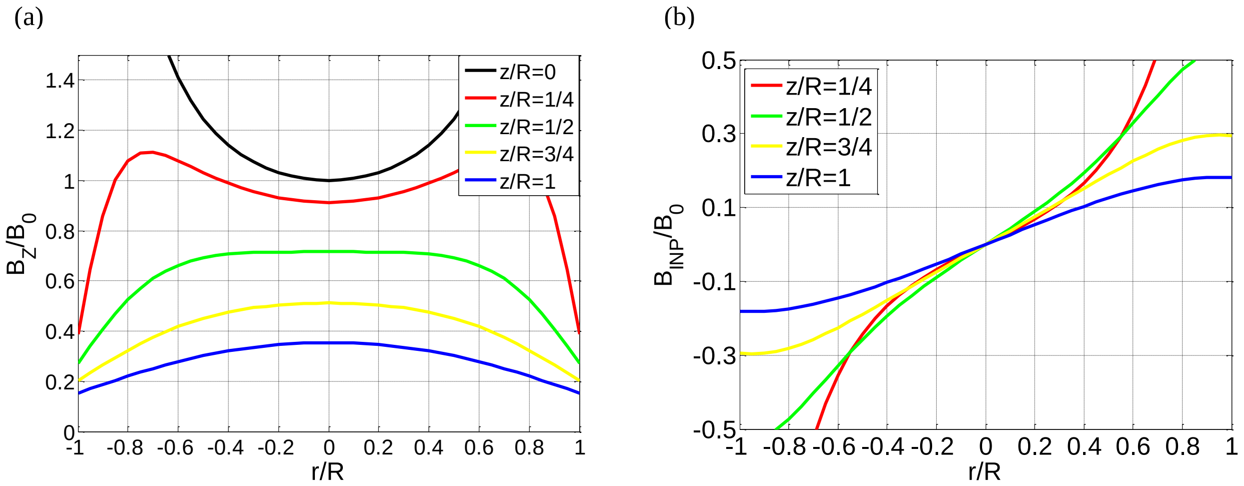

Figure 3-11 Magnetic field produced by a coil of single turn with a radius R. The vertical axis represents (a) the perpendicular component (i.e. in z-direction) and (b) the in-plane component of the field. Each line denotes the distribution of the field in a plane which is parallel to the surface of the coil and with a distance z to the coil. The field is normalized by the field $B_0=\mu_0 I/(2R)$, equaling to the field produced in the center of the coil. The abscissa axis denotes the radical coordinates normalized by R. Note that these relationships are always valid, irrespective of the dimension of R and I.

of the coil. In addition, increasing the section of the copper wire is another method to reduce the Joule heating. However, the size of the coil should be considered when determining the thickness of the wire.

Although increasing the number of turns is helpful to elevate the magnitude of the field, one has to be careful because the increase of inductance goes faster. Indeed, B increases as N but L increases as N^2. Then, N-value too high would damage the rise time, as described in Eq. (3-11).

At last, reducing the radius of the coil favors both the elevation of the magnitude of the field and a faster response speed of the coil. However, the homogeneity of the field near the center axis should be considered. An inhomogeneity of produced field can cause the difficulty of calibration of the coil and can also result in a field gradient in the field of vision. In addition, the magnitude of the field decreases with R for a given distance between the coil and sample, with a factor $1/(1+z^2/R^2)^{3/2}$, as described in Eq.(3-7). We have numerically calculated the distribution of the field produced by a single turn coil based on the Eq. (3-4) & (3-5). The normalized field vs. the normalized coordinate of the point of view is plotted, as shown in Figure 3-11. We can see that the order of the field and the homogeneity area depend on the relative distance of the point of view to the coil with respect to the radius of the coil. A distance about R/2 from the point of view to the coil is optimal to get a satisfying magnitude and homogeneity of the field, with R the radius of the coil.

In the practical implementation, the coil cannot be very close to the sample because of several constraints, such as the thickness of the sample (~0.5mm), the thickness of the sample holder (~1.5mm) and the interspace between the coil and sample holder (~0.3mm, this interspace is necessary in order that the sample is removable for the focusing and to change the observed structure). We were not able to implement the coil between the objective and the sample because of the short work distance of the 100× objective (3.4 mm). Moreover, the further electric test requires a wire connection before the sample. At last, the coil is placed in the back of the sample holder, with a distance about 2.3 mm to the focus plane. Considering this distance, a coil with a radius of 4.5 mm is optimal for our configuration.

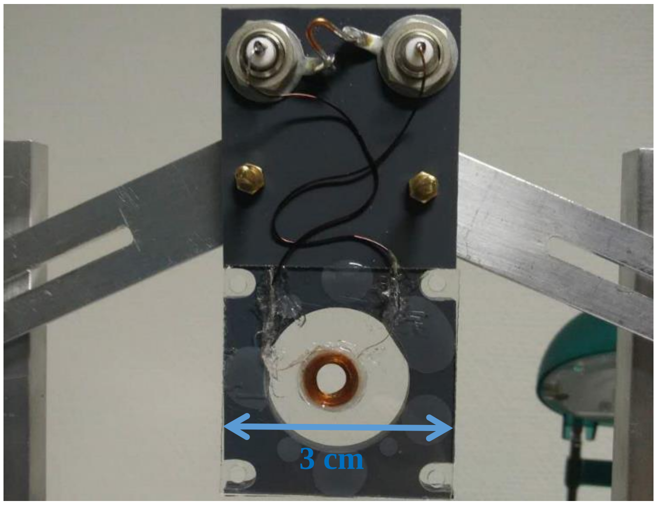

Figure 3-12 An example of the mounted coil.

As can be seen from Figure 3-11, the field viewed by the sample falls rapidly as the distance from the sample to the coil increases. Therefore, the width of the coil w_c should not be too large to make sure that fields produced by all the turns are effective in the tested area.

At last, a series of coils with an average diameter of 6 to 8 mm, and a thickness w_c of 1mm were fabricated. Here, w_c is the thickness of the coil, as

Table 3-1 Parameters of the coil fabricated. The inductance is measured with a handheld multimeter, the uncertainty may be very large.

N° of coil	Nb of turns	Diameter (mm)	Resistance (Ω)	Rise time when connected in series with 50 ohm (μs)	Inductance (μH)	Field (mT/A)	Distance from coil to sample (mm)
10	100	6.5-11	8.9	1.68	151	8.95	2.3
12	120	6-10	10	1.92	192	10.2	2.3
13	60	6-8	4.9	0.32	47	4.65	2.3
14	40	6-7.8	3.2	0.18	28	3.49	2.3
15	20	6-7	1.9	0.045	13	1.55	2.3
16_int	120	6-10.5	10.5	2.16	175	9.4	2.3
16_ext	20	10.5-12	2.6	0.228	19	1.63	
17_int	120	5-8	9.4	1.72	164	8.9	2.5
17_ext	20	19	4.3	0.26	30	0.92	
Helmholtz coil	60/side	116-132	1.1 (two in series)	20	1900	0.91	In center

illustrated in Figure 3-9. The section diameter of the varnished copper wire used are 80 μm or 100 μm. The number of turns ranges from 20 to 120. The picture of an example of the coil is shown in Figure 3-12. Configurations of these coils, as well as their performances, are listed in Table 3-1.

To nucleate a DW, a field pulse with a higher amplitude (typically more than 100 mT in our structure) is required while a rise time of 2 μs is sufficient. However, to study the DW dynamic until precessional flow regime, a field of 20 mT is sufficient while a fast response is more important. It is necessary to be able to go from one coil to another without dismounting, because it is not possible to guarantee an absolutely identical repositioning after each disassembly/reassembly operation. These can induce significant differences in the actually applied field and it would be a disaster to compare the DW behaviors in different structures, which vary with the amplitude of applied field. To solve this contradiction, double-mini-coils were fabricated.

As illustrated in Figure 3-13, a coil of 120 turns was winded in the inner layers and a coil of 20 turns was winded in the outer layers. The two coils have separated connection ports. When one of the coils was used, the circuit of the other one was opened, so that no current could be induced inside and it had no effect.

The performance of the double-mini-coils is shown in Table 3-1 (N°16 & N°17). With these double-coils, we can first nucleate a DW and then measure the DW velocity using the other coil, without the disassembly operation. The uncertainty of field magnitude caused by the change of the relative position between the coil and the field of vision was avoided in this way.

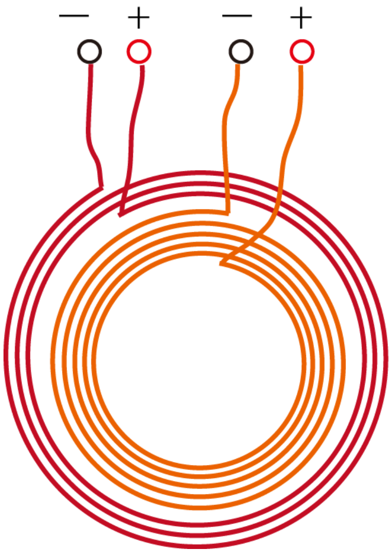

Figure 3-13 Sketch of the double-coil with separated connection ports.

3.2.1.2 Calibration of mini coils

The field produced by the coil is calibrated by taking advantage of the linear relationship between ln(velocity) and $B^{-1/4}$ of the DW motion in the creep regime, as shown in Figure 2-8. First, a Helmholtz coil (characteristics of this coil can be found in Table 3-1) is well calibrated with a magnetometer and is used to measure the DW velocity in creep regime. Then a ln(velocity) vs. the $B^{-1/4}$ relationship is obtained. Then, the coil to be calibrated is mounted and the DW velocity is measured again in the same condition. At last, by fitting with the ln(v) vs. $B^{-1/4}$ relationship obtained with the Helmholtz coil, the field generated by the new coil can be deduced. This method has a high-reliability thanks to the high sensibility of the DW velocity to the magnitude of the field in creep regime.

3.2.1.3 Mounting of the coil and the sample

The mounting of the sample is shown in Figure 3-14. The sample is sandwiched between two plastic plates and the plates are fixed on a solid holder with screws. The left plate has a hole. The sample relies on the right plate and is pressed on it by the left plate, which touches the sample only on the four corners. So that, the nanostructures on the sample are in the hole and can be seen directly. The coil is mounted on a support, as shown in Figure 3-12, and is placed in the back of the sample holder. The support of the coil and the sample holder are independently fixed. The center of the coil is on the axis of the lens. So that, the viewed area of the sample is always in the center of the coil. The sample can be moved to find the interesting area without modifying this fact.

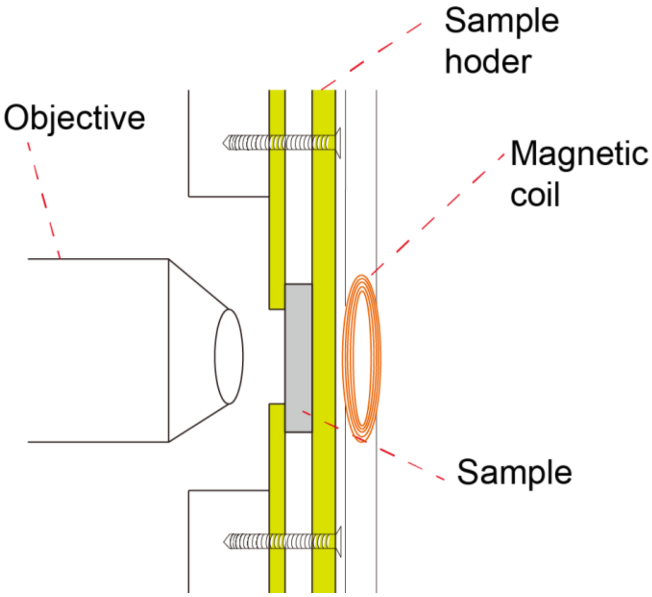

Figure 3-14 Configuration of the set up near the sample.

It is to note that almost all the elements near the sample are insulating, including the holder of coil and the holder of sample. Our experiments have demonstrated that the eddy current in a metallic sample holder aroused by the fast-changing magnetic field can significantly lengthen the rising edge of the field pulse. While this problem is avoided by a no conductive implementation.

3.2.2 Power supply for the coil

The magnetic fields used in our experiments are mainly a constant field or a square magnetic pulse. An alternating magnetic field is not required. A good power supply system for the coil must have the following characteristics: first, the output power and the supplied current should be large enough during the period of the field pulse. Second, a stable current output is required to obtain a stable field, especially at the beginning and at the end of the field pulse. An overshot is catastrophic for the measurement of the DW velocity. Third, the rise time of the power supply should be fast, at least faster than the rise time of the coil.

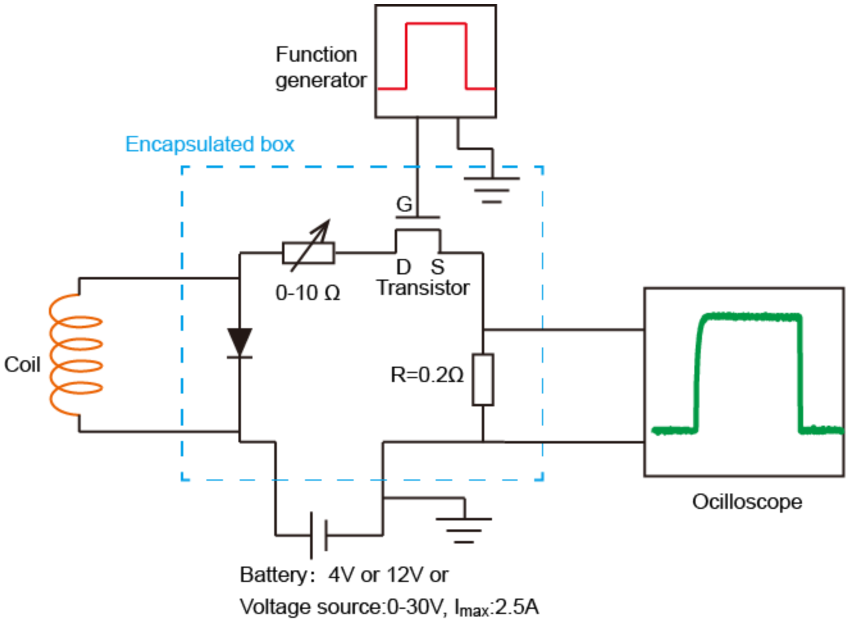

Figure 3-15 A power supply circuit for the coil to produce a field pulse ≥ 50 μm.

Figure 3-15 shows the circuit diagram of a power supply system which allows us to obtain a field pulse with width from 100 μs to the order of seconds. The ON-OFF is controlled by a transistor whose gate voltage is governed by the signal from a function generator. A shunt resistor of 0.2 Ω is connected into the circuit so that the current passed the circuit can be completely supervised via an oscilloscope. A battery or a voltage supply can be used as the power source. The rise time of the voltage supply we used is about 100 μs (i.e. when the transistor is set to ON, the output voltage reaches a stable state after 100 μs). The response speed of battery is very fast, much faster than the coil. A proper field pulse with a width of several hundred microseconds can be obtained with this system equipped with the mini coil we fabricated. If a battery is used as the power supply, the amplitude of the field pulse can be adjusted via a rheostat. A current pulse as high as 3A can be applied with this system. The key constraints that limit the amplitude the current flowing in the coil are the current of the transistor and the coil itself because of the Joule heating if the pulse duration is relatively long. Two examples of the field pulse produced with this power

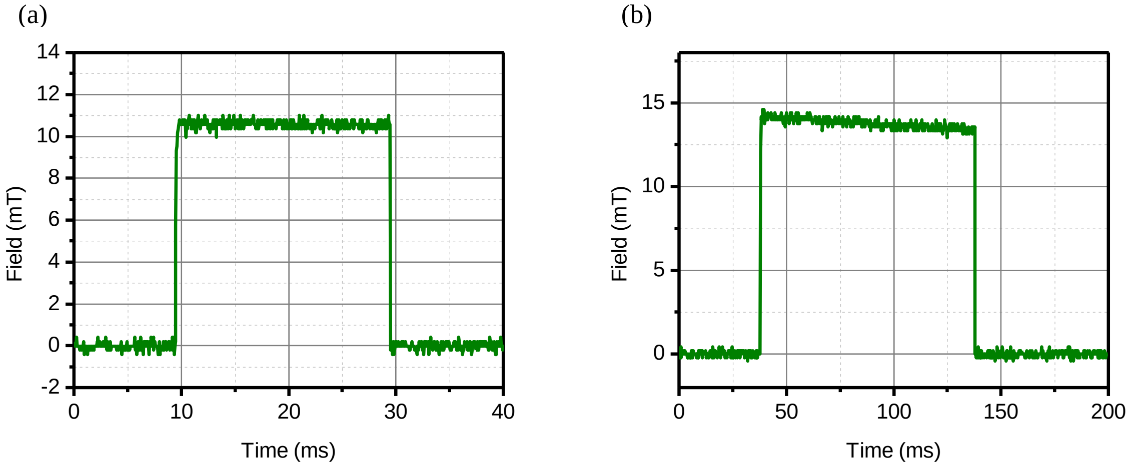

Figure 3-16 Two examples of the field pulses produced by coil N°12 (see Table 3-1) with the power supply shown in Figure 3-15. (a) A voltage source of 12V is used. (b) The voltage supplied is increased to 16V and the pulse width is increased to 100ms. We can see that the current supervised drops gradually due to the Joule heating in the coil.

supply system are shown in Figure 3-16. The corresponding current is about 1A in Figure 3-16 (a) and 1.3A in Figure (b). Parameters of the coil N° 12 used can be found in Table 3.1. According to Eq. (3-15), the temperature rise is estimated to be 4℃ for a 1A current with a duration of 20 ms and about 30℃ for a current of 1.3 A with a duration of 100 ms. The drops of the magnitude of the field in Figure (b) is caused by this temperature rise.

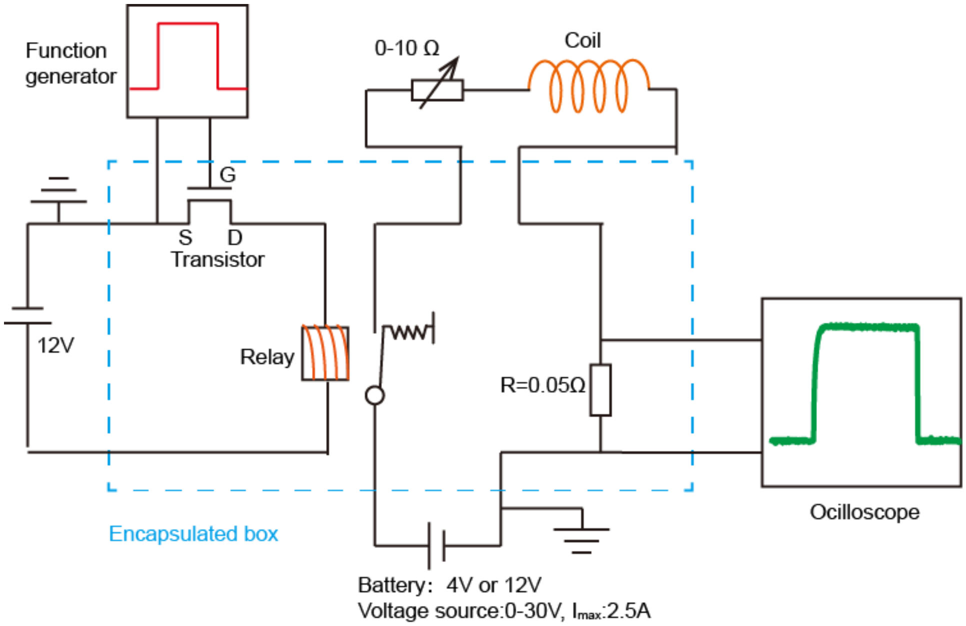

Figure 3-17 A power supply system with a relay, allowing an output with a relative high current and long duration.

To overcome the constraint of current density by the transistor, a more robust power supply system was created. As shown in Figure 3-17, the OFF-ON of the power supply circuit is governed by a relay. The circuit controlling the OFF-ON of the relay is governed by a transistor and a function generator. This system allows a relatively large current density (20A, precisely) and longer width of the pulse. However, the relay introduced a delay of the field pulse about 15 ms after the command from the function generator.

We have used another implementation that can produce a field pulse with both large amplitude and short rise time. As can be seen from Eq. (3-13), to decrease the rise time of the field pulse, a large resistance can be connected in series with the coil. Eq. (3-4) shows that to obtain a high field, a large current is necessary, thus requiring a very high voltage supply after the introduction of the large resistance. An ordinary voltage/current source cannot supply such a high power and with a fast response speed. A power supply based on the discharge of condenser bank can solve this issue[127,128]. As shown in Figure 3-18, a current supply of this type is implemented. The condenser bank is charged with a high-voltage supply. Once the transistor is ON, a high current will be generated by the discharge of the condensers.

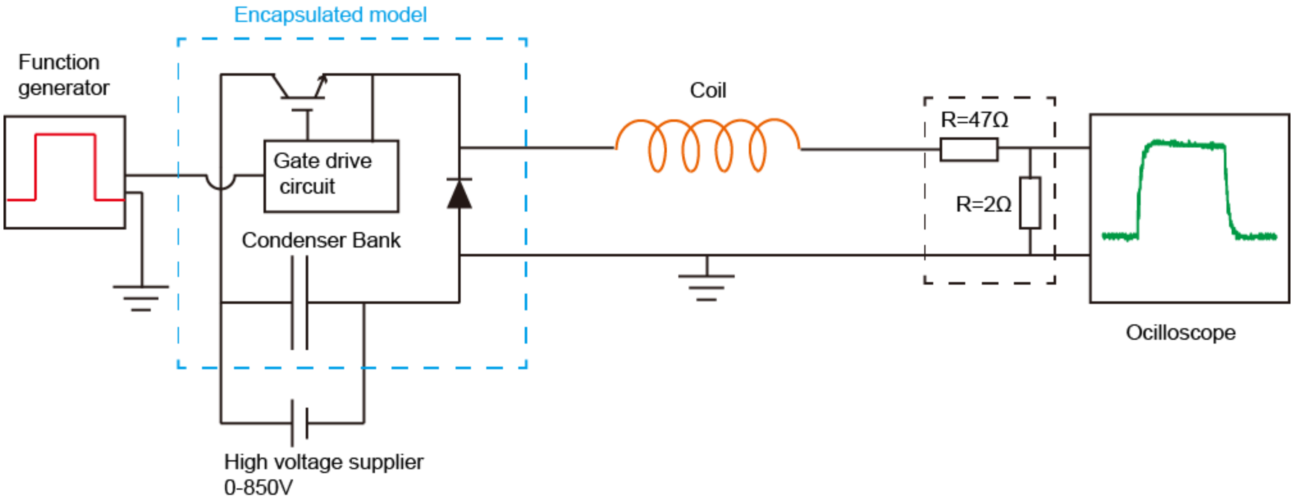

Figure 3-18 A power supply system based on the discharge of a condenser bank.

Figure 3-19 shows two examples of the field pulses generated with this system. With a coil of 120 turns and 8 mm large, the amplitude of the field pulse has reached 130 mT. This field is sufficient to nucleate a DW in the microstructure. The rise time (falling time) is less than 2 μs. Thanks to the short falling edge, the nucleated DW still remains in the structure after the pulse. Using a coil of 20 turns, an even shorter rising edge is obtained. The field can reach the plateau within 500 ns. This field allows us to measure the DW velocity in the nanostructure with very high precision. An amplitude of 23 mT is sufficient to study the DW behavior in processional flow regime in soft material such as the CoFeB.

However, compared with the former two power supply system, the disadvantage of this supply is the relatively short rated pulse duration of only 10 μs.

With the above three power supply systems and coils with various configurations, different kind of field pulses can be generated, allowing us to study the DW dynamics in different regimes.

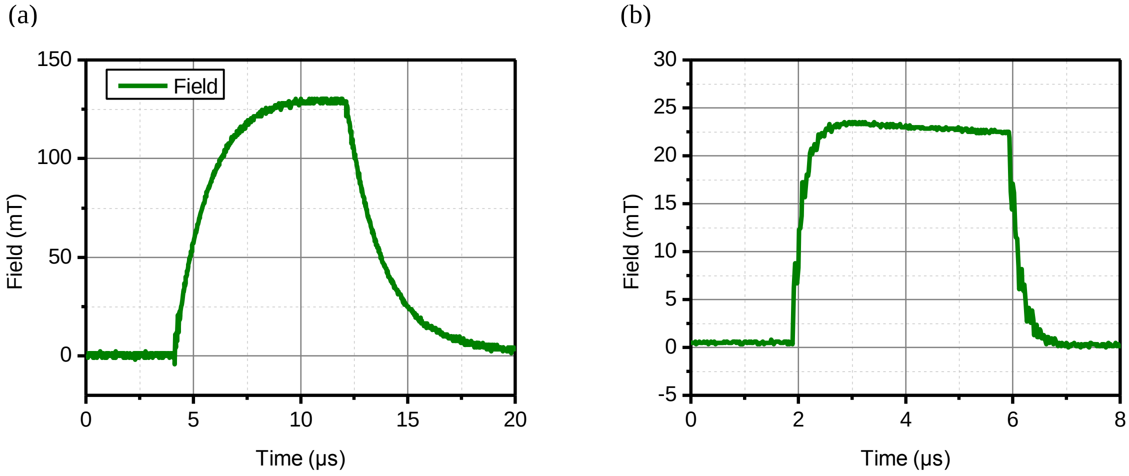

Figure 3-19 Two examples of the magnetic field pulse produced with power supply system shown in Figure 3-18. (a) The coil used is coil N°12 (see Table 3-1), with 120 turns. (b) The coil used is N°16_ext, with 20 turns.

3.3 Configurations for electrical tests

It is interesting to study the DW dynamics when the magnetic field and the electric current are applied simultaneously. We have developed a system in which a clear magnetic field pulse and a current pulse are compatible.

As discussed above, in order to ensure the magnitude of the pulse viewed by the sample, the distance between the sample and the coil should be as short as 2 mm when a mini coil is used. Moreover, the sample holder should be insulating. An ordinary chip carrier is not a good choice. In this case, we have printed several conductive strips in the sample holder (the plastic plate in the back of the sample, as shown in Figure 3-14). In these experiments, the implementation in Figure 3-14 is a little changed: the sample is stick into the right plastic plate with silver lacquer and the plate in front of the sample is removed. Then, the nanostructure was connected into the electric test circuit after wire bonding between the electrodes and these conductive strips. An example of the configuration is shown in Figure 3-20.

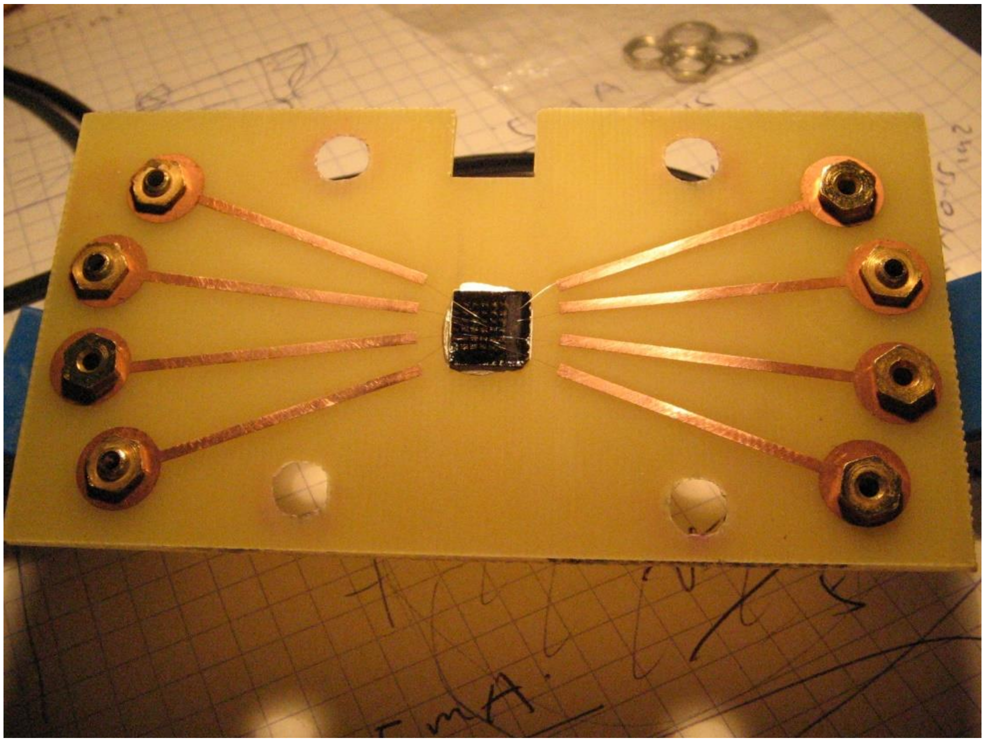

Figure 3-20 An example of the electrical test configuration: the sample is stick into a plastic plate with silver lacquer and the electrodes of microstructures are wire bonded with the copper stripes.

Figure 3-21 gives a schematic diagram of the complete configuration of the electrical tests circuit. The pulse generator can supply a voltage pulse of 20V (high impedance mode). By measuring the voltage

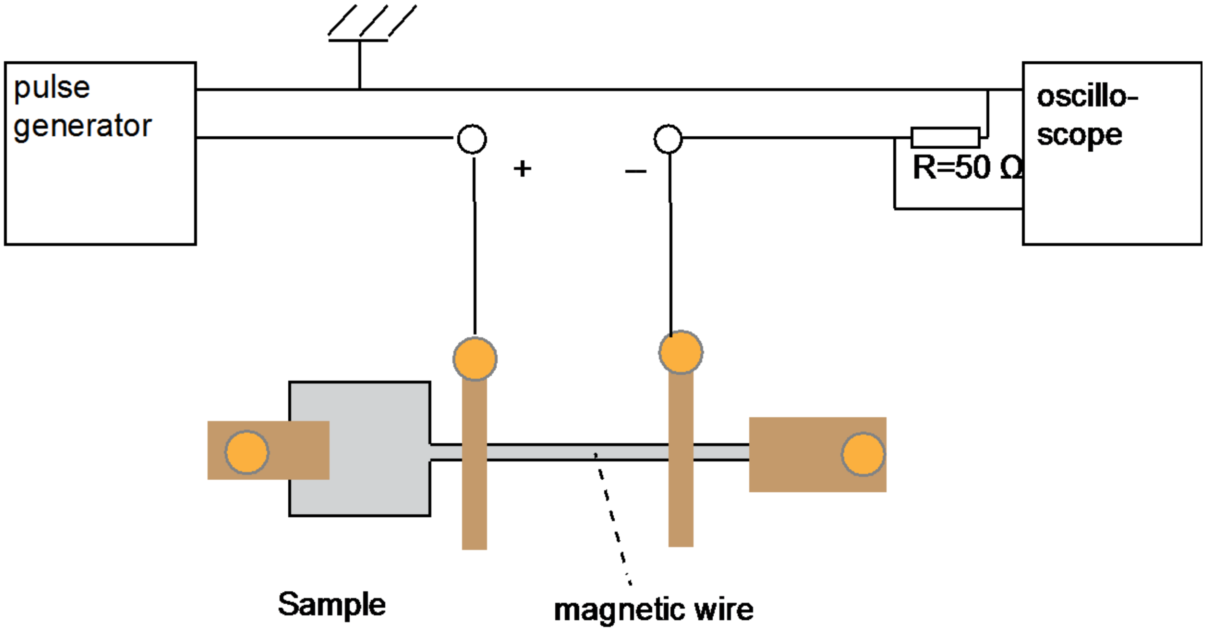

Figure 3-21 Sketch showing the complete configuration for electrical tests.

across the 50 Ω termination on the oscilloscope, we are able to check the current actually flowing in the nanowire.

In order to protect the nanostructures from being damaged by the static electricity, the conducting stripes in the sample holder were short circuit with a switching group before the wire bonding. They are disconnected only after the connection of the test circuit was finished and the all the instruments connected into the circuit were prepared. In addition, all the lead feet of the structure were connected to the ground every time when changing the configuration of the test system.

3.4 Samples and the measurements procedures

3.4.1 Samples

The sample studied is a Ta(5nm)/$Co_{40}Fe_{40}B_{20}$(1nm)/MgO (2nm)/Ta(5nm) multilayers stack with perpendicular anisotropy, which is a well-known material[90,129]. It was annealed at 300 °C for two hours. Several properties of the samples were experimentally characterized: saturation magnetization $M_S = 1.1 \times 10^6 A/m$, effective anisotropy $K_{eff} = 2.2 \times 10^5 J/m^3$, the damping constant is α=0.013, and the DW width was estimated to be $\Delta = 10.7$ nm[90], the DMI constant measured in our system is less than

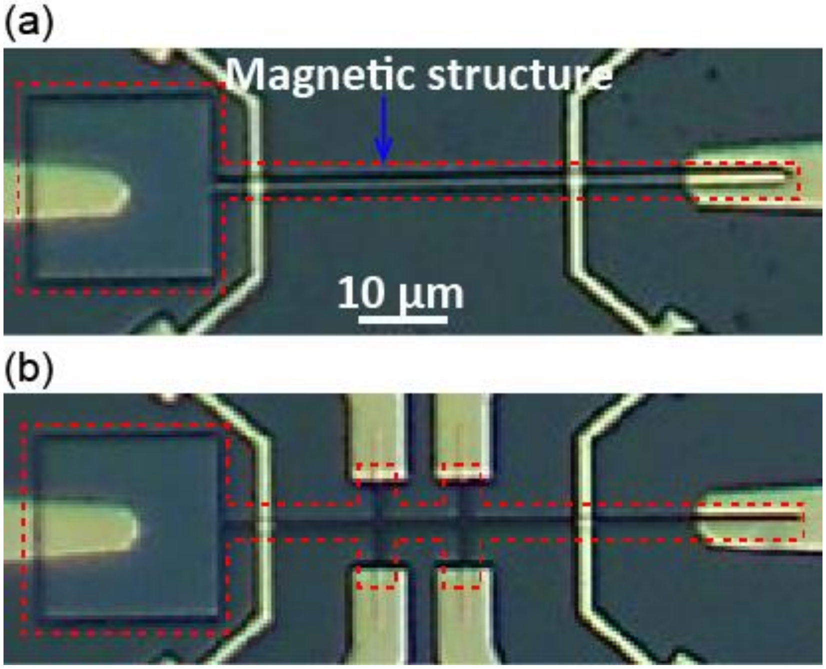

Figure 3-22 Optical image of two of the samples studied, (a) with and (b) without the Hall cross. The zone surrounded by the red dashed line is the magnetic structure. The yellow parts are electrodes.

0.01mJ/m^2, meaning that its effect on the DW surface energy is negligible[24]. This result is also confirmed by Brillouin light scattering experiments.

One sample remains unpatterned and studied as a reference. Another sample was patterned by conventional electron beam lithography and ion beam etching into 50 μm long narrow wires connected with a 20μ×20μm square (nucleation pad), as shown in Figure 3-22. The size of the magnetic square is 20 μm ×20 μm and the width of the wire in different structures are 200nm, 400nmm 600nm, 1μm and 1.5μm respectively. In some structures, Hall crosses were patterned, as shown in Figure 3-22 (b). Several golden electrodes were added on the magnetic structure for the electrical tests.

3.4.2 Nucleation of DW

As stated at the beginning of the section 3.2 , our methods to nucleate a DW in the nanostructure is applying a large and short magnetic field pulse. First, the magnetic structure is saturated in one direction by a permanent magnet or by a large field pulse (~ 130 mT). Then, a field pulse in the opposite direction is applied by a magnetic coil with 120 turns. One typical waveform of the pulse is shown in Figure 3-19 (a). Usually, a magnetic reversal (DW nucleation) first occurs in the nucleation pad owing to its large surface, which promises a large probability to have a nucleation point. To ensure that the nucleated DW stay still in the nanostructure after the field pulse, the length of the field pulse should be well controlled. According to our experiments, a DW can be obtained in most of the structures studied when applying a field pulse by an exponential field pulse with an amplitude of 130 mT and a pulse width of 4 – 8 μs.

3.4.3 Measurement of the DW velocity

The DW motion velocities in all our experiments were obtained through observing the DW motion distance by a field pulse. Precisely, before and after applying a field pulse with width T_P, we take two Kerr images respectively. After comparing these two Kerr images, we can obtain the DW motion distance D during this pulse. Then, the corresponding DW motion velocity can be calculated as $v=D/T_P$.

In particular, for the DW velocity measurement in the nanostructure, the width of the field pulse should be very short. In these experiments, after nucleating a DW with the 120-turns-coil of the double coils, we pass to the 20-turns-coil without disassembly the coil implantation. A 220 ns rise time of this coil gives a very good rectangle square waveform field pulse with a width of several microseconds, as shown in Figure 3-19 (b). In order to improve the accuracy of the measurement, we used the differential methods. That is to say, first, we measured the DW motion distance D_1 by applying a field pulse with a relatively long width t_1; then, we measure the DW motion distance D_2 after a field pulse width a relatively short width t_2. The DW velocity is calculated as, $v = (D_1 - D_2)/(t_1 - t_2)$.

At the beginning of the thesis, in order to have a global view of the characteristic of the sample to be studied, the field-induced DW motion velocity in the infinite film was measured with a large field range, as shown in Figure 3-23.

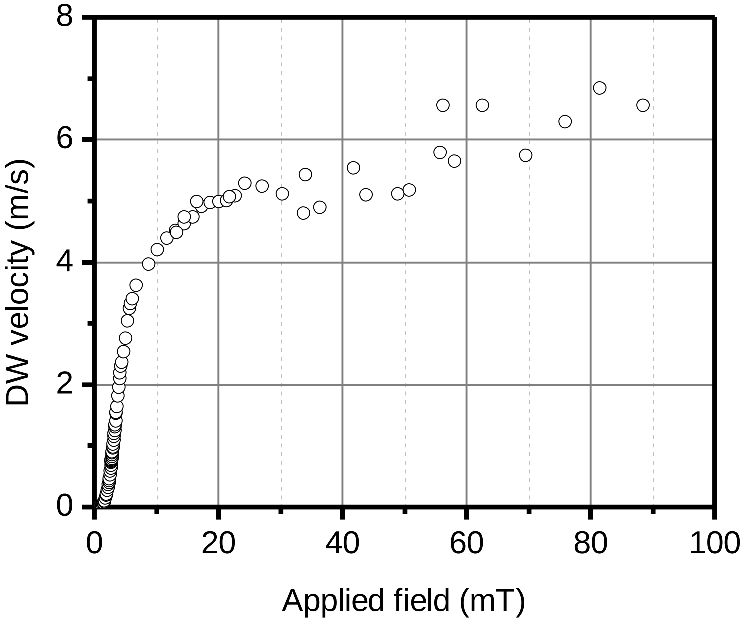

Figure 3-23 DW motion velocity in the Ta/CoFeB/MgO infinite film vs. the applied field.

Chapter 4 Surface energy of domain walls

The DW surface energy γ_{DW} plays a very important role in the dynamics and statics of the DW. For example, it affects the DW pinning and depinning process [130–132], the DW creep motion[50], and the tilting angle of a moving DW in narrow wires[79]. In this chapter, we present several experiments in which the DW surface energy plays a dominant role. The DW pinning at some artificial geometries is explained in terms of the DW surface energy. At last, a new type of magnetic sensor based on the surface tension is presented.

4.1 Direct observation of the effect of DW surface tension and measurement of the domain wall surface energy

4.1.1 Spontaneous contraction of the magnetic bubble

This experiment was done based on the magnetic structure shown in Figure 4-1. In this experiment, we used a double coils (coil 16 listed in Table 3-1). First, using the inner coil and the current supply system illustrated in Figure 3-18, we were able to create a field pulse of 130 mT and of several microseconds. A DW can be created in the structure (normally, the DW nucleates first in the square but it stops in the wire at the end of this large pulse). Then, the DW was injected from the wire into the square using the outer coil, which can produce a square field pulse of several microseconds thanks to its short rising time. At the end of the pulse, the result was a semi-circular bubble domain, as shown in Figure 4-2.

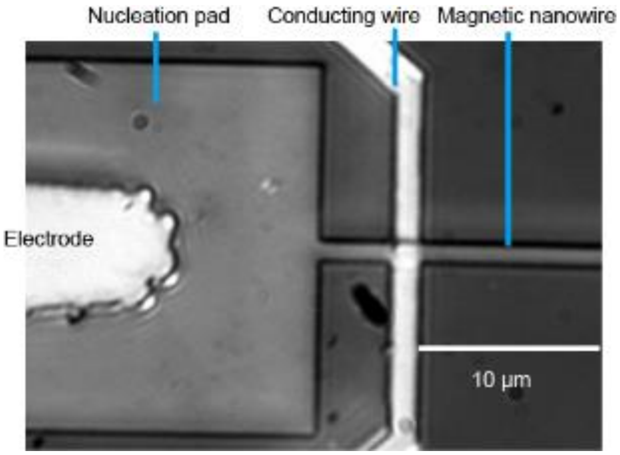

Figure 4-1 the Optical image of the magnetic structure used in this experiment. The size of the nucleation pad is 20 µm × 20 µm and the width of wire is 1 µm in this image. The conducting line and electrodes were not used in this experiment. A complete view of this structure can be found in Figure 3-22.

Subsequently, although the magnetic field was zero, we found that the bubble could contract spontaneously until the DW had come back to the entrance of the nucleation pad, i.e., the neck. Furthermore, the speed of contraction depended on the radius of curvature of the DW circle. The smaller the radius, the faster was the contraction. As shown in Figure 4-3, when the radius of the bubble is approximately 9 μm, the DW contraction is observable only after 20 s. However, when the radius of the DW bubble shrinks to 4 μm, DW returns to the neck after several seconds. After returning to the neck, no more DW motion could be observed during several minutes; the state is stable.

We checked that there was no remnant parasitic field that could induce such an effect. The sample holder was made of a non-magnetic material, and a Hall probe was used to check the magnetic field around the sample. In addition, the experiment was conducted with both directions of the magnetization of the

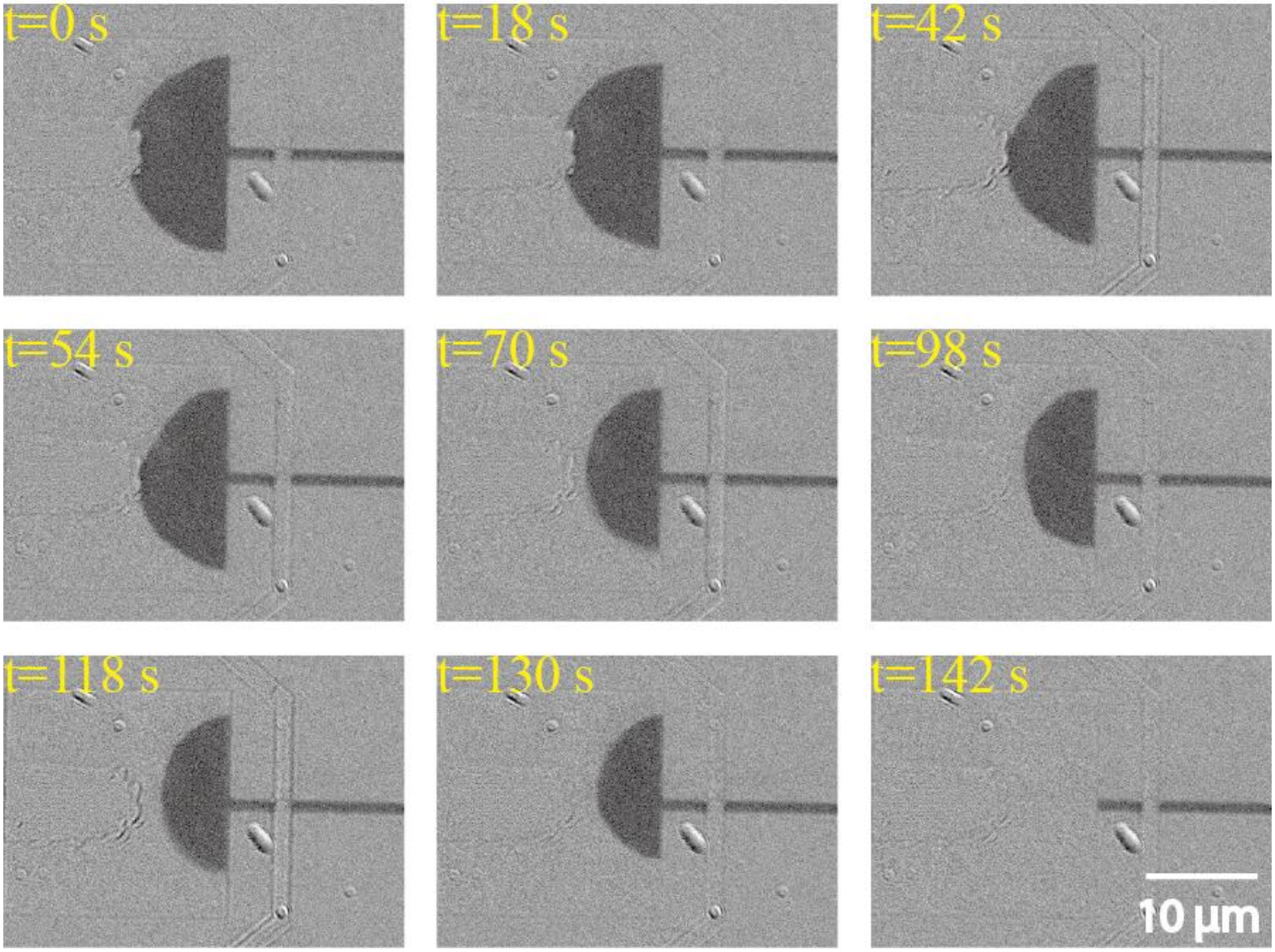

Figure 4-2 Spontaneous contraction of the semicircular domain bubble in a zero external field.

bubble and the result was exactly the same, which would not have been the case if there had been a remnant field.

4.1.2 The Laplace pressure of a bend DW

In physics, the concept of the Laplace pressure is commonly used to explain the surface and interface phenomena[133,134]. The Laplace pressure indicates the pressure difference between the inside and the outside of a curved surface or interface.

A DW can be seen as an elastic membrane with energy γ_{DW} per unit area[135]. For a bend DW, there is also such a pressure. In a bulk magnetic material, the Laplace pressure of a spherical DW expressed as[135],

$$P_\gamma = \gamma_{DW}/\left(\frac{1}{R_1}+\frac{1}{R_2}\right) \tag{4-1}$$

where R_1 and R_2 are the principal radii of curvature of the wall at the point considered.

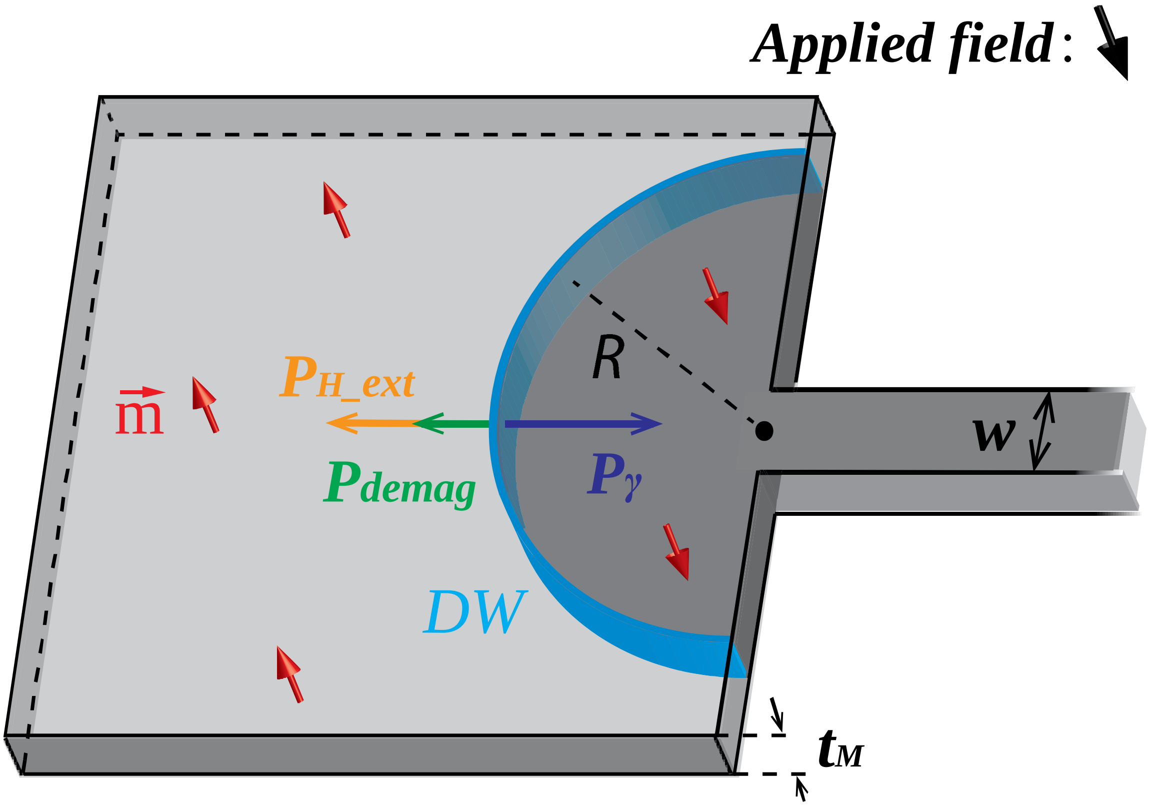

Figure 4-3 3D sketch of the profile of the semicircular magnetic bubble stabilized in the square. The arrows on the DW show the forces induced by the different pressures on this part. As the pressures are isotropic, the direction of the local forces point perpendicularly to the surface of DW and changes according to the position on the DW.

In a thin film, the curved DW is a cylindrical surface of radius R, as shown in Figure 4-3. Then the Laplace pressure can be written as[134–136],

$$P_\gamma = \gamma_{DW}/R \tag{4-2}$$

Where R is the curvature of radius of the DW. (Appendix 1 presents a demonstration of this result).

The Laplace pressure is high enough to induce some movement on the bubble in the creep regime. Note that it remains a relatively low force; the movement is possible because CoFeB is very soft[40]. Moreover, the bubbles created had a quite small radius (<10 μm), which induces a quite big Laplace pressure. In agreement with $P_\gamma = \gamma_{DW}/R$, the spontaneous contraction was faster as the radius of the domain reduced.

4.1.3 Stabilization of the magnetic bubble and estimation of the DW surface energy

To quantify the Laplace pressure, the external field needed to compensate this pressure and stabilize domain bubble was measured by the following way: First, a very small static field is applied using the inner coil of the double-coils. Second, we created a semicircular bubble domain using a large square-shaped field pulse produced by the outer coil. In the experiments, the initial size of the semicircular domain bubbles can be controlled through the magnitude and the duration of the field pulse when blowing the DW into the square. To check whether it is stable or not under the static field, we have waited for 60 s. If no movement was detected after 60 s (for example, in the case of Figure 4-4 (b), there is a movement), the state can be considered as stable. Then the static field was increased (or decreased) by step of 20 μT until a movement is detected. In Figure 4-4(c), critical fields for expansion and for contraction were plotted as a function of the inverse of the radius of the domain bubble. The equilibrium field is between the two clouds of critical fields for expansion and for contraction. Its magnitude is quite well defined. As could be expected, this field had to be applied along the magnetization direction inside the bubble.

It was found that the magnitude of the external field to stabilize the semicircular domain bubble depended on the size of bubbles. As the radius of the domain bubble is reduced, the stabilization field increased sharply.

Theoretically, a circular DW is at equilibrium only when the pressure due to the magnetic field exactly cancels out the excess pressure from the DW tension. The Zeeman pressure given by the external field H_{ext} is expressed as

$$P_H = 2\mu_0 H_{ext} M_S \tag{4-3}$$

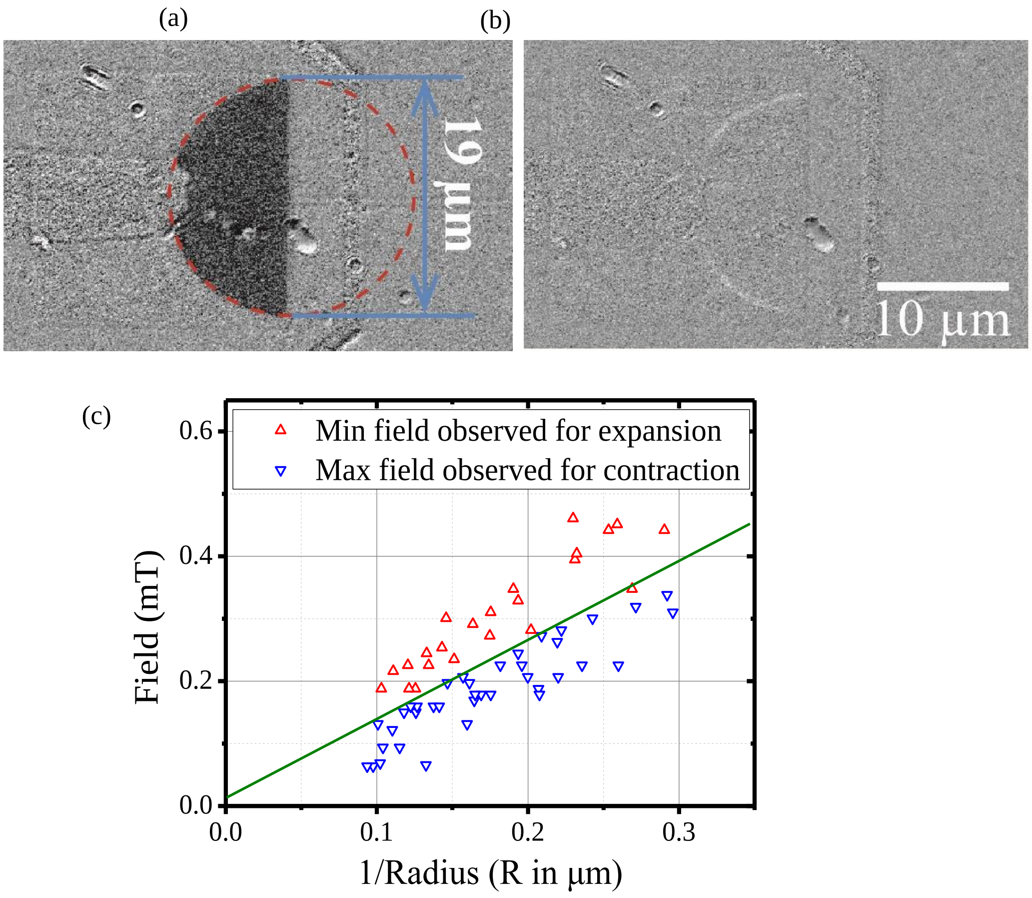

Figure 4-4(a) A semi bubble is stabilized by an external field $\mu_0 H_{ext} = 0.11\ mT$ and no DW motion is observed during 60s; (b) The external field decreases to $\mu_0 H_{ext} = 0.094\ mT$ T and the domain bubble contracts slightly. This image is the difference between two images: the first one was acquired before decreasing the applied field and the second one was acquired 66s after having decreased the applied field. The white circular trace shows the DW displacement; (c) Critical field for expansion and contraction as a function of the inverse of the radius of the semicircular domain bubble. Two structures associated with 600 nm wide wire were used to get more statistics.

According to Eq. (4-2), the Laplace pressure increases linearly as the inverse of the radius of the DW bubble. The field required to stabilize the semi-bubble should be inversely proportional to the radius. In Figure 4-4(c), the stabilizing field appears as the boundary between the expansion points and contraction points. We can see Figure 4-4(c) that there is a very good agreement between the predicted behavior and the experimental one, the slope being $k_{equ} \approx 1.2\ mT \cdot \mu m$.

However, one should be careful because there are two contributions for the magnetic field: the externally applied field and the demagnetizing field. We have numerically calculated the demagnetizing field. To obtain this field, we have used the magnetization current[1,137]. Let us remember that the magnetization is defined as the volume density of magnetic moment $\vec{\boldsymbol{\mu}}_m$ (see Eq.(2-1)) and each elementary magnetic moment can be seen as a loop of current of magnetic moment $d\vec{\boldsymbol{\mu}}_m = Id\vec{\boldsymbol{S}}$, where I is the current flowing inside the loop and $d\vec{\boldsymbol{S}}$ is the surface of the loop. For a uniformly magnetized out-of-plane domain, the magnetization density can be expressed as,

$$M_s\vec{z} = I\frac{dS\vec{z}}{dV} = \frac{I}{t_M}\vec{z} \tag{4-4}$$

where $\vec{z}$ is the unit vector in the out of plane direction. Let's note that, looking at picture 4.5, it is straightforward: the effective current of each elementary magnetic dipole is cancelled by the neighboring dipoles, except for the dipoles at the edge of the domain. For the structure we studied in the experiments, the demagnetizing field can be deduced from the electrical circuit shown in Figure 4-6(a). Using MATLAB, we calculated the demagnetizing field for a radius from 3 µm to 10 µm. The result is plotted in Figure 4-6(b). It can be seen that, in this range, this demagnetizing field can be approximated by a linear law, of slope $k_{demag} \approx 1.24\, mT \cdot \mu m$.

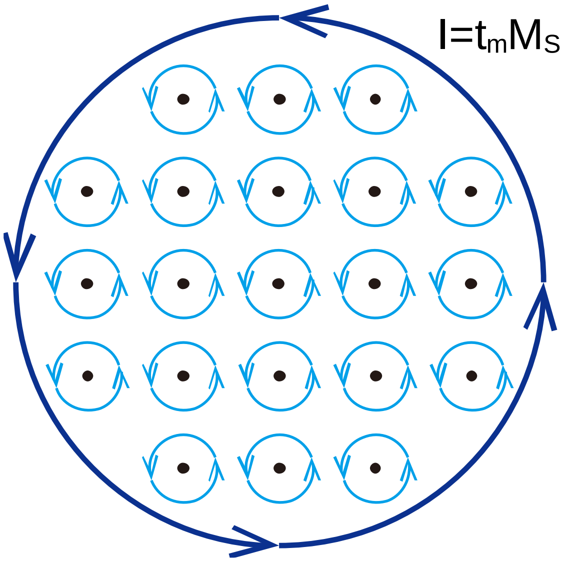

Figure 4-5 Magnetization current of the magnetic structure (a uniformly magnetized disk in this sketch)

From the above considerations, equilibrium of the pressures can be written as follows:

$$2\mu_0 H_{ext} M_S + 2\mu_0 H_{demag} M_S - \frac{\gamma_{DW}}{R} = 0 \tag{4-5}$$

Using the linear laws found for $\mu_0 H_{demag} = k_{demag}/R$ and the equilibrium field $\mu_0 H_{equ} = k_{equ}/R$, and simplifying by 1/R, the surface energy of DW is given by:

$$\gamma_{DW} = 2M_S(k_{equ} + k_{demag}) \tag{4-6}$$

From Eq. (4-3), we get $\gamma_{DW} \approx 5.4\ \mathrm{mJ}/m^2$. From[138,139], the exchange stiffness A_{ex} in this type of material was found to be between 10 and 28 pJ/m. For our sample, the effective anisotropy was measured as $K_{eff} = 2.2 \times 10^5 J/m^3$ [90]. According to the formula $\gamma_{DW} = 4\sqrt{A_{ex}K_{eff}}$, it gives γ_{DW} between 6 and 10 mJ/m^2. It can be seen that our value is in good agreement with the previous results. Note that the formula used here to calculate the surface energy γ applies only for films without DMI. In fact, the DMI

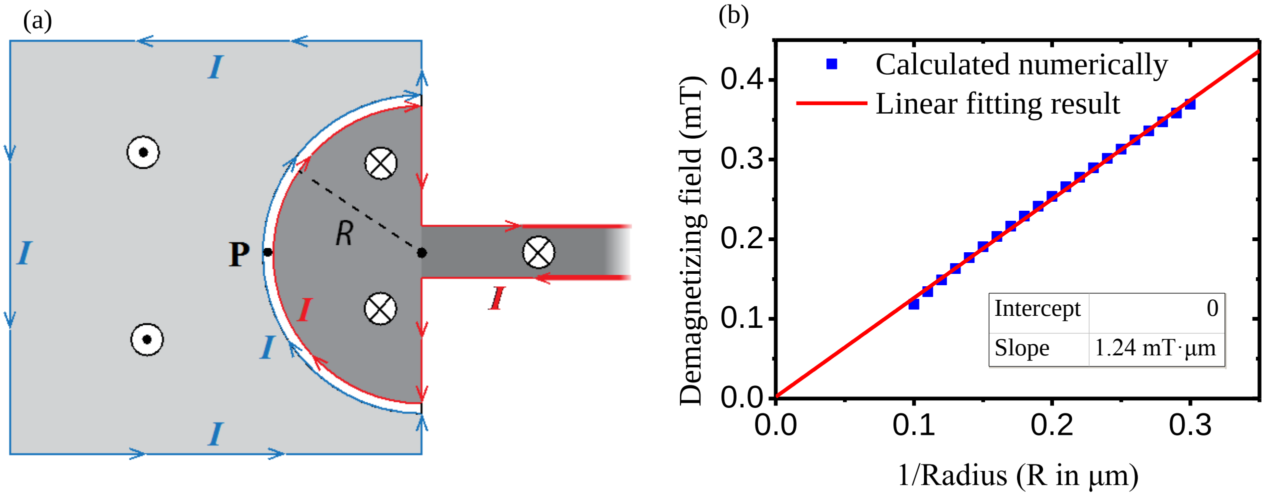

Figure 4-6 (a) Electrical circuit identical to the current created by the magnetization at the edges of structure and along the DW. Then, using Biot-Savart law, stray field can be calculated; (b) Numerically calculated demagnetizing field at point P as a function of the inverse of radius of bubble.

constant measured in our system is less than $0.01mJ/m^2$, meaning that its effect on the DW surface energy is negligible[24]. This result is also confirmed by Brillouin light scattering experiments.

4.1.4 Interactions of two magnetic domain bubbles

As suggested before, the behavior of magnetic bubbles induced by the surface energy is similar to that of soap bubbles. There is a very well-known experiment in which two soap bubbles are connected to each other, as illustrated in Figure 4-7; the result is not what one might expect intuitively. Instead of obtaining two bubbles of equal size, the smaller bubble contracts while the bigger one expands due to the unbalanced Laplace pressure [134,136,140].

Here, we observed the same phenomenon. We simultaneously created two semicircular bubbles with different sizes in a magnetic square, as shown in Figure 4-8. An external field $\mu_0 H_{ext} = 0.41mT$ was applied to avoid the collapse of both bubbles. In the beginning, the smaller magnetic bubble was stable while the larger one expanded slowly. When the two bubbles got close, the bigger bubbles continued to expand while the smaller one contracted back to the neck, as shown in Figure 4-8.

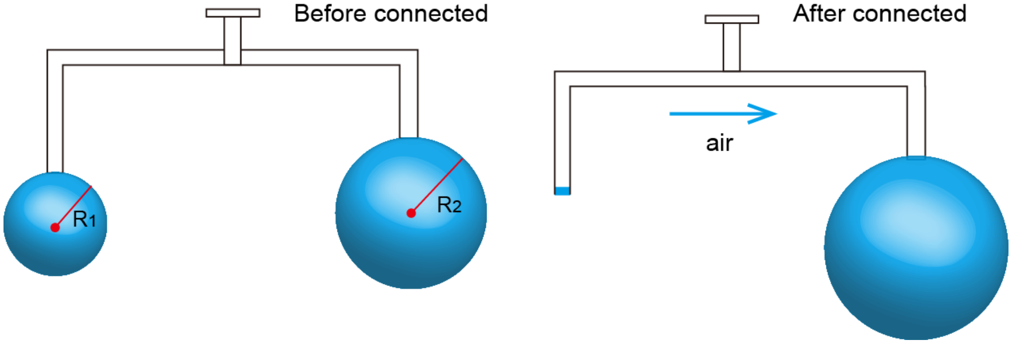

Figure 4-7 Sketch of experiments about the interplay of two soap bubbles.

The competition of three pressures governs this process: the Zeeman pressure tends to enlarge the size of both bubbles; the repulsive pressure between the two bubbles due to dipolar interaction[1] hinders the merger of the two bubbles; the Laplace pressure tends to reduce the sizes of the bubbles. The strength

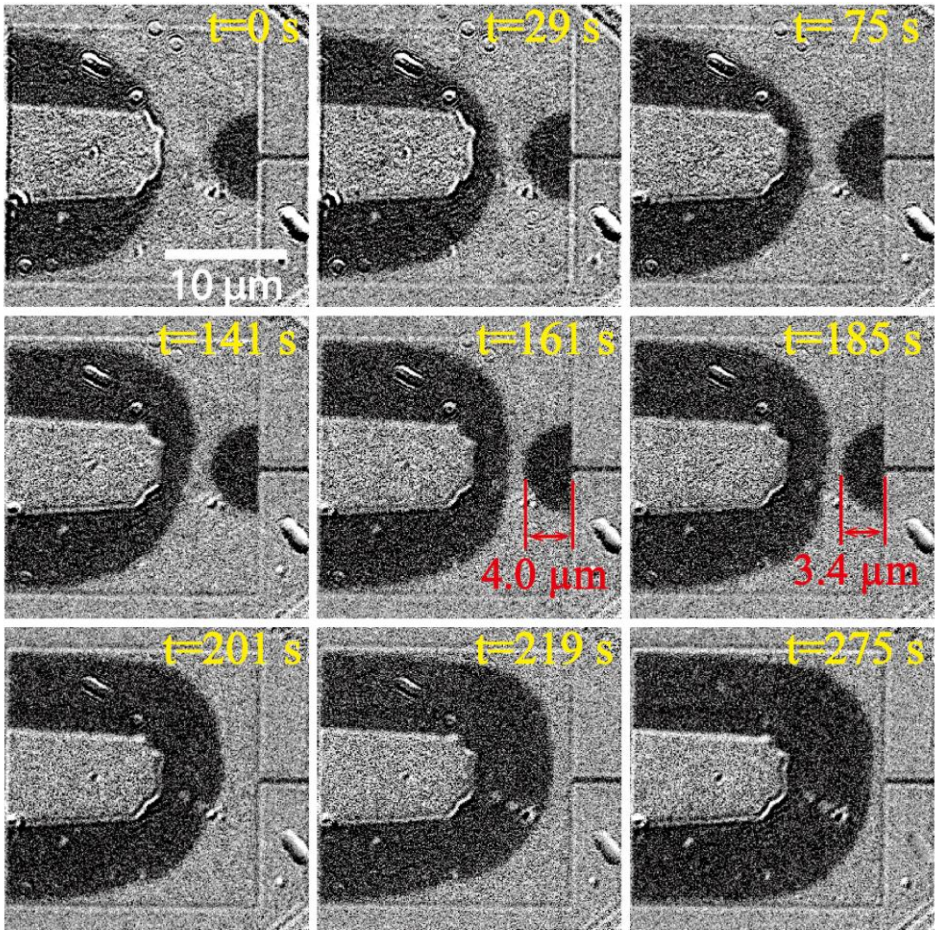

Figure 4-8 Size evolution of two semicircular bubbles under applied field 0.41 mT. The bigger bubble expands and squeezes the smaller one because of the unbalanced Laplace pressure. The movie on this dynamic process can be download online.

of the former two pressures is equal for the two bubbles while the Laplace pressure is higher for the smaller bubble, as predicted by Eq. (4-1). Finally, the smaller bubble is squeezed by the larger one.

4.1.5 DW pinning and depinning at Hall crosses or at necks

Thanks to the theory of the DW surface energy and the Laplace pressure, it becomes possible to explain the origin of the DW pinning effects in some geometries, such as the connection of the wire with the nucleation pad, and the Hall cross.

Indeed, when injecting a DW from the narrow wire into the square, we found that the DW was pinned at the neck and would not be depinned until the applied field reached a threshold value. As shown in Figure 4-9(a), the DW was moved by a field pulse. After the pulse, we could see that the DW stopped at

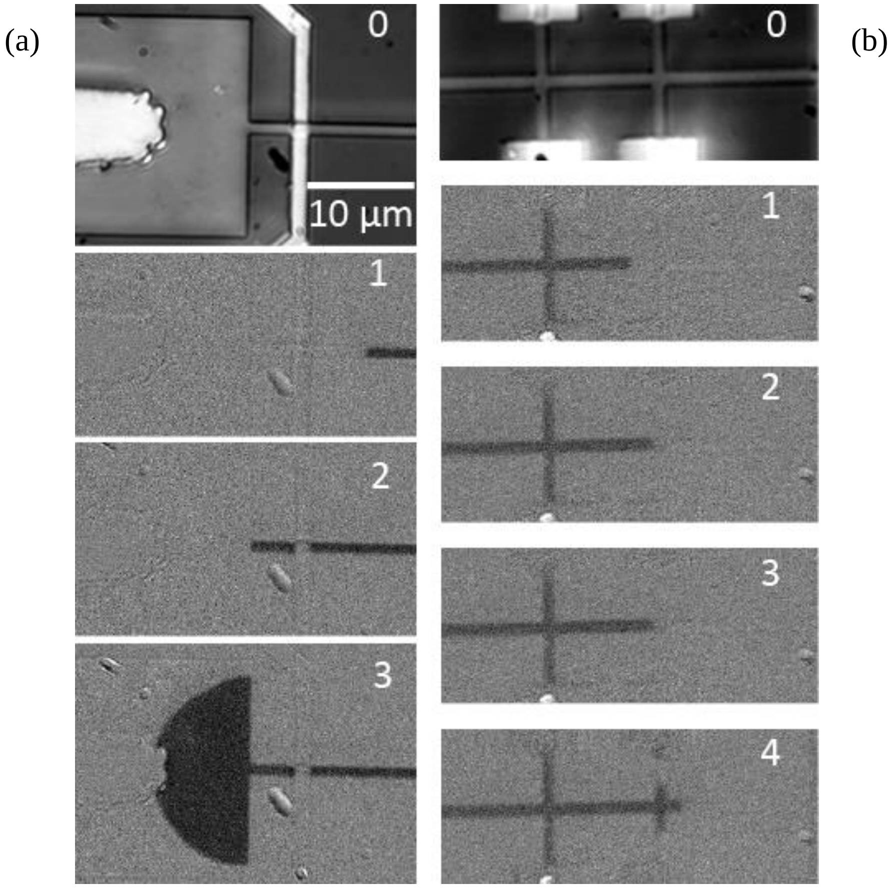

Figure 4-9 (a) DW depinning at the neck: Image n°0 is the raw image of a structure, with a 1µm wide wire. As the magnetization was saturated before acquiring it, it is used as the reference image to remove the background and get the Kerr image. Image n°1 shows the initial position of the DW. After a field pulse of 5.8mT and 5 µs, the DW moves to the neck (image n°2). One more identical pulse could not move it. After increasing the magnitude of pulse to 5.9 mT, the DW is depinned and expands to a semicircular bubble (on image n°3); (b) DW depinning at a Hall cross: the sequence is similar to sequence (a), n°0 is the raw reference image of a 1 µm wide wire. Between each picture from n°1 to n°3, a pulse of 5.9 mT and 5 µs is applied. With these pulses, the DW is moved in the wire but is pinned at the Hall cross. Between n°3 and n°4, a field pulse of 6.0 mT and 5 µs is applied and the DW is depinned.

the neck. We tried to send more pulses of the same magnitude, but no more movement occurred; the DW remained pinned at the neck. To depin the DW, we had to increase the magnitude of the field; the critical field to achieve the movement is called the depinning field H_{dep} here. It should be noted that the duration of field pulse was always 5 µs in these measurements. We repeated this experiment several times for each sample. The depinning field was almost always the same. For Hall crosses, the behavior is the same [(Figure 4-9(b)]: pinning, if the magnetic field is below a critical field, and movement above it.

The interesting point is that the depinning field depends on the width of the wire. We have plotted H_{dep} in Figure 4-9 (c). It can be seen that there is a linear dependence of H_{dep} as a function of the inverse of the width. Furthermore, the dependence is almost same for the Hall cross or for the neck of the pad. Let us note that when 1/R tends to zero, the depinning field tends to $\mu_0 H_0 = 3\ mT$. This is explained by the velocity law. Below 3mT, for pulses of 5µs, no effective movement is possible. Movement requires a field larger than a minimum value H_P, which can be estimated at 3 mT[90]. Indeed, even if for magnetic fields lower than 3mT, a DW can move in this kind of sample, after the end of the pulse, since it could not go very far with a 5 µs pulse, it is driven back by the surface energy, as described Figure 4-2. Typically, for the Hall cross, with a wire width between 200 nm and 1.5 µm, the DW has to propagate over at least 200 nm (up to 1.5 µm) to reach the opposite wire, which means a velocity greater than 40mm/s (300mm/s) and a field of approximately 3mT (almost the same value) are required (see Figure 2-8 for DW velocities vs. driving field in this material).

Now, our experiments show that the pinning is due to DW surface energy. Indeed, we can do the same analysis as in section B; in this case, the minimum radius of the bubble is w/2, where w is the wire width (see Figure 4-10). Therefore, the maximum pressure induced by the Laplace interface force is 2γ/w. Movement can occur only if the overall pressure due to the magnetic field and Laplace pressure is larger than the critical pressure $2\mu_0 H_0 M_S$ defined by the depinning field H_0 along,

$$2\mu_0 H_{ext} M_S + 2\mu_0 H_{demag} M_S - \frac{2\gamma_{DW}}{w} \geq 2\mu_0 H_0 M_S \qquad (4\text{-}7)$$

For the magnetic field, there are two contributions: the externally applied field and the demagnetizing field. From this equation, the depinning field is predicted to be:

$$\mu_0 H_{dep} = \frac{\gamma_{DW}}{M_S w} - \mu_0 H_{demag} + \mu_0 H_0 \qquad (4\text{-}8)$$

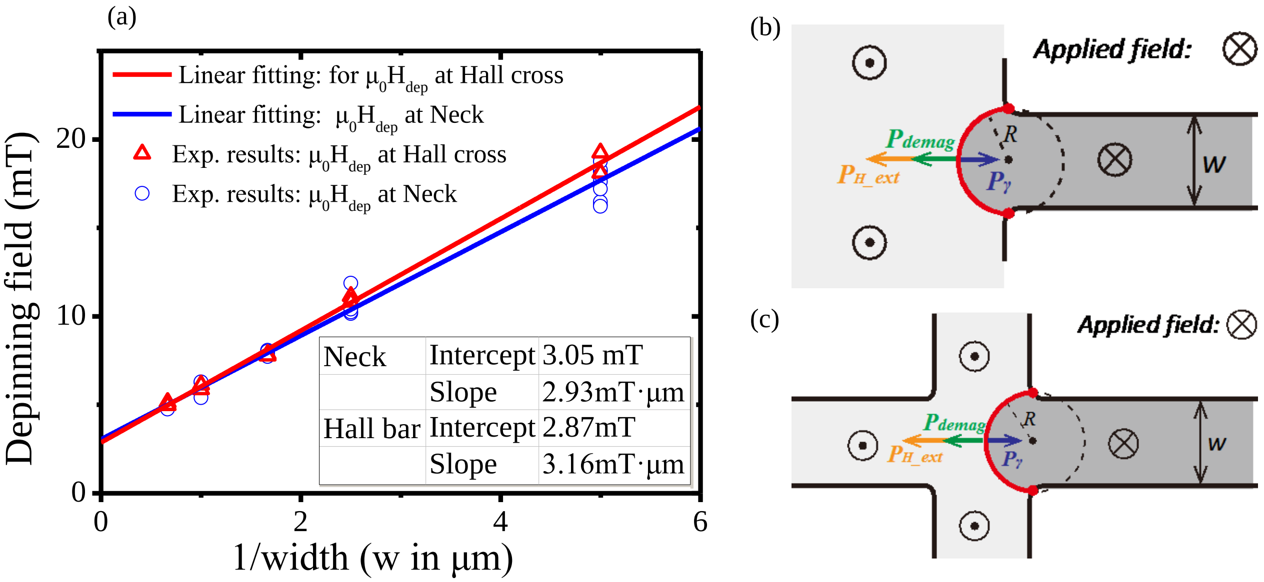

Figure 4-10 (a) DW depinning field as a function of the inverse of the wire width. Blue: for DW depinning at the neck, red: DW depinning at the Hall crosses; (b) & (c) sketch of pressures acting on the DW pinned at the corners of a neck or a Hall cross. It can be seen the minimum radius (corresponding to the highest Laplace pressure possible) of these arcs of circle is w/2.

As before, $\mu_0 H_{demag}$ can be numerically calculated and we have found again an approximate linear law: $\mu_0 H_{demag} \approx k_{demag}/w$, where $k_{demag} = 0.81\, mT.\mu m$ in the case of pinning at the neck and $k_{demag} = 0.55\, mT.\mu m$ at the Hall cross.

$$\mu_0 H_{dep} = \left(\frac{\gamma_{DW}}{M_S} - k_{demag}\right)\frac{1}{w} + \mu_0 H_0 \tag{4-9}$$

This prediction fits perfectly with our experimental results. The last thing to check is the value of γ. We have found an experimental slope k=2.9 mT·μm for necks (3.2 mT·μm for Hall crosses). The surface tension γ can be calculated by identifying the slope of Eq. (4-9) to experimental k:

$$\gamma_{DW} = M_S\left(k + k_{demag}\right) \tag{4-10}$$

It gives $\gamma_{DW} = 4.1\ \mathrm{mJ}/m^2$, in good agreement with our previous results. The slight discrepancy could arise from the edges of the Hall crosses, which are probably slightly rounded, inducing some small enlargement of the width of the wire at the entrance of the cross or nucleation pad.

Note that the experiments we have presented here present a new and very interesting method of measuring the surface energy of DWs. One should prepare some pads or Hall crosses by lithography with wires of different width. Then, by checking the depinning field as a function of the width, the surface energy of the DW can be deduced.

4.1.6 Precision of the DW surface energy measured using the two approaches

Now, let us estimate the precision of the surface energy extracted based on the above two methods. For the first method (measuring the DW surface energy based on the stabilizing field of the semicircular domain bubble), the uncertainty mainly comes from 3 contributions:

(1) The measurement of the size of the bubble. This term is mainly determined by the resolution of the Kerr microscope. As the radius of the bubble observed here varies from 3 μm to 10 μm and the spatial resolution of our Kerr microscope is 500nm, the uncertainty introduced by this term is about 10% for one point of measurement. This uncertainty has been reduced to a low level by repeating the measurements with different sized bubbles.

(2) The magnitude of the stabilizing field. This term is mainly determined by the calibration of the electromagnetic coil and can be reduced by a careful calibration.

(3) The calculation of the demagnetizing field. In this calculation, three parameters are involved: Ms, t_M, and Δ. The former two parameters can be precisely measured (e.g. using the vibrating sample magnetometer or the SQUID). $M_S \cdot t_M = \boldsymbol{m}/S$, where **m** is the magnetic moments measured and S is the

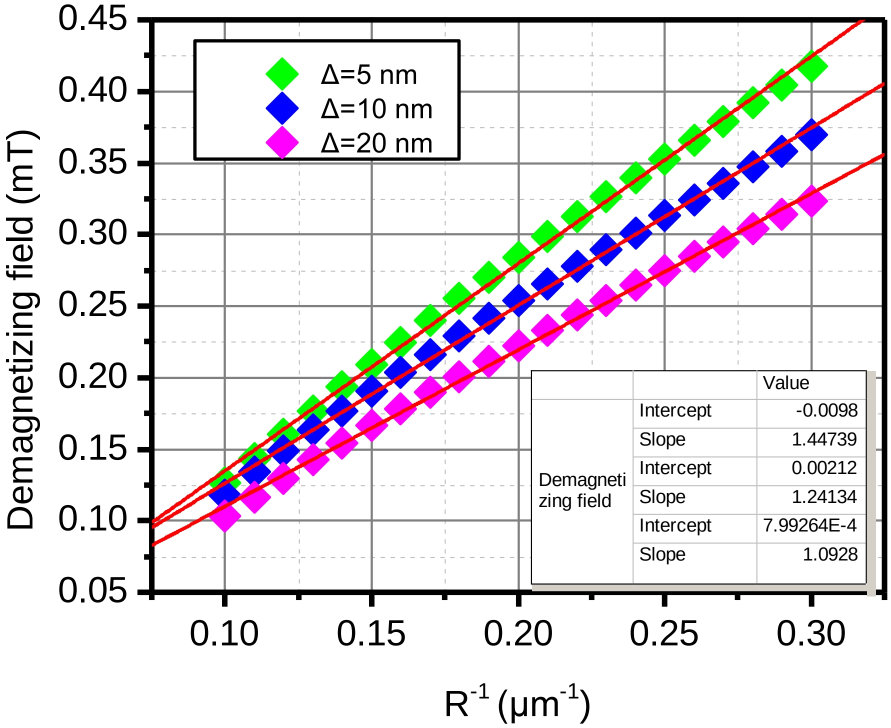

Figure 4-11 The demagnetizing field as a function of the size of bubble for different DW width Δ. The diamonds are the calculated results based on the magnetic current model and the red lines are the linear fitting results.

area of the sample measured. The calculation result of the demagnetizing field is not sensitive to Δ. As shown in Figure 4-11, the uncertainty introduced by this term is limited within 10%. In fact, the slope of the calculated demagnetizing field changes by less than 17% if the DW width was changed by 2 times. In view that the contribution from the demagnetizing field to the calculation of the DW surface energy is less than ½, the uncertainty caused by the calculation of the demagnetizing field is at a low level.

As for the second method (measurement of the DW surface energy using the depinning field at Hall crosses or necks), uncertainties originate from three contributions:

(1) the uncertainty of the width of the wires. This may be caused by size fluctuation of the wire or the rounded corner of the Hall cross or necks due to the nanofabrication technique. According to the Scanning Electron Microscope (SEM) image of the sample that we studied, the corner is a little rounded, as shown in Figure 4-12(a). This rounded corner will increase the effective width of wire that determines the depinning field. As illustrated in Figure 4-12(b), since the surface tension is always along the tangential direction of the DW surface and is always perpendicular to the edge of the structure, in an equilibrium state, the endpoint of a DW should be always perpendicular to the edge of the structure, as demonstrated by Eq.(0-21) in Appendix 1. In the critical state of depinning (corresponding to the minimum curvature radius of the DW), the endpoints of the DW should have slid to the end of the rounded corner. If the real width of the wire is w, because of the rounded corner, the effective width accounted for depinning is enlarged to w+2Δw. This enlargement will cause the decrease of the measured depinning field. Compared

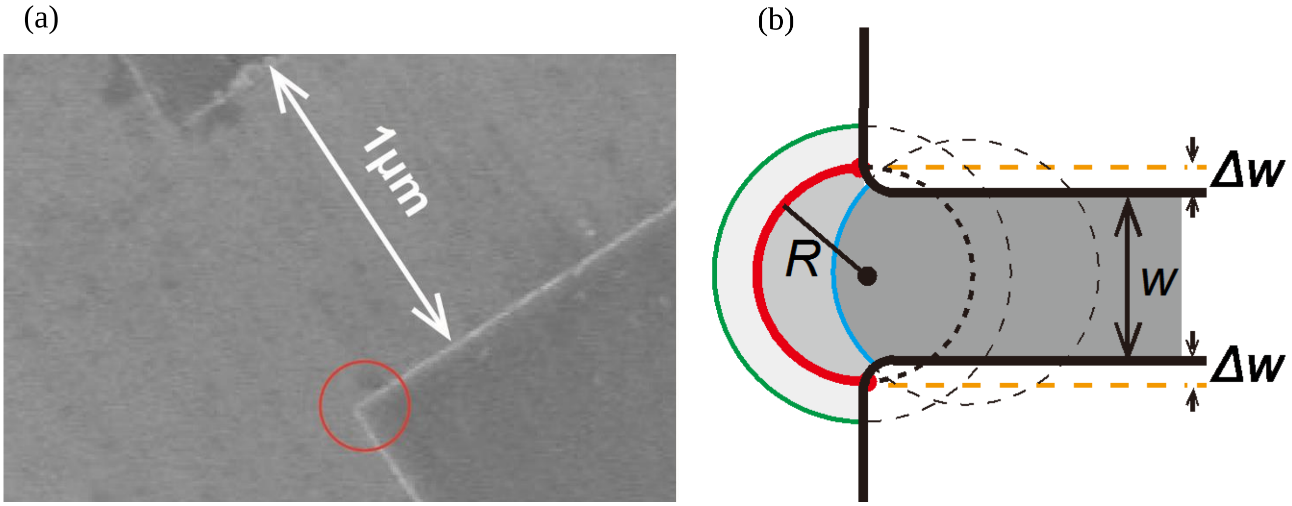

Figure 4-12 SEM image of a studied sample. The zone displayed here is the connection part (neck) of a 1 μm wire and a nucleation pad. We can see that the corner surrounded by red circle is a little rounded. (b) DW depinning at a structure (a Hall cross or a neck) with rounded corner. The blue circular arc describes the DW before depinning; the red semicircular arc describes the DW in the critical state for depinning; the green semicircular arc describes the DW after depinning.

with the real width, this enlargement is less important for structures with large size (e.g. 1.5µm wire) but more important for small size (e.g. 200 nm wire). Therefore, the effect of the rounded corner will cause a slight decrease of the slope in Figure 4-10(a) and thus lead to the underestimation of the DW surface tension. This effect may be one reason that the result of the second method is lower by 20% than the first method. This effect should be maximally avoided during the fabrication.

(2) The measurement of the depinning field (this term may be caused by the calibration of the magnetic coil). In addition, the thermal activation may also introduce the uncertainty for the measurement of the depinning field. Note that the thermal activation tends to increase the chance of depinning before arriving at the threshold condition[49] (i.e. lead to a decrease of measured depinning field). Since the structure with small size is more sensitive to the thermal activation due to the small activation volume[49], the thermal activation will lead to the underestimation of the DW surface energy. In our experiments, we have tried to reduce this effect by applying a field pulse with identic duration and the pulse is as short as 5 µs.

(3) The calculation of the demagnetizing field, as discussed above.

In summary, the first method is expected to have a better precision, with an uncertainty less than 20%.

4.2 Magnetic sensors based on the DW surface tension

In this section, we propose a novel mechanism based on the elasticity of DWs for the design of magnetoresistive sensors: the magnetic field can be detected via the field-induced DW expansion in the free layer of the spin valve or in the MTJ.

4.2.1 Concept and mechanism

As presented in the above sections, the elasticity (or the surface tension) of the DW becomes dominant for the DW behavior in a material with weak intrinsic pinning, e.g. CoFeB. A curved DW could contract spontaneously due to the Laplace pressure. The stabilizing field is approximately linear to the inverse of the radius R of the semi-bubble. Moreover, the threshold field to depin the DW at the entrance of the pad is approximately proportional to the inverse of the wire width.

Note that the propagation of the DW results in a local change of the magnetization. In the free layer of an MTJ, this change can be accurately detected through the change of the magnetoresistance. Interestingly, the structure near the free layer of the generally used MTJ, composed of MgO/CoFeB/heavy metal, has got many excellent properties, which facilitate the accurate DW manipulation, for example, the high PMA[88] and the ultralow intrinsic pinning fields[90]. We give in the following an example to show the principle to measure the magnetic field using the elasticity of DWs and the method to tune the performance of sensors through manipulating the geometry and the size of devices.

4.2.2 Device design and simulations

The structure of one example we proposed based on the above mechanism is shown in Figure 4-13 Structure of a sensor device proposed based on the elasticity of the DW. Two MTJs are connected via a bridge while the pinned layer and the upper electrodes are isolated. The free layer of two or more MTJs are connected via wire bridges while the pinned layer of MTJs are isolated. Free layers have a PMA and magnetizations of pinned layers are perpendicularly initialized in the same direction.

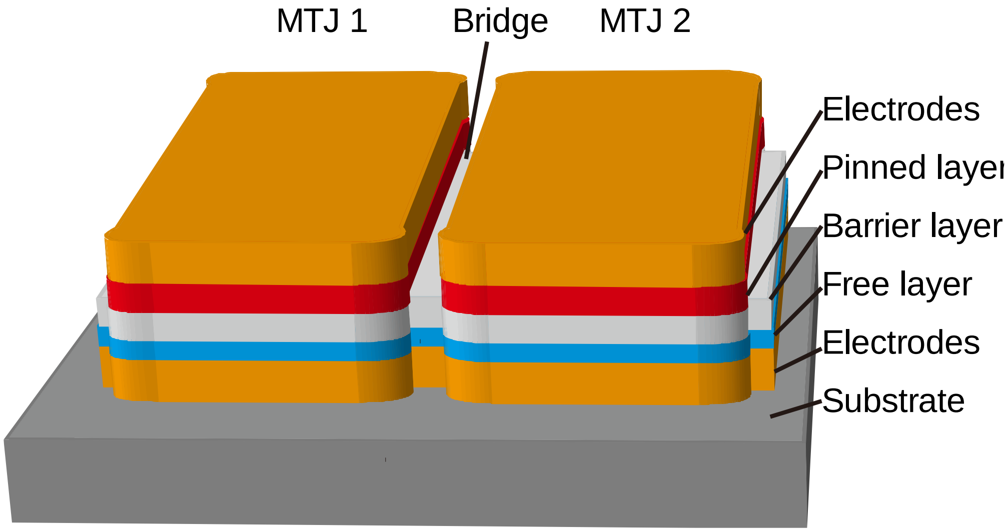

Figure 4-13 Structure of a sensor device proposed based on the elasticity of the DW. Two MTJs are connected via a bridge while the pinned layer and the upper electrodes are isolated.

Before working, opposite current pulses should be applied so that the magnetization of the free layer of two adjacent MTJs are initialized to opposite directions via the spin transfer torque. A DW will be created in the bridge. When the device is put in an external field, the DW will be moved in either of the two directions, depending on the direction of the external field. At equilibrium, in an external field, the DW is pinned at the bridge. As described by Eq. (4-5), in equilibrium, the DW will be of a circular arc shape and the radius can be given as follows,

$$R = \frac{\gamma_{DW}}{2\mu_0 M_S (H_d + H_{ext})} \tag{4-11}$$

Here, the demagnetizing field H_d is determined by the magnetic state and the structure of the device, varying with H_{ext}. Other parameters are all intrinsic. Therefore, the radius of the DW arc is solely dependent on H_{ext}.

For a given width w of the bridge, the area reversed in the free layer caused by the expansion of the DW can be expressed as,

$$S = R^2 \sin^{-1}\left(\frac{w}{2R}\right) - \frac{w}{4}\sqrt{4R^2 - w^2} \tag{4-12}$$

The change of this area leads to the change of the magnetoresistance. In this way, the external field is quantified through the resistance of the MTJ. Since the readout of the magnetoresistance can be realized with very low current density, the effect of this current on the behavior of the DW can be neglected.

In order to verify the functionality of this proposed device, the response of the magnetization in the free layer of the device versus external fields was simulated via micromagnetic using Mumax[94]. Parameters used are[90]: saturation magnetization $M_S = 1.1 \times 10^6\ A/m$, uniaxial perpendicular anisotropy energy $K_U = 9.5 \times 10^5\ J/m^3$, exchange stiffness $A_{ex} = 1 \times 10^{-11}\ J/m$, damping constant α=0.013. The thickness of the free layer is supposed to be 1nm.

As shown in Figure 4-14, a DW was set in the middle of the bridge as the initial state. Then a magnetic field was applied. After the DW was pinned at the entrance, the magnitude of the magnetic field is

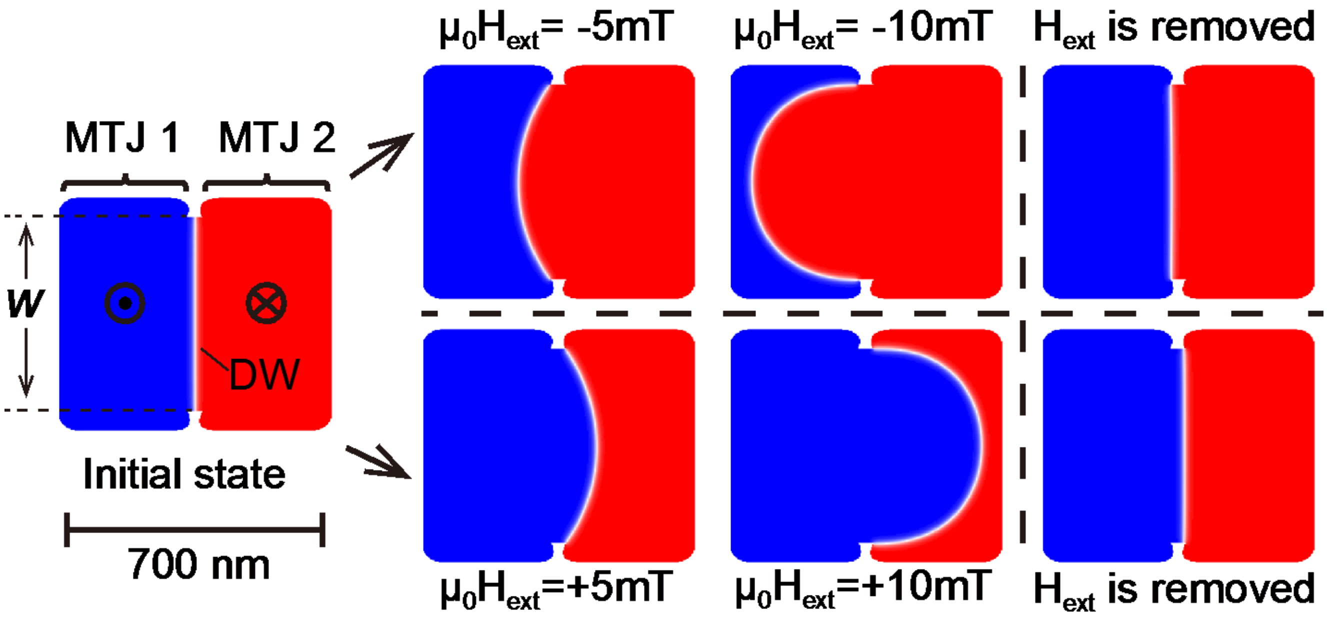

Figure 4-14 DW states in the free layer of two coupled MTJs: First, DW was set in the middle of the bridge of the device. Then an external perpendicular field of -5 mT (+5 mT), -10 mT (+10 mT) was applied and the stable state of the DW was snapshotted, respectively. At last, the external field was removed and the DW returned to the bridge due to its elasticity. *w*=500 nm in this example and the width of the notch is 30 nm.

increased gradually and the corresponding DW states were shown in Figure 4-14. We can see that the radius of the DW decreases and that the DW expands into the MTJ as the field increases. After the external field is removed, DW can come back to the bridge owing to its elasticity.

During the simulation, the perpendicular component of the average magnetization $\bar{M}_z$ of the free layer was extracted and was plotted as a function of the external field, as shown in Figure 4-15(a). Since the resistance of the spin valve or the MTJ is directly determined by $\bar{M}_z$, these figures can be seen as an indicator of the resistive response of the devices to the measured field. From Figure 4-15(a), we can see that the response of the magnetization of the free layer of the two MTJs to the external field are complementary, because the initial magnetization are set to be opposite. Therefore, a couple of MTJs must work together to realize the detection of the magnetic field in opposite directions.

From the comparison of the figure in left and right in Figure 4-15(a), we can see that the device with larger size (here, the size is characterized by the width of the bridge w) has a better sensitivity but the measuring range is relatively small; vice versa. In Figure 4-15(b), the measuring range and the sensitivity of the device versus the size of devices were plotted. Here, the sensitivity is defined as the rate of the change of the average perpendicular magnetization (normalized from -1 to 1) with respect to the change of the external field, i.e., dMz/dB.

In order to verify the response of the device to the alternating field, we simulated the change of the magnetization in a 500nm wide device when a sinusoidal field with an amplitude of 12.5 mT and a frequency of 1MHz was applied. The perpendicular component of the average magnetization is plotted in Figure 4-15 (c).

4.2.3 Discussions

When the DW is blown from the bridge into the free layer, the radius of the DW arc decreases as H_{ext} increases. When H_{ext} reaches a threshold value, the diameter of the arc becomes equal to the width of the bridge and DW will be depinned, leading the entire reversal of the free layer. Therefore, the depinning field is the upper limit of the range of the device. As can be seen from Eq. (4-7), the measuring range of the device is mainly determined by the width of the bridge. For a narrower bridge, the measuring range will be raised. According to our previous experiments, in a Ta/CoFeB/MgO structure, the depinning field when injecting a DW from a 200 nm wire into a larger area is about 20mT (ref [141]). If the size of the device scales down to a hundred nanometers, a measuring range of almost a hundred mT is expected.

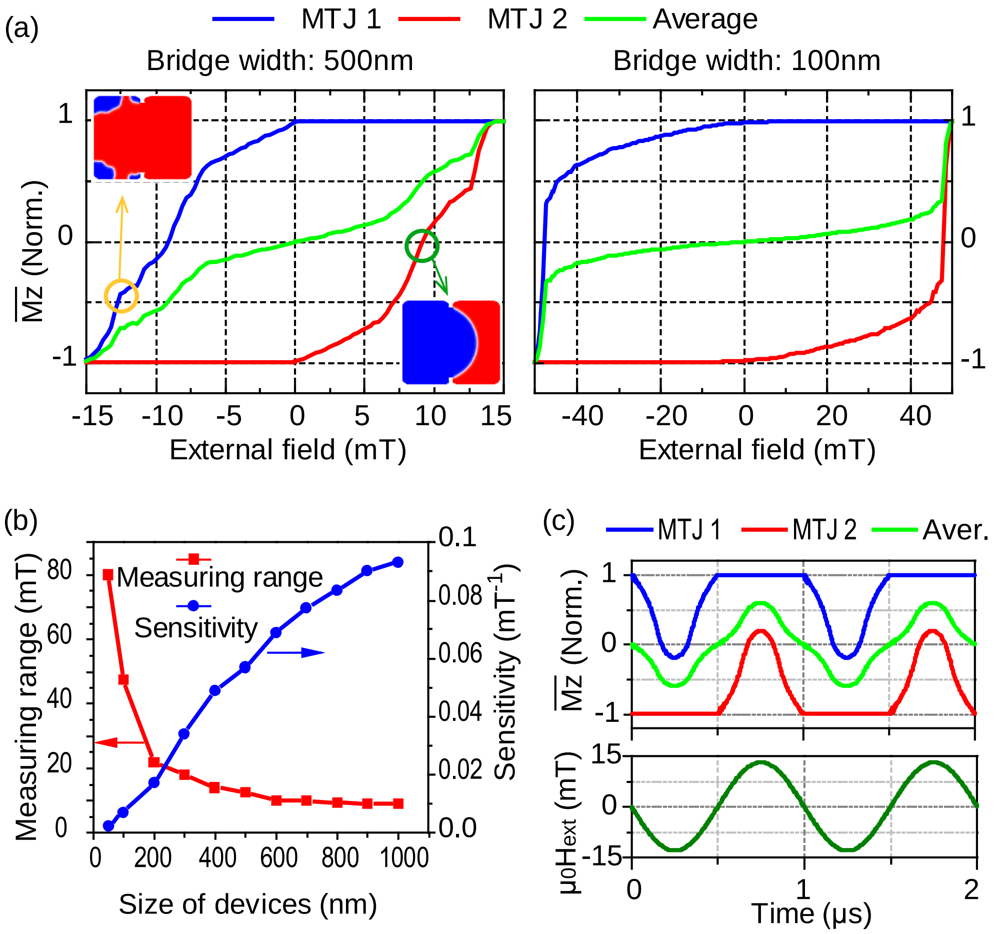

Figure 4-15 The average magnetization in the free layer of the device as a function of the external field. The width of the bridge in the device simulated is 500 nm in the left and 100 nm in the right. Insets show the DW state in the free layer. When external field exceeds the measuring range (13mT, marked in yellow), domain bubble breaks. (b) The measuring range and the sensibility of devices as a function of the size of devices. (c) Average perpendicular magnetization in the free layer of MTJs when an alternating field is applied. The width of the bridge in this simulation is 500nm.

While for a larger bridge, the measuring range decrease but the sensitivity increases, as shown in Figure 4-15 (b).

Simulation results have shown that these devices have a satisfactory performance for the detection of the alternating field with a frequency of MHz. In fact, the response speed is limited by the DW motion velocity in the free layer. According to our measurements (see Figure 3-23) in the Ta/CoFeB/MgO film, the DW motion velocity can reach more than 5m/s soon when the applied field H_{ext} exceeds the intrinsic pinning field. Supposing that in a device of hundreds nm, the external field can be detected in less than 100 ns. For a lower external field, DW motion velocity is dominated by the intrinsic defects and decreases rapidly, obeying the creep law, (Figure 2-8). Still, a movement of 100nm can be achieved in less than 1ms when the measured field decreases to 0.5 mT, according to our experimental results. For the detection of a lower field, the wall coercivity and discontinuous domain wall motion known as the Barkhausen effect may cause a problem. Fortunately, experiments of G. Wang et al. have demonstrated that this problem could be well solved by applying an oscillating AC current[142].

Note that the above device is only an example to demonstrate the concept we proposed and to verify the performance of this type of sensors. The monotonous and reversible response of the elastic DW to the magnetic field provides a new aspect to design sensors. Another example of the design of magnetic sensors based on the elasticity of DWs can be found in Appendix 2.

For the magnetic sensors proposed above, various devices with different size and geometry, thus with different performance (e.g. measuring range, sensitivity etc.) can be fabricated in the same chip based on this mechanism. No modulation of the intrinsic properties of the film, such as the PMA, is required. Therefore, magnetic sensors based on the elasticity of DWs promise a higher integration level and a better performance.

4.3 Conclusions

In this chapter, we have presented a series of experiments in which the DW surface tension becomes the dominant effect, such as the spontaneous collapse of the semicircular domain bubble, the interplay of two bubbles, the DW depinning at the Hall crosses. Two methods to quantify the DW surface energy were proposed. At last, a novel type of magnetic sensors based on the DW surface tension (elasticity) was proposed and verified using micromagnetic simulations.

Most of what have been presented up to now assume a perfect film without defects. It is true that CoFeB films are really very good, but there are still some pinning defects: can these defects be neglected? Obviously, they induce a creep behavior in 2D films, but, is it still true in nanowires?

Chapter 5 Domain walls motion and pinning effects in nanowires

In this chapter, we focus on the DW dynamic behaviors in nanowires. DWs motion velocities in nanowires induced by a magnetic field or by the combined effects of field and current have been measured. DW pinning and depinning effects caused by the randomly distributed hard pinning sites have been systematically studied. At last, a ring-shape racetrack memory based on the complementary work of SOT and STT was proposed and verified via micromagnetic simulations.

5.1 Field-induced DWs motion in nanowires

Velocities of the field-induced DWs motions in 200 nm to 1.5 μm wide wires were measured using a mini coil with a rising time of 220 ns. The measuring results are shown in Figure 5-1. The method of measurement can be found in chapter 3.

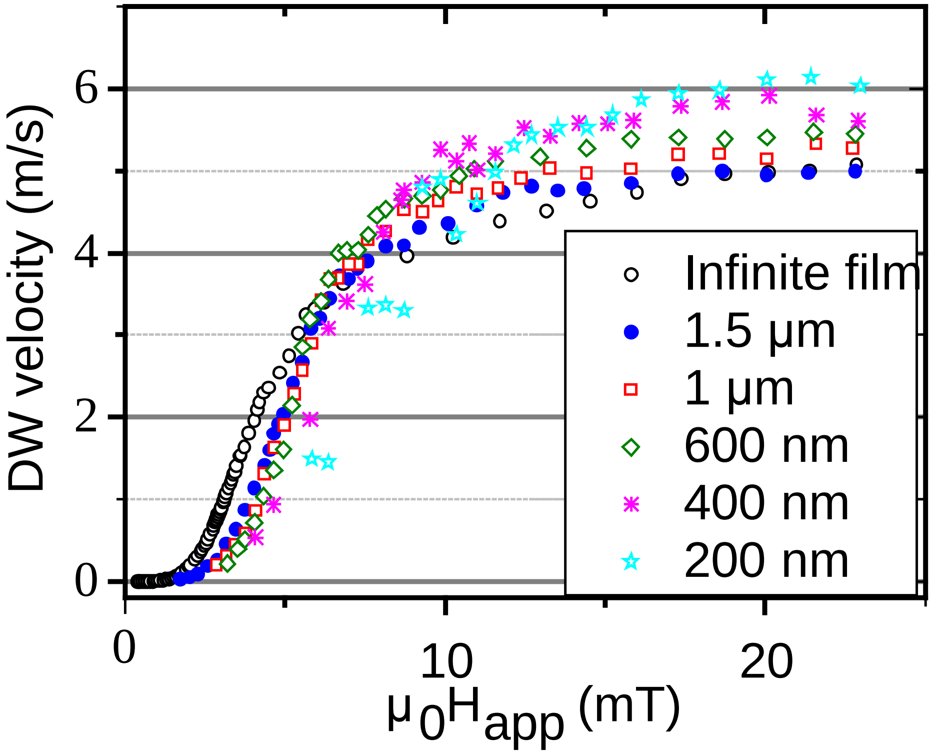

Figure 5-1 Velocities of the field-induced DW motion measured in infinite film and in nanowires of different width.

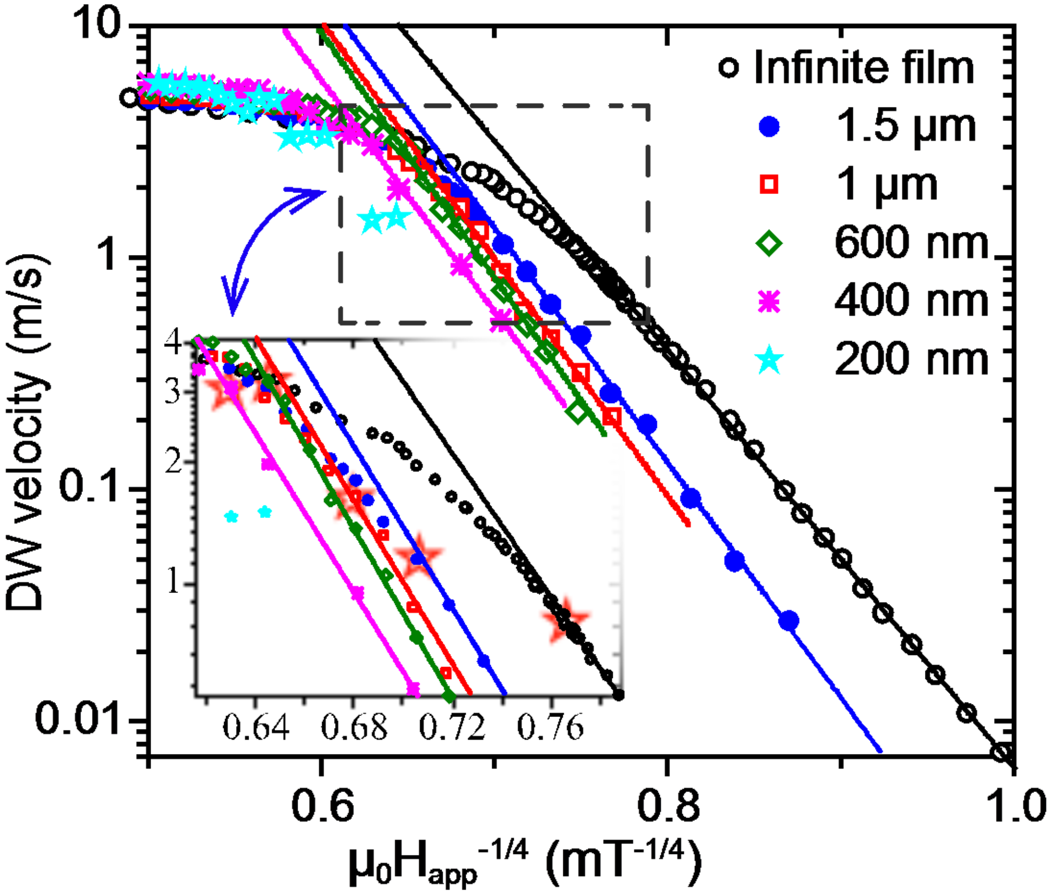

Figure 5-2 Field-induced creep motion of DWs in the nanowires. The ☆ in the inset denotes the critical point where the DW motion velocities leave the creep regime. The corresponding field was extracted and plotted in Figure 5-3.

Propagation of DW in nanowires is different from the case in the infinite film, where DW can circumvent the hard pinning sites (see Figure 2-5). In nanowire, DW can be completely trapped by a hard pinning site. This makes the DW motion stochastic when driven by a weak magnetic field. The motion distance depends not only on the magnitude of the applied field but also on whether hard pinning sites exist. It is to note that the velocities measured here are based on the DW motion in the relatively smooth section of the wire, where the DW was not completely pinned by the hard pinning sites. In addition, measurements with the same field pulse were repeated for several times in different part of the wire and it was always the maximum velocity observed that was kept here.

Depending on the field range, the influence of the dimension reduction is different: under a low field, DWs move faster in broader wires; under a high field, DWs move faster in narrower wires, as shown in Figure 5-1.

When the driving field lowers down, the pinning effects become dominant. In a narrower wire, the pinning effect is stronger, which will be discussed in the next section, so the velocity is smaller. We plotted DW velocities in a logarithm form in function of $H^{-1/4}$, as shown in Figure 5-2. Interestingly, although DW can be entirely trapped by hard pinning sites, DW motion in relatively smooth sections between the hard pinning sites can still exhibit a creep mode, except that in the 200 nm wide nanowire. This means that intrinsic pinning effects play still an important role in DW motion in narrow wires. The lines of ln(velocity) vs. $H^{-1/4}$ shift to the left when wire width scales down. This may be caused by the roughness of the edge[29].

Meanwhile, it can be seen that the creep regime holds to higher velocities and higher fields when wire widths scale down. This effect can also be concluded to the friction from the edge. Here we define the effective depinning field H_{dep_eff} as the critical field where DW motion leaves creep regime in wires, as denoted by the red stars in the inset of Figure 5-2. We found that H_{dep_eff} increased in a linear-like mode with the inverse of wire width, with a no negligible slope, as shown in Figure 5-3. This means that the roughness from the edge plays an important role in DW motion and DW pinning effects in nanowires.

Furthermore, we found that the DW will be entirely stuck by the pinning sites and no motion was observable within several ms when the applied field decreased down to a threshold value. We may call it

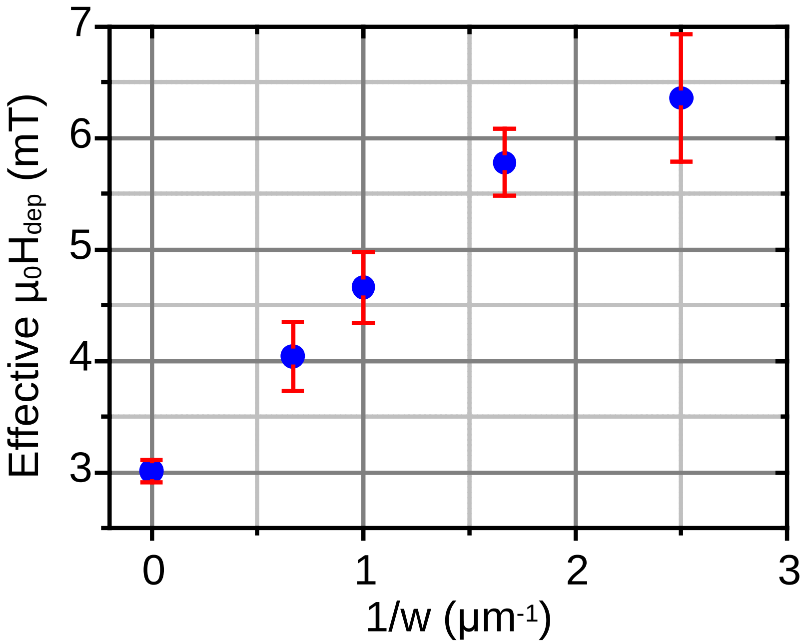

Figure 5-3 The effective depinning field H_{dep_eff} vs. the wire width, extracted from the value denoted by the red stars ☆ in Figure 5-2.

the dead field. With the scaling down of the wire width, the dead field increases. For example, in the 200 nm wire, DW motion is not possible when the applied field is lower than 6mT.

Both previous studies[90] and our experiments show that in our sample, when the applied field is higher than 15 mT, the motion of DWs is in a precessional flow regime. In the narrow wire, the roughness of edge can reduce the turbulence of the moving DW and thus accelerate a little the velocity. In a narrower wire, this damping is more effective, so the DW velocity is higher[143]. Our experiments about the DWs motion in nanowires driven by a high field is in agreement with this assumption, as shown in Figure 5-1.

5.2 Randomly distributed hard pinning sites in nanowire

To be sure to avoid artefacts arising from pinning defects, we have to check where are the strongest pinning points on the nanowires and what are the depinning field associated.

5.2.1 Experiments

After nucleating a DW in the wire, pulses of small amplitudes and 5μs long were applied. We have used the coil N°16_ext (see Table 3.1), whose rise time is as short as 220 ns (see Figure 5-4 (a)). After one or several pulses to induce DW motion along the wire, it can be observed that the propagation can be fully stopped (Figure 5-4 (b)(n°2&3)), indicating that the DW cannot overcome the energy potential induced by the strong pinning sites.

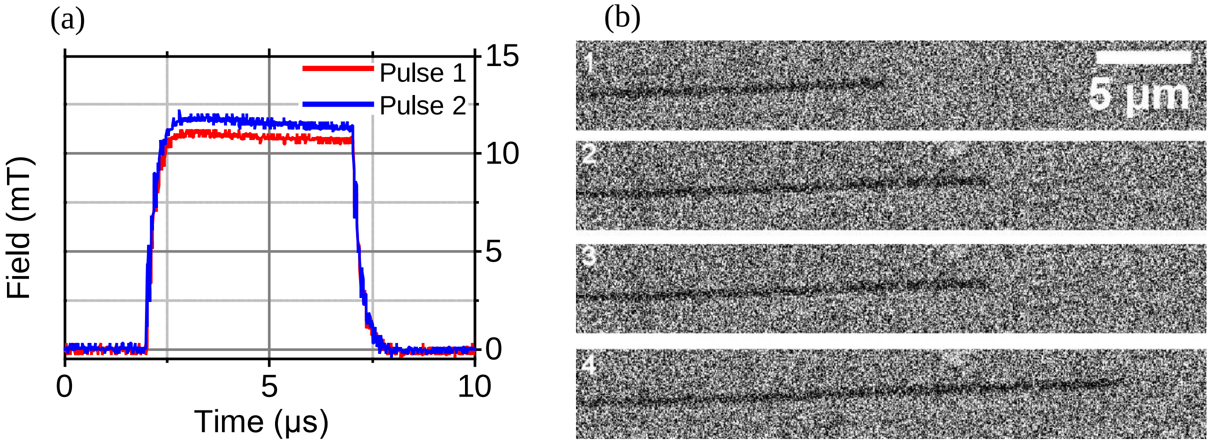

Figure 5-4 (a) Example of two field pulses with the same length and different magnitude, used to measure the DW depinning field. (b) DW pinning and depinning in a 200 nm wire: DW moves from (image n°1) to (n°2) by a lower field pulse 1 (12.1 mT), then trapped (n°2 and n°3), DW is depinned and continue to move from (n°3) to (n°4) by a higher field pulse 2 (13.2 mT).

After the DW is trapped in a wire, the amplitude of the pulse was increased step by step (pulse 2, Figure 5-4 (a)), until the depinning occurs (Figure 5-4 (b)(n°4)). The minimum field that can depin the trapped DW is defined as the depinning field H_{dep} here. For a given pinning defect, the experiment was repeated several times and the depinning field values were reproducible with an error bar lower than 0.3mT. In order to improve the statistics, for each width, we have studied DW motion in several nanowires (from 3 to 6) and we have selected the five strongest pinning sites along the 50μm wire.

5.2.2 Depinning field distribution

As an example, we give the position of the several largest pinning sites measured in a 1 μm wire and the corresponding depinning fields Figure 5-5 (a). Typical depinning fields in our sample range from 2 to 13 mT, depending on the wire width.

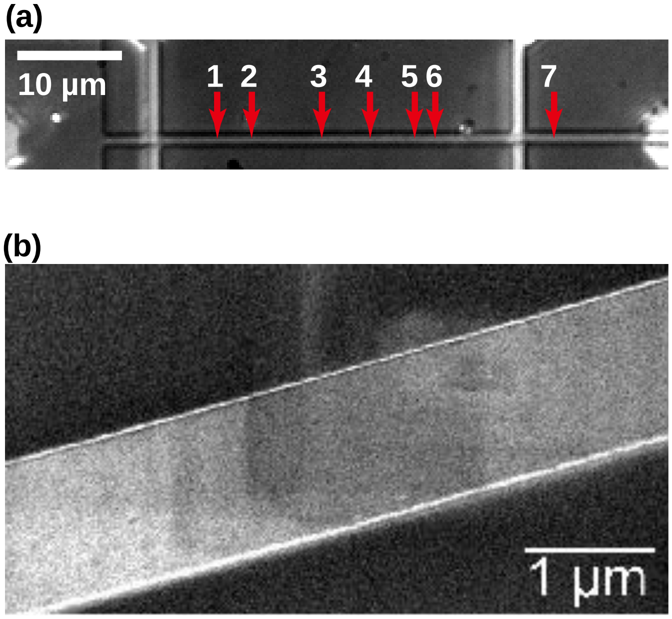

Figure 5-5 (a) Position of the several largest pinning sites in a 1 μm wire. The corresponding depinning field of sites from 1-7 are: 5.2, 5.2, 6.1, 5.4, 5.5, 5.0, 4.5 (mT). (b) SEM image of a 1 μm wide wire studied.

The main important result of this study is the presence of several strong pinning sites along the wires[28,144]. This is different from the DW depinning behaviors in the infinite film. As shown in Figure 2-5, in 2D film, if a domain wall is pinned at one point, it can keep on propagating on the sides, creating a 360° domain wall, ended by a circle at the position of the pinning. Then, because of the Laplace pressure, the DW can overcome the pinning. In narrow wires, there are no sides, and strong pinning can completely prevent the DW from moving since the wall is fully stopped at several locations along the wires.

The origin of the hard pinning sites is difficult to figure out just by morphological observation. Figure 5-5 (b) is the profile of a 1 μm wires observed with a scanning electron microscope (SEM). No obvious notch in the edge or visible defects on the surface of wire can be found. Here we try to explore the origin of these hard pinning sites based on statistical analysis of the experimental data.

The distribution of the strongest depinning fields as a function of the wire width is indicated in Figure 5-6. It can be observed that the distribution is shifted towards higher values as the width of the nanowire

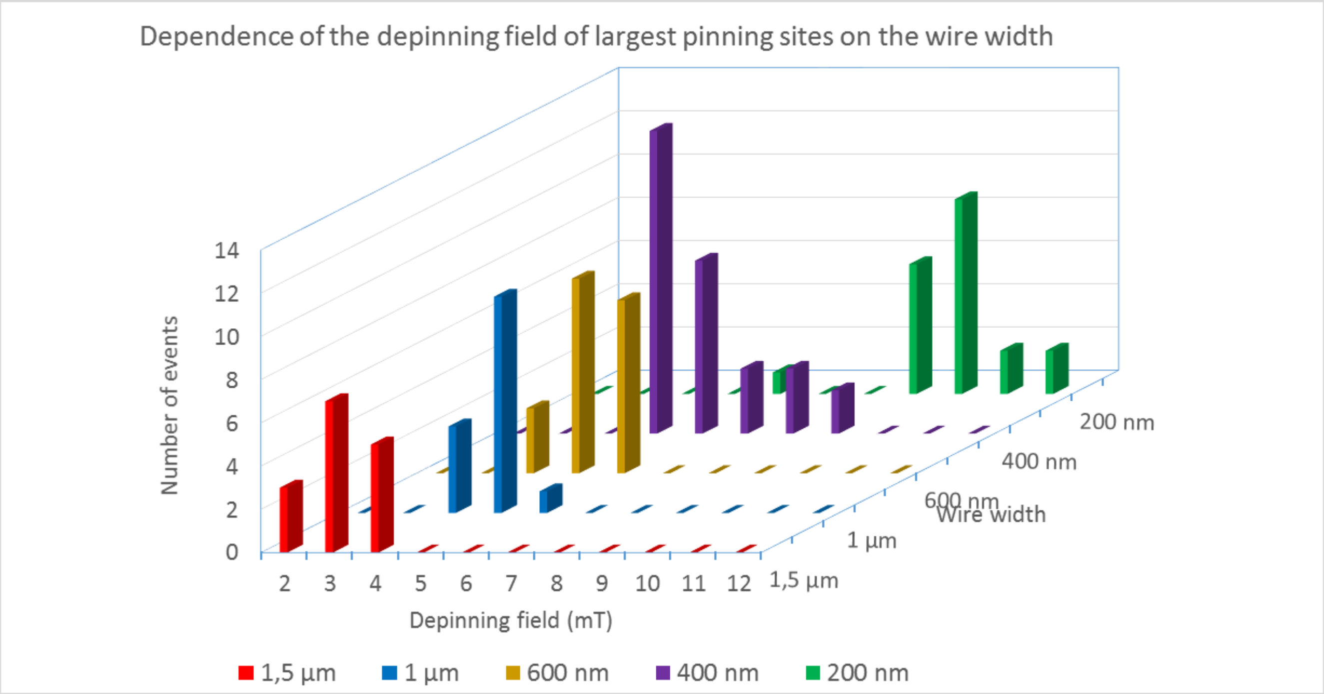

Figure 5-6 histogram distribution of depinning field obtained for the strongest defects, using the five strongest ones for each wire included in the statistics.

is decreased. This shift can be explained by taking into account the different forces acting on the DW in the wires. First, the pressure $2\mu_0 H_{ext} M_S$ due to the external applied field μ_0H_{ext} integrated over the section of the wire, gives a force $2\mu_0 H_{ext} M_S w t_M$, where t_M is the thickness of the film and w the width of the wire[141]. Then, the presence of intrinsic pinning defects in the films induces a force F_F. These intrinsic defects alone are not strong enough to stop the DW since the magnetic fields applied for observing DW depinning in the nanowires are much higher than those needed to move DW in the films (typically < 1mT). The effect of intrinsic pinning effects can be described using a friction force that depends on the number N of defects and is proportional to the section. It leads to a maximum force $F_F w t_M$, opposite to the induced motion. Finally, the strong pinning sites evidenced here creates a pinning force F_{SD}. Considering the action of these three different forces, the depinning process occurs when the pressure from external field overcomes the overall pinning forces $F_{SD} + F_F w t_M$. The depinning field $\mu_0 H_{dep}$ is deduced from this threshold condition:

$$\mu_0 H_{dep} = \frac{F_F}{2M_s} + \frac{F_{SD}}{2M_S t_M}\frac{1}{w} \qquad (5\text{-}1)$$

It has to be noted that the quantities M_S, t_M, F_F can be assumed to be constant. However, F_{SD} requires a more careful analysis. Indeed, F_{SD} is related here to the tail of the distribution of the pinning forces. As such, the probability to get a very strong pinning force is small and increases with the overall number N of pinning sites. Therefore, this parameter may depend on the area and on the length of the wire as described below.

5.2.3 Data analysis and the origin of the pinning effects

To describe the distribution of F_{SD}, we have assumed it to be Gaussian and centered on zero. As the number of pinning sites is huge, we have assumed that we have the same behavior for the average value of the five strongest pinning sites as for the value of the strongest pinning site alone. Then, two cases can be considered. First, the strong pinning sites are of extrinsic origin such as the roughness of the edge introduced by the patterning process. In this case, their number should depend on the length of the edges, which is the same for all wires, whatever the width is. Therefore, the overall number of strong defects as well as F_{SD} should be a constant and, according to equation (5-8), H_{dep} should increase linearly as a function of 1/w.

Second, the strong pinning sites are of intrinsic origin and they originate from the magnetic films[145]. Then, their number N is proportional to the area of the wire, which means here to the width w of the wire. In order to get a pinning force $F=F_M$ for the strongest pinning site, it means that all the other pinning sites have a pinning force lower than F_M. In this case, the probability to get F as the strongest pinning force is:

$$\mathrm{P}(\mathrm{F}=F_M)=\mathrm{N}P^{N-1}(F_{SD}<F_M)P(F_M) \qquad (5\text{-}2)$$

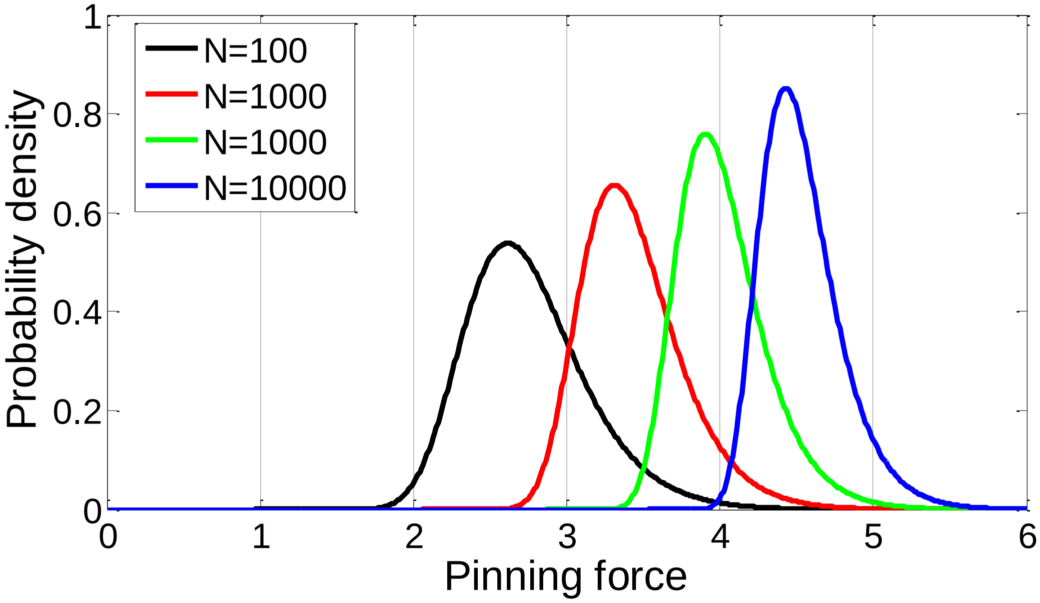

Figure 5-7 Expected distribution of the strongest pinning force as a function of the overall number of defects (N), assuming a Gaussian distribution of defects centered on zero and with standard distribution σ=1.

where the function P holds for the probability function. As we have assumed a Gaussian distribution, we get the following functions for P(F) and P(F_{SD}< F):

$$P(F) = \frac{1}{\sigma\sqrt{2\pi}} exp\left(-\frac{F^2}{2\sigma^2}\right) \tag{5-3}$$

$$P(F_{SD} < F) = \int_0^F \frac{1}{\sigma\sqrt{2\pi}} exp\left(-\frac{F^2}{2\sigma^2}\right) dF = \text{erf}\left(\frac{F}{\sqrt{2}\sigma}\right) \tag{5-4}$$

Injecting Eq. (5-10) and (5-11) in Eq. (5-9), the distribution probability of F_M for several values of N can be simulated, as seen in Figure 5-7. It can be observed that the average value of expected F_M is shifted towards the high values as N increases. To get a meaningful shift, there must a quite large increase of N. For instance, when N is multiplied by ten, the increase of F_M is around 20%. In our experiment, the width goes from 200 nm to 1.5 µm, which is almost a factor of ten. Furthermore, for the strongest intrinsic pinning effect in a wire, the pinning may be caused by the resultant force of two or several pinning sites that coincidently cluster. This cluster of pinning sites range along the transverse direction of wire and behavior as a single solid pinning site. For a wider wire, the probability of having such clusters is larger than that in a narrower wire. As a result, the decrease of the expected F_M should be much larger than 20% as w increases from 200nm to 1.5 µm. Noting that, from Eq. (5-8), F_{SD} determines the slope of this function. If F_{SD} decreases as 1/w, the slope of the curve should drop down when 1/w increases and the relation

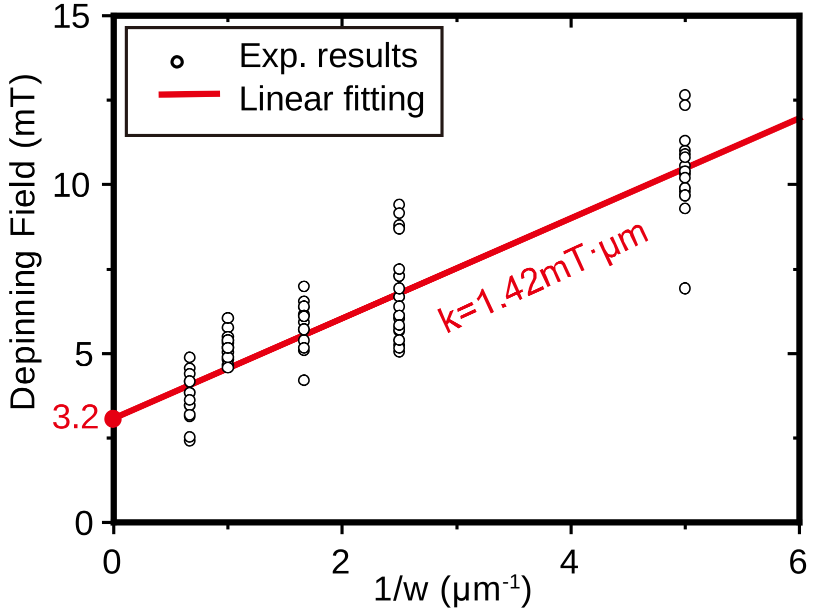

Figure 5-8 Depinning fields of the strongest defects experimentally obtained as a function of 1/w, where w is the width of the wire.

between H_{dep} and 1/w should not be linear. The experimental value of B_{dep} as a function of 1/w is plotted in Figure 5-8.

We can observe a very good linear behavior indicating no evidence of a drop down of the slope. Let's note, the intercept equals to 3.2 mT, consisting with the experimentally measured intrinsic pinning field in infinite film, above which the DW motion leaves the creep regime (see Figure 2-8). This result is consistent with an extrinsic nature of the strongest pinning sites in our samples, probably due to the edge roughness introduced by the patterning process. This result is also consistent with a recent result of NV center microscopy indicating the presence of strong pinning sites related to the edges in 200nm wide wires[146].

5.3 DW motion induced by the combined effect of magnetic fields and electric current

The current-driven DWs motion, as well as the DW motion driven by the synchronized magnetic field and current pulse, was studied in this section.

5.3.1 Current-induced DW motion

In the beginning, we tried to induce the DW motion in a 1.5 µm wire in zero external magnetic fields, using only current. As shown in Figure 5-9, a magnetic wire was connected into the electric circuit via two of the electrodes. The complete circuit diagram for this experiment was given in Figure 3-21.

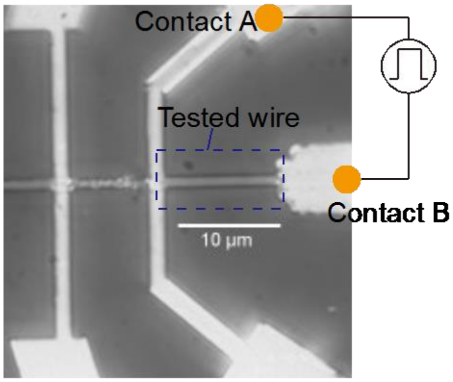

Figure 5-9 Optical image of the tested structure. The current was always applied via contact A and B.

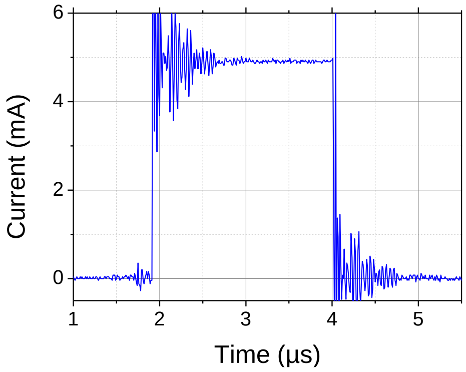

Figure 5-10 An example of the current pulse applied on the sample, supervised by an oscilloscope.

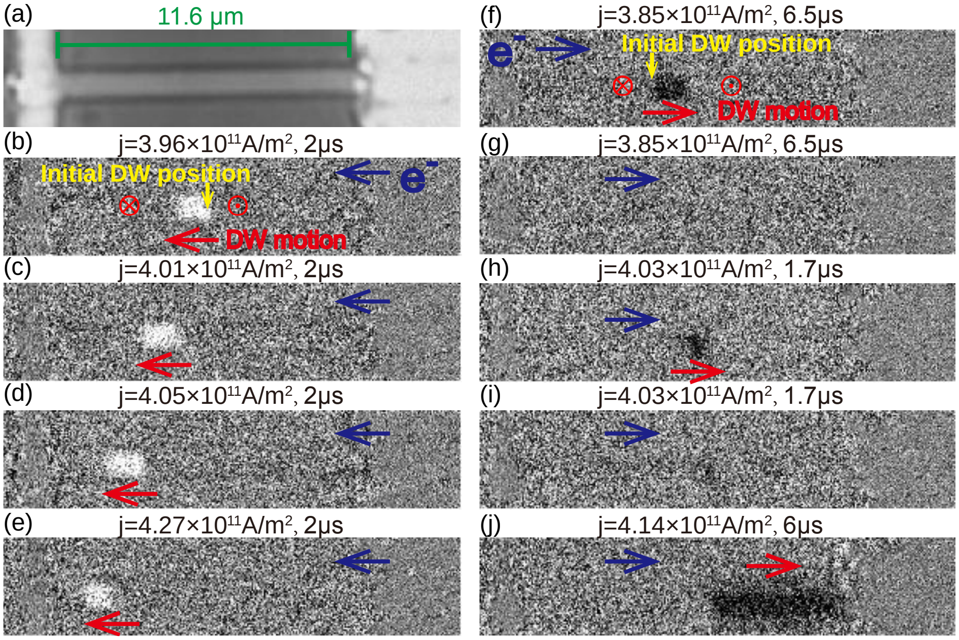

Figure 5-11 Current-induced DW motion in a 1.5 µm wire. Blue arrows indicate the direction of electrons flow and red arrows indicate the DW motion direction. (a), An optical image of the wire. (b)-(e) a series of DW motion driven by successive current pulses to left and ((f)-(j) to right, respectively). Each picture from (b) to (e) and (f) to (j) are obtained by making the difference between a picture taken just before the pulse and a picture taken just after the pulse. So, they show the change of magnetization which has occurred during the pulse.

First, a DW was created by a large and short magnetic field pulse (~130 mT, 8 µs) in the wire. Then, an electric field pulse was applied by a pulse generator. Figure 5-10 is an example of the current pulse supervised by the oscilloscope. Two Kerr images were acquired before and after the current pulse. The DW motion can be identified by comparing the two Kerr images.

We found that it was difficult to induce the DW motion by a current alone. When the applied current density is about $3 \times 10^{11} A/m^2$, no DW motion can be observed even the current pulse lasted for a hundred micro second. Some weak and irreproducible DW motions in the direction of electrons flow could be observed until the current density was increased to about $4 \times 10^{11} A/m^2$, as shown in Figure 5-11. Note that the current density in the CoFeB layer was obtained using the resistivity of CoFeB $\rho_{CFB} = 170\ \mu\Omega \cdot cm$, which was estimated by L. Liu et al based on their experimental measurement in the Heavy metal/CoFeB/MgO structure[75]. The detailed discussion about the resistivity will be given later in section 5.3.3 and appendix 3.

Surprisingly, as the density of the applied current increased to about $4.5 \times 10^{11} A/m^2$, the direction of DW motion becomes stochastic, as shown in Figure 5-12.

Next, we further increased the density of applied current. We found a more strange behavior of the DW in this tested wire. As shown in Figure 5-13, when the density of the applied current reached a critical value (about $4.5 \times 10^{11} A/m^2$) the final position of the DW was not determined by the direction of applied current or the initial DW configuration (⊙|⊗ or ⊗|⊙). The DW always move to the right and disappeared into the electrode in the right end. Here, we just note this confusing phenomenon and cannot give an appropriate explanation.

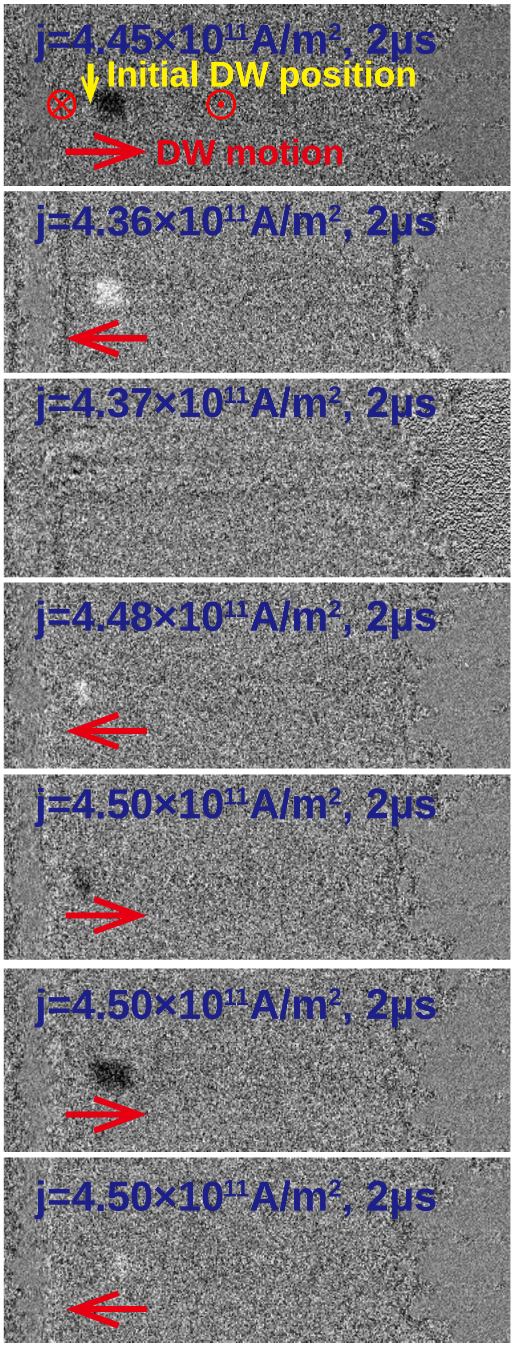

Figure 5-12 The current-induced stochastic motion of DW in the 1.5 μm wide wire. The direction of the electron flow were always to the left in this experiment. Each picture are obtained by making the difference between a picture taken just before the pulse and a picture taken just after the pulse. So, they show the change of magnetization which has occurred during the pulse.

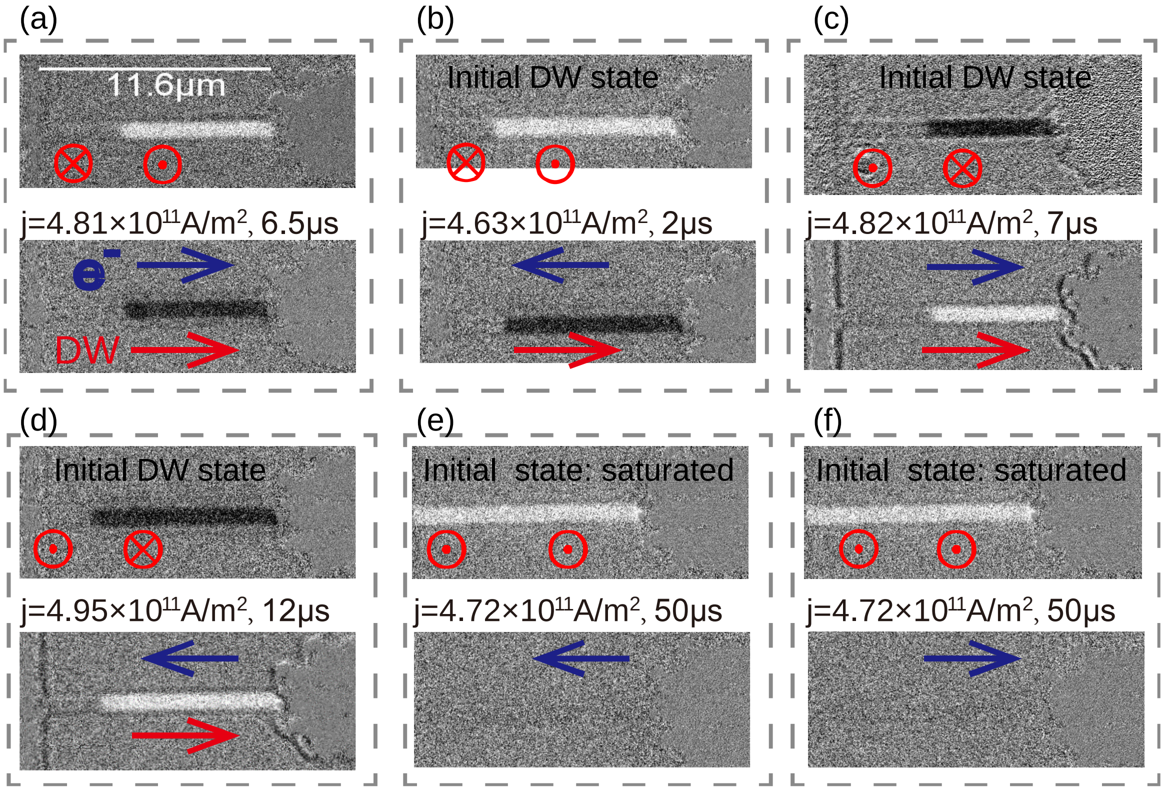

Figure 5-13 DW motion induced by a relatively high current. (a-d), DW move always to the right and disappeared into the electrode in the right end, no matter the initial state of DW or the direction of the applied current. (e,f), if the magnetization of the wire is initially saturated, i.e., no DW exists, there is no change in the magnetization even the current pulse last for 50 μs. For each group of picture, the first pictures show the magnetic state (a saturated reference have been used to get the magnetic picture), while the second show the change of magnetization (difference between pictures acquired just before and just after the pulse).

5.3.2 DWs motion induced by synchronized current pulses and magnetic field pulses

Since the DW is difficult to be moved by a low current and the DW behavior induced by a high current is irregular, we begin to search for the regular and reproducible DW motions induced by the combined effects of magnetic field and electrical current pulse.

5.3.2.1 Experiments and results

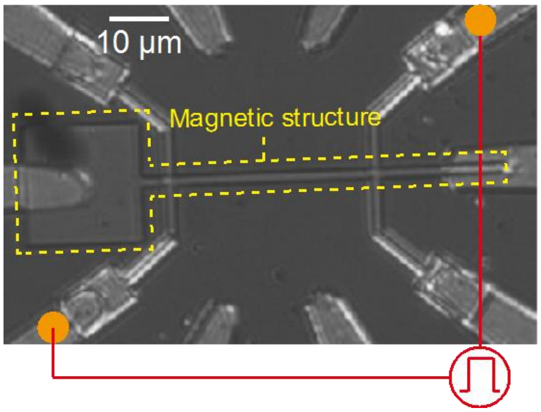

Figure 5-14 Optical image of the 1.5 wide wire tested and the configuration of electric measurement.

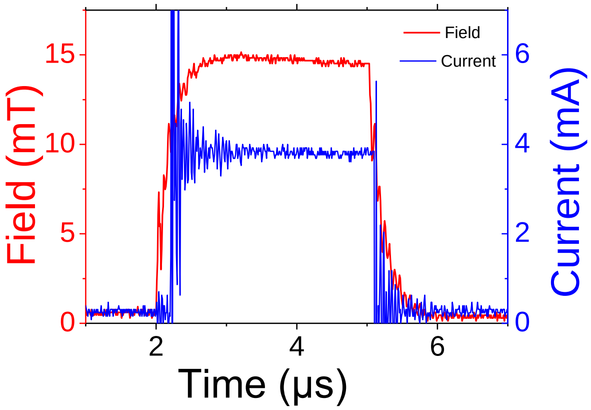

Figure 5-15 an example of the synchronized electric current pulse and magnetic field pulse applied on the tested sample. These pulses are supervised by an oscilloscope.

The width of the wire tested here is 1.5 μm, as shown in Figure 5-14. After the DW nucleation, the synchronized magnetic field pulse and current pulse were applied. Figure 5-15 shows an example of the field pulse and current pulse supervised by an oscilloscope. A small delay between the field and the current was set, so that, the magnetic field had reached its plateau when the current started to flow in the wire.

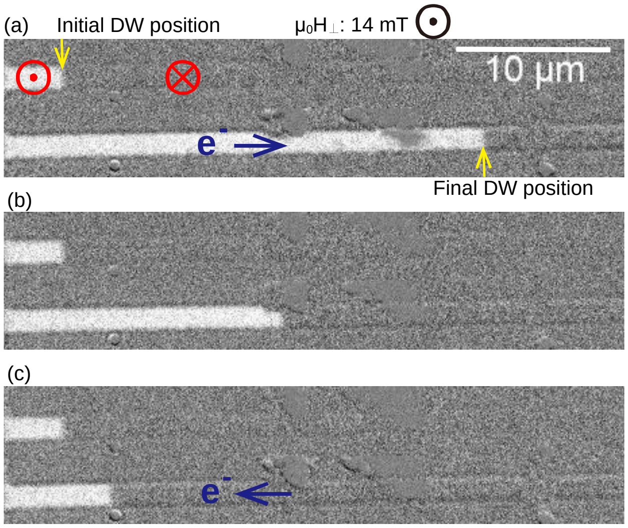

Figure 5-16 DWs motion in a 1.5 μm wide wire induced by synchronized magnetic field pulses and current pulses. An external field of 14 mT and 3μs was applied along the perpendicular direction. A current pulse of 3.7 mA was applied synchronously in the left direction (a) and in right direction (c). No current was applied in (b).

We found that, compared with DW motions induced by the magnetic field alone, the DW motion velocity was changed obviously when the current is introduced. The DW motion was accelerated in the direction of the electrons while it was slowed down when the DW motion is opposite to the direction of the electron flow, as shown in Figure 5-16.

Velocities of DW motion with different current density and perpendicular field were measured systematically, as shown in Figure 5-17. One can find that the DW velocity is obviously accelerated in the direction of electrons in the plateau (i.e., the DW motion when $\mu_0 H_\perp \geq$

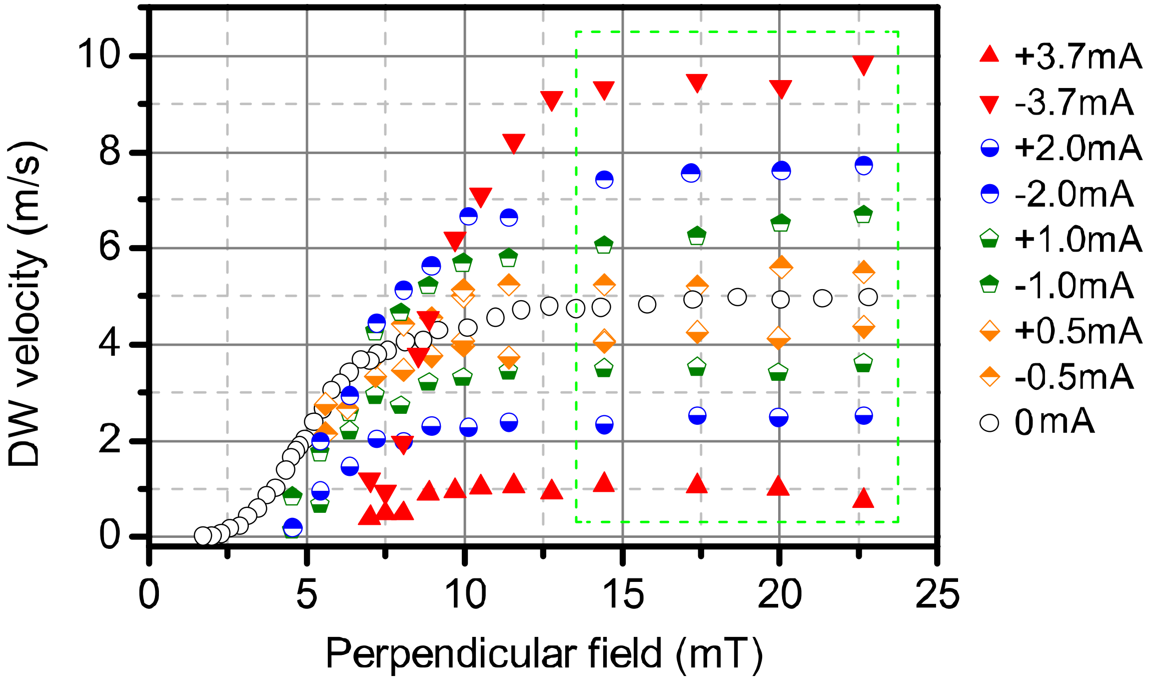

Figure 5-17 DW motion velocities induced by different fields and current densities. Current flowing along the field-induced DW motion direction is defined as positive. Velocities in the plateau, boxed by the dashed green line, is averaged and the plotted as a function of the current in Figure 5-18

14 mT). However, DW velocities decrease and become stochastic for a lower driving field (creep regime and depinning transition mode) when current is introduced, no matter the direction of the current. In fact, during the measurements, we found that the DW pinning effect is obviously enhanced when a current is introduced. The larger the current is, the stronger the pinning effects are. This phenomenon will be discussed in section 5.4 .

Now, let us first analyze the DW motion velocity in the plateau, i.e. for the driving field in the range from 14 mT to 25 mT. According to Eq.(2-26) and a damping constant α=0.013 [90], the Walker breakdown field of this sample is about $\mu_0 H_W = \alpha\mu_0 M_S/2 = 0.8$ mT for the field-driven DW motion. This value is far smaller than 14mT and is masked by the creep motion. When a current is introduced, the Walker breakdown has not occurred. We can tell that the plateau of velocity we see here is in fact in the precessional flow mode. Since the DW motion velocity in this range remains stable, we did an average on the velocities (enclosed in green dashed line in Figure 5-17) for each current and plotted the mean velocities as a function of the applied current, as shown in Figure 5-18. A very good linear relationship between the DW velocity and the magnitude of the applied current was obtained. After a linear fitting, an

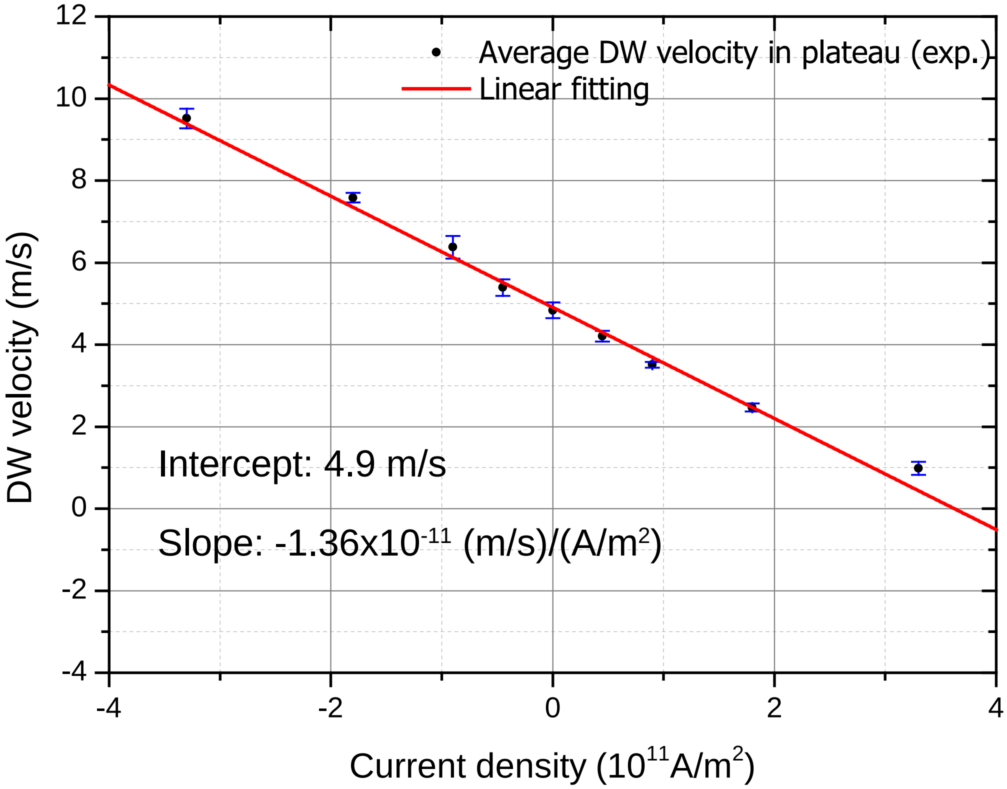

Figure 5-18 Average velocities obtained based on the results in Figure 5-17 (enclosed in green). The error bar was taken as the standard deviation. The red line is a linear fitting on all these velocities. The current density in the CoFeB layer estimated using ρ_{CFB}=170 μΩ·cm.

intercept of 4.9 m/s is obtained. This term is DW velocity induced by the magnetic field alone. The slope represents the contribution from the current induce motion.

5.3.2.2 **Discussions**

In the precessional mode, the azimuth angle φ of magnetization in the center of DW $\vec{m}_{DW}$ alternates from 0 to 2π, and the $\overline{\sin\varphi} = 0$ (the same for cosφ and sin2φ). Moreover, the DMI is very weak in this sample, here, to begin with, we assume SOT negligible. The current-induced part is mainly contributed by the STT. By neglecting the pinning potential, the 1D model described by Eq.(2-43)- (2-45) can be reduced to be [61,83],

$$\dot{\varphi} + \frac{\alpha}{\Delta}\dot{q} = \gamma_0 H_Z + \frac{\xi u}{\Delta} \tag{5-5}$$

$$-\alpha\dot{\varphi} + \frac{\dot{q}}{\Delta} = \frac{\gamma_0 H_K}{2} + sin\,2\varphi\frac{u}{\Delta} \tag{5-6}$$

By assuming $\overline{\sin 2\varphi} = 0$, we can get,

$$v_{STT+B} = v_{STT} + v_B \tag{5-7}$$

With

$$v_{STT} = \frac{1+\alpha\xi}{1+\alpha^2} \cdot \frac{\mu_B P}{eM_s} j_{STT} \tag{5-8}$$

where P is the spin polarization of the magnetic material and j_{STT} is the current density in magnetic layer. In view that $\alpha \ll 1$, v_{STT} can be approximated to,

$$v_{STT} = \frac{\mu_B P}{eM_s} j_{STT} \tag{5-9}$$

Now, our results confirmed the above analysis: the DW motion velocities in the precessional flow mode under the combined effect of the STT and the magnetic field pulse is the sum of the velocities that induced by either of these driving forces alone.

5.3.3 Polarization of CoFeB in the Ta/CoFeB/MgO structure

In fact, the relationship described in Eq. (5-7) has been observed in some experiment performed on the material with the in-plane anisotropy such as the permalloy[13,147,148] or on the [CoNi]$_n$ superlattice with PMA[149]. However, to our knowledge, it is the first time that this relationship is observed in the heavy metal/ferromagnet/insulator multilayers. In such a multilayer, some part of the current flows in the Ta layers, which is not magnetic.

In the presented model, the important parameter is the current density in the ferromagnetic layer, which cannot be deduced as simply as in the previous cases, for which all the conductive layers were ferromagnetic. How to get the meaningful density of current?

Indeed, for the structure composed of ultra-thin films, such as the Ta/CoFeB/MgO/Ta studied here (Figure 5-19), it is difficult to identify the current flowing in each layer because in such thin films without isolation in the interface, conducting electrons are not constrained in specified layers. They diffuse among different layers and go forward with a non-straight trajectory due to scatterings.

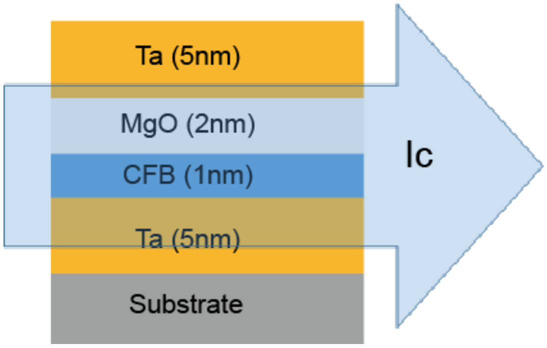

Figure 5-19 Sketch of the structure of the multilayers studied.

One may count the proportion of the current for each layer according to their conductivity. Under such an assumption, the effective current flowing in the FM layer can be estimated as,

$$j_{STT} = \frac{R}{l\rho_{CFB}} I_C \tag{5-10}$$

where R and l are the resistance and the width of the wire connected into the electric circuit, ρ_{CFB} is the resistivity of the CoFeB and Ic is the current flowing the whole section of the wire. For the wire tested here, R=5.2 kΩ, l=33.3 μm. Now, the estimation of the resistivity of the CoFeB thin film becomes the key point.

According to the published litteratures[75,78,150] (see also the Appendix 2), the resistivity of CoFeB layer in similar structures have been found between 160 and 330 μΩ·cm. From these results and our own tests (see Appendix 3), we have assumed a resistivity of 170 μΩ·cm for CFB and 190μΩ·cm for Ta. Using the Eq. (5-10), the current density in the CoFeB layer j_{STT} was estimated, and the dependence of the DW velocities on j_{STT} was replotted, as shown in Figure 5-18. A slope $k = -1.36 \times 10^{-11}\ (m/s)/(A/m^2)$ was obtained.

According to Eq. (5-9), this slope is,

$$k = \frac{\mu_B P}{e M_s} \tag{5-11}$$

Then, we can get the polarization of CoFeB in this structure: P= 26%.

The polarization obtained by measuring the in-plane current-induced DW motion is much lower than the polarization measured through the Point-Contact Andreev Reflection (65%)[151] or through the superconducting tunneling spectroscopy (53%)[91–93] in the heavy metal/CoFeB/Oxide layer structure.

The low polarization measured through the STT induced DW motion in Ta/CoFeB/MgO structure may be caused by the following reasons. First, the spin injection into the CoFeB layer or spin accumulation at the CoFeB/Ta interface due to spin Hall effects may reduce the spin polarization of CoFeB. Second, because of the scatterings of electrons, conductive electrons will interpenetrate between the Ta layer and

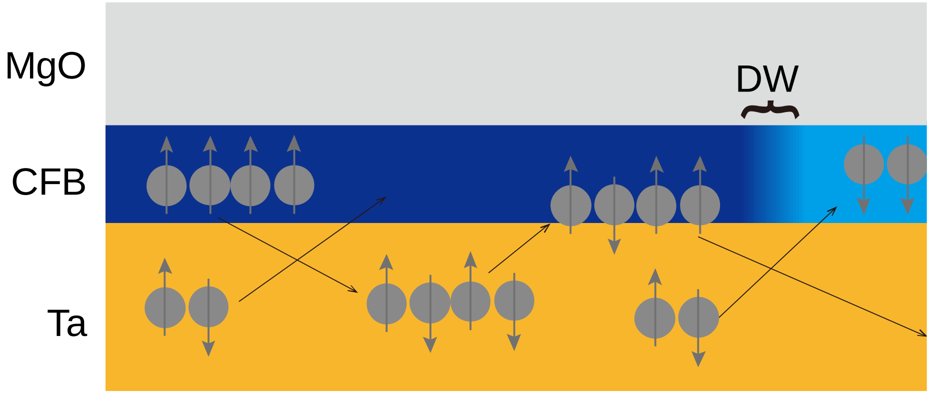

Figure 5-20 Sketch of the electrons transport in the Ta/CoFeB/MgO multilayers structure.

CoFeB layer, as illustrated in Figure 5-20. The diffusion of electrons from Ta layer may reduce the spin polarization of CoFeB. Third, scatterings of electrons in the MgO/CoFeB interface and CoFeB/Ta interface may decay the polarization.

Note that we have found that it was difficult to observe the DW motion driven by electric current along in this structure. The low polarization in the structure CFB/Ta may be one of the reasons to explain this difficulty.

5.4 Enhancement of DW pinning effects by spin hall current

In our experiments, we have found that under a low driving field ($B_Z < 10$ mT), the DW motion velocity was lowered down and becomes stochastic when a current was introduced, irrespective of the relative direction of the DW motion to the current direction, as shown in Figure 5-17. It seems that this reduction of velocity is caused by the enhanced pinning effects. To address this issue, we further experimentally characterized the pinning effects in the narrow wire when a current was applied together with the field.

5.4.1 Experiments and results

As stated before, we can nucleate and move a DW to any part of the wire with a short field pulse. When DW is propagating along the wire, it can be completely stopped by a pinning site. The minimum value to depin the DW has been defined as the depinning field H_{dep}. Here, we measured the DW depinning field of the strong pinning sites in a 1.5 μm wide and 30 μm long wire when a current was applied simultaneously. Figure 5-21 gives two examples of these measurements. The applied current changed

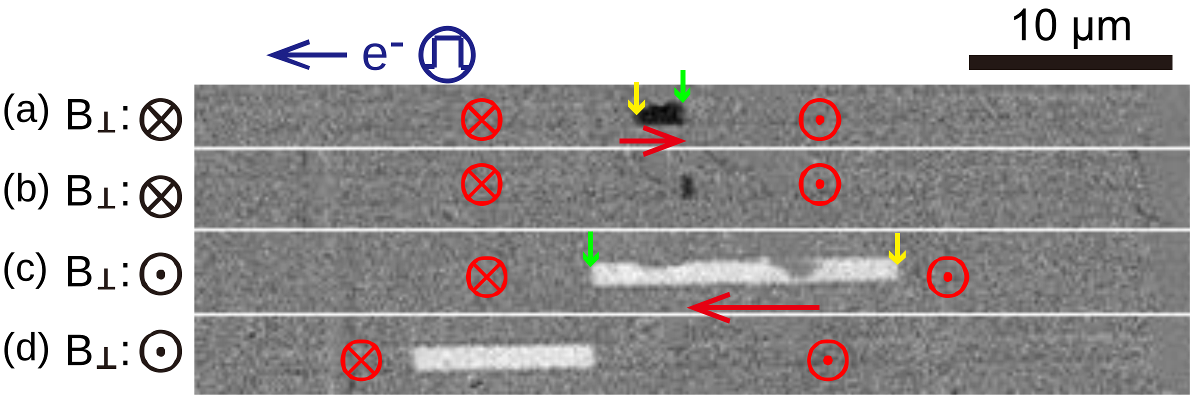

Figure 5-21 The pinning and depinning of the DW in a 1.5 μm wire. The direction of the electron flow is always to the left. (a) & (c), DW moves after a lower field pulse and then pinned at the pinning site (violet arrow). (b) & (d), DW continues to move after increasing the magnitude of the field pulse. Red arrows: direction of DW motion; yellow arrows: initial DW position; green arrows: position of pinning sites.

from 0 to 300 GA/m^2. The depinning fields for both DW motion direction were measured and the position of these pinning sites are noted. Both depinning field of the ⊙|⊗ and ⊗|⊙ DWs were measured. All the pulses applied in this experiment were 5 µs. More detailed information about this measurement can be found in Appendix 4.

The measured DW depinning fields without current have been plotted in Figure 5-22(a). The abscissa axis represents the longitudinal position of the pinning sites and the height of the bar holds for the amplitude of the depinning field. The sign of the field driving DWs to right is defined as positive and that to left is negative. We can find that the depinning field of the several largest pinning sites along the wire is about 5mT without applied current.

DW depinning fields of the several largest pinning sites when a current was applied were shown in Figure 5-22 (b)-(d). We found that the observed pinning effects were enhanced. In addition, several characteristics could be found: (i), the

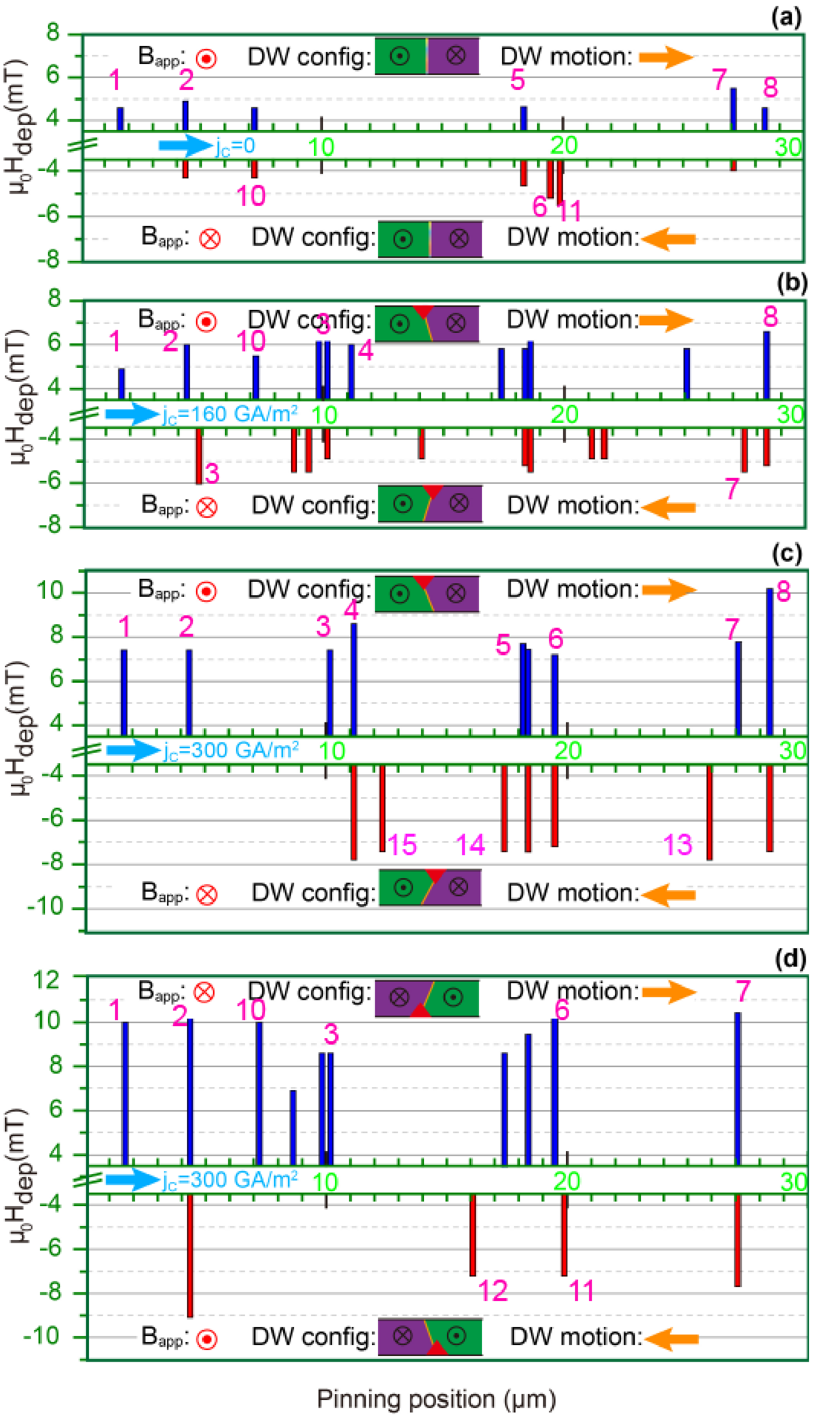

Figure 5-22 The position and the corresponding depinning field of the largest pinning sites in a 1.5 µm wide 30 µm long wire in different cases. The blue arrows denote the direction of current. The inset short wires denote the configuration and the tilting direction of DW. The small red triangle denotes the edge on which the extrinsic pinning effects are enhanced. The pink number is the index of the pinning sites, which will be referred by the analysis in the Annex 3.

depinning field increases as the density of the applied current increases, irrespective of the direction of DW motion or the DW configuration (i.e., ⊙|⊗ or ⊗|⊙); (ii), the enhancement of pinning effects are stronger for DW motion in the direction of charge current; (iii), pinning effects for DW motions in different directions or for different DW configurations are not very correlative when the current presents. For example, the pinning site n°2 is not so large in the case of Figure 5-22 (c) but becomes the hugest pinning sites in the case of (d); the pinning site n°8 is the hardest pinning site in the case (c) but disappeared in case (d). Note that according to our previous experiments, in the case without applied current, the deviation of the DW depinning field for a specified pinning site in different measurements is not so large.

When a current $j_C = 3.0 \times 10^{11} A/m^2$ was applied, the average value of DWs depinning field increased by 3 -5 mT. Here, j_C indicates the average current density in the Ta(5nm)/CFB(1nm) layer, calculated using Eq. (5-10) and the average resistivity of 190 μΩ. We have numerically calculated the perpendicular component of the Oersted field based on the Biot-Savart law, by assuming that the current distributes uniformly along the transverse section of the multilayer strip. For a test current I=3.7 mA (corresponds to $j_C = 3.0 \times 10^{11} A/m^2$ in Ta/CFB layers), perpendicular component of the Oersted field is shown in Figure 5-23. We found it to be less than 2.2 mT in the FM layer even closed to the edge. Moreover, the direction of the perpendicular component of the Oersted field is opposite in the two edge. Therefore, it could not be responsible to such an increase of the depinning field. Let's note, we acquired a Kerr image of the sample when a current $j_C = 6 \times 10^{11} A/m^2$ was being applied permanently and found that the contrast of the Kerr image did not show an observable fading, suggesting that the magnetization does not change due to Joule heating in the framework of these experiments.

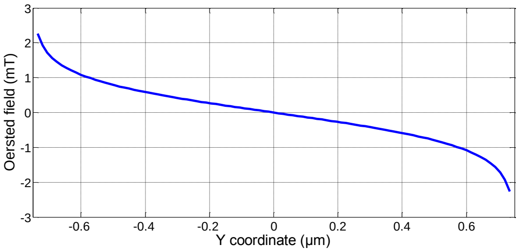

Figure 5-23 The perpendicular component of the Oersted field as a function of the transverse position in a 1.5 μm wire. The calculation is based on the Biot-Savart law, assuming that a current I=3.7 mA (corresponds to a density of j_C=300 GA/m^{2}in the CoFeB layer) is homogenous in the transverse direction of the wire. The thickness of the wire is supposed to be infinitely thin. Value in the edge, i.e. y=±0.75 μm was not given because the calculation is not convergent here.

5.4.2 Influence of the SH current on the DW depinning process

For current-induced DW motion in a wire with the HM/FM/Oxide structure, several effects could be involved in this dynamic. First, there is the STT [132] by the current flowing in the FM layer, which can move the DW in the direction of electrons flow. Considering that the enhancement of pinning effect observed in our experiments occurred irrespective of the relative direction of the DW motion and the current direction, it could not be caused by the STT. Second, the spin Hall current from the HM will induce two torques, namely, the damping like SOT (DL-SOT) and field like SOT (FL-SOT)[73]. According to Eq.(2-40), the effective fields associated with these torques can be expressed as,

$$\vec{H}_{SH} = -\frac{\hbar\theta_{SH} j_{HM}}{2eM_s t_M}(\vec{\sigma}_{SH} \times \vec{m}) \tag{5-12}$$

Where $\vec{\sigma}_{SH}$ is the polarizing direction of the SH current. The magnitude of SH angle θ_{SH} depends on the composition and lattice structure of HM. In the β phase Ta, θ_{SH} can reach a value as large as 0.12, with a negative sign [69,75] (see also the Table 2-1). The FL-SOT has been evidenced to be several orders smaller than the DL-SOT[73]. In materials without DMIs, such as the sample studied here, the DW is of Bloch type. If the DW is aligned along the transverse direction i.e. y-direction, the magnetization in the center of DW $\vec{m}_{DW}$ is also aligned along the transverse direction, parallel to $\vec{\sigma}_{SH}$. According to Eq.(2-40) the torque induced by the SH current is zero. However, in the case of the DW pinning, $\vec{m}_{DW}$ is not always along the transverse direction because of the curvature of the DW surface. Thus, the influence of the SH current on the DW is no longer zero. As shown in Figure 5-24, the effective field generated by the SH current $\vec{H}_{SH}$ can be parallel or opposite to the externally applied field $\vec{H}_{ext}$, depending on the tilting direction of $\vec{m}_{DW}$. This effect must be considered carefully.

In the following, we investigate the influence of the SH current on the DW pinning effects using micromagnetic simulations, which may provide a possible explanation for the enhancement of pinning

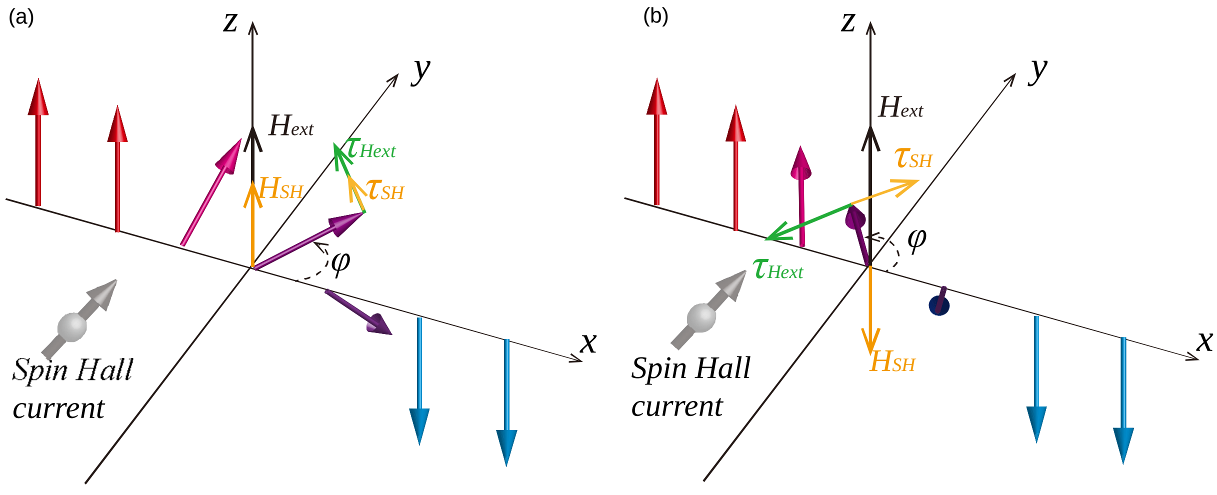

Figure 5-24 DL-SOT imparted by the SH current and the associated effective field in cases of different DW tilting direction.

effects observed in our experiments. Here, we divide the DW pinning effects into two types: one type is caused by the isolated hard pinning sites. This effect may arouse from the large defects on the edge of the wires introduced during the nanofabrication (commonly called as extrinsic pinning effects) or a single hard pinning in the wire. Another type is caused by the collective pinning effect of small and densely distributed defects in the wire, which arouse from the random inhomogeneities of the magnetic film (commonly called intrinsic pinning effects of the magnetic film).

5.4.2.1 **Influence of the SH current on the isolated pinning effects**

First, the influence of the SH current on the isolated pinning effects, including the pinning effects caused by the huge defects along the edge or caused by an isolated huge defect in the wire, is studied.

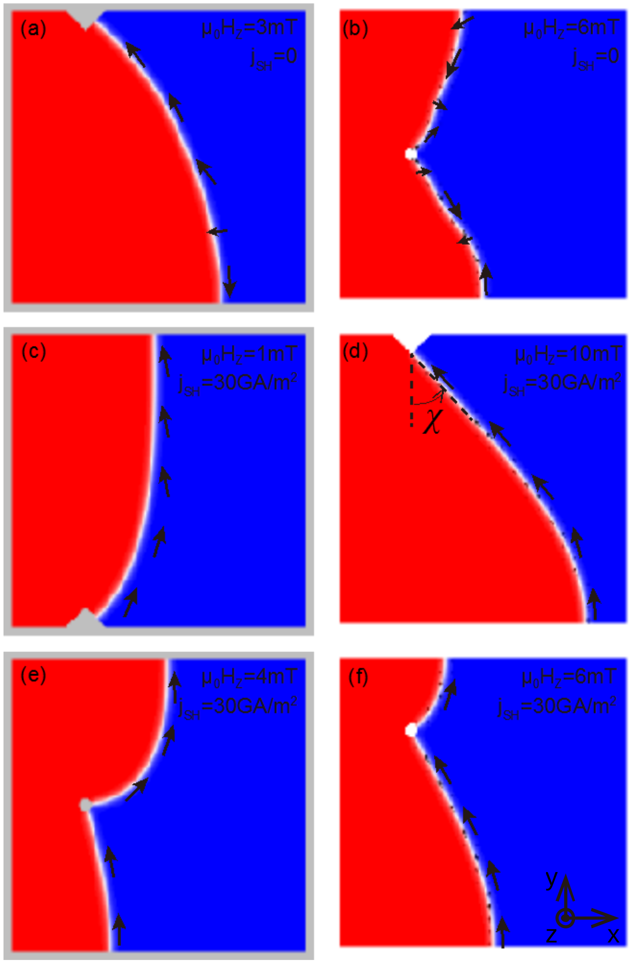

Figure 5-25 The profile of the pinned DWs in different cases (by simulations). Red: $\vec{m}$ in ⊙ direction; blue: ⊗. The black arrow indicate the direction of $\vec{m}_{DW}$. Each picture is acquired just before or during the DW depinning process. The size of each figure is 1 μm×1 μm. The depth of the notch in (a)(c)&(d) is 70 nm. The diameter of hole in (b)(e)&(f) is 50 nm. Other parameters: MS=1.1x106A/m3, Aex=25pJ/m, Ku=9.9×105J/m3, no DMI, no STT.

The DW depinning process was simulated using MuMax code[94,152]. The simulation is based on the Landau–Lifshitz–Gilbert equation in which the Slonczewski torque by the SH current is included. As shown in Figure 5-25, we introduced a defect in the edge of a 1 μm wide wire by creating a triangular notch (70 nm deep) or inside the wire by creating a circular hole (a diameter of 50 nm). Figure 5-25(a) and (b) show the DW profile when a perpendicular field was applied while the SH current was zero; in Figure 5-25 (c)-(f), a perpendicular field and a pure spin current polarized along the +y (up) direction with a density $j_P = 3 \times 10^{10} A/m^2$ were applied.

From the simulation results, we can find that in the absence of SH current, the DW is of Bloch type and the spiral of the DW alternates, separated by the so-called Bloch points. While $\vec{m}_{CDW}$ switches to +y direction when the SH current is introduced. When the DW is

Table 5-1 DWs depinning field (in mT) without and with the SH current for different position of pinning sites. *The letter in the bracket indicates the case described in Figure 5-25 with the same label.

Defect position	**Lower edge (c)***	**Center (b)**	**Up-center (f)**	**Top edge (d)**
without j_{SH}	3	6	6	3
With j_{SH}	1	4	7	11

hindered by a defect, the DW surface will tilt and bend. The tilting direction depends on the position of defect.

At last, we noted the depinning field for different cases in these simulations, as shown in Table 5-1. It is found that the presence of the SH current can significantly affect the depinning field of pining caused by the defect on the edges. Moreover, this effect is not symmetric for the two edges: it tends always to enhance the pinning effect in one edge while weaken the pinning effect in the other edge. Whereas, the pinning caused by the defect inside the wire is not so sensitive to the SH current.

In the equilibrium state, alternative spirals of the BW can minimize the magneto-static energy. However, if the SH current is strong enough, the DL-SOT can switch $\vec{m}_{DW}$ to the direction of $\vec{\sigma}_{SH}$ since $\vec{\sigma}_{SH}$is the equilibrium direction favored by this damping like torque.

When the DW propagation is hindered by a defect, the surface of the DW will tilt and bend under the Zeeman pressure from the applied field. $\vec{m}_{DW}$ will deviate away from transverse direction to adapt for the BW profile, which can minimize the magneto-static energy. In this case, the SOT is no longer zero. The DL-SOT behave as an effective perpendicular field, as described by the Eq. (5-12). This field can either enhance or weaken the effect of $\vec{H}_{ext}$, depending on the tilting direction of $\vec{m}_{DW}$, as illustrated in Figure 5-25. Moreover, the more $\vec{m}_{DW}$ tilts, the larger $\vec{H}_{SH}$ is. If this field tends to enhance the DW tilting (i.e., on the same direction as $\vec{H}_{ext}$, corresponding to the Figure 5-25(c)), the DW tilting and bending will be further enlarged. On the other hand, the DW surface tension tends to decrease the area of the DW surface, thus hindering this tilting and curvature. The final profile of the DW is the compromised result of the pressure from the $\vec{H}_{ext}$ and $\vec{H}_{SH}$ and the DW surface tension. Definitively, the criterion for the DW depinning from the defect is the comparison between the pinning potential and the resultant force from $\vec{H}_{ext}$ and $\vec{H}_{SH}$.

The SH current will assist the DW depinning if $\vec{H}_{SH}$ is on the same direction as the applied field. On the contrary, if the tilting direction of the DW results in a $\vec{H}_{SH}$ opposite to $\vec{H}_{ext}$, the effective field produced by the SH current will significantly enhance the pinning effect. For the defects lying inside the wire, the tilt of the DW in its two sides is on different directions. The effect of the SOT is partially canceled out in the vicinity of the pinning site, so the depinning field is not so affected by the SH current, unless the defect is very close to the edge.

Note that whether the pinning effect is enhanced or weakened in the vicinity of a specified pinning site in the edge depends on the relative direction between $\vec{H}_{ext}$ and $\vec{H}_{SH}$. $\vec{H}_{ext}$ is applied depending on the desired DW motion direction for a specified configuration of DW (⊙|⊗ or ⊗|⊙). According to Eq. (5-12), $\vec{H}_{SH}$ is determined by the relative direction between $\vec{\sigma}_{SH}$ and $\vec{m}_{DW}$. $\vec{\sigma}_{SH}$ will change if the current direction is reversed while $\vec{m}_{DW}$ depends the DW motion direction (considering the DW pinning and tilting), the position of the pinning site (upper or lower edge) and the current direction (because the transverse component of $\vec{m}_{DW}$ should be in the same direction than $\vec{\sigma}_{SH}$ due to DL-SOT). In particular, in the configuration shown in Figure 5-22 (b)&(c), it is always the pinning caused by defects in the upper edge that is enhanced, no matter the direction of the DW motion. While in Figure 5-22 (d), it is the pinning caused by defects in the lower edge that is enhanced.

This analysis predicts that the measured pinning fields will be less correlative between the two cases with different DW configuration: ⊙|⊗ and ⊗|⊙, while other parameters remain unchanged. On the other hand, the measured depinning fields will still be correlative if only one the following parameters are reversed and others parameters remain unchanged: (1), the direction of the applied current is reversed; (2) the DW motion direction is reversed, providing that the pinning site itself is symmetric with respect to the y-axis.

In particular, Figure 5-25 (d) shows that if the pinning site is on the upper edge, the tilted DW is almost rectilinear, except for the small segment closed to the lower edge. For a curved DW, an equilibrium between the Laplace pressure and Zeeman force is required in steady state, as described by Eq.(4-5), i.e., $\gamma_{DW}/R = 2\mu_0 H M_S$. Here H includes all the effective field exerting on the DW, including the H_{SH}. In the rectilinear part of the tilting DW, DW surface tension is nearly zero, meaning that $\vec{H}_{ext}$ is entirely cancelled out by $\vec{H}_{SH}$, i.e.,

$$\vec{H}_{ext} - \frac{\hbar \theta_{SH} j_{HM}}{2eM_s t_M} (\vec{\sigma}_{SH} \times \vec{m}_{DW}) = 0 \tag{5-13}$$

While for the DW segment closed to the lower edge, $\vec{H}_{SH}$ is not sufficient to cancel out $\vec{H}_{ext}$ owing to the smaller tilting angle of $\vec{m}_{DW}$. It is this disequilibrium that keep the tilting of the whole DW. We suppose that the tilting angle of the pinned DW from the y-axis is χ, as marked in Figure 5-25 (d), and the tilting angle of $\vec{m}_{DW}$ from the x-axis direction is φ. We can also expect an approximation that $\chi \approx \varphi$ because of the Bloch type configuration of the DW. From Eq. (5-13), we have

$$sin\chi \approx \frac{\hbar\theta_{SH} j_{HM}}{2eM_s t_M H_{ext}} \tag{5-14}$$

We can find that the tilting angle of the pinned DW is determined by the magnitude of the SH current and the external perpendicular field. This relationship may provide us a new method to measure the SH angle. Assuming that in a wider wire with an artificial notch patterned in the edge, a perpendicular field and a permanent current is applied, the DW tilting angle could be measured. Then the SH angle could be deduced. However, in our device, we were not able to acquire the Kerr image of the tilting DW because the duration of the field pulse and current pulse applied is 5μs, much shorter than the exposure time of the camera. While the pinning effects caused by the random defects cannot last for long duration because of thermal activation.

5.4.2.2 **Influence of the SH current on DW pinning by array of inhomogeneities**

In this section, we numerically show that the DW pinning caused by the densely distributed defects array inside the magnetic wire can also be significantly enhanced by the SH current if no DMI or H_X exists. Note that the intrinsic DW pinning in magnetic films caused by weak defects in the film is usually modeled by the array of randomly and densely distributed small inhomogeneities[153], this result implicates that the intrinsic DW pinning effects can also be enhanced by the SH current.

Simulations and results:

In a 1024 nm wide wire, defects are simulated by the inhomogeneity of the perpendicular anisotropy Ku. As shown in Figure 5-26, Ku in the region marked as black dots is reduced by 50%. The diameter of dots is 30 nm. Ku in the other regions is homogeneous, equal to 9.9×10^5 J/m^3. There is no edge roughness in this simulation. Other parameters are homogeneous, $M_S=1.1\text{x}10^6$ A/m^3, Aex=30 pJ/m.

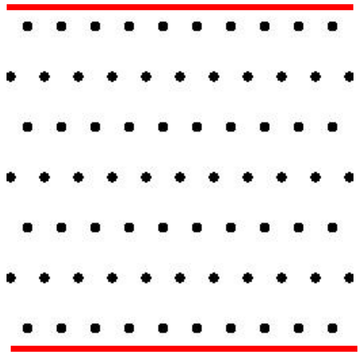

Figure 5-26 Distribution of anisotropy of the simulated sample. In this assumption, the anisotropy Ku of the region in black is set to be half of the other regions. There is not edge roughness in this simulation. Size simulated: 1024 nm ×1024 nm.

A perpendicular field B_Z=13mT and a SH current polarized along the +y direction $j_{SH}=3\text{x}10^{10}$ A/m^2 was applied. Some key frame of the DW motion is shown in Figure 5-27. DW tilts in an anti-clockwise direction and completely pinned after t=56 ns.

Our further simulations show that, DW can be depinned from these arrays by a field B_Z=8mT and move continuously if

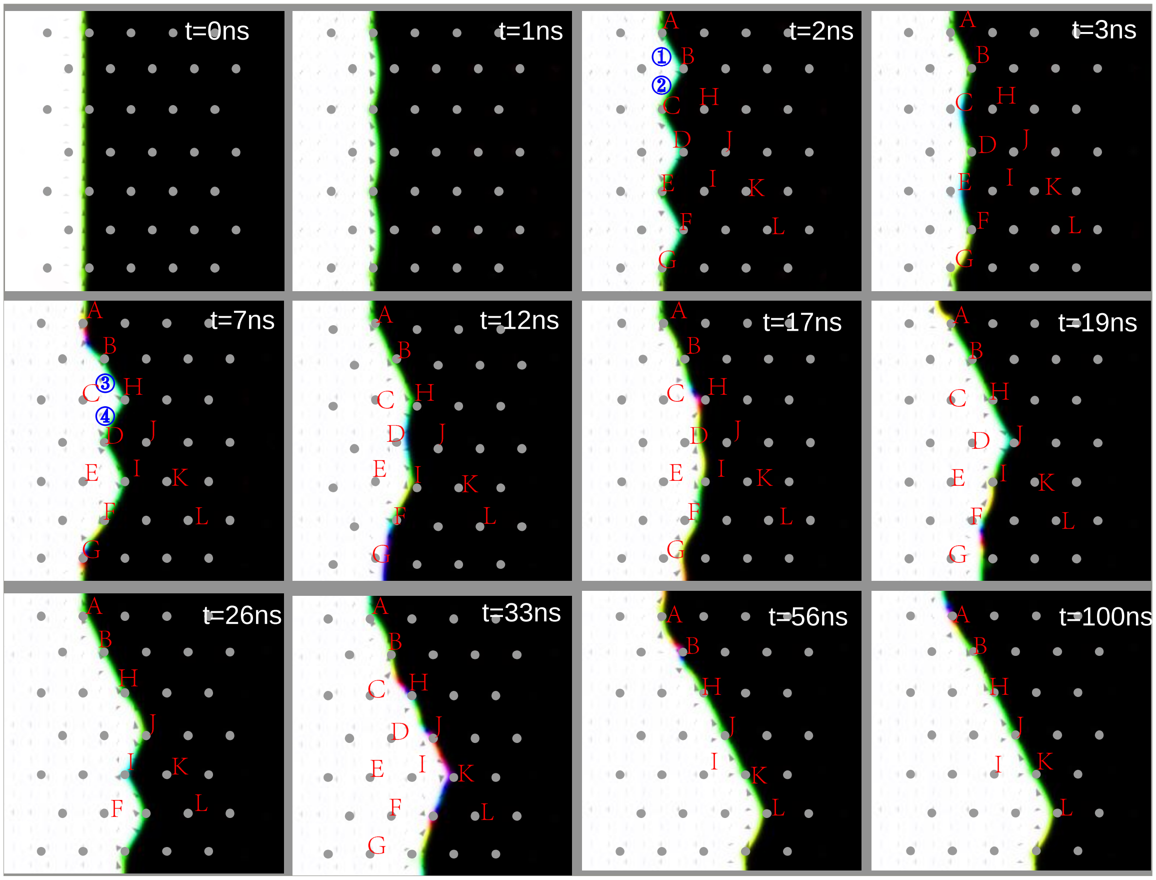

Figure 5-27 Key images of the simulated DW motion in a wire with array of defects (the distribution of the defects is described in Figure 5-26). B_Z=13 mT, j_{SH}=3x10^{10} A/m^2. White (black) indicates +z (-z, respectively) magnetization and gray points indicates the defects. Size of each picture: 1024 nm×1024 nm. The duration of the simulation is 100 ns.

no SH current is introduced, i.e., the DW depinning field has significantly increased when the SH current was introduced.

Discussions:

The above phenomena can be explained as follows. In an array of defects, DW moves in the form of "unit step" [153]. The pinned DW will bow out under the competition between the Zeeman pressure and the Laplace pressure. When H_{ext} is sufficiently large, DW will break away from one pinning site and realize one step of jump. Then it will be pinned by the next pinning site. In a film with dense pinning sites, DW is not a straight line. As shown in Figure 5-27, when SH current exists, in the case we simulated here, for the segment of DW tilting in an anti-clockwise direction (marked ① in Figure 5-27) the effective field produced by the SH current $\vec{H}_{SH}$ is opposite to $\vec{H}_{ext}$. As a result, the DW depinning at the two adjacent pinning sites, A and B, is impeded. For the DW tilting in clockwise direction, as marked ②, $\vec{H}_{SH}$ is in the same direction as $\vec{H}_{ext}$, so it will help the DW depinning at site C. After DW breakaway from pinning site C (Figure 5-27, t=11ns), the SH current will further impede the DW depinning from pinning site H. Due to the same reason, the DW depinning from J and K is impeded. Finally, the whole DW is tilting and pinned, as shown in Figure 5-27 (t=56ns). There is no further DW motion after t=56ns.

It is to note that, different from the huge defects in the edge, the array of densely distributed pinning sites are statistically homogeneous in the surface of wire, so the enhancement of pinning caused by the SH current should be statistically the same for different DW configurations (⊙ | ⊗ or ⊗ |⊙), i.e., the enhancement should be systematic.

5.4.3 Comparison of the models with the experimental results

In the preceding section, we have studied the effect the SH current on two types of DW pinning effects: the pinning effects created by isolated strong pinning sites, which were simulated by the geometric notches on the edge or inside the wire; the collective pinning effects caused by weak defects in the film, which were simulated by the array of weak inhomogeneities. For the former case, the SH current tends to enhance the pinning effects in one edge but weaken it in the other edge. For the latter case, the SH current tends to enhance the pinning systematically.

Now, let us compare this analysis with the experimental results. Globally, according to the experimental results, the average level of the depinning field of the strongest pinning sites has increased. However, through a one by one analysis of the nature of the pinning sites shown in Figure 5-22, we found that the enhancement of the pinning effect caused by the applied current is not systematic (more detailed analysis please see Appendix 4). For example, the pinning effect at site 10 appeared in the case without current, (Figure 5-22 (a)) but disappeared in the case of (c). The pinning effect at site 8 appeared in the case without current but disappeared in the case of (d). If we compared the case (c) and (d), the configuration of DW is reversed from ⊙ | ⊗ to ⊗ |⊙, the increase of depinning field of most of the pinning sites is different in these two cases.

According to the studies in section 4.1.5 and section 5.2 , although the hard DW pinning effects on nanowires are probably caused by the presence of huge defects on the edge, the DW pinning force at these hard pinning sites is the sum of two contributions (5-1): the pinning force caused by the isolated hard defects and the pinning force given by the inhomogeneities of the film of the wire (corresponding to the slope and the intercept of the fitted line in Figure 5-8, respectively). Now, according to the simulation results, when a SH current exists, it is not surprised that the level of the depinning field increases globally but the increase for each pinning site is different in case (c) and (d). This difference is consistent with the nature of the pinning sites on the edge, which play different roles in the cases plotted in Figure 5-22 (c) and (d). Note that the edge on which the pinning effects are enhanced is marked with the notch in each sub-figure.

At last, we can also find from the experimental results that the depinning field was a little smaller for DW motion in the direction of the electron flow. This may be caused by the driving force from the STT.

Let's note, as stated at the beginning of this chapter, we have tried to observe the DW motion driven by a current without an external field in our device. Some weak and fitful DW movements could be observed only when the injected current reached a very high density, $j_C = 4 \times 10^{11} A/m^2$. The SH current enhanced DW pinning effects may be one of the reasons to explain this difficulty of pure current-driven DW motion.

5.5 Application: a ring-shaped racetrack memory based the complementary work of STT and SOT

One of the most promising applications of the DW motion in the nanowire is for information storage, e.g. the racetrack memory (RM). The conventional structure of RM is stripe-shaped (see Figure 5-28 (a)), whether in 2D or in 3D [18]. Even though the stripe-shaped structure is relatively compact for design and fabrication, it suffers from some formidable obstacles hindering its practical application for future electronics. Among them, the data overflow issue is normally considered as its Achilles' heel: as the data are serially stored in RM, the operation of an individual bit certainly stimulates synchronous motions of the others; in the stripe-shaped case, this would lead to a part of data moving out of the device. Some attempts might solve this problem, for example, adding peripheral registers for storing the overflowing data, or extending the nanowire for avoiding the overflow[154]. However, these remedial methods unavoidably result in performance degradation in aspects of density, speed and power consumption. J. Franken et al. proposed a ring structure with DW ratchets [32], aiming to address the data overflow issue without any additional overhead. However, it still relies on the manipulation of the magnetic field and is impossible to realize large capacity.

In this section, we propose and study a ring-shaped RM based on the complementary work of the SOT driven and STT driven DW motions.

5.5.1 Ring-shaped RM structure and configurations

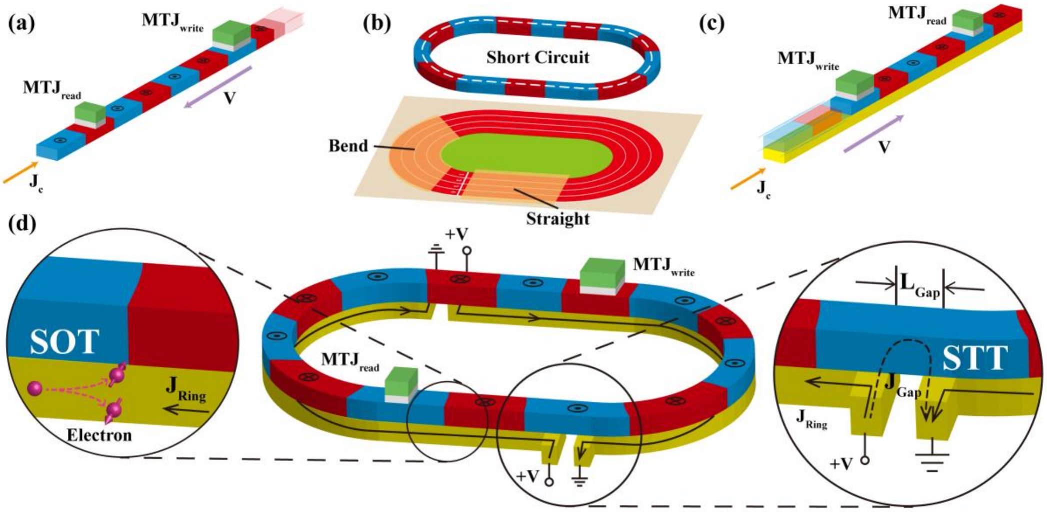

Figure 5-28 (a) Conventional spin transfer torque (STT) driven racetrack memory (RM), in which current flows through the ferromagnetic (data storage) layer. (b) Real racetrack shape leads to short circuit issue for STT driven RM. (c) Spin orbit interaction (SOI) driven RM, in which current is injected in the heavy metal layer underneath the data storage layer. (d) Ring-shaped SOI driven RM schematic. Domain walls (DWs) can be nucleated and detected by magnetic tunnel junctions (MTJ$_{write}$ and MTJ$_{read}$). Two gaps are introduced to avoid the short circuit issue. Current flows through heavy metal layer and leaks partially through the ferromagnetic layer above the gap (see inset). The leakage current could also induce DW motions, which guarantees the continuation of data transfer.

Figure 5-28(e) shows the schematic of the ring-shaped RM. From the functional point of view, it is composed of three parts: write head for DW nucleation, read head for magnetization detection and nanowire for DW motions. The write and read heads can be constructed by magnetic tunnel junctions (i.e. MTJ$_{write}$ and MTJ$_{read}$), as same as those for the conventional RM[14,155]. Particularly for the magnetic nanowire, the magnetic layer (e.g. CoFeB) is entirely closed while the adjacent heavy metal layer (e.g. Pt, W, Ta, Hf) has tiny gaps for avoiding short-circuit (see Figure 5-28 (c)). When the voltages are given on these gaps, due to the small resistance of heavy metal (e.g. Pt), the current mainly flows through the heavy metal layer, which thus induces SOT driven chiral DW motions in the parts apart from the gap. On the other hand, a leakage current can still flow through the magnetic layer over the gap part (see inset of Figure 5-28 (e)), whose value is related to the size of the gap. If the value is high enough, STT can be exerted in the gap part. The influence of the gap on the whole structure will be investigated in the following discussion section.

It is noteworthy that the direction of chiral DW motions driven by SOT can be either along or against the charge current direction in the heavy metal layer, depending on the sign of the SH angle and DW chirality of given multilayer system[78]. As the direction of STT driven DW motions is always against the current direction, we choose Pt/CoFeB/MgO as the material configuration in order to shift the data circularly and continuously in the ring structure. In addition, Pt has a relatively low resistivity among these heavy metals, which is also much lower than that of ferromagnetic materials, such as CoFeB. Although recent progress show that β-phase Ta and W can provide higher SH angle[78], their high resistivity are unfavorable to the ring-shaped design.

5.5.2 Micromagnetic simulations

The functionality of the device proposed is investigated via micromagnetic simulations with Mumax by introducing SOT and DMI into the Landau Lifshitz Gilbert (LLG) equation [152], as presented in section 2.4 . In the gap part without sub heavy metal layer, the adiabatic and no adiabatic STT is introduced.

The following parameters were used in the simulation: the Gilbert damping constant is 0.015, the non-adiabatic constant is 0.2, the spin Hall angle is 0.01, the Exchange stiffness is 20 pJ/m^2, the spin polarization rate is 0.5, the saturation magnetization is 1 MA/m, the uniaxial anisotropy is 800 kJ/m^3, the ferromagnetic layer thickness is 1 nm, the DMI parameter is 1.5 mJ/m^2.

5.5.3 Results

From the point of view of DW trajectory, the ring-shaped RM can be divided into two parts: the "Straight" and the "Bend". Firstly, Figure 5-29 (a-d) demonstrates the chiral DW motions in the "Straight": a 40-nm-wide 1.28-um-long nanowire of Pt(2 nm)/CoFeB(0.6 nm)/MgO. DW motion velocity can reach 400 m/s with a current of 1×10^{11} A/m^2. The motion velocity increases with the magnitude of injected current and approaches the saturation when the current exceeds 3×10^{11} A/m^2. Secondly, Figure 5-29 (e-h) shows chiral DW motions in the "Bend". The geometry of magnetic layer is designed to be a circle whose external diameter is 1.024 um, width is 40 nm. The gap length of the heavy metal layer is fixed to 100 nm. The material parameters are the same as the "Straight" above. J_{Gap} and J_{Ring} are the current densities through the gap and ring parts which are 1.4×10^{12} A/m^2 and 3×10^{11} A/m^2. With the drive of

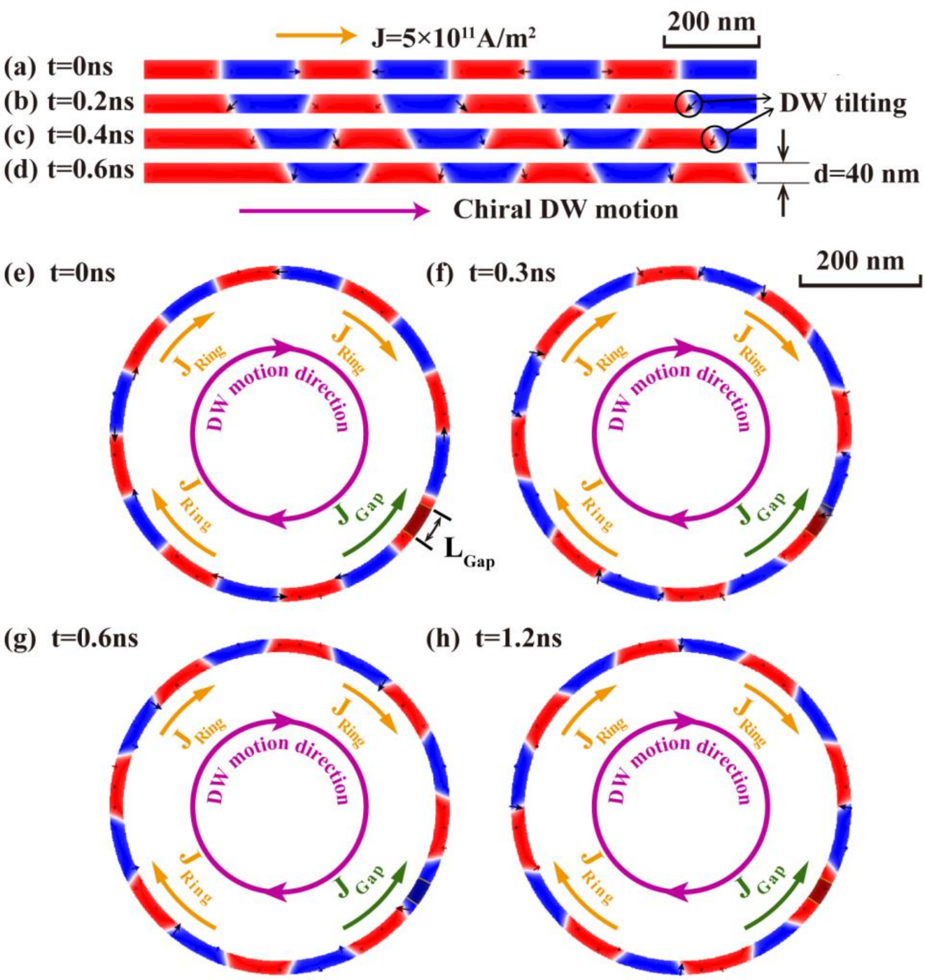

Figure 5-29 The top-view of the SOI driven chiral DW motions in the "Straight" and "Bend". Red represents +z magnetization, blue represents –z magnetization. (a-d) The "Straight": 40 nm-wide and 1.28 um-long Pt(2 nm)/CoFeB(0.6 nm)/MgO. DW motion velocity can reach 400 m/s with a current of 5×10^{11} A/m^2. DW tilting occurs which agrees with experimental results. (e-h) The "Bend": external diameter D_{ext} is 1024 nm, width d is 40 nm. The gap length of the heavy metal layer L_{gap} is 100 nm. Current injected into the heavy metal layer for SOI part J_{Ring} is 3×10^{11} A/m^2 and leakage current in the gap part inducing STT J_{Gap} is 1.4×10^{12} A/m^2. The different directions of current for these two parts guarantee the uni-direction of DW motions.

the STT on the gap part and the drive of the SOT on the other part, DWs move along the ring synchronously.

Compared with the circular structure, the racetrack-shaped structure, combining the "Straight" and the "Bend" as shown in Figure 5-28 (b), promises the benefit in term of storage density. Figure 5-30 shows the complete process of chiral DW motions in a really racetrack-shaped 16-bit RM. J_{Gap} and J_{Ring} are 5×10^{12} A/m^2 and 1×10^{12} A/m^2 respectively, which are larger than those in Figure 5-29, aiming to overcome the pinning force from the pinning sites. The length of the gap is 100 nm each. From the results, due to the DW motion inertia, the DWs can move synchronously and fluently with a 0.6-ns current pulse. Here, adding the pinning sites is an important mean to optimize the controllability of DW shifting. Note that the DMI stabilized SOT induced DWs are tilted and the tilting directions of the neighboring DWs alternate[79]. This requires that the pinning sites should be symmetry on both sides of the racetrack in order to make the equal effect on DWs with different tilting directions.

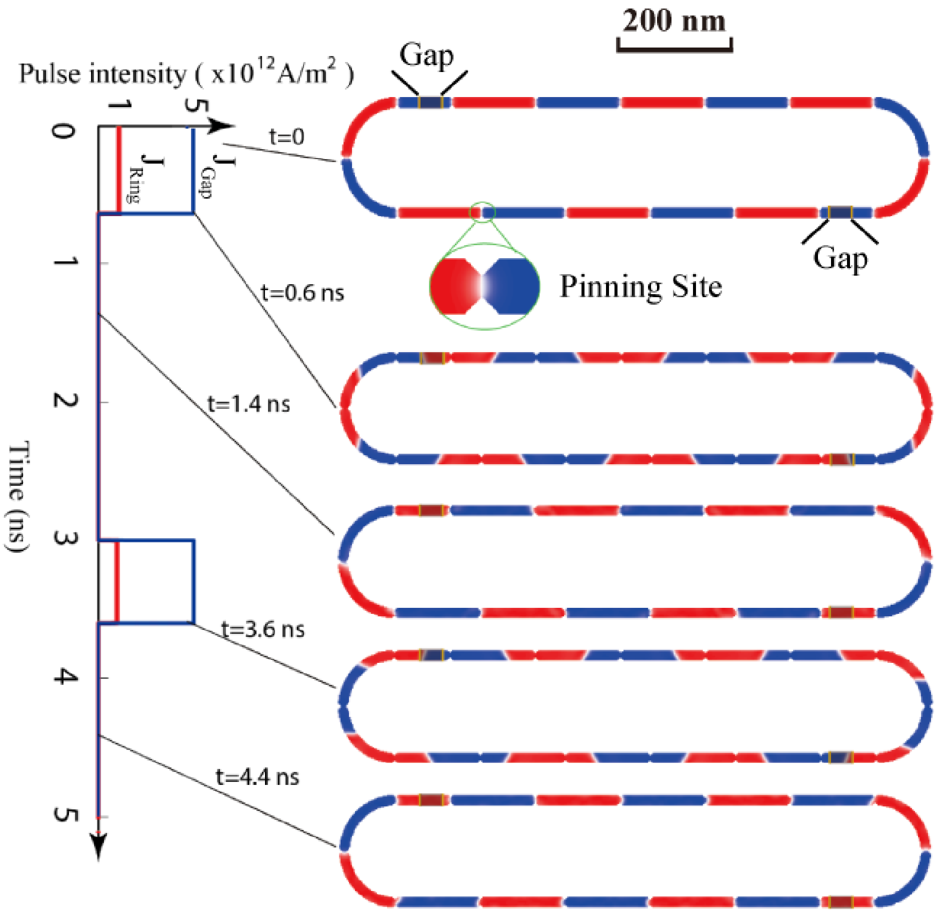

Figure 5-30 16-bit Racetrack-shaped RM schematic. Two gaps and symmetric pinning sites (see inset) are used for ensuring the functionality and stability of the RM. J_{Gap} and J_{Ring} are 5×10^{12} A/m^2 and 1×10^{12} A/m^2. The length of gap is 100 nm each. 0.6 ns current pulses are sufficient for DW motions due to the inertia.

5.5.4 Discussions

To guarantee the functionality of the ring-shaped RM, one of the most critical conditions is that the velocity of DW motions should be harmonious, which means DWs in ring part and gap part should at least move with comparative speeds. First, both the velocity of the SOT driven DW motion in the ring part and the STT driven DW motion in the gap part depend on the current density in the heavy metal layer or in the FM layer. These current densities have the following relationship,

$$J_{Ring}\rho_{Ring}L_{Ring} = J_{Gap}\rho_{Gap}L_{Gap} \tag{5-15}$$

where ρ_{Ring} and $\rho_{\mathrm{Gap}}$are the resistivity of the heavy metal layer and the FM layer, L_{Ring} and L_{Gap} are the lengths of the ring (without gap) and the gap. Therefore, the current density in the ring part and gap part can be adjusted by the length ratio between L_{Ring} and L_{Gap}. Because of the relatively shorter distance of the gap, the current density in the FM of the gap part can be very large, thus promise a fast DW velocity. Still, one should mind that the current in the gap part should not excess destructing density. According to experimental observations, the STT driven DW velocity can reach only about a hundred meters per second [55]. This velocity is still not able to match with the SOT driven DW velocity, which can reaches several hundred meter per second [70,71]. In order to solve this mismatch of velocities, we can set a shorter distance for the storage unit covering the gap part. For example, in the 16-bit RM shown in Figure 5-30, a storage unit is defined by the section of nanowire between two notches. The length of the storage unit covering the gap is only 100nm while a storage unit in the other part is about 150 nm. The DW can pass the unit with gap and shift to the next notch with approximately the same time as others. In addition, in the simulations that we performed, we didn’t observe a very large decrease of DW velocity in the gap part as expected. This can be explained by the inertia of the DW[156,157]. The roughness is neglected in our simulations and the ferromagnetic material that we applied, CoFeB, has a relatively small damping constant. This allows the DWs to continue moving over a distance by a force of inertia[156,157].

Compared to conventional stripe-shaped structure, this ring-shaped structure can keep all the data during the shifting process, without increasing overhead and requiring additional manipulations. We believe this ring-shaped RM will vitalize the development and practical application of RM[158].

5.6 Conclusion

In this chapter, the DW motion in the nanowire driven by the magnetic field or by the combined effect of the field and electrical current was experimentally studied. The polarization ratio of CoFeB in the Ta/CoFeB/MgO structure has been extracted based on the contribution of STT on the DW motion velocity and was found to be as low as 26%, much lower than the value measured through the Point-Contact Andreev Reflection (65%)[151] or through the superconducting tunneling spectroscopy (53%)[91–93] in the heavy metal/CoFeB/Oxide layer structure. This low polarization ratio may be caused by the injection of SH current or the diffusion of electrons from the Ta layer.

The DW pinning effects in the nanowire and the dependence of the depinning field on the width of wire was measured and analyzed. The enhancement of pinning effects when a current was applied was observed and a possible explanation is an effect of the SH current. At last, a ring-shaped RM, which can avoid the data overflow, was proposed and verified with micromagnetic simulations.

Chapter 6 General conclusions and perspectives

This thesis is devoted to the study of magnetic DW properties and dynamics in Ta/$Co_{40}Fe_{40}B_{20}$/MgO thin films and nanowires with PMA. The observation of domain structures and DW dynamics relied mainly on Kerr microscopy. In order to study the DW behavior in the nanostructures, very short magnetic pulses of high amplitude were required. We could reach this aim by creating small coils of very low inductance and by connecting them to a high current pulse generator. We have succeeded to create microsecond magnetic pulses, with a rise time shorter than 200 ns. Electric current pulses have been applied on the nanowires and we were able to create the synchronized magnetic field pulse and electric current pulse with a duration of several microseconds.

Thanks to the high-resolution Kerr microscope and the proper magnetic field pulse produced by the mini coil, we have conducted a series of experiments related to the DW surface tension. We studied the dynamic of DW in the nanowires, including the DW pinning effects and the DW motion driven by a magnetic field or current, or by their combined effects.

The main contributions of this thesis are:

- DWs surface tension was directly observed using a Kerr microscope and DWs surface energy was directly quantified. In zero external field, the spontaneous collapse of semicircular domain bubble was observed. This phenomenon was explained with the concept of the Laplace pressure due to the DW surface energy. The DW surface energy was quantified by measuring the external field required to stabilize the domain bubble.
- The origin of the DW pinning effects in some artificial structures, such as Hall crosses or the entrance from nanowire to the nucleation pad, were explained using the concept of DWs surface tension. The linear dependence of the DW depinning field in these structures on the width of wire was used to quantify the DW surface energy.
- A new type of magnetic sensor based on the elasticity of DWs has been designed and verified using micromagnetic simulations.
- The DW pinning effects in CoFeB nanowires was characterized. A linear dependence of the depinning field of the strong pinning sites on the width of wire was observed and analyzed. It points to an extrinsic nature of these strong pinning points, which would be on the edges of the nanowires and due to the nanopatterning.

- Velocities of the field-driven and the current-driven DW motion in heavy metal/CoFeB/MgO nanowires was measured. We have found experimentally that the velocity of the DW motion driven by the combined effect of the field and the current equals to the sum of the velocity contributed by these two forces separately. The spin polarization of CoFeB was extracted and was found equal to 26%. A possible explanation for this low spin polarization of CoFeB is an injection of differently polarized spin from Ta to CoFeB due to the spin Hall effect. The diffusion of electrons between the CoFeB and Ta layer, which has a strong SOC, may also be a reason for this low spin polarization.
- We found that the DW depinning field in nanowires increased significantly when a current was applied simultaneously, irrespective of the relative DW motion direction and the current direction. We think this could arise from spin Hall current coming from the Ta layer. Using micromagnetic simulations, we show that the intrinsic DW pinning effects in magnetic wires can be enhanced by the SH current. However, only the extrinsic pinning effects in one of the two edges can be enhanced.
- A ring-shaped racetrack memory device based on the combined works of the STT and SOT driven DW motion in nanowires was designed and verified using micromagnetic simulations. This racetrack memory can avoid the data drop out compared with traditional line-shaped racetrack memory.

Our results have brought some interesting results and have explained several phenomena. We have found new ways, which could be used to answer some still opened questions. Furthermore, our work has also risen several new questions:

1. We have developed two methods to measure the DW surface energy γ_{DW}. These methods may be useful to quantify the intrinsic parameter of material, such as the DMI constant, the exchange stiffness.

Among the various methods to quantify the strength of DMI with Kerr microscope, e.g. by probing the asymmetric propagation of circular DW in creep regime when an in-plane field is present[5], or by observing the in-plane field that changes the direction of the spin Hall current-induced DW motion[159], only the effective DMI field H_{DM} can be obtained. We have[160],

$$D = \mu_0 H_{DM} M_S \sqrt{\frac{A_{ex}}{K_{eff}}} \tag{6-1}$$

It is difficult to access directly to the intrinsic parameter D, since the exchange stiffness A_{ex} is difficult to be quantified with Kerr microscope.

In fact, the quantification of A_{ex} in ultra-thin films is always a difficult issue. The commonly used methods to measure A_{ex} are mainly based on the spin wave frequency and dispersion[125] (e.g. using Brillouin light scattering (BSL)[161–163], spin-polarized electron energy loss spectroscopy, ferromagnetic resonance (FMR)[139,164]). However, for ultrathin films less than 10 nm, the above methods become less useful because they are not sufficiently sensitive to detect spin waves[165]. Moreover, it was found that the value of A in the ultra-thin film is different than that in bulk material (thickness larger than ~10nm) due to the interfacial effect. The value of A_{ex} obtained in bulk material cannot be used in ultrathin film[165].

Now, A_{ex} can be extracted once the DW surface energy γ_{DW} is accurately quantified, since $\gamma_{DW} = 4\sqrt{A_{ex}K_{eff}}$ in film without DMI.

Furthermore, if DMIs exist, the DW surface energy changes[166],

$$\gamma_{DW} = 4\sqrt{A_{ex}K_{eff}} - \pi D \tag{6-2}$$

Once the DW surface energy γ_{DW} is obtained with our methods, we can deduce directly the value of D from Eq.(6-1) & (6-2),

$$D = \frac{\gamma_{DW}}{\frac{4K_{eff}}{\mu_0 H_{DM} M_S} - \pi} \tag{6-3}$$

and,

$$A_{ex} = \frac{K_{eff}\,\gamma_{DW}^2}{\left(4K_{eff} - \pi\mu_0 H_{DM} M_S\right)^2} \tag{6-4}$$

From Eq. (6-3), the expected uncertainty of the extracted D is in the same order than γ_{DW}, assuming that other parameters such as K_{eff}, H_{DM}, and M_S are well quantified.

This method needs to be explored in the future studies.

2. We have experimentally observed the enhancement of the DW pinning effect in Ta/CoFeB narrow wire when a current is applied. With micromagnetic simulation, we show that a spin Hall current injected into the magnetic layer can result in this enhancement. However, further experiments are needed to study this effect more clearly. For example, one can etch some regular notches in the edge of wires to observe the change of the profile of the DW when a current was applied because a DW tilting is predicted by the

simulation in this case. The wire can be enlarged (e.g. to more than 10 μm) so that the DW behavior can be observed clearly, because, with the Kerr microscope, we were not able to clearly observe the shape of the DW in the 1.5 μm wire studied. The simulation has predicted a variation of DW tilting angle as a function of applied current density, through which the SH angle may be extracted. Further experiments can be conducted to explore this method.

3. We have found that in the Ta/CoFeB/MgO narrow wire, when the applied easy-axis field is weak or zero, the DW is very difficult to be moved by the current. When the current increased to a critical value, the DW motion direction becomes stochastic. This phenomenon has not been completely understood. Further studies are needed to understand this question.

4. We have observed the DW motion driven by the synchronized current and the magnetic field applied along the easy axis and explained the DW velocity by the combined effects of the field and STT. However, in the heavy metal/magnetic layer/MgO structure, the SH current from the heavy metal layer begins to work when an in-plane field is applied. It might be interesting to implement an in-plane field in addition to the present system and study the combined effect of the magnetic field, the STT and the SOT on the DW motion. Some important parameters such as the SH angle, the non-adiabatic constant might be

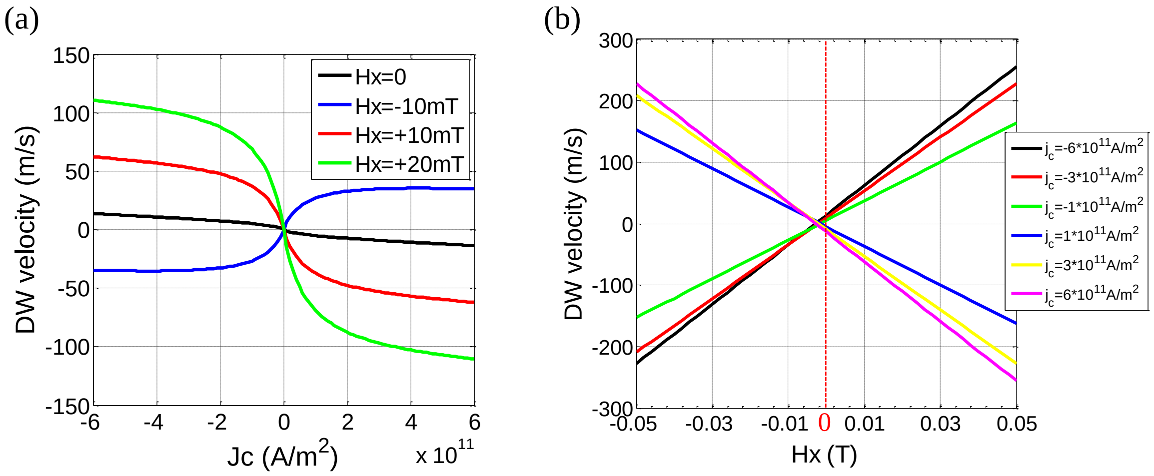

Figure 6-1The DW motion velocity predicted by the 1D model. Parameters: No field was applied along the z-axis (easy axis), DW width: 10 nm, shape anisotropy field H_k: 105 A/m; both the adiabatic STT, non-adiabatic STT from the in-plane current in FM layer, and the SOT caused by the injection of the SH current are considered. Non adiabatic constant β=0.1; the polarization P=0.26 for in-plane current. The spin Hall angle is supposed to be ΘSH=-0.05. An in-plane field along the longitudinal direction (x-axis, DW motion direction) was applied. (a) DW motion velocities vs. current density. (b) DW velocities vs. the in plane field.

properly extracted based on these experiments. Based on the numerical calculation of 1D model, we found that the DW motion induced by the combined effect of the STT and SOT is linear as a function of the magnitude of the in-plane field, as shown in Figure 6-1 (b). The vertical intercept represents the contribution from the STT and the slope represents the contribution from the SOT. If this relationship could be experimentally measured, the spin Hall angle could be extracted by linearly fitting the experimental results with the 1D model.

In addition, we found that the horizontal intercept changes with the non-adiabatic constant ξ, as shown in Figure 6-2. Because both the SOT and non-adiabatic STT enters the 1D model in the form effective fields. The change of the horizontal intercept with β is the result of the competition between this two terms. By locating this intercept, the non-adiabatic constant might be extracted.

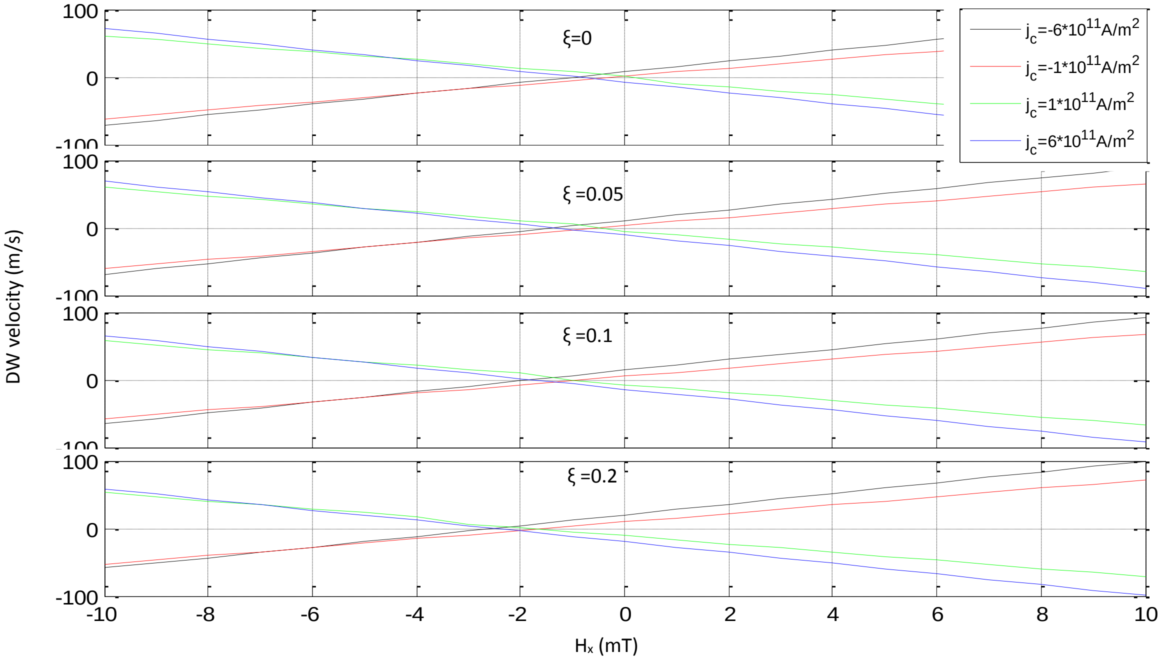

Figure 6-2 Numerically calculated DW motion velocities based on the 1D model. Non-adiabatic constant ξ changes from 0 to 0.2. Other parameters are same as that in Fig. 6-1

5. Through numerical calculations based on the 1D model, we have found that the damping like SOT due to the injection of the SH current tends to stabilize the magnetization of DW in the polarizing direction of the SH current. Consequently, the arrival of the precessional mode will be delayed, i.e., the Walker breakdown field increase, as shown in Figure 6-3. It should be interesting if this prediction could be experimentally observed. To reach this aim, one should find a material/structure with a relatively large

damping parameter and weak pinning field in order that the Walker breakdown point ($H_W = \alpha M_S/2$) is not hidden by the creep depinning transition regime.

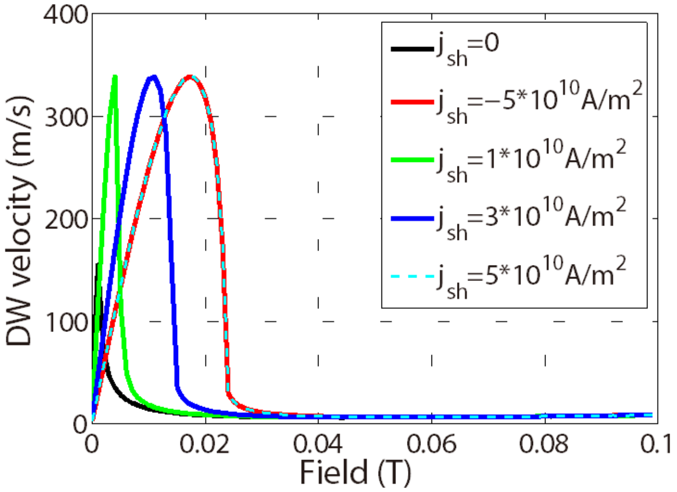

Figure 6-3 Numerically calculated DW motion velocities based on the 1D model when only a magnetic field along the easy axis (perpendicular direction) and the SH current are considered. The DMI, HX or STT from the current in FM layer are not considered. DW width: 10 nm, shape anisotropy field Hk: 105 A/m.

References

1. Vernier, N.; Adam, J. P.; Eimer, S.; Agnus, G.; Devolder, T.; Hauet, T.; Ocker, B.; Garcia, F.; Ravelosona, D. Measurement of magnetization using domain compressibility in CoFeB films with perpendicular anisotropy. *Appl. Phys. Lett.* **2014**, *104*, 122404, doi:10.1063/1.4869482.
2. Yamanouchi, M.; Jander, A.; Dhagat, P.; Ikeda, S.; Matsukura, F.; Ohno, H. Domain Structure in CoFeB Thin Films With Perpendicular Magnetic Anisotropy. *IEEE Magn. Lett.* **2011**, *2*, 3000304, doi:10.1109/LMAG.2011.2159484.
3. Haghgoo, S.; Cubukcu, M.; Von Bardeleben, H. J.; Thevenard, L.; Lemaître, A.; Gourdon, C. Exchange constant and domain wall width in (Ga,Mn)(As,P) films with self-organization of magnetic domains. *Phys. Rev. B* **2010**, *82*, 041301, doi:10.1103/PhysRevB.82.041301.
4. Buford, B.; Dhagat, P.; Jander, A. Estimating exchange stiffness of thin films with perpendicular anisotropy using magnetic domain images. *IEEE Magn. Lett.* **2016**, *7*, 1–5, doi:10.1109/LMAG.2016.2611681.
5. Je, S.-G.; Kim, D.-H.; Yoo, S.-C.; Min, B.-C.; Lee, K.-J.; Choe, S.-B. Asymmetric magnetic domain-wall motion by the Dzyaloshinskii-Moriya interaction. *Phys. Rev. B* **2013**, *88*, 214401, doi:10.1103/PhysRevB.88.214401.
6. Currivan-Incorvia, J. A.; Siddiqui, S.; Dutta, S.; Evarts, E. R.; Zhang, J.; Bono, D.; Ross, C. A.; Baldo, M. A. Logic circuit prototypes for three-terminal magnetic tunnel junctions with mobile domain walls. *Nat. Commun.* **2016**, *7*, 10275, doi:10.1038/ncomms10275.
7. Allwood, D. A.; Xiong, G.; Faulkner, C. C.; ATKINSON, D.; Petit, D.; Cowburn, R. P. Magnetic Domain-Wall Logic. *Science* **2005**, *309*, 1688–1692, doi:10.1126/science.1108813.
8. Sengupta, A.; Shim, Y.; Roy, K. Proposal for an all-spin artificial neural network: Emulating neural and synaptic functionalities through domain wall motion in ferromagnets. *IEEE Trans. Biomed. Circuits Syst.* **2016**, *10*, 1152–1160, doi:10.1109/TBCAS.2016.2525823.
9. Sharad, M.; Augustine, C.; Panagopoulos, G.; Roy, K. Spin-based neuron model with domain-wall magnets as synapse. *IEEE Trans. Nanotechnol.* **2012**, *11*, 843–853, doi:10.1109/TNANO.2012.2202125.
10. Fan, D.; Shim, Y.; Raghunathan, A.; Roy, K. STT-SNN: A Spin-Transfer-Torque Based Soft-Limiting Non-Linear Neuron for Low-Power Artificial Neural Networks. *IEEE Trans. Nanotechnol.* **2015**, *14*, 1013–1023, doi:10.1109/TNANO.2015.2437902.

11. Wagner, K.; Kákay, A.; Schultheiss, K.; Henschke, A.; Sebastian, T.; Schultheiss, H. Magnetic domain walls as reconfigurable spin-wave nanochannels. *Nat. Nanotechnol.* **2016**, *11*, 432–436, doi:10.1038/nnano.2015.339.

12. Parkin, S.; Yang, S.-H. Memory on the racetrack. *Nat. Nanotechnol.* **2015**, *10*, 195–198, doi:10.1038/nnano.2015.41.

13. Parkin, S. S. P.; Hayashi, M.; Thomas, L. Magnetic domain-wall racetrack memory. *Science* **2008**, *320*, 190–194, doi:10.1126/science.1145799.

14. Ikeda, S.; Miura, K.; Yamamoto, H.; Mizunuma, K.; Gan, H. D.; Endo, M.; Kanai, S.; Hayakawa, J.; Matsukura, F.; Ohno, H. A perpendicular-anisotropy CoFeB-MgO magnetic tunnel junction. *Nat. Mater.* **2010**, *9*, 721–724, doi:10.1038/nmat2804.

15. Wells, J.; Krzysteczko, P.; Caprile, A.; Gribkov, B.; Schumacher, H. W.; Lee, J. H.; Cowburn, R.; Kazakova, O. Magnetic Particle Nanosensing by Nucleation of Domain Walls in Ultra-Thin CoFeB/Pt Devices. *IEEE Trans. Magn.* **2016**, *52*, doi:10.1109/TMAG.2016.2524074.

16. Ikeda, S.; Hayakawa, J.; Ashizawa, Y.; Lee, Y. M.; Miura, K.; Hasegawa, H.; Tsunoda, M.; Matsukura, F.; Ohno, H. Tunnel magnetoresistance of 604% at 300 K by suppression of Ta diffusion in CoFeBMgOCoFeB pseudo-spin-valves annealed at high temperature. *Appl. Phys. Lett.* **2008**, *93*, 2006–2009, doi:10.1063/1.2976435.

17. Jang, Y.; Nam, C.; Kim, J. Y.; Cho, B. K.; Cho, Y. J.; Kim, T. W. Magnetic field sensing scheme using CoFeB/MgO/CoFeB tunneling junction with superparamagnetic CoFeB layer. *Appl. Phys. Lett.* **2006**, *89*, 163119, doi:10.1063/1.2370876.

18. Zhang, Y.; Zhao, W. S.; Ravelosona, D.; Klein, J. O.; Kim, J. V.; Chappert, C. Perpendicular-magnetic-anisotropy CoFeB racetrack memory. *J. Appl. Phys.* **2012**, *111*, 2010–2015, doi:10.1063/1.4716460.

19. Stöhr, J.; Siegmann, H. C. *Magnetism:FromFundamentals to Nanoscale Dynamics*; Springer Berlin Heidelberg: Berlin, Heidelberg, 2006; ISBN 978-3-540-30282-7.

20. Babujian, H. M. Exact solution of the isotropic Heisenberg chain with arbitrary spins: Thermodynamics of the model. *Nucl. Physics, Sect. B* **1983**, *215*, 317–336, doi:10.1016/0550-3213(83)90668-5.

21. Hubert, A.; Schäfer, R. *Magnetic Domains,The Analysis of Magnetic Microstructures*; 3rd ed.; Springer: New York, 1998; ISBN 978-3-540-85054-0.

22. Zhang, B.; Cao, A.; Qiao, J.; Tang, M.; Cao, K.; Zhao, X.; Eimer, S.; Si, Z.; Lei, N.; Wang, Z.; Lin, X.; Zhang, Z.; Wu, M.; Zhao, W. Influence of heavy metal materials on magnetic properties of Pt/Co/heavy metal tri-layered structures. *Appl. Phys. Lett.* **2017**, *110*, doi:10.1063/1.4973477.

23. Thiaville, A.; Rohart, S.; Jué, É.; Cros, V.; Fert, A. Dynamics of Dzyaloshinskii domain walls in ultrathin magnetic films. *EPL (Europhysics Lett.)* **2012**, *100*, 57002, doi:10.1209/0295-5075/100/57002.

24. Tetienne, J.-P.; Hingant, T.; Martínez, L. J.; Rohart, S.; Thiaville, A.; Diez, L. H.; Garcia, K.; Adam, J.-P.; Kim, J.-V.; Roch, J.-F.; Miron, I. M.; Gaudin, G.; Vila, L.; Ocker, B.; Ravelosona, D.; Jacques, V. The nature of domain walls in ultrathin ferromagnets revealed by scanning nanomagnetometry. *Nat. Commun.* **2015**, *6*, 6733, doi:10.1038/ncomms7733.

25. Nakatani, Y.; Thiaville, A.; Miltat, J. Head-to-head domain walls in soft nano-strips: A refined phase diagram. *J. Magn. Magn. Mater.* **2005**, *290–291 PA*, 750–753, doi:10.1016/j.jmmm.2004.11.355.

26. Kaplan, B.; Gehring, G. A. The domain structure in ultrathin magnetic films. *J. Mag. Mag. Mat.* **1993**, *128*, 111–116, doi:10.1016/0304-8853(93)90863-W.

27. Nguyen, V. D.; Vila, L.; Marty, A.; Pillet, J. C.; Notin, L.; Beigné, C.; Pizzini, S.; Attané, J. P. Dimensionality effects on the magnetization reversal in narrow FePt nanowires. *Appl. Phys. Lett.* **2012**, *100*, doi:10.1063/1.4721672.

28. Ryu, J.; Choe, S. B.; Lee, H. W. Magnetic domain-wall motion in a nanowire: Depinning and creep. *Phys. Rev. B* **2011**, *84*, 1–12, doi:10.1103/PhysRevB.84.075469.

29. Cayssol, F.; Ravelosona, D.; Chappert, C.; Ferré, J.; Jamet, J. P. Domain Wall Creep in Magnetic Wires. *Phys. Rev. Lett.* **2004**, *92*, 107202–1, doi:10.1103/PhysRevLett.92.107202.

30. Schellekens, a. J.; van den Brink, a.; Franken, J. H.; Swagten, H. J. M.; Koopmans, B. Electric-field control of domain wall motion in perpendicularly magnetized materials. *Nat. Commun.* **2012**, *3*, 847, doi:10.1038/ncomms1848.

31. Franke, K. J. A.; Van de Wiele, B.; Shirahata, Y.; Hämäläinen, S. J.; Taniyama, T.; van Dijken, S. Reversible electric-field-driven magnetic domain-wall motion. *Phys. Rev. X* **2015**, *5*, 1–9, doi:10.1103/PhysRevX.5.011010.

32. Franken, J. H.; Swagten, H. J. M.; Koopmans, B. Shift registers based on magnetic domain wall ratchets with perpendicular anisotropy. *Nat. Nanotechnol.* **2012**, *7*, 499–503,

doi:10.1038/nnano.2012.111.

33. Zhu, J.; Han, Z.; Su, Y.; Hu, J. Energy-imbalance mechanism of domain wall motion induced by propagation spin waves in finite magnetic nanostripe. *J. Magn. Magn. Mater.* **2014**, *369*, 96–100, doi:10.1016/j.jmmm.2014.06.015.

34. Wang, X. G.; Guo, G. H.; Nie, Y. Z.; Wang, D. W.; Zeng, Z. M.; Li, Z. X.; Tang, W. Microwave-assisted domain-wall motion induced by alternating spin-polarized current. *Phys. Rev. B* **2014**, *89*, 2–7, doi:10.1103/PhysRevB.89.144418.

35. Kim, J.-S.; Stärk, M.; Kläui, M.; Yoon, J.; You, C.-Y.; Lopez-Diaz, L.; Martinez, E. Interaction between propagating spin waves and domain walls on a ferromagnetic nanowire. *Phys. Rev. B* **2012**, *85*, 174428, doi:10.1103/PhysRevB.85.174428.

36. Tatara, G.; Kohno, H. Theory of Current-Driven Domain Wall Motion: Spin Transfer versus Momentum Transfer. *Phys. Rev. Lett.* **2004**, *92*, 086601, doi:10.1103/PhysRevLett.92.086601.

37. Kläui, M.; Jubert, P.-O.; Allenspach, R.; Bischof, A.; Bland, J. A. C.; Faini, G.; Rüdiger, U.; Vaz, C. A. F.; Vila, L.; Vouille, C. Direct observation of domain-wall congurations transformed by spin currents. *Phys. Rev. Lett.* **2005**, *95*, 26601.

38. Rubio-Marcos, F.; Campo, A. Del; Marchet, P.; Fernández, J. F. Ferroelectric domain wall motion induced by polarized light. *Nat. Commun.* **2015**, *6*, doi:10.1038/ncomms7594.

39. Schlickeiser, F.; Ritzmann, U.; Hinzke, D.; Nowak, U. Role of entropy in domain wall motion in thermal gradients. *Phys. Rev. Lett.* **2014**, *113*, 1–5, doi:10.1103/PhysRevLett.113.097201.

40. Metaxas, P. J.; Jamet, J. P.; Mougin, A.; Cormier, M.; Ferré, J.; Baltz, V.; Rodmacq, B.; Dieny, B.; Stamps, R. L. Creep and flow regimes of magnetic domain-wall motion in ultrathin Pt/Co/Pt films with perpendicular anisotropy. *Phys. Rev. Lett.* **2007**, *99*, 217208, doi:10.1103/PhysRevLett.99.217208.

41. Cormier, M.; Mougin, A.; Adam, J.; Metaxas, P.; Ferré, J. *Domain wall dynamics in ultrathin films: Size and thickness influence- Application to perpendicularly magnetized films*; Orsay, 2006;

42. Mougin, A.; Cormier, M.; Adam, J. P.; Metaxas, P. J.; Ferré, J. Domain wall mobility, stability and Walker breakdown in magnetic nanowires. *Europhys. Lett.* **2007**, *78*, 57007, doi:10.1209/0295-5075/78/57007.

43. Infante, G.; Varga, R.; Badini-Confalonieri, G. A.; Vázquez, M. Locally induced domain wall damping in a thin magnetic wire. *Appl. Phys. Lett.* **2009**, *95*, 1–4, doi:10.1063/1.3174919.

44. Weindler, T.; Bauer, H. G.; Islinger, R.; Boehm, B.; Chauleau, J. Y.; Back, C. H. Magnetic damping: Domain wall dynamics versus local ferromagnetic resonance. *Phys. Rev. Lett.* **2014**, *113*, 1–5, doi:10.1103/PhysRevLett.113.237204.

45. Glathe, S.; Mattheis, R.; Berkov, D. V. Direct observation and control of the Walker breakdown process during a field driven domain wall motion. *Appl. Phys. Lett.* **2008**, *93*, 1–4, doi:10.1063/1.2975181.

46. Thiaville, A.; García, J. M.; Miltat, J. Domain wall dynamics in nanowires. *J. Magn. Magn. Mater.* **2002**, *242–245*, 1061–1063, doi:10.1016/S0304-8853(01)01353-1.

47. Attané, J. P.; Ravelosona, D.; Marty, A.; Nguyen, V. D.; Vila, L. Coercivity enhancement in FePt nanowires due to the suppression of available paths for domain wall propagation. *Phys. Rev. B* **2011**, *84*, 1–6, doi:10.1103/PhysRevB.84.144418.

48. Chen, T. Y.; Erickson, M. J.; Crowell, P. A.; Leighton, C. Surface roughness dominated pinning mechanism of magnetic vortices in soft ferromagnetic films. *Phys. Rev. Lett.* **2012**, *109*, 1–5, doi:10.1103/PhysRevLett.109.097202.

49. Attané, J. P.; Ravelosona, D.; Marty, A.; Samson, Y.; Chappert, C. Thermally activated depinning of a narrow domain wall from a single defect. *Phys. Rev. Lett.* **2006**, *96*, 1–4, doi:10.1103/PhysRevLett.96.147204.

50. Lemerle, S.; Ferré, J.; Chappert, C.; Mathet, V.; Giamarchi, T.; Le Doussal, P. Domain Wall Creep in an Ising Ultrathin Magnetic Film. *Phys. Rev. Lett.* **1998**, *80*, 849–852, doi:10.1103/PhysRevLett.80.849.

51. Diaz Pardo, R.; Savero Torres, W.; Kolton, A. B.; Bustingorry, S.; Jeudy, V. Universal depinning transition of domain walls in ultrathin ferromagnets. *Phys. Rev. B* **2017**, *95*, 1–7, doi:10.1103/PhysRevB.95.184434.

52. Ralph, D. C.; Stiles, M. D. Spin transfer torques. *J. Magn. Magn. Mater.* **2008**, *320*, 1190–1216, doi:10.1016/j.jmmm.2007.12.019.

53. Slonczewski, J. C. Currents, torques, and polarization factors in magnetic tunnel junctions. *Phys. Rev. B* **2005**, *71*, 1–10, doi:10.1103/PhysRevB.71.024411.

54. Slonczewski, J. C. Current-driven excitation of magnetic multilayers. *J. Magn. Magn. Mater.* **1996**, *159*, L1–L7, doi:10.1016/0304-8853(96)00062-5.

55. Yamanouchi, M.; Chiba, D.; Matsukura, F.; Ohno, H. Current-induced domain wall switching in a

ferromagnetic semiconductor structure. *Nature* **2004**, *428*, 539–542, doi:10.1038/nature02425.1.

56. Berger, L. Domain drag effect in the presence of variable magnetic field or variable transport current. *J. Appl. Phys.* **1979**, *50*, 2137–2139, doi:10.1063/1.327083.
57. Berger, L. Low-field magnetoresistance and domain drag in ferromagnets. *J. Appl. Phys.* **1978**, *49*, 2156–2161, doi:10.1063/1.324716.
58. Freitas, P. P.; Berger, L. Observation of s-d exchange force between domain walls and electric current in very thin Permalloy films. *J. Appl. Phys.* **1985**, *57*, 1266–1269, doi:10.1063/1.334524.
59. Hung, C. Y.; Berger, L. Exchange forces between domain wall and electric current in permalloy films of variable thickness. *J. Appl. Phys.* **1988**, *63*, 4276–4278, doi:10.1063/1.340201.
60. Li, Z.; Zhang, S. Domain-wall dynamics driven by adiabatic spin-transfer torques. *Phys. Rev. B* **2004**, *70*, 1–10, doi:10.1103/PhysRevB.70.024417.
61. Boulle, O.; Malinowski, G.; Klaui, M. Current-induced domain wall motion in nanoscale ferromagnetic elements. *Mater. Sci. Eng. R Reports* **2011**, *72*, 159–187, doi:10.1016/j.mser.2011.04.001.
62. Zhang, J.; Levy, P. M.; Zhang, S.; Antropov, V. Identification of transverse spin currents in noncollinear magnetic structures. *Phys. Rev. Lett.* **2004**, *93*, 2–5, doi:10.1103/PhysRevLett.93.256602.
63. Thiaville, A.; Nakatani, Y.; Miltat, J.; Suzuki, Y. Micromagnetic understanding of current-driven domain wall motion in patterned nanowires. **2004**, *990*, doi:10.1209/epl/i2004-10452-6.
64. Hayashi, M.; Thomas, L.; Rettner, C.; Moriya, R.; Bazaliy, Y. B.; Parkin, S. S. P. Current driven domain wall velocities exceeding the spin angular momentum transfer rate in permalloy nanowires. *Phys. Rev. Lett.* **2007**, *98*, 1–4, doi:10.1103/PhysRevLett.98.037204.
65. Yamanouchi, M. Universality Classes for Domain Wall. *Cell* **2008**, *1726*, 1–5, doi:10.1126/science.1145516.
66. DuttaGupta, S.; Fukami, S.; Zhang, C.; Sato, H.; Yamanouchi, M.; Matsukura, F.; Ohno, H. Adiabatic spin-transfer-torque-induced domain wall creep in a magnetic metal. *Nat. Phys.* **2016**, *12*, 333–336, doi:10.1038/nphys3593.
67. Duine, R. A.; Smith, C. M. Creep of current-driven domain-wall lines: Effects of intrinsic versus extrinsic pinning. *Phys. Rev. B* **2008**, *77*, 1–6, doi:10.1103/PhysRevB.77.094434.
68. Gambardella, P.; Miron, I. M. Current-induced spin-orbit torques. *Philos. Trans. R. Soc. A Math.*

Phys. Eng. Sci. **2011**, *369*, 3175–3197, doi:10.1098/rsta.2010.0336.

69. Sinova, J.; Valenzuela, S. O.; Wunderlich, J.; Back, C. H.; Jungwirth, T. Spin Hall effects. *Rev. Mod. Phys.* **2015**, *87*, 1213–1260, doi:10.1103/RevModPhys.87.1213.
70. Miron, I. M.; Moore, T.; Szambolics, H.; Buda-Prejbeanu, L. D.; Auffret, S.; Rodmacq, B.; Pizzini, S.; Vogel, J.; Bonfim, M.; Schuhl, A.; Gaudin, G. Fast current-induced domain-wall motion controlled by the Rashba effect. *Nat. Mater.* **2011**, *10*, 419–423, doi:10.1038/nmat3020.
71. Ryu, K.-S.; Thomas, L.; Yang, S.-H.; Parkin, S. Chiral spin torque at magnetic domain walls. *Nat. Nanotechnol.* **2013**, *8*, 527–533, doi:10.1038/nnano.2013.102.
72. Emori, S.; Bauer, U.; Ahn, S.-M.; Martinez, E.; Beach, G. S. D. Current-driven dynamics of chiral ferromagnetic domain walls. *Nat. Mater.* **2013**, *12*, 611–616, doi:10.1038/nmat3675.
73. Khvalkovskiy, A. V.; Cros, V.; Apalkov, D.; Nikitin, V.; Krounbi, M.; Zvezdin, K. A.; Anane, A.; Grollier, J.; Fert, A. Matching domain-wall configuration and spin-orbit torques for efficient domain-wall motion. *Phys. Rev. B* **2013**, *87*, 2–6, doi:10.1103/PhysRevB.87.020402.
74. Perez, N.; Martinez, E.; Torres, L.; Woo, S. H.; Emori, S.; Beach, G. S. D. Chiral magnetization textures stabilized by the Dzyaloshinskii-Moriya interaction during spin-orbit torque switching. *Appl. Phys. Lett.* **2014**, *104*, 092403, doi:10.1063/1.4867199.
75. Liu, L.; Pai, C.-F.; Li, Y.; Tseng, H. W.; Ralph, D. C.; Buhrman, R. A. Spin-Torque Switching with the Giant Spin Hall Effect of Tantalum. *Science* **2012**, *336*, 555–558, doi:10.1126/science.1218197.
76. Haazen, P. P. J.; Murè, E.; Franken, J. H.; Lavrijsen, R.; Swagten, H. J. M.; Koopmans, B. Domain wall depinning governed by the spin Hall effect. *Nat. Mater.* **2013**, *12*, 299–303, doi:10.1038/nmat3553.
77. Ramu, M.; Goolaup, S.; Gan, W. L.; Krishnia, S.; Lim, G. J.; Lew, W. S. Spin orbit torque induced asymmetric depinning of chiral Néel domain wall in Co/Ni heterostructures. *Appl. Phys. Lett.* **2017**, *110*, doi:10.1063/1.4980120.
78. Torrejon, J.; Kim, J.; Sinha, J.; Mitani, S.; Hayashi, M.; Yamanouchi, M.; Ohno, H. Interface control of the magnetic chirality in CoFeB/MgO heterostructures with heavy-metal underlayers. *Nat. Commun.* **2014**, *5*, 1–8, doi:10.1038/ncomms5655.
79. Boulle, O.; Rohart, S.; Buda-Prejbeanu, L. D.; Jué, E.; Miron, I. M.; Pizzini, S.; Vogel, J.; Gaudin, G.; Thiaville, A. Domain Wall Tilting in the Presence of the Dzyaloshinskii-Moriya Interaction in Out-of-Plane Magnetized Magnetic Nanotracks. *Phys. Rev. Lett.* **2013**, *111*, 217203,

doi:10.1103/PhysRevLett.111.217203.

80. Ryu, K. S.; Thomas, L.; Yang, S. H.; Parkin, S. S. P. Current induced tilting of domain walls in high velocity motion along perpendicularly magnetized micron-sized Co/Ni/Co racetracks. *Appl. Phys. Express* **2012**, *5*, 1–3, doi:10.1143/APEX.5.093006.
81. Kim, K. W.; Lee, H. W. Thermal fluctuation field for current-induced domain wall motion. *Phys. Rev. B* **2010**, *82*, 1–16, doi:10.1103/PhysRevB.82.134431.
82. Yang, S. H.; Ryu, K. S.; Parkin, S. Domain-wall velocities of up to 750 m s-1driven by exchange-coupling torque in synthetic antiferromagnets. *Nat. Nanotechnol.* **2015**, *10*, 221–226, doi:10.1038/nnano.2014.324.
83. Thomas, L.; Hayashi, M.; Jiang, X.; Moriya, R.; Rettner, C.; Parkin, S. S. P. Oscillatory dependence of current-driven magnetic domain wall motion on current pulse length. *Nature* **2006**, *443*, 197–200, doi:10.1038/nature05093.
84. Martinez, E.; Emori, S.; Beach, G. S. D. Current-driven domain wall motion along high perpendicular anisotropy multilayers: The role of the Rashba field, the spin Hall effect, and the Dzyaloshinskii-Moriya interaction. *Appl. Phys. Lett.* **2013**, *103*, doi:10.1063/1.4818723.
85. Boulle, O.; Buda-Prejbeanu, L. D.; Jué, E.; Miron, I. M.; Gaudin, G. Current induced domain wall dynamics in the presence of spin orbit torques. *J. Appl. Phys.* **2014**, *115*, 17D502, doi:10.1063/1.4860946.
86. Martinez, E.; Emori, S.; Perez, N.; Torres, L.; Beach, G. S. D. Current-driven dynamics of Dzyaloshinskii domain walls in the presence of in-plane fields: Full micromagnetic and one-dimensional analysis. *J. Appl. Phys.* **2014**, *115*, 213909, doi:10.1063/1.4881778.
87. Peng, S.; Wang, M.; Yang, H.; Zeng, L.; Nan, J.; Zhou, J.; Zhang, Y.; Hallal, A.; Chshiev, M.; Wang, K. L.; Zhang, Q.; Zhao, W. Origin of interfacial perpendicular magnetic anisotropy in MgO/CoFe/metallic capping layer structures. *Sci. Rep.* **2015**, *5*, 3–8, doi:10.1038/srep18173.
88. Peng, S.; Zhao, W.; Qiao, J.; Su, L.; Zhou, J.; Yang, H.; Zhang, Q.; Zhang, Y.; Grezes, C.; Amiri, P. K.; Wang, K. L. Giant interfacial perpendicular magnetic anisotropy in MgO/CoFe/capping layer structures. *Appl. Phys. Lett.* **2017**, *110*, doi:10.1063/1.4976517.
89. Yang, H. X.; Chshiev, M.; Dieny, B.; Lee, J. H.; Manchon, A.; Shin, K. H. First-principles investigation of the very large perpendicular magnetic anisotropy at Fe|MgO and Co|MgO interfaces. *Phys. Rev. B* **2011**, *84*, 1–5, doi:10.1103/PhysRevB.84.054401.

90. Burrowes, C.; Vernier, N.; Adam, J.-P.; Herrera Diez, L.; Garcia, K.; Barisic, I.; Agnus, G.; Eimer, S.; Kim, J.-V.; Devolder, T.; Lamperti, A.; Mantovan, R.; Ockert, B.; Fullerton, E. E.; Ravelosona, D. Low depinning fields in Ta-CoFeB-MgO ultrathin films with perpendicular magnetic anisotropy. *Appl. Phys. Lett.* **2013**, *103*, 182401, doi:10.1063/1.4826439.

91. Paluskar, P. V.; Kohlhepp, J. T.; Swagten, H. J. M.; Koopmans, B. Co[sub 72]Fe[sub 20]B[sub 8]: Structure, magnetism, and tunneling spin polarization. *J. Appl. Phys.* **2006**, *99*, 08E503, doi:10.1063/1.2163328.

92. Swagten, H. J. M.; Paluskar, P. V.; Lavrijsen, R.; Kohlhepp, J. T.; Koopmans, B. Tunneling spin polarization and annealing of Co72Fe20B8. *J. Magn. Magn. Mater.* **2007**, *310*, 2012–2014, doi:10.1016/j.jmmm.2006.10.921.

93. Paluskar, P. V.; Kohlhepp, J. T.; Swagten, H. J. M.; Koopmans, B.; Wolters, R.; Boeve, H.; Snoeck, E. Influence of interface structure on the tunnelling spin polarization of CoFeB alloys. *J. Phys. D. Appl. Phys.* **2007**, *40*, 1234–1237, doi:10.1088/0022-3727/40/5/S04.

94. Vansteenkiste, A.; Leliaert, J.; Dvornik, M.; Helsen, M.; Garcia-Sanchez, F.; Van Waeyenberge, B. The design and verification of MuMax3. *AIP Adv.* **2014**, *4*, 107133, doi:10.1063/1.4899186.

95. Catalan, G.; Seidel, J.; Ramesh, R.; Scott, J. F. Domain wall nanoelectronics. *Rev. Mod. Phys.* **2012**, *84*, 119–156, doi:10.1103/RevModPhys.84.119.

96. Negulescu, B.; Lacour, D.; Montaigne, F.; Gerken, A.; Paul, J.; Spetter, V.; Marien, J.; Duret, C.; Hehn, M. Wide range and tunable linear magnetic tunnel junction sensor using two exchange pinned electrodes. *Appl. Phys. Lett.* **2009**, *95*, 112502, doi:10.1063/1.3226676.

97. Ripka, P.; Janosek, M. Advances in Magnetic Field Sensors. *IEEE Sens. J.* **2010**, *10*, 1108–1116, doi:10.1109/JSEN.2010.2043429.

98. Lenz, J.; Edelstein, S. Magnetic sensors and their applications. *IEEE Sens. J.* **2006**, *6*, 631–649, doi:10.1109/JSEN.2006.874493.

99. Guo, Y.; Deng, Y.; Wang, S. X. Multilayer anisotropic magnetoresistive angle sensor. *Sensors Actuators, A Phys.* **2017**, *263*, 159–165, doi:10.1016/j.sna.2017.06.001.

100. Guo, Y.; Ouyang, Y.; Sato, N.; Ooi, C. C.; Wang, S. X. Exchange-Biased Anisotropic Magnetoresistive Field Sensor. *IEEE Sens. J.* **2017**, *17*, 3309–3315, doi:10.1109/JSEN.2017.2695238.

101. Koch, R. H.; Deak, J. G.; Grinstein, G. Fundamental limits to magnetic-field sensitivity of flux-

gate magnetic-field sensors. *Appl. Phys. Lett.* **1999**, *75*, 3862–3864, doi:10.1063/1.125481.

102. Sander, D.; Valenzuela, S. O.; Makarov, D.; Marrows, C. H.; Fullerton, E. E.; Fischer, P.; McCord, J.; Vavassori, P.; Mangin, S.; Pirro, P.; Hillebrands, B.; Kent, A. D.; Jungwirth, T.; Gutfleisch, O.; Kim, C. G.; Berger, A. The 2017 Magnetism Roadmap. *J. Phys. D. Appl. Phys.* **2017**, *50*, 363001, doi:10.1088/1361-6463/aa81a1.
103. Wisniowski, P.; Dabek, M.; Wrona, J. Field noise in tunneling magnetoresistance sensors with variable sensitivity. *Appl. Phys. Lett.* **2015**, *106*, 052404, doi:10.1063/1.4907621.
104. Pérez, N.; Melzer, M.; Makarov, D.; Ueberschär, O.; Ecke, R.; Schulz, S. E.; Schmidt, O. G. High-performance giant magnetoresistive sensorics on flexible Si membranes. *Appl. Phys. Lett.* **2015**, *106*, 153501, doi:10.1063/1.4918652.
105. Jogschies, L.; Klaas, D.; Kruppe, R.; Rittinger, J.; Taptimthong, P.; Wienecke, A.; Rissing, L.; Wurz, M. C. Recent developments of magnetoresistive sensors for industrial applications. *Sensors* **2015**, *15*, 28665–28689, doi:10.3390/s151128665.
106. Mancoff, F. B.; Dunn, J. H.; Clemens, B. M.; White, R. L. A giant magnetoresistance sensor for high magnetic field measurements. *Appl. Phys. Lett.* **2000**, *77*, 1879–1881, doi:10.1063/1.1311316.
107. Parkin, S. S. P. Flexible giant magnetoresistance sensors. *Appl. Phys. Lett.* **1996**, *69*, 3092–3094, doi:10.1063/1.117315.
108. Inomata, K. Giant magnetoresistance and its sensor applications. *J. Electroceramics* **1998**, *2*, 283–293, doi:10.1023/A:1009930724459.
109. Multiturn Sensor Series RSM2800 analogue Preliminary data sheet Available online: https://www.novotechnik.de/en/products/rotary-sensors/ (accessed on Jan 22, 2018).
110. Heinze, D.; Borie, B.; Grimm, H.; Wahrhusen, J.; Kläui, M. Angular dependence of the domain wall depinning field in sensors with segmented corners. *J. Phys. Conf. Ser.* **2017**, *903*, 012053, doi:10.1088/1742-6596/903/1/012053.
111. Borie, B.; Kehlberger, A.; Wahrhusen, J.; Grimm, H.; Kläui, M. Geometrical dependence of domain-wall propagation and nucleation fields in magnetic-domain-wall sensors. *Phys. Rev. Appl.* **2017**, *8*, 024017, doi:10.1103/PhysRevApplied.8.024017.
112. Zhao, W. S.; Zhang, Y.; Klein, J.; Wang, Z. H.; Ravelosona, D. Design and Analysis of Racetrack Memory Based on Magnetic Domain Wall Motion in Nanowires. **2014**, 71–76.
113. Thomas, L.; Yang, S.-H.; Ryu, K.-S.; Hughes, B.; Rettner, C.; Wang, D.-S.; Tsai, C.-H.; Shen, K.-

H.; Parkin, S. S. P. Racetrack Memory: A high-performance, low-cost, non-volatile memory based on magnetic domain walls. *Electron Devices Meet. (IEDM), 2011 IEEE Int.* **2011**, 24–24.2.4, doi:10.1109/IEDM.2011.6131603.

114. Zhang, Y.; Zhao, W.; Klein, J. O.; Ravelsona, D.; Chappert, C. Ultra-high density content addressable memory based on current induced domain wall motion in magnetic track. *IEEE Trans. Magn.* **2012**, *48*, 3219–3222, doi:10.1109/TMAG.2012.2198876.

115. Yang, S.-H.; Ryu, K.-S.; Parkin, S. Domain-wall velocities of up to 750 m s−1 driven by exchange-coupling torque in synthetic antiferromagnets. *Nat. Nanotechnol.* **2015**, *10*, 221–226, doi:10.1038/nnano.2014.324.

116. Kerr, J. XLIII. On rotation of the plane of polarization by reflection from the pole of a magnet. *Philos. Mag. Ser. 5* **1877**, *3*, 321–343, doi:10.1080/14786447708639245.

117. Weinberger, P. John Kerr and his effects found in 1877 and 1878. *Philos. Mag. Lett.* **2008**, *88*, 897–907, doi:10.1080/09500830802526604.

118. Qiu, Z. Q.; Bader, S. D. Surface magneto-optic Kerr effect (SMOKE). *J. Magn. Magn. Mater.* **1999**, *200*, 664–678, doi:10.1016/S0304-8853(99)00311-X.

119. Oakberg, T. Magneto-optic Kerr effect Available online: http://www.hindsinstruments.com/wp-content/uploads/Magneto-Optic-Kerr-Effect.pdf.

120. Ali, M. Growth And Study Of Magnetostrictive FeSiBC Thin Films For Device Applications, The University of Sheffield, 1999.

121. Moog, E. R.; Liu, C.; Bader, S. D.; Zak, J. Thickness and polarization dependence of the magnetooptic signal from ultrathin ferromagnetic films. *Phys. Rev. B* **1989**, *39*, 6949–6956, doi:10.1103/PhysRevB.39.6949.

122. Ram, S.; Ward, E. S.; Ober, R. J. Beyond Rayleigh’s criterion: A resolution measure with application to single-molecule microscopy. *Proc. Natl. Acad. Sci.* **2006**, *103*, 4457–4462, doi:10.1073/pnas.0508047103.

123. Walker, J. G. Optical imaging with resolution exceeding the rayleigh criterion. *Opt. Acta (Lond).* **1983**, *30*, 1197–1202, doi:10.1080/713821367.

124. Schmitt, O.; Steil, D.; Alebrand, S.; Ganss, F.; Hehn, M.; Mangin, S.; Albrecht, M.; Mathias, S.; Cinchetti, M.; Aeschlimann, M. Kerr and Faraday microscope for space- and time-resolved studies. *Eur. Phys. J. B* **2014**, *87*, 219, doi:10.1140/epjb/e2014-50257-3.

125. Sugawara, E.; Nikaido, H. *Modern Techniques for Characterizing Magnetic Materials*; Zhu, Y., Ed.; Springer-Verlag: New York, 2005; Vol. 58; ISBN 1-4020-8007-7.

126. 徐國誠 圓形載流線圈的磁場與電感. 科學教育月刊 **2012**, 21–30.

127. Chikazumi, S.; Tanuma, S.; Oguro, I.; Ono, F.; Tajima, K. Production of Pulse Magnetic Fields Higher Than 400 kOe and Their Applications to Various Magnetic Measurements. *IEEE Trans. Magn.* **1969**, *5*, 265–268, doi:10.1109/TMAG.1969.1066538.

128. Rezal, M.; Ishak, D.; Sabri, M. High voltage magnetic pulse generation using capacitor discharge technique. *Alexandria Eng. J.* **2014**, *53*, 803–808, doi:10.1016/j.aej.2014.10.001.

129. Jiang, W.; Upadhyaya, P.; Zhang, W.; Yu, G.; Jungfleisch, M. B.; Fradin, F. Y.; Pearson, J. E.; Tserkovnyak, Y.; Wang, K. L.; Heinonen, O.; te Velthuis, S. G. E.; Hoffmann, A. Blowing magnetic skyrmion bubbles. *Science* **2015**, *349*, 283–286, doi:10.1126/science.aaa1442.

130. Sangiao, S.; Viret, M. Electrical detection of internal dynamical properties of domain walls. *Phys. Rev. B* **2014**, *89*, 104412, doi:10.1103/PhysRevB.89.104412.

131. O’Shea, K. J.; Tracey, J.; Bramsiepe, S.; Stamps, R. L. Probing nanowire edge roughness using an extended magnetic domain wall. *Appl. Phys. Lett.* **2013**, *102*, 062409, doi:10.1063/1.4792314.

132. Burrowes, C.; Mihai, a. P.; Ravelosona, D.; Kim, J.-V.; Chappert, C.; Vila, L.; Marty, a.; Samson, Y.; Garcia-Sanchez, F.; Buda-Prejbeanu, L. D.; Tudosa, I.; Fullerton, E. E.; Attané, J.-P. Non-adiabatic spin-torques in narrow magnetic domain walls. *Nat. Phys.* **2010**, *6*, 17–21, doi:10.1038/nphys1436.

133. Akhatov, I.; Gumerov, N.; Ohl, C. D.; Parlitz, U.; Lauterborn, W. The Role of Surface Tension in Stable Single-Bubble Sonoluminescence. *Phys. Rev. Lett.* **1997**, *78,* 227, doi:10.1103/PhysRevLett.78.227.

134. Isenberg, C. *The Science of Soap Films and Soap Bubbles*; 2nd ed.; DOVER PUBLICATIONS, INC.: New York, 1992; ISBN 0486269604.

135. Gaunt, P. The frequency constant for thermal activitation of a ferromagnetic domain wall. *J. Appl. Phys.* **1977**, *48*, 3470–3474, doi:10.1063/1.324195.

136. de Gennes, P.-G.; Brochard-Wyart, F.; Quéré, D. *Capillarity and Wetting Phenomena*; Reisinger, A., Ed.; Springer-Verlag NewYork, Inc.: New York, 2004; ISBN 978-1-4419-1833-8.

137. Purcell, E. *Electricity and magnetism*; 1rt ed.; McGraw-Hill book company: New York, 1963; Vol. 2nd; ISBN 1107014026.

138. You, C.-Y. Dependence of the switching current density on the junction sizes in spin transfer torque. *Appl. Phys. Express* **2012**, *5*, 103001, doi:10.1063/1.4792728.
139. Bilzer, C.; Devolder, T.; Kim, J.-V.; Counil, G.; Chappert, C.; Cardoso, S.; Freitas, P. P. Study of the dynamic magnetic properties of soft CoFeB films. *J. Appl. Phys.* **2006**, *100*, 053903, doi:10.1063/1.2337165.
140. Video:Laplace Pressure Available online: https://www.youtube.com/watch?v=ZRVxr4-gls8.
141. Zhang, X.; Vernier, N.; Zhao, W.; Yu, H.; Vila, L.; Ravelosona, D. Direct observation of domain wall surface tension by deflating or inflating a magnetic bubble. *arXiv* **2017**, doi:https://aps.arxiv.org/abs/1708.06719.
142. Wang, G. A.; Masuda, Y.; Kato, T.; Iwata, S. Design and performance of domain wall displacing-type field sensors using a magnetic tunnel junction and a giant magnetoresistive device. *J. Phys. D. Appl. Phys.* **2010**, *43*, 455001, doi:10.1088/0022-3727/43/45/455001.
143. Nakatani, Y.; Thiaville, A.; Miltat, J. Faster magnetic walls in rough wires. *Nat. Mater.* **2003**, *2*, 521–523, doi:10.1038/nmat931.
144. Chauve, P.; Giamarchi, T.; Le Doussal, P. Creep and depinning in disordered media. *Phys. Rev. B* **2000**, *62*, 6241–6267, doi:10.1103/PhysRevB.62.6241.
145. Vogel, A.; Wintz, S.; Kimling, J.; Bolte, M.; Strache, T.; Fritzsche, M.; Im, M. Y.; Fischer, P.; Meier, G.; Fassbender, J. Domain-wall pinning and depinning at soft spots in magnetic nanowires. *IEEE Trans. Magn.* **2010**, *46*, 1708–1710, doi:10.1109/TMAG.2010.2042285.
146. Tetienne, J.-P.; Hingant, T.; Kim, J.- V.; Diez, L. H.; Adam, J.-P.; Garcia, K.; Roch, J.-F.; Rohart, S.; Thiaville, A.; Ravelosona, D.; Jacques, V. Nanoscale imaging and control of domain-wall hopping with a nitrogen-vacancy center microscope. *Science* **2014**, *344*, 1366–1369, doi:10.1126/science.1250113.
147. Beach, G. S. D.; Knutson, C.; Nistor, C.; Tsoi, M.; Erskine, J. L. Nonlinear domain-wall velocity enhancement by spin-polarized electric current. *Phys. Rev. Lett.* **2006**, *97*, 8–11, doi:10.1103/PhysRevLett.97.057203.
148. Hayashi, M.; Thomas, L.; Bazaliy, Y. B.; Rettner, C.; Moriya, R.; Jiang, X.; Parkin, S. S. P. Influence of current on field-driven domain wall motion in permalloy nanowires from time resolved measurements of anisotropic magnetoresistance. *Phys. Rev. Lett.* **2006**, *96*, 25–28, doi:10.1103/PhysRevLett.96.197207.

149. Le Gall, S.; Vernier, N.; Montaigne, F.; Thiaville, A.; Sampaio, J.; Ravelosona, D.; Mangin, S.; Andrieu, S.; Hauet, T. Effect of spin transfer torque on domain wall motion regimes in [Co/Ni] superlattice wires. *Phys. Rev. B* **2017**, *95*, 184419, doi:10.1103/PhysRevB.95.184419.

150. Cho, S.; Baek, S.-H. C.; Lee, K.-D.; Jo, Y.; Park, B.-G. Large spin Hall magnetoresistance and its correlation to the spin-orbit torque in W/CoFeB/MgO structures. *Sci. Rep.* **2015**, *5*, 14668, doi:10.1038/srep14668.

151. Huang, S. X.; Chen, T. Y.; Chien, C. L. Spin polarization of amorphous CoFeB determined by point-contact Andreev reflection. *Appl. Phys. Lett.* **2008**, *92*, 242509, doi:10.1063/1.2949740.

152. Vansteenkiste, A.; De Wiele, B. Van MUMAX: A new high-performance micromagnetic simulation tool. *J. Magn. Magn. Mater.* **2011**, *323*, 2585–2591, doi:10.1016/j.jmmm.2011.05.037.

153. Gaunt, P. Ferromagnetic domain wall pinning by a random array of inhomogeneities. *Philos. Mag. Part B* **1983**, *48*, 261–276, doi:10.1080/13642818308228288.

154. Zhang, C.; Sun, G.; Zhang, X.; Zhang, W.; Zhao, W.; Wang, T.; Liang, Y.; Liu, Y.; Wang, Y.; Shu, J. Hi-fi Playback:Tolerating position errors in shift operations of racetrack memory. In *42nd Annu. Int. Symp. Comput. Archit. - ISCA '15*; 2015; pp. 694–706.

155. Worledge, D. C.; Hu, G.; Abraham, D. W.; Sun, J. Z.; Trouilloud, P. L.; Nowak, J.; Brown, S.; Gaidis, M. C.; O'Sullivan, E. J.; Robertazzi, R. P. Spin torque switching of perpendicular Ta|CoFeB|MgO-based magnetic tunnel junctions. *Appl. Phys. Lett.* **2011**, *98*, 96–99, doi:10.1063/1.3536482.

156. Torrejon, J.; Martinez, E.; Hayashi, M. Tunable inertia of chiral magnetic domain walls. *Nat. Commun.* **2016**, *7*, 1–7, doi:10.1038/ncomms13533.

157. Thomas, L.; Moriya, R.; Rettner, C.; Parkin, S. S. P. Dynamics of Magnetic Domain Walls Under Their Own Inertia. *Science* **2010**, *330*, 1810–1813, doi:10.1126/science.1197468.

158. Zhang, Y.; Zhao, W. Ultra-High Density Content Addressable Memory Based on Current Induced Domain Wall Motion in Magnetic Track. *IEEE Trans. Magn.* **2012**, *48*, 3219–3222, doi:10.1109/TMAG.2012.2198876.

159. Vanatka, M.; Rojas-Sanchez, J.-C.; Vogel, J.; Bonfim, M.; Thiaville, A.; Pizzini, S. Velocity asymmetry of Dzyaloshinskii domain walls in the creep and flow regimes. **2015**, *326002*, doi:10.1088/0953-8984/27/32/326002.

160. Ha Pham, T.; Vogel, J.; Sampaio, J.; Vaňatka, M.; Rojas-Sánchez, J.-C.; Bonfim, M.; Chaves, D.

S.; Choueikani, F.; Ohresser, P.; Otero, E.; Thiaville, A.; Pizzini, S. Very large domain wall velocities in Pt/Co/GdOx and Pt/Co/Gd trilayers with Dzyaloshinskii-Moriya interaction. *EPL (Europhysics Lett.)* **2016**, *113*, 67001, doi:10.1209/0295-5075/113/67001.

161. Liu, X.; Steiner, M. M.; Sooryakumar, R.; Prinz, G. A.; Farrow, R. F. C.; Harp, G. Exchange stiffness, magnetization, and spin waves in cubic and hexagonal phases of cobalt. *Phys. Rev. B* **1996**, *53*, 12166–12172, doi:10.1103/PhysRevB.53.12166.
162. Eyrich, C.; Huttema, W.; Arora, M.; Montoya, E.; Rashidi, F.; Burrowes, C.; Kardasz, B.; Girt, E.; Heinrich, B.; Mryasov, O. N.; From, M.; Karis, O. Exchange stiffness in thin film Co alloys. *J. Appl. Phys.* **2012**, *111*, 2012–2015, doi:10.1063/1.3679433.
163. Cho, J.; Jung, J.; Cho, S. Y.; You, C. Y. Effect of annealing temperature on exchange stiffness of CoFeB thin films. *J. Magn. Magn. Mater.* **2015**, *395*, 18–22, doi:10.1016/j.jmmm.2015.06.073.
164. Klingler, S.; Chumak, A.; Mewes, T.; Khodadadi, B.; Mewes, C.; Dubs, C.; Surzhenko, O.; Hillebrands, B.; Conca, A. Measurements of the exchange stiffness of YIG films using broadband ferromagnetic resonance techniques. *J. Phys. D. Appl. Phys.* **2015**, *48*, 15001, doi:10.1088/0022-3727/48/1/015001.
165. Devolder, T.; Kim, J. V.; Nistor, L.; Sousa, R.; Rodmacq, B.; Diény, B. Exchange stiffness in ultrathin perpendicularly magnetized CoFeB layers determined using the spectroscopy of electrically excited spin waves. *J. Appl. Phys.* **2016**, *120*, doi:10.1063/1.4967826.
166. Rohart, S.; Thiaville, A. Skyrmion confinement in ultrathin film nanostructures in the presence of Dzyaloshinskii-Moriya interaction. *Phys. Rev. B* **2013**, *88*, 184422, doi:10.1103/PhysRevB.88.184422.
167. Miccoli, I.; Edler, F.; Pfnür, H.; Tegenkamp, C. The 100th anniversary of the four-point probe technique: the role of probe geometries in isotropic and anisotropic systems. *J. Phys. Condens. Matter* **2015**, *27*, 223201, doi:10.1088/0953-8984/27/22/223201.
168. Cormier, M.; Mougin, A.; Ferré, J.; Thiaville, A.; Charpentier, N.; Piéchon, F.; Weil, R.; Baltz, V.; Rodmacq, B. Effect of electrical current pulses on domain walls in Pt/Co/Pt nanotracks with out-of-plane anisotropy: Spin transfer torque versus Joule heating. *Phys. Rev. B* **2010**, *81*, 024407, doi:10.1103/PhysRevB.81.024407.
169. Chen, Y.-T.; Hsieh, W. H. Thermal, magnetic, electric, and adhesive properties of amorphous Co60Fe20B20 thin films. *J. Alloys Compd.* **2013**, *552*, 283–288, doi:10.1016/j.jallcom.2012.09.112.

170. Chen, Y.-T.; Xie, S. M. Magnetic and Electric Properties of Amorphous Co40Fe40B20 Thin Films. *J. Nanomater*. **2012**, *2012*, 1–5, doi:10.1155/2012/486284.

171. Kettler, W. Electrical resistivity and thermopower of amorphous FexCo80−xB20 alloys. *J. Appl. Phys.* **1982**, *53*, 8248, doi:10.1063/1.330297.

Appendices

Appendix 1: Mathematic demonstration of the expression of Laplace pressure in magnetism and the associated DW behavior

Here, we provide an analytical calculation to study the behavior of a DW with surface energy γ when it is pinned by hard pinning sites and to give a new demonstration of the Laplace pressure.

- **DW pinned in two terminals**

Supposing a segment of DW whose two terminals are pinned by two hard pinning sites in (x1,y1) and (x2,y2). A field H_{app} is applied along z-axis. In this model, only the DW surface energy and the Zeeman energy due to H_{app} are considered. And the pinning sites are supposed to be strong enough so that the two endpoints of the DWs are never depinned. To simplify the analysis, except for the two strong pinning defects at the endpoints, the other defects are assumed to be so weak, so that the film can be considered as perfect. About pinning force, it means we assume a perfect film without any pinning defect except the two endpoint.

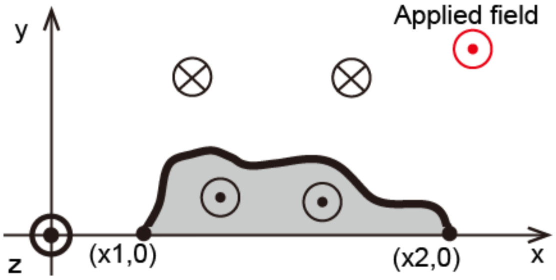

Figure 0-1 Sketch showing a segment of DW (black line) pinned by two hard pinning sites (x1,0) and (x2, 0).

We may suppose the trajectory of DW can be described by a function y=f(x), with the two endpoints pinned at (x1, 0) and (x2, 0). To simplify the problem, we assume that the y=f(x) is a single mapping function in [x1,x2]. Zeeman energy is proportional to the area of inversed domains,

$$E_z(f) = -2\mu_0 H_{app} M_S t_M S = -2\mu_0 H_{app} M_S t_M \int_{x1}^{x2} f(x)dx \tag{0-1}$$

DW interfacial energy is proportional to the length of DW, writing,

$$E_\gamma(f') = \gamma_{DW} t_M L = \gamma_{DW} t_M \int_{x1}^{x2} \sqrt{1+f'(x)^2}dx \tag{0-2}$$

Where $f'(x)$ is the derivative of $f(x)$. The total free energy is

$$E(f,f') = -2\mu_0 H_{app} M_S t \int_{x2}^{x2} f(x)dx + \gamma_{DW} t \int_{x1}^{x2} \sqrt{1+f'(x)^2}dx \tag{0-3}$$

where Ms is saturation magnetization, t_M is thickness of magnetic layer.

In equilibrium state, the curve function of DW should be the function minimizing the free energy of system, i.e,

$$\hat{f}(x) = \left\{ f(x) \in G \middle| E\left(\hat{f},\hat{f}'\right) = \min_{f\in G} E(f,f') \right\} \tag{0-4}$$

where G $= \{f(x) | f(x) \in C^1(x1, x2)\ and\ f(x1) = 0, f(x2) = 0\}$ is a set of function.

Now we try to solve Eq. (0-4).

To simplify, supposing

$$e(f(x), f'(x)) = -2\mu_0 H_{app} M_S t\, f(x) + \gamma_{DW} t\sqrt{1 + f'(x)^2} \tag{0-5}$$

Then $E(f, f') = \int_{x1}^{x2} e(f(x), f'(x))dx$

If $f(x) \in G$, $g(x) \in G$ and $\lambda \in R$, (here R indicates the set of real numbers), then $f(x) + \lambda g(x) \in G$. If $\hat{f}(x) \in G$ is the solution of Eq.(0-4), an essential condition is

$$\left.\frac{\partial E(\hat{f}+\lambda g, \hat{f}'+\lambda g')}{\partial \lambda}\right|_{\lambda=0} = 0, \forall g \in G \tag{0-6}$$

$$\frac{\partial E}{\partial \lambda} = \int_{x1}^{x2} \frac{\partial e(\hat{f} + \lambda g, \hat{f}' + \lambda g')}{\partial f(x)} g(x) + \frac{\partial e(\hat{f} + \lambda g, \hat{f}' + \lambda g')}{\partial f'(x)} g'(x)dx$$

$$= \left[\frac{\partial e(\hat{f}+\lambda g, \hat{f}'+\lambda g')}{\partial f'} g(x)\right]_{x1}^{x2} + \int_{x1}^{x2} \left(\frac{\partial e(\hat{f}+\lambda g, \hat{f}'+\lambda g')}{\partial f(x)} - \frac{\partial}{\partial x}\left(\frac{\partial e(\hat{f}+\lambda g, \hat{f}'+\lambda g')}{\partial f'(x)}\right)\right) g(x)dx \tag{0-7}$$

$$\frac{\partial E}{\partial \lambda}\Big|_{\lambda=0} = \left[\frac{\partial e(\hat{f}, \hat{f}')}{\partial f'(x)} g(x)\right]_{x1}^{x2} + \int_{x1}^{x2} \left(\frac{\partial e(\hat{f}, \hat{f}')}{\partial f(x)} - \frac{\partial}{\partial x}\left(\frac{\partial e(\hat{f}, \hat{f}')}{\partial f'(x)}\right)\right) g(x)dx = 0,\ \forall g \in G$$

(0-8)

$\left[\frac{\partial e(\hat{f}, \hat{f}')}{\partial f'(x)} g(x)\right]_{x1}^{x2} = 0$ is always true because $g(x1) = g(x2) = 0$.

So Eq. (0-8) requires that

$$\frac{\partial e(\hat{f}, \hat{f}')}{\partial f(x)} - \frac{\partial}{\partial x}\left(\frac{\partial e(\hat{f}, \hat{f}')}{\partial f'(x)}\right) = 0, \forall x \in [x1, x2] \tag{0-9}$$

By substitute Eq. (0-5) into (0-9), we obtain,

$$2\mu_0 H_{app} M_S t + \gamma_{DW_{DW}} t \frac{\partial}{\partial x}\left(\frac{\hat{f}'(x)}{\sqrt{1+\hat{f}'(x)^2}}\right) = 0 \tag{0-10}$$

After an integration of this equation,

$$\frac{\hat{f}'(x)}{\sqrt{1+f'(x)^2}} = -\frac{2\mu_0 H_{app} M_S}{\gamma_{DW}} x + C \tag{0-11}$$

Where C is a constant. Then we have,

$$\hat{f}'(x) = \pm\sqrt{\frac{\left(\frac{2\mu_0 H_{app} M_S}{\gamma_{DW}} x + C\right)^2}{1 - \left(\frac{2\mu_0 H_{app} M_S}{\gamma_{DW}} x + C\right)^2}} \tag{0-12}$$

Note that here the sign before the root depends on the sign of $\frac{2\mu_0 H_{app} M_S}{\gamma_{DW}}x + C$.

$$\hat{f}(x) = \pm \int \sqrt{\frac{\left(\frac{2\mu_0 H_{app} M_S}{\gamma_{DW}}x+C\right)^2}{1-\left(\frac{2\mu_0 H_{app} M_S}{\gamma_{DW}}x+C\right)^2}}\,dx \tag{0-13}$$

Now, the last step is to solve Eq. (0-13). By substituting $\frac{2\mu_0 H_{app} M_S}{\gamma_{DW}}x + C$ with $\sin\theta$, we get,

$$\hat{f}(x) = \pm \frac{\gamma_{DW}}{2\mu_0 H_{app} M_S} \int \sqrt{\frac{sin^2\,\theta}{1-sin^2\,\theta}}\,d\,sin\,\theta = \pm \frac{\gamma_{DW}}{2\mu_0 H_{app} M_S} cos\,\theta + Q \tag{0-14}$$

where Q is constant. That is,

$$\hat{f}(x) = \pm \frac{\gamma_{DW}}{2\mu_0 H_{app} M_S} \sqrt{1-\left(\frac{2\mu_0 H_{app} M_S}{\gamma_{DW}}x + C\right)^2} + Q \tag{0-15}$$

Since $\hat{f}(x1) = \hat{f}(x2) = 0$, we obtain

$$C = -\frac{\mu_0 H_{app} M_S}{\gamma_{DW}}(x1 + x2) \tag{0-16}$$

The final solution is

$$f(x) = \begin{cases} \pm\left(\sqrt{R^2 - (x - x_0)^2} - \sqrt{R^2 - \left(\frac{d}{2}\right)^2}\right) & if\ \mu_0\left|H_{app}\right| \leq \frac{\gamma_{DW}}{dM_S} \\ no\ solution & if\ \mu_0\left|H_{app}\right| > \frac{\gamma_{DW}}{dM_S} \end{cases} \tag{0-17}$$

With $x_0 = \frac{x1+x2}{2}$, $d = x2 - x1$, $R = \frac{\gamma_{DW}}{2\mu_0|H_{app}|M_S}$.

One can find that when $\mu_0\left|H_{app}\right| \leq \frac{\gamma_{DW}}{dM_S}$, two solutions with opposite sign appears. This ambiguity is introduced by the derivation from Eq. (0-11) to Eq. (0-12). In fact, once the sign of the H_{app} is well defined, only one solution stands. One can examine which is the correct one by substituting Eq. (0-16) and (0-17) into Eq. (0-11). For example, for a positive H_{app} and $\mu_0 H_{app} \leq \frac{\gamma_{DW}}{dM_S}$ (here positive means that the direction of H_{app} is parallel to the magnetization in zone inside the trajectory of DW: y=f(x)), the solution can be written in a form as follows,

$$(x - x_0)^2 + \left(y + \sqrt{R^2 - (d/2)^2}\right)^2 = R^2, \text{and } y \geq 0 \tag{0-18}$$

We can interpret this mathematical solution into the following physical pictures:

If applied field is inferior to a critical value, i.e. $\mu_0 H_{app} \leq \frac{\gamma_{DW}}{dM_S}$, a solution for Eq. (0-4) exists, expressed as Eq. (0-18). This means that an equilibrium state under the competition of pressure from applied field and the pressure caused by the DW surface energy can be reached. DW shape is a circle, as shown in Figure 0-2(a). The radius $R = \frac{\gamma_{DW}}{2\mu_0 H_{app} M_S}$. In the framework of the analogy with interface physics, the magnetic field can be seen as an effective, the pressure induced by the applied field can be expressed as

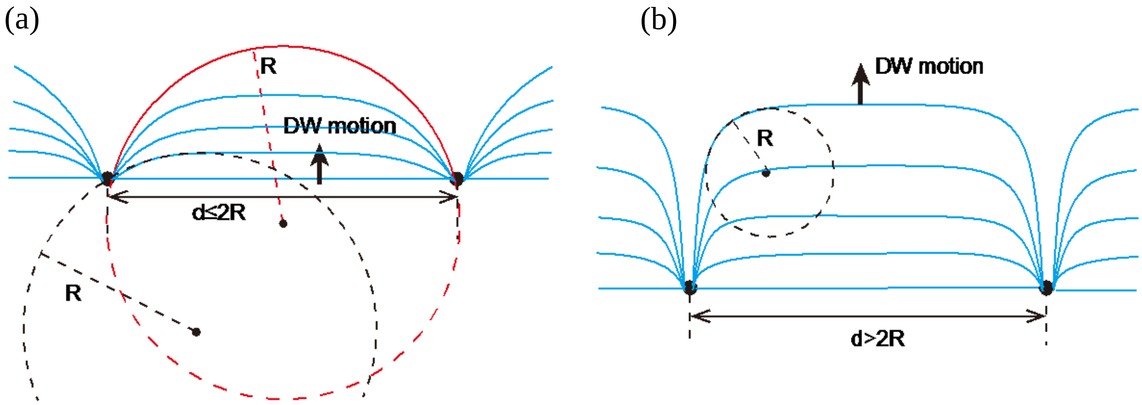

Figure 0-2 The DW state with two terminals solidly pinned and an applied field is applied. (a) When the distance d between the pinning sites is smaller than 2R, the DW propagates at the beginning (blue line). With the DW propagation, the radius of the curvature decreases and the DW reaches equilibrium when $R = \gamma_{DW}/(2\mu_0 H_{app} M_S)$, described by the red line; (b) DW circumvent by the pinning sites when d is larger than 2R. R is determined by the extremal field.

$$P_H = 2\mu_0 H_{app} M_S \tag{0-19}$$

Now, this pressure is totally balanced by the effective pressure associated to the DW surface energy, i.e., $P_H = P_\gamma$. According to this calculation, we can get the same expression as Eq. (4-2), $P_\gamma = \gamma_{DW}/R$, known as the Laplace pressure.

If applied field exceeds this value, DW cannot stay in equilibrium state because the Laplace pressure cannot withstand the pressure from Zeeman force, as shown in Figure 0-2(b). DW will continuously expand. So there is no mathematical solution in this case.

The critical applied field to overcome DW elasticity is $\mu_0 H_c = \frac{\gamma_{DW}}{dM_S}$.

- **DW pinned by a single hard pinning site in narrow wire**

In the following, we discuss the DW behavior when one of its terminals is solidly pinned by a hard pinning sites while the other terminal can move freely along a wire. As shown in Figure 2-2, we suppose that the one endpoint of the DW is always fixed in (x1,0) while the other endpoint lies on the line x=x2.

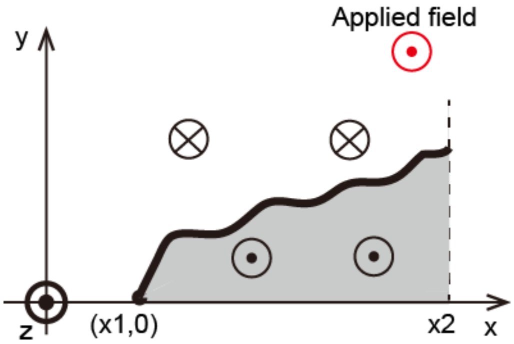

Figure 0-3 Sketch showing a segment of DW (black line) pinned by one hard pinning site (x1,0) in one terminal and the other terminal can move freely along the line x=x2.

In this case, the expression of the free energy of the system has the same expression as Eq. (0-3). To determine the curve function of the DW in equilibrium state, we search for the function $f(x) \in G'$ that minimize the free energy of the system, where G' is a set of function $\{f(x) | f(x) \in C^1(x1, x2)\ and\ f(x1) = 0\}$.

supposing $\hat{f}(x) \in G'$ is the function, then, the Eq. (0-6) applies also in this case, but g $\in G'$. After a similar calculation, we can obtain the solution of the Eq. (0-6)

$$\begin{cases} \left.\frac{\partial e(\hat{f},\hat{f}')}{\partial f'(x)}\right|_{x2} \cdot g(x2) - \left.\frac{\partial e(\hat{f},\hat{f}')}{\partial f'(x)}\right|_{x1} \cdot g(x1) = 0 \\ \frac{\partial e(\hat{f},\hat{f}')}{\partial f(x)} - \frac{\partial}{\partial x}\left(\frac{\partial e(\hat{f},\hat{f}')}{\partial f'(x)}\right) = 0 \end{cases} \quad and \qquad (0\text{-}20)$$

Since $g(\mathrm{x}1) = 0$ is true but the value of $g(x2)$ is not fixed. The upper term of Eq. (0-20) requires,

$$\left.\frac{\partial e(\hat{f},\hat{f}')}{\partial f'(x)}\right|_{x2} = \frac{\hat{f}'(x2)}{\sqrt{1+\hat{f}'(x2)^2}} = 0 \qquad (0\text{-}21)$$

This means that the trajectory of the DW is always perpendicular to the line of x=x2 in this endpoint.

Using the similar integrations as given in Eq. (0-10) - (0-17), the lower term of Eq. (0-20) can be used to deduce the function of the trajectory of DW. By considering the initial condition $y_0 = f(x_0)$, the final solution is

$$f(x) = \begin{cases} \sqrt{R^2 - \left(x-(x2)\right)^2} - \sqrt{R^2 - L^2} & if\ \mu_0 H_{app} \leq \frac{\gamma_{DW}}{2LM_S} \\ no\ solution & if\ \mu_0 H_{app} > \frac{\gamma_{DW}}{2LM_S} \end{cases} \qquad (0\text{-}22)$$

with $\mathrm{R} = \frac{\gamma_{DW}}{2\mu_0 H_{app} M_S}$ and L=x2-x1.

in the case $\mu_0 H_{app} \leq \frac{\gamma_{DW}}{2LM_S}$, the solution can also be written in the following expression,

$$\left(x-(x2)\right)^2 + \left(y - \left(y_0 - \sqrt{R^2 - L^2}\right)\right)^2 = R^2 \qquad (0\text{-}23)$$

The above model can be ued to study the behavior of DW when only one of the endpoint is solidly pinned by a hard pinning site in a wire. This hard pinning site may lie on the edge or inside the wire. The other edge is relatively smooth, allowing the free displacement of the DW. As shown in Figure 0-4. We can interpret this mathematical solution into the following physical pictures:

If applied field is inferior to a critical value, i.e. $\mu_0 H_{app} \le \frac{\gamma_{DW}}{2LM_S}$, DW can stay in an equilibrium state under the competition of pressure from applied field and its elasticity. In this state, DW shape is a circle, with one endpoint passing the pinning site and other endpoint lying in the edge and the DW trajectory is perpendicular to the edge in this end, as shown in Figure 0-4(a).

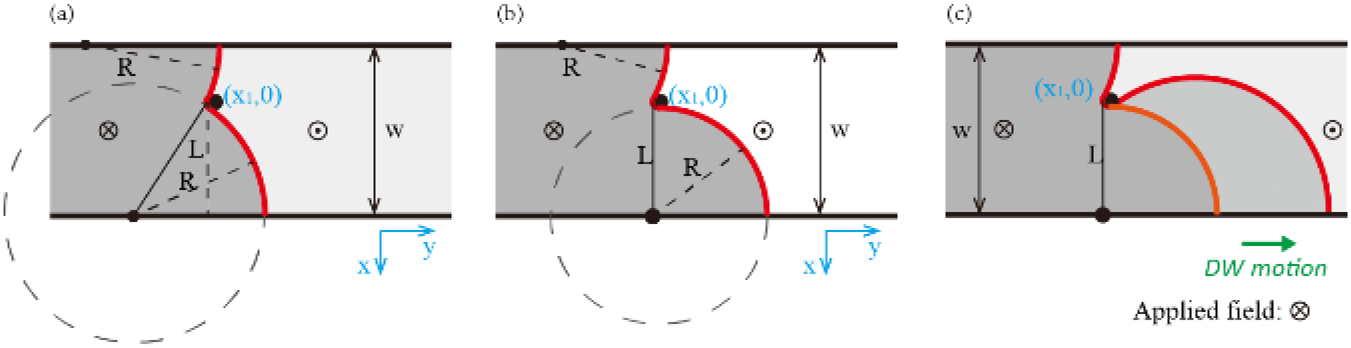

Figure 0-4 (a) DW pinned by a single hard pinning site when applied field $\mu_0 H_{app} < \frac{\gamma_{DW}}{2LM_S}$;(b) applied field reaches the critical field of depinning, $\mu_0 H_{app} = \frac{\gamma_{DW}}{2LM_S}$, the radius of DW R=L; (c)when field $\mu_0 H_{app} > \frac{\gamma_{DW}}{2LM_S}$, DW circumvent from the pinning site and depins.

If applied field exceeds this value, DW cannot stay in equilibrium state because DW elasticity cannot withstand the pressure from Zeeman force, as shown in Figure 0-4(c). DW will circumvent from the pinning site and depins. So there is no mathematical solution in this case.

Therefore, the critical applied field to overcome DW elasticity is $\mu_0 H_c = \frac{\gamma_{DW}}{2LM_S}$. Under this threshold field, the radius of DW circle equals to the distance from pinning site to the edge L.

It is to note that this solution is deduced under the assumption that the edge of wire is perfectly smooth. In fact, due to the roughness of edge and intrinsic pinning field, DW depinning field from one hard pinning site by circumventing should be larger than this critical value.

Appendix 2: Another example of magnetic sensors based on the elasticity of DWs

Here, we show another effect related to the elasticity (surface tension) of DWs which can be used to design DW based magnetic sensors. In a magnetic wire with a gradient width, we found that the DW motion is reversible. As shown in Figure 0-5, in a magnetic wire with perpendicular magnetic anisotropy (PMA), the width of the wire is 120 nm in left and 40 nm in right and the width gradually changes. A DW was initially set in the right of wire. When a perpendicular field of 20 mT was applied, DW moves to the left hand. When the external field was removed, the DW tended to spontaneously move to the right hand and return to the initial position. This movement is possible since the motion of DW to the right will decrease the DW length, thus minimizing the DW surface energy (this surface energy of DWs is the source of the elasticity). The effective field produced by the DW elasticity is [29],

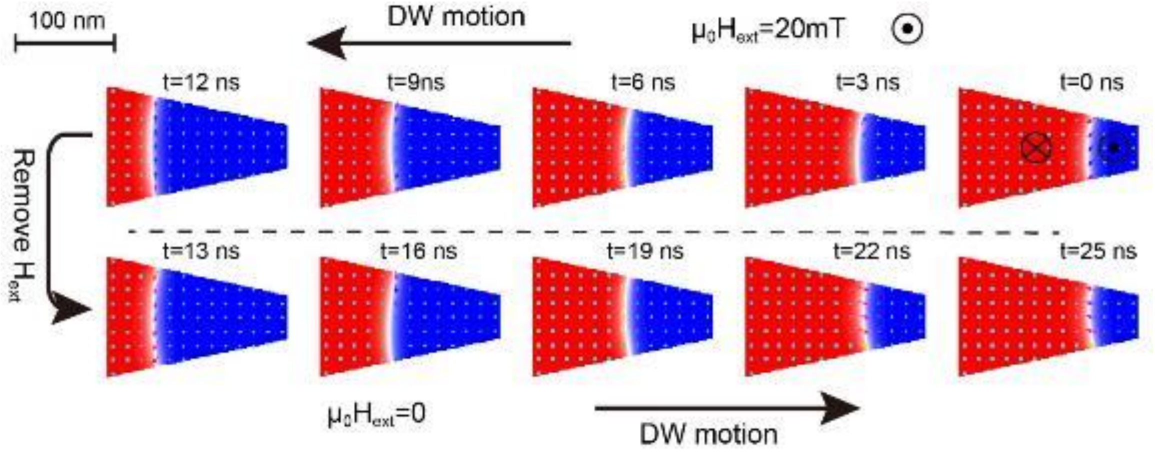

Figure 0-5 The asymmetric DW motion in a wire with gradient of width (simulation results). From 0 to 12ns, an external field along ⊙ direction was applied and DW moves to left while from12ns to 25ns, DW return to right spontaneously due to the effective field of elasticity.

$$H_{eff} = \frac{\gamma}{2\mu_0 M_S w} \cdot \frac{dw}{dx} \tag{0-24}$$

Where w is w(x) is the width of the wire. We can see that this effective field is determined by w and the gradient of w.

Since the design of magnetic sensors requires that the output signal has a monotonous and reversible response to the input magnetic field, this phenomenon provides a possible way to design the DWs based sensors.

Here, we give an example based on the above mechanism. In a double-anchors shaped magnetic structure with PMA, the gradient of the width increases from the middle to the terminals, as shown in Figure 0-6. DW was set in the middle as the initial state. When an external field in ⊙ (or ⊗) presents, DW move to left (right, respectively). Because of the gradient of the wire width, the effective field produced by the DW elasticity increases as DW moves to the terminal. The position of the DW in the stable state is determinated when the external is fixed. When the external field is removed, DW will return to the initial position spontaneously due to the effective field of elasticity.

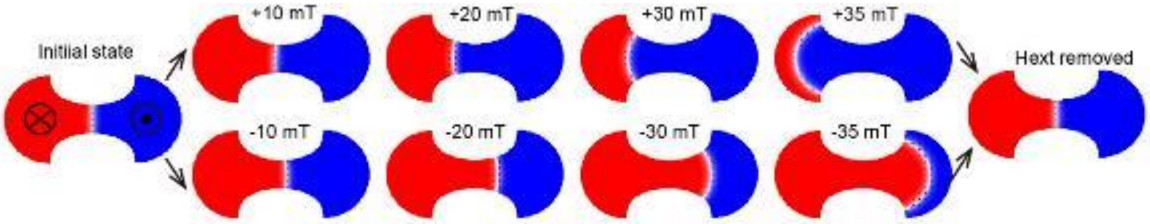

Figure 0-6 DW position in stable state under a certain external perpendicular field (simulation reults).

From the above example, we can see that the DW motion can show a monotonous and reversible response to the external field. If the free layer of MTJs or spin valves is etched into this double anchors structure, since the DW motion means a fluctuation of the magnetization, the motion can be characterized by the change of the magneto-resistance thanks to the tunneling magnetoresistance or giant magnetoresistance effect. In this way, the external field can be measured.

Appendix 3: Experimental measurements of the resistivity of the CoFeB thin film

Here, we summarized the information about the resistivity of CoFeB thin film based on experiments performed on the similar structures as us. The resistivity of thin films of CoFeB obtained varies from 160 to 330 μΩ·cm. In addition, the composition of the CoFeB, the structure and the preparing condition in these references are different from that of our and that the results have a wide variation. In view that this value is of key importance for the extraction of the polarization of CoFeB, we performed some experiments to estimate the CoFeB thin film in our sample.

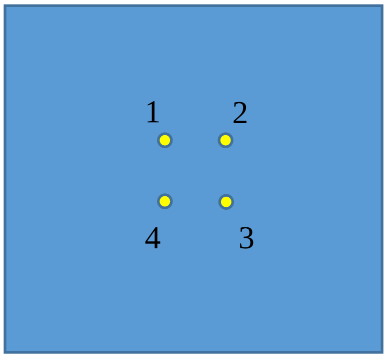

Figure 0-7 Schematic of the configuration to measure the square resistance of a film using the four probes method.

As shown in Figure 0-8 (b) & (c), 2cm×2cm films with two different layer structures were deposited using sputtering: Substrate/MgO(2)/CoFeB(t)/Ta(5) and Substrate/Ta(3)/CoFeB(t)/MgO(2)/Ta(2) with thickness in nm and t varying from 0 to 3. All these samples

Table 0-1 Resistivity of CoFeB in measured similar structures according to published results. Note that the structure of our sample studied is Ta(5)/Co40Fe40B20/MgO(2)/Ta(5), annealed at 300°C for 2h.

Resistivity of CFB (μΩ·cm)	Resistivity of Ta (μΩ·cm)	Composition and structure (thickness in nm)	Thickness of CFB (nm)	Annealing condition	Measurement method	Reference
160	189	Sub/TaN(t)/CoFeB(1)/MgO(2)/Ta(1)	1	300°C, 1 h	R vs. thickness of TaN in wire	J. Torrejon et al. (2014), [78]
170	190	Si/Co40Fe40B20/Ta(8)	4	unknown	R vs. thickness of Ta in wire	Luqiao Liu et al. (2012), [75]
330	--	W(2-7)/Co32Fe48B20/MgO	0.8-1.4	250°C, 30 min	R vs. thickness of W in wire (measured by TR-MOKE)	S. Cho et al. (2015) [150]
140	--	Co60Fe20B20	100	350°C,1 h	four-point sheet resistance meter	Y-T. Chen et al. (2013) [169]
250	--	Co40Fe40B20	10	No	four- point sheet resistance meter	Y-T. Chen et al. (2012) [170]
114	--	Co40Fe40B20	bulk	Amorphous		W. Kettler et al. (1982) [171]

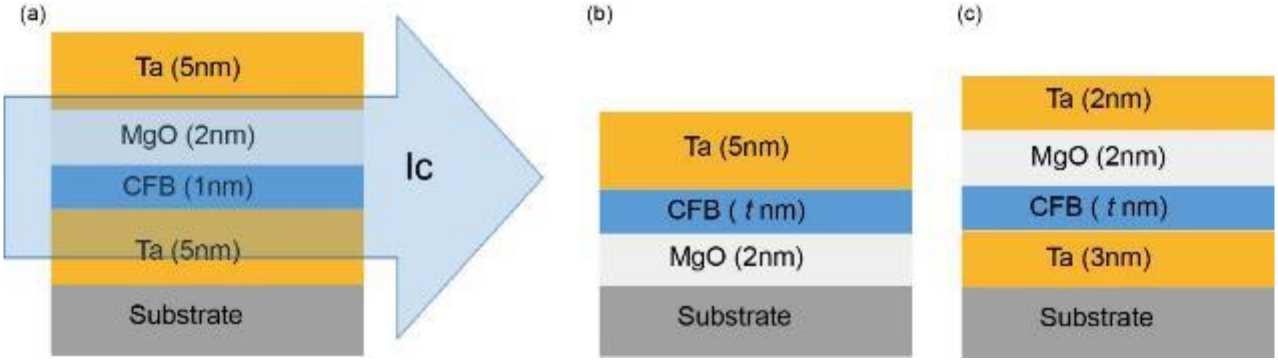

Figure 0-8 (a) The multilayers structure of the sample studied; (b)&(c) Multilayers structures with thinner Ta layers and varying thickness of CoFeB used for the measurement of the resistivity of CoFeB.

were annealed at 300°C for 2 hours and the composition are all $Co_{40}Fe_{40}B_{20}$. The square conductance was measured using the four probes method [167]. The measuring steps are: first, four pointed probes were connected in the center of a 2cmx2cm sample. The four probes form a square and the size of the square is far smaller than the sample, as shown in Figure 0-7. Second, a current $I_{i,j}$ was applied via two of the neighboring probes and the voltage $V_{k,l}$was measured via the other two probes, where i, j, k, l are the index of the probes. A resistance was obtained by $R_{ij,kl} = V_{k,l}/I_{i,j}$. Then, this measurement was repeated by changing the probes applying the current. At last, the square resistivity of the multi-layer stack can be obtained with the following formula [167],

$$R_S = \frac{\pi}{2\ln 2}\left(R_{12,34} + R_{23,41+}R_{34,12+}R_{41,23}\right) \tag{0-25}$$

The square conductance can be defined as $G_S = 1/R_S$. If the conductance of the multilayers stack can be seen as the accumulation of the conductance of the Ta layers and the CoFeB layer,

$$G_S = \sigma_{CFB}t_{CFB} + \sigma_{Ta}t_{Ta} \tag{0-26}$$

where σ_{CFB} and σ_{Ta} are the conductivity of CoFeB and Ta, t_{CFB} and t_{Ta} are the thickness of CoFeB and Ta. If the thickness dependence of conductivity (Fuchs-Sondheimer model) [168] is neglected, the conductance of the CoFeB can be extracted from the variation of Gs vs. the thickness of CoFeB, as plotted in Figure 0-9.

According to the measurements on the Sub/MgO(2)/CoFeB(t)/Ta(5) structure, the resistivity of the CoFeB is extracted to be 256 μΩ·cm; according to the measurements on the Sub/Ta(3)/CoFeB(t)/MgO(2)/Ta(5) structure, the resistivity of CoFeB is extracted to be 168 μΩ·cm. These results are close to the results measured by L. Liu et al. (2012), [75], J. Torrejon et al. (2014), [78]. However, the conductivity of the Ta is difficult to be extracted from our experiments since the thickness

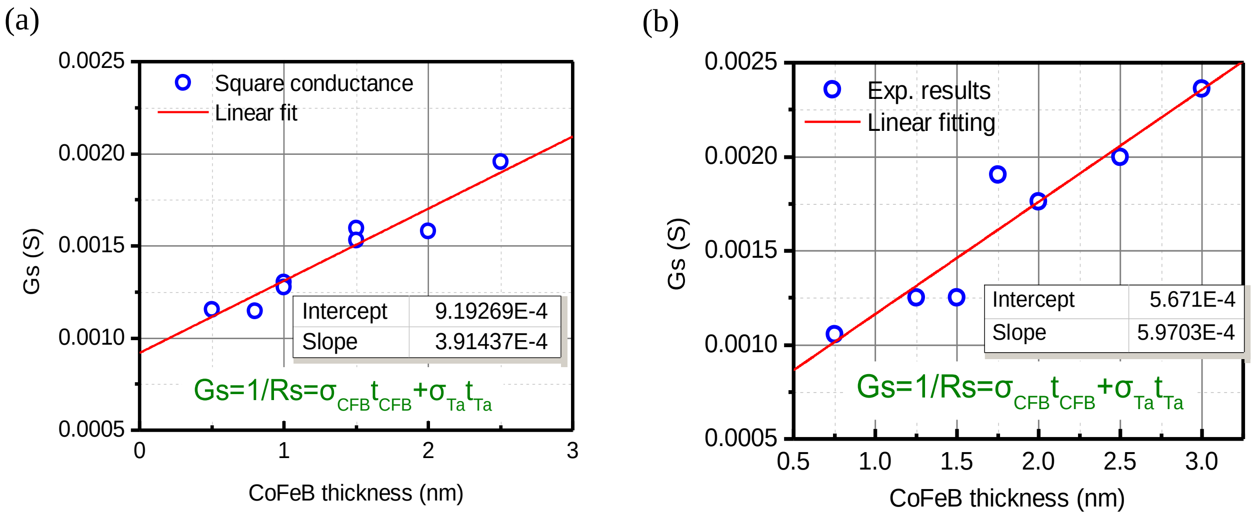

Figure 0-9 Square conductance of the film vs. the thickness of CoFeB in (a) the MgO(2)/CoFeB(t)/Ta(5) structure and (b) in the /Ta(3)/CoFeB(t)/MgO(2)/Ta(2) structure. Note that the measurement of the square conductance on the sample with 0nm CoFeB (a) and the sample with 0 and 0.5nm CoFeB (b) was failed because of the high contact resistance.

of oxidized Ta is unknown. In the following analysis, we adopt the results of Liu et al. (2012), [75], i.e., $\rho_{CFB} = 170\ \mu\Omega \cdot cm$ and $\rho_{Ta} = 190\ \mu\Omega \cdot cm$.

Appendix 4: More information about the DW depinning field in Figure 5-22

1. More detailed explanations about the measurement

In case (a), for DW motion on → direction, field pulses with magnitude of B=4.01mT and duration T=5μs were used to drive DW from left to right for one time. All pinning sites with B_{dep}> 4.01 mT were detected and measured. For DW motion in ← direction, the same method, all pinning sites with B_{dep}> 4.01 mT were measured.

In case (b), for both DW motion directions, field pulses with magnitude of B=4.63mT and duration T=5μs were used to drive DW motion. However, not all the pinning sites above 4.63 mT are measured because the pinning in this level are much thicker than case (a) and many pinning sites are masked by others. However, all the pinning sites with B_{dep}>6mT are identified and plotted.

In case (c), for both DW directions, field pulses with magnitude of B=7.17 mT and duration T=5μs were used to drive DW motion. All the pinning sites with B_{dep}>7.17 mT were identified and all the pinning below this value were not identified.

In case (d), for both DW directions, the measurement was more rigorous, field pulses with magnitude of B=6.88 mT and duration T=5μs were used to drive DW motion. All the pinning sites with B_{dep}>7.17 mT were identified and all the pinning sites blow 6.88 mT were not identified. It is to note that in the lower case, i.e., for DW motion ←, I scanned two times with B=6.88 mT, but only four pinning sites are found.

2. Analysis of the pinning sites in Figure 5-22 one by one

First, in case (c), the largest pinning site is n°8. Pinning n°8 is not the largest one in case (a) without current, but become more obvious when current is applied in case (b); as the current further increased, in case (c), the pinning was also enhanced and became much larger than the others. However, in case (d), this pinning disappeared. It can be explained that this pinning site is in the top edge and it was enhanced only in case (b) and (c).

In case (c), the second large pinning site is the pinning n°4, it is not measurable in case (a) and occurs in (b) as current is applied. It becomes obvious in case (c) as current increases. However, it disappears in case (d). It means that this pinning site is also in the top edge.

Noting that pinning n°8 and pinning n°4 are very large for both the DW moving direction in (c) while they disappear for both DW direction in (d). This is consistent with the prediction that they are both in the top edge.

For case (d), the largest pinning site is pinning n°7. However, it disappears in case (b) and although it appears in case (c), its pinning force is not so strong compared with others. The second large pinning are n°2 and n°6, they exist in (c) but not so large compared with other pinnings. The third large pinning is n°10 in case (d) but it disappears in case (c). Other examples about the incoherence between (c) and (d) are pinning n°11, n°12, n°13, n°14 and n°15.

The pinning sites that seem correlated between (c) and (d) are pinning n°1, n°3, n°5 and n°6, i.e., these pinning are enhanced systematically. This nature conforms to the enhancement of intrinsic pinning by SH current or enhancement of the pinning caused by the convoluted effect of edge roughness and some huge defects inside the wire. Maybe the origin of these four pinning sites is very complex, being the hybrid result of different cases.

In addition, as the largest pinning sites in case (a), including the pinning n°2, n°10, n°5, n°11 n°7 and n°8 are enhanced by current either in case (c) and (d) and this enhancement is not correlated. This means that most of the huge pinning we have measured are on either of the two edges, or very closed to the edge.

In summary, from the above analysis, we can see that the enhancement of the pinning effect by current is not systematic. Most of them are enhanced either in case (c) or in (d). This conforms to the model of SHE enhanced DW pinning effects caused by the huge defects in the edge. The pinning we measured is the largest ones. When a current is applied, if the pinning in either of the two edges is enhanced, the largest pinning we observed will increase. In addition, for the several pinning sites that is enhanced both in case (c) and case (d), it conforms to the second model: SH current enhanced intrinsic pinning effect.

Appendix 5: List of publications during the doctoral research

1. Zhang, Y.; **Zhang, X. (co-first author);** Hu, J.; Nan, J.; Zheng, Z.; Zhang, Z.; Zhang, Y.; Vernier, N.; Ravelosona, D.; Zhao, W. Ring-shaped Racetrack memory based on spin orbit torque driven chiral domain wall motions. *Sci. Rep.* **2016**, *6*, 35062, doi:10.1038/srep35062.

2. **Zhang, X.**; Vernier, N.; Zhao, W.; Vila, L.; Ravelosona, D. Extrinsic pinning of magnetic domain walls in CoFeB-MgO nanowires with perpendicular anisotropy. *AIP Adv.* **2018**, *8*, 56307, doi:10.1063/1.5006302.

3. **Zhang, X.**; Vernier, N.; Zhao, W.; Yu, H.; Vila, L.; Zhang, Y.; Ravelosona, D. Direct Observation of Domain-Wall Surface Tension by Deflating or Inflating a Magnetic Bubble. *Phys. Rev. Appl.* **2018**, *9*, 24032, doi:10.1103/PhysRevApplied.9.024032.

4. **Zhang, X.**; Cai, W.; Zhang, X.; Wang, Z.; Li, Z.; Zhang, Y.; Cao, K.; Lei, N.; Kang, W.; Zhang, Y.; Yu, H.; Zhou, Y.; Zhao, W. Skyrmions in Magnetic Tunnel Junctions. *ACS Appl. Mater. Interfaces* **2018**, 10, 16887–16892, doi:10.1021/acsami.8b03812.

5. Zhang, L.; **Zhang, X. (co-first author);** Wang, M.; Wang, Z.; Cai, W.; Cao, K.; Zhu, D.; Yang, H.; Zhao, W. Size dependence of the spin-orbit torque induced magnetic reversal in W/CoFeB/MgO nanostructures. *Appl. Phys. Lett.* **2018**, *112*, 142410, doi:10.1063/1.5022824.

6. Zhang, Y.; Zhang, C.; Nan, J.; Zhang, Z.; **Zhang, X**.; Klein, J. O.; Ravelosona, D.; Sun, G.; Zhao, W. Perspectives of Racetrack Memory for Large-Capacity On-Chip Memory: From Device to System. *IEEE Trans. Circuits Syst. I Regul. Pap.* **2016**, *63*, 629–638, doi:10.1109/TCSI.2016.2529240.

7. Zhang, Y.; **Zhang, X. (co-first author)** ; Vernier, N.; Zhang, Z.; Agnus, G.; Coudevylle, J.; Lin, X.; Zhang, Y.; Zhang, Y.; Zhao, W.; Ravelosona, D. Domain Wall Motion Driven by Laplace Pressure in CoFeB-MgO Nanodots with Perpendicular Anisotropy. **2017**. (Accepted by Physical Review Applied) https://arxiv.org/abs/1711.11334

8. **Zhang, X.**; Vernier, N.; Cao, Z.; Leng, Q.; Cao, A.; Ravelosona, D.; Zhao, W. Magnetoresistive sensors based on the elasticity of domain walls. arXiv 2018, 1–13, http://arxiv.org/abs/1801.01343.

9. Anni Cao, **Xueying Zhang (co-first author)** et al. Tuning the Dzyaloshinskii-Moriya Interaction in Pt/Co/MgO heterostructures through MgO thickness (Accepted by Nanoscale) https://arxiv.org/abs/1710.09051

Résumé en français

1. Motivation

Dans les films minces magnétiques, l'aimantation s'organise en domaines, qui sont des zones où l'aimantation est uniforme. Le passage d'un domaine à l'autre se fait via une zone tampon très étroite appelée "paroi de domaines" (acronyme : "DW" pour "Domain Wall"), dans laquelle l'aimantation change progressivement de direction. Parmi les mécanismes qui permettent d'expliquer le retournement de l'aimantation du film considéré, celui le plus couramment rencontré est la nucléation d'un petit domaine en un point de facile retournement, suivi de la propagation de la paroi ainsi apparue. De ce fait, les parois de domaines peuvent être considérées comme des pseudo-objets et l'étude de leur comportement est un des gros enjeux actuels. Par exemple, via des expériences bien choisies, cela permet d'accéder à certains paramètres fondamentaux tels que l'aimantation à saturation M_S [1], la rigidité d'échange A ou la constante d'amortissement α.

La maitrise de la propagation des parois de domaines est un très gros enjeu actuel, car beaucoup de dispositifs de stockage d'informations et de traitement de données sont basés sur la manipulation de la structure en domaines. Par exemple, citons des dispositifs logiques à base de parois de domaines [6,7] ou des réseaux neuronaux artificiels basés sur des parois de domaines [8–10]. Les parois de domaines peuvent être aussi utilisées comme canal de transmission d'ondes de spin [11]. La proposition du concept de mémoire de type Racetrack par S. Parkin [12,13], qui stocke sur des nanofils magnétiques, a déclenché une explosion soutenue des recherches sur les mouvements des parois de domaines dans les nanofils.

Au cours des deux dernières décennies, le mouvement de parois de domaines induit par courant polarisé en spin est apparu comme une nouvelle technique prometteuse, car elle peut permettre un mouvement de translation globale de toute la structure en domaines, contrairement au mouvement induit par champ magnétique, qui ne peut que faire grandir les domaines bien orientés. Mais, cette technique est loin d'être maitrisée, car, souvent, de nombreux phénomènes s'entremêlent lorsqu'on la met en oeuvre. Il y a d'abord le couple de transfert de spin (usuellement appelé STT pour Spin Tranfer Torque), qui apparait lorsqu'un courant polarisé en spin traverse la paroi, et qui peut se décomposer en deux contributions (adiabatique et non adiabatique). Il y a aussi l'interaction spin-orbite (SOT, Spin Orbit Torque), qui peut introduire un couple supplémentaire pour déplacer les parois via des mécanisme tels que l’Effet Hall de Spin (SHE, Spin Hall Effect) lorsque le film magnétique a été déposé sur un métal non magnétique. Du fait de la présence de nombreuses interfaces dans les multicouches magnétiques utilisées, il peut être aussi nécessaire de prendre en compte l’interaction de Dzyaloshinskii-Moriya (DMI, Dzyaloshinskii-Moriya Interaction). Ces différents mécanismes ouvrent des perspectives très intéressantes, puisqu'ils permettent de déplacer les parois de domaines à des vitesses beaucoup plus élevées que le champ magnétique.

Dans le cadre de ce travail, nous nous sommes concentrés sur un matériau émergent en vue des applications, qui est le CoFeB [14–18] : il a un faible coefficient d'amortissement et un faible champ de dépiégeage, ce qui promet une meilleure efficacité pour les dispositifs basés sur des parois du domaine. La structure de ces films fait qu'ils faut potentiellement prendre en compte tous les effets évoqués ici, ce qui rend le comportement de ces films complexes. Le rôle des différents mécanismes sur le mouvement des parois doit être clarifié.

Cette thèse se concentre sur l'étude des propriétés statiques et dynamiques des parois de domaines dans des nanofils CoFeB. Certaines propriétés peuvent se comprendre de manière très simple à l'aide du concept d’énergie interfaciale. D'autres problèmes, tels que le piégeage des parois ou la détermination de l'efficacité du couple de transfert de spin, nécessite une analyse plus poussée. Pour déterminer certains paramètres fondamentaux tels que le taux de polarisation en spin des porteurs de charge, la propagation induite par un champ magnétique et un courant électrique simultanément appliqués apporte des renseignements nouveaux et très importants.

2. Echantillons et méthodes

Les échantillons étudiées sont des couches minces de Ta(5nm)/$Co_{40}Fe_{40}B_{20}$(1nm)/MgO(2 nm)/Ta(5nm) avec anisotropie perpendiculaire. Ils sont structurés aux nanofils longs de 50 μm, avec un plot de nucléation. Les largeurs des fils sont : 200 nm, 400 nm, 600 nm, 1 μm et 1.5 μm. Certains nanofils présentent des croix de Hall pour les mesures électriques. Toutes les structures sont équipées d'électrodes pour des tests électriques. Il est à noter que la constante DMI mesurée dans notre système est très faible, inférieure à 0,01 mJ/m^2, et ces interactions peuvent être négligées.

Les observations du comportement des parois ont été réalisées grâce à un microscope Kerr, capable de visualiser l'état magnétique des nanofils jusqu'à la largeur de 200 nm. L'utilisation de champs magnétiques impulsionnels est apparue comme un outil essentiel pour nos études. Avec une petite bobine de 120 tours et de 6 mm de rayon, alimentées par un générateur d'impulsion haute tension, nous avons pu créer une impulsion de champ magnétique d'amplitude 130 mT, ayant un temps de montée de 1.9 μs. Ce type d'impulsions très courtes permet de créer une paroi de domaine dans une nanostructure, sans pour autant retourner toute la structure du fait de la propagation qui s'ensuit, et, donc, de conserver une structure multidomaine avec présence de paroi dans la nanostructure. Avec une bobine de 20 tours, nous avons pu

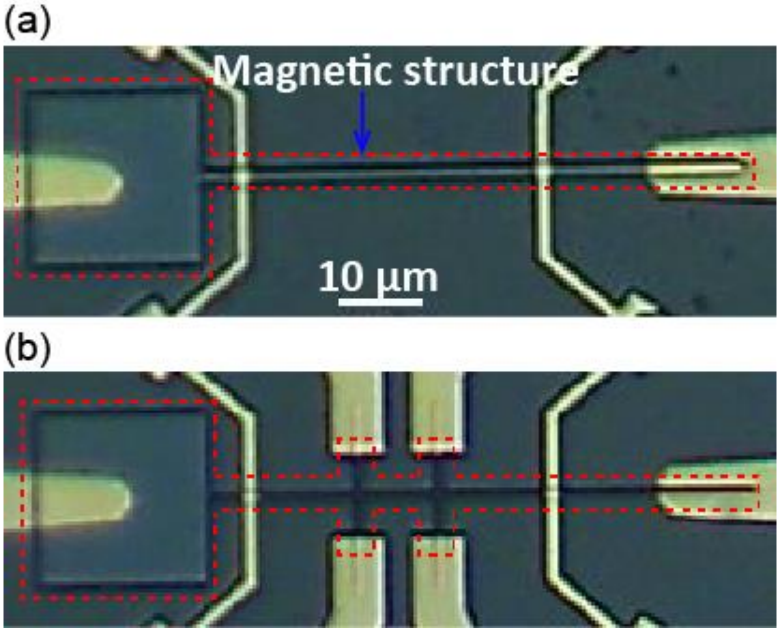

Figure 1 Images optique de deux des échantillons étudiés, (a) avec et (b) sans la croix de Hall. La zone entourée par la ligne pointillée rouge est la structure magnétique. Les parties jaunes sont des électrodes.

réduire le temps de montée de l'impulsion de champ à 220 ns. Cela nous a permis de mesurer la vitesse de mouvement des parois dans nos nanofils de manière précise. Pour terminer, les impulsions de champ ont pu être synchronisées avec une impulsion de courant électrique à travers le nanofils, pour étudier le comportement des parois sous l’effet combinée de ces deux actions.

3. Résultats

a. L’énergie interfaciale des parois du domaine

Nous avons d'abord pu mettre en évidence le rôle dominant et direct de la tension interfaciale de paroi dans certaines expériences. D'habitude, cette tension n'apparait que de manière très indirecte.

Pour commencer, nous avons observé qu'une bulle magnétique semi-circulaire dans un petit carré devenait instable et disparaissait spontanément lorsque le champ externe est nul. Nous avons expliqué cela grâce à la pression de Laplace induite par l'énergie interfaciale lorsque la paroi de domaine présente une courbure. En vérifiant le champ magnétique nécessaire pour stabiliser le domaine semi-circulaire, nous avons pu estimer l'énergie interfaciale des parois dans notre structure, nous avons obtenu 5,4 mJ/m^2.

Ensuite, nous avons observé l'effet de l'interaction entre deux bulles semi-circulaires dans le petit carré constitué par le plot de nucléation lorsqu'un champ externe est appliqué. La bulle plus grosse commence par croitre de manière continue. Lorsque les deux bulles sont assez proches, la répulsion dipolaire induit la contraction de la bulle plus petite jusqu'à sa disparition. Cette expérience fait penser à

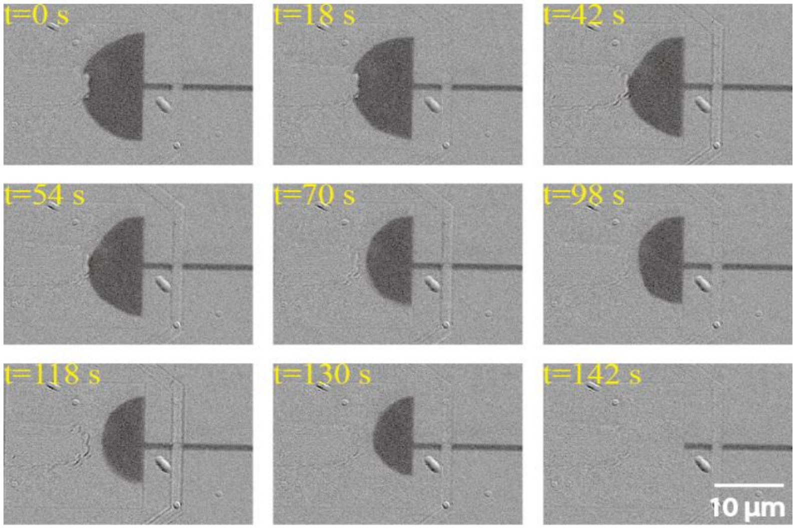

Figure 2 Contraction spontanée de la bulle de domaine semi-circulaire dans un champ

celle classique (pour les spécialistes des mousses) des deux bulles de savon reliées, dans laquelle la grosse bulle "mange" la petite. Cela est encore une fois expliqué par la pression de Laplace, qui est plus grande pour la petite bulle.

Pour finir, nous avons identifié l'origine de piégeage de la paroi auprès des croix du Hall ou à la connexion entre un fil étroit et un grand plot magnétique. C'est encore la pression de Laplace qui intervient. En effet, la force liée à l'énergie interfaciale doit être surmontée quand la paroi commence à se dilater dans le plot. Conformément aux prédictions théoriques, nous avons constaté que le champ de dépiégeage augmente de façon proportionnelle à $1/w$, où w est la largeur du fil. L'étude du champ de dépiégeage en fonction de $1/w$ apparaît comme une très bonne méthode pour mesurer l'énergie de interfaciale de paroi du domaine. Grâce à cette deuxième méthode, nous avons refait une mesure de l'énergie de interfaciale de parois, qui a donné 4,1 mJ/m^2, ce qui est en bon accord avec notre première valeur compte-tenu des incertitudes expérimentales.

Nos expériences ont montré l'importance de l'énergie interfaciale de paroi: elles expliquent le piégeage de paroi dans des nanofils dus à des défauts ou des encoches, notamment aux croix de Hall, ce qui est critique pour des applications telles que la mémoire de type "racetrack". De plus, notre méthode de mesure de l'énergie interfaciale pourrait être très utile dans l'étude des couches minces présentant le DMI, car ces interactions modifient radicalement l'énergie interfaciale [23].

Enfin, un nouveau prototype de capteur magnétique basé sur la tension interfaciale (ou l’élasticité) des parois du domaine magnétique a été proposé et émulé avec des simulations micromagnétiques. Ces nouveaux capteurs montrent une bonne performance sur la mesure du champ direct ou alternatif. Des performances telles que la plage de mesure et la sensibilité peuvent être ajustées en manipulant la géométrie et la taille ou le dispositif. Le dispositif proposé peut améliorer le niveau d'intégration et les performances des capteurs magnétiques.

b. Le mouvement des parois et l’effet de piégeage dans des nanofils

Pour commencer, nous avons vérifié les vitesses de propagation des parois dans des nanofils induit par le champ magnétique, ainsi que les positions des plus gros défauts de piégeage et le champ critique de dépiégeage associé à chacun de ces défauts.

Nous avons constaté une augmentation du champ de dépiégeage des plus gros défauts proportionnelle à 1/w, w étant la largeur des pistes (figure 3). Cela nous a conduit à penser que ces gros défauts sont de nature extrinsèque, c'est-à-dire liés à la rugosité des bords des fils induite par la nanostructuration.

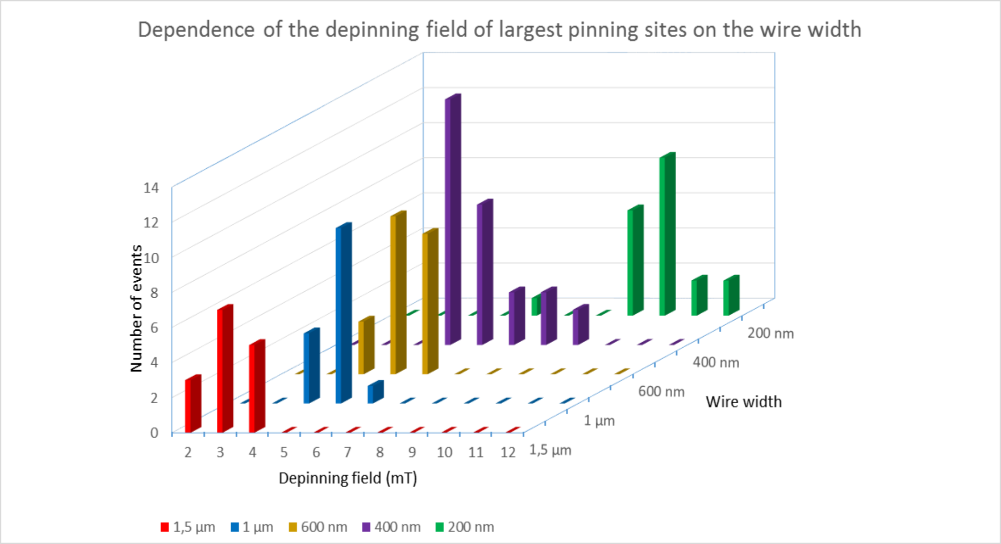

Figure 3. histogramme de distribution du champ de dépiégeage des défauts les plus forts, en utilisant les cinq défauts les plus forts pour chaque fil inclus dans les statistiques.

Ensuite, la vitesse de mouvement de paroi induit par impulsion du champ et de courant synchronisées a été mesurée. En régime précessionnel (champ magnétique élevé), il est prévu que la vitesse du mouvement de la paroi induit par l'effet combiné du champ et du STT est égale à la somme V_B+V_J, où V_B aurait été la vitesse obtenue en appliquant uniquement le champ magnétique et $V_J=g\mu_B Pj/2eM$ est une vitesse de dérive des porteurs de charge, j étant la densité de courant, μ_B le magnéton de Bohr, M la densité d'aimantation, e la charge d'un porteur et P le taux de polarisation des porteurs de charge(figure 4 et 5).

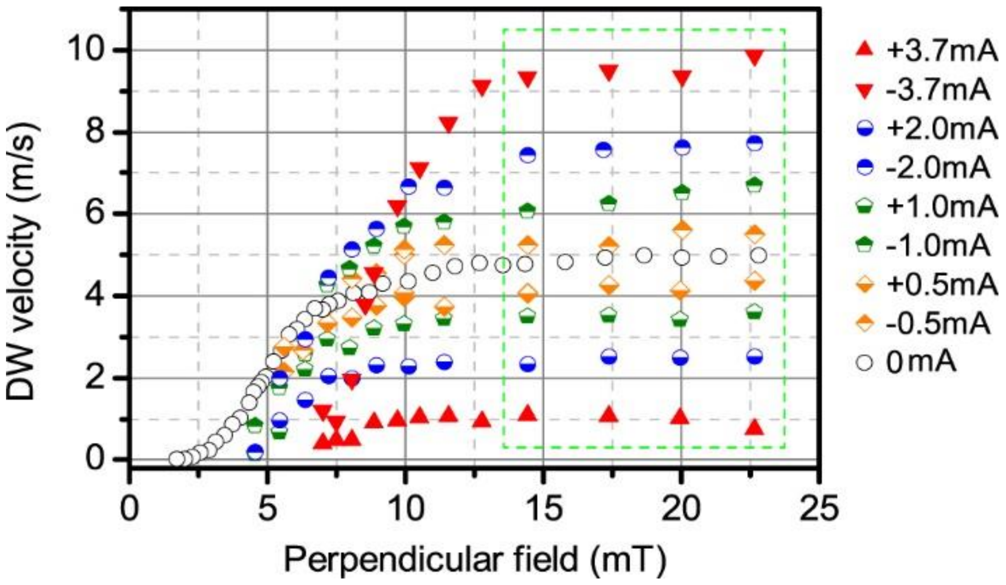

Figure 4. Vitesses de mouvement de la paroi du domaine induites par différents champs et densités de courant. Le courant circulant le long de la direction de mouvement de la paroi est défini comme positif. Les vitesses dans le plateau, encadrées par la ligne verte en pointillés, sont moyennées et représentées en fonction du courant de la figure 5.

Nos résultats expérimentaux s'avèrent en remarquable accord avec cette prédiction (figure 5). La pente de la figure 5 nous permet d'accéder au taux de polarisation P : nous avons trouvé P=26%. Cette valeur est très inférieure à la polarisation mesurée par la réflexion Point-Contact Andreev (65%) [151] ou par la spectroscopie tunnel supraconductrice (53%) [91–93]. La diffusion des électrons et les effets de couplage spin-orbite dans la couche de Ta sont des explications possibles pour expliquer la faible polarisation de spin dans cette structure.

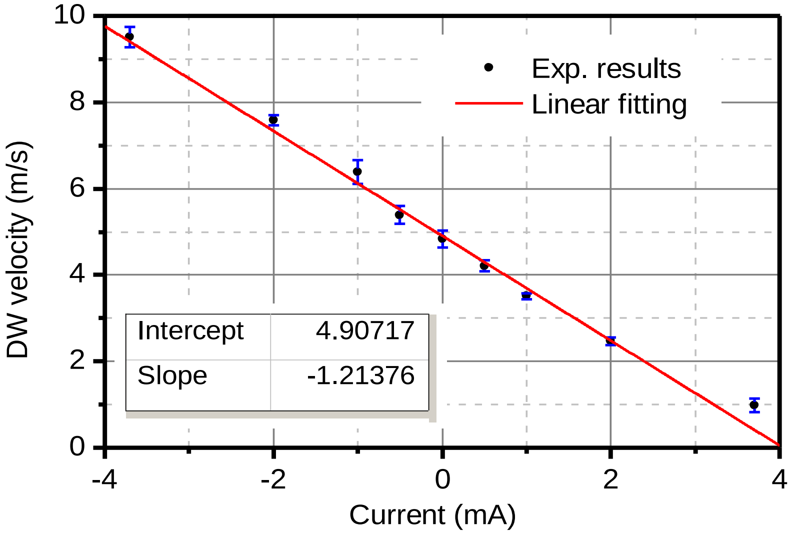

Figure 5 Vélocités moyennes obtenues à partir des résultats de la figure 4 (encadrés en vert). La barre d'erreur a été prise comme l'écart-type. La ligne rouge est un ajustement linéaire sur toutes ces vitesses.

De plus, nous avons constaté que le champ de dépiégeage liés aux gros défauts des nanofils augmentait de façon significative lorsqu'un courant était appliqué simultanément au champ magnétique, quelle que soit la direction de mouvement de la paroi par rapport à la direction de courant d’électrique. Une explication possible de cet effet est un courant de Spin Hall (SH) provenant de la couche de Ta au-dessous, qui induirait un couple supplémentaire. L'effet de ce couple été testé de manière numérique, nos calculs ont débouchés sur un renforcement du piégeage dans certains cas. Cependant, seuls les effets de piégeage extrinsèques sur l'un des deux bords peuvent être renforcée.

Pour finir, un dispositif de mémoire de type racetrack en forme d'anneau basé sur le mouvement de paroi induit par les effets combinés de STT et SOT dans des nanofils a été conçu et émulé à l'aide de calculs micromagnétiques. Ce type de dispositif permet d'éviter la perte de données par rapport à la mémoire de racetrack traditionnelle en forme de ligne.

4. Conclusions et perspectives

Dans cette thèse, nous avons étudié les propriétés et la dynamique des parois de domaines magnétiques dans des films de CoFeB à anisotropie perpendiculaire. Des phénomènes dus à la tension interfaciale des parois ont été observées et la valeur de l’énergie interfaciale a été quantifiée directement. L’effet de piégeage des parois dans des nanofils a été étudié, il est apparu que les plus gros défauts seraient de nature extrinsèque, c'est-à-dire liés à la rugosité de bord induite par la nanostructuration. Le mouvement des parois dans des nanofils induit par le champ et par l’effet combiné du champ et de courant a été étudié. Cela nous a permis d'évaluer le taux polarisation des porteurs de charge dans le CoFeB. Le faible taux trouvé permet d'expliquer les difficulté rencontrées par les différentes équipes pour mettre en mouvement les parois uniquement avec du courant.

D'autres études sont nécessaires pour poursuivre ce projet :

Les deux méthodes développées pour mesurer la tension interfaciale des parois du domaine peuvent être utilisées pour quantifier la constante de DMI et la rigidité d'échange A, paramètres difficiles à mesurer actuellement.

Les effets du courant de SH provenant de la couche de Ta peuvent expliquer le renforcement des effets de piégeage de paroi dans le fil étroit lorsqu'un courant est appliqué. Mais, cette explication n'a été testée qu'avec des simulations micromagnétiques. D'autres expériences sont nécessaires pour étudier cet effet et déterminer si l'origine de notre effet peut être expliqué ainsi. Par exemple, on peut graver des encoches régulières dans le bord des fils pour observer l'influence du courant sur les effets de piégeage de paroi. Le fil peut aussi être agrandi à plus de 10 micromètres de sorte que le comportement des parois pourra être observé clairement, par exemple, l'angle d'inclinaison de la paroi devrait varier en fonction de la densité de courant appliquée, comme prédit par la théorie. L'angle de SH pourrait être extrait de ces expériences.

En ce qui concerne le mouvement de paroi induit champ magnétique et le courant simultané, s'il est vrai qu'il peut être expliqué par les effets combinés du champ et du STT, dans la structure métal lourd/couche magnétique/MgO, il faudrait prendre en compte le courant SH provenant de la couche de métal lourd. Il pourrait être intéressant de mettre en œuvre un champ dans le plan en plus du système actuel et d'étudier l'effet combiné du champ magnétique, du STT et du SOT sur le mouvement de paroi. Certains paramètres importants tels que l'angle SH, la constante non-adiabatique pourraient être correctement extraites grâce à de telles expériences.

ÉCOLE DOCTORALE
Physique et ingénierie : électrons, photons, sciences du vivant (EOBE)

Titre : Le mouvement des parois des domaines magnétiques dans le fil de CoFeB induit par le courant polarisé

Mots clés : Paroi de domaine magnétique, Microscopie Kerr, Nanofil de CoFeB, Tension interfaciale, Couple de transfert de spin, Magnétisme

Résumé : Cette thèse est consacrée aux recherches des propriétés statiques et dynamiques des parois de domaines magnétiques (DW pour Domain Wall) dans les nanofils CoFeB. Un système de mesure basé sur un microscope Kerr à haute résolution a été mis en place et utilisé pour ces recherches.

Tout d'abord, les phénomènes liés à la tension interfaciale des parois ont été étudiés. La contraction spontanée des bulles de domaine a été observée directement en utilisant le microscope Kerr. Ce phénomène a été expliqué en utilisant le concept de la pression de Laplace due à l'énergie interfaciale des parois. L'énergie interfaciale des parois a été quantifiée en mesurant le champ externe nécessaire pour stabiliser ces bulles. Le mécanisme de la piégeage et de la dépiégeage des parois dans certaines géométries artificielles, comme la croix de Hall ou l'entrée reliant un carré de nucléation et un fil, a été expliqué en utilisant le concept de tension interfaciale des parois et a été utilisé pour extraire l'énergie interfaciale des parois. Bénéficiant de ces études, une méthode permettant de quantifier directement le coefficient des Interactions de Dzyaloshinskii- Moriya (DMI pour Dzyaloshinskii- Moriya Interaction) à l'aide du microscope Kerr a été proposée. En outre, un nouveau type de capteur magnétique basé sur l'expansion réversible de paroi en raison de la tension interfaciale a été proposé et vérifié en utilisant des simulations micromagnétiques.

Deuxièmement, les propriétés dynamiques des parois dans le film et les fils Ta / CoFeB / MgO ont été étudiées. La vitesse du propagation des parois induite par le champ magnétique ou par l'effet combiné des impulsions de champ magnétique synchronisées et des impulsions de courant électrique a été mesurée. En régime précessionne, la vitesse du mouvement DW induite par l'effet combiné du champ et du courant est égale à la superposition des vitesses entraînées par le champ ou le courant indépendamment. Ce résultat nous a permis d'extraire la polarisation de spin de CoFeB dans cette structure. Les effets de piégeage du mouvement des parois dans les fils étroits ont été étudiés. Des champs de dépiégeage associés aux gros défauts pour le mouvement des parois induit par champ dans les nanofils a été mesurée. Il a été constaté que les effets de piégeage deviennent plus sévères lorsque la largeur w des fils diminue. Une relation linéaire entre le champ de piégeage et 1/w a été trouvée. L'origine de ces sites d'ancrage durs ainsi que leurs influences sur la vitesse de mouvement des parois ont été discutées. En outre, il a été constaté que l'effet d'épinglage était amélioré lorsque le courant était appliqué, quelle que soit la direction relative entre le mouvement des parois et le courant. Cet accroissement pourrait être expliqué par l'effet du courant de Hall de spin de la sous-couche (Ta). Bien qu'il n'y ait pas eu de DMI ou de champ planaire, le courant de Hall de spin, polarisé dans la direction transversale, peut exercer un couple sur la parois de type de Bloch, une fois que la paroi s'éloigne de la direction transversale.

Enfin, un dispositif mémoire de circuit en forme d'anneau basée sur le travail combiné de STT et SOT a été proposée. Comparée à la mémoire de piste traditionnelle en forme de ligne, cette mémoire en forme d'anneau permet au paroi de demaine de se déplacer dans un nanofil en forme d'anneau sans être éjecté, évitant ainsi la perte des informations associées. Le travail de conception et d'optimisation a été réalisé avec des simulations micromagnétiques.

Title : Spin-polarized current-induced domain wall motion in CoFeB nanowires

Keywords : Domain Wall (DW), Kerr microscopy, CoFeB nanowire, Surface tension, Spin transfer torque (STT), Magnetism

Abstract : This thesis is dedicated to the research of the static and dynamic properties of magnetic Domain Walls (DWs) in CoFeB nanowires. A measurement system based on a high-resolution Kerr microscope was implemented and used for these research.

First, phenomena related to the DW surface tension was studied. A spontaneous collapse of domain bubbles was directly observed using the Kerr microscope. This phenomenon was explained using the concept of the Laplace pressure due to the DW surface energy. The surface energy of DW was quantified by measuring the external field required to stabilize these bubbles. The DW pinning and depinning mechanism in some artificial geometries, such as the Hall cross or the entrance connecting a nucleation pad and a wire, was explained using the concept of DW surface tension and was used to extract the DW surface energy. Benefited from these studies, a method to directly quantify the coefficient of Dzyaloshinskii- Moriya Interactions (DMI) using Kerr microscope has been proposed. In addition, a new type of magnetic sensor based on the revisable expansion of DW due to DW surface tension was proposed and verified using micromagnetic simulations.

Second, the dynamic properties of DWs in Ta/CoFeB/MgO film and wires were studied. The velocity of DW motion induced by magnetic fields or by the combined effect of synchronized magnetic field pulses and electrical current pulses was measured. In steady flow regime, the velocity of DW motion induced by the combined effect of the field and the current equals to the superposition of the velocities driven by field or current independently. This result allowed us to extract the spin-polarization of CoFeB in this structure. Pinning effects of DW motion in narrow wires was studied. Depinning fields of hard pinning sites for the field-driven DW motion in nanowires was measured. It was found that the pinning effects become severer as the width w of the wires scaled down. A linear relationship between the depinning field and w was found. The origin of these hard pinning sites, as well as their influences on the DW motion velocity, was discussed. Furthermore, it was found that the pinning effect was enhanced when a current was applied, no matter the relative direction between the DW motion and the current. We propose a possible explanation, which would be an effect of the spin Hall current from the sublayer (Ta). Although there was no DMI or in-plane field, the spin Hall current, which was polarized in the transverse direction, can still exert a torque on the Bloch DW, once the DW tilts away from the transverse direction.

At last, a ring-shaped racetrack memory based on the combined work of STT and has been proposed. Compared with the traditional line-shaped racetrack memory, this ring-shaped memory allows the DW moving in a ring-shaped nanowire and the data dropout problem can be avoided. The design and optimization work was performed with micromagnetic simulations.